Quanitifying myocardial blood flow using dynamic contrast enhanced cardiac magnetic resonance imaging

John David Biglands

Submitted in accordance with the requirements for the degree of
Doctor of Philosophy (PhD)

The University of Leeds
School of Medicine

School of Computing

October, 2012

The candidate confirms that the work submitted is his own, except where work which has formed part of jointly-authored publications has been included. The contribution of the candidate and the other authors to this work has been explicitly indicated below. The candidate confirms that appropriate credit has been given within the thesis where reference has been made to the work of others.

Chapter 7 is based on the jointly authored publication: “Biglands J, Magee D, Boyle R, Larghat A, Plein S, Radjenovic A, Evaluation of the effect of myocardial segmentation errors on myocardial blood flow estimates from DCE-MRI. *Physics in medicine and biology*. 2011;56(8):2423–43.” J. Biglands carried out the perfusion analysis, computational modelling, statistical analysis and software development, generated all the results and wrote the final manuscript under the supervision of D. Magee, R. Boyle and A. Radjenovic. The MRI investigations on volunteers were conducted by A. Larghat under the supervision of S. Plein using an imaging sequence designed and tested by A. Radjenovic.

Chapter 2, Sections 2.7 to 2.9 are based on the jointly authored publication: “Biglands, John D, Radjenovic A, Ridgway JP. Cardiovascular magnetic resonance physics for clinicians: part II. *Journal of Cardiovascular Magnetic Resonance*. 2012;14(66).” J. Biglands wrote the sections in this publication entitled “Using exogenous contrast agents to modify contrast” and “Myocardial perfusion imaging”, which have been modified for inclusion in chapter 2. Other sections of the publication were written by J. Ridgway and A. Radjenovic and all authors proof read and approved the final manuscript.

In addition the algorithms and methods described in this thesis have been used in a number of publications. These are referenced below along with a description of the involvement of the author of this thesis.

Full papers

Motwani M, Fairbairn TA, Larghat A, Mather AN, Biglands JD, Radjenovic A, Greenwood JP, Plein S. Systolic versus Diastolic acquisition in Myocardial Perfusion MRI Imaging. *Radiology*. 2012;262(3). MBF estimates were derived using software developed by the author. Signal values were converted to concentrations using software developed by the author. The author proof read, commented on and approved the final manuscript.

Larghat A, Biglands J, Maredia N, Greenwood JP, Ball SG, Jerosch-Herold M, Radjenovic A, Plein S. Endocardial and epicardial myocardial perfusion determined by semi-quantitative and quantitative myocardial perfusion magnetic resonance. *The international journal of cardiovascular imaging*. 2011; 28(6): 1499-511. MBF estimates were derived using software developed by the author. Signal values were converted to contrast agent concentrations using software developed by the author. The author proof read, commented on and approved the final manuscript.

Johnstone RI, Greenwood JP, Biglands JD, Plein S, Ridgway JP, Radjenovic A. Assessment of tissue edema in patients with acute myocardial infarction by computer-assisted quantification of triple inversion recovery prepared MRI of the myocardium. *Magnetic resonance in medicine.* 2011;66(2):564–73. The author assisted in the development of software to process the images for this study. The author proof read, commented on and approved the final manuscript.

Radjenovic A, Biglands JD, Larghat A, Ridgway JP, Ball SG, Greenwood JP, Jerosch-Herold, M, Plein S. Estimates of systolic and diastolic myocardial blood flow by dynamic contrast-enhanced MRI. *Magnetic resonance in medicine*. 2010;64(6):1696–1703. The author assisted in the development of software to process the images for this study. The author proof read, commented on and approved the final manuscript.

Meeting abstracts

Society of cardiac magnetic resonance (SCMR) meeting

Biglands JD, Magee DR, Boyle R, Larghat AM, Jerosch-Herold M, Plein S, Radjenovic A. Evaluation of the effect of myocardial localisation errors on myocardial blood flow estimates from DCE-MRI. *Journal of Cardiovascular Magnetic Resonance*. 2010;12(Suppl 1):P235. The author carried out the perfusion analysis, computational modelling, statistical analysis, software development, generated all the results and wrote the final abstract.

Broadbent DA, Biglands JD, Larghat AM, Sourbron S, Plein S, Buckley DL. Myocardial microvascular function at rest and stress measured with dynamic contrast-enhanced MRI. *Journal of Cardiovascular Magnetic Resonance*. 2012;14(Suppl 1):P283. Signal values were converted to concentrations using software developed by the author. The author proof read, commented on and approved the final abstract.

Motwani M, Fairbairn T, Larghat AM, Mather AN, Biglands JD, Radjenovic A, Greenwood JP, Plein S. Systolic versus diastolic myocardial blood flow in patients with suspected coronary artery disease - a cardiovascular magnetic resonance study. *Journal of Cardiovascular Magnetic Resonance*. 2012;14(Suppl 1):P17. MBF estimates were derived using software developed by the author. Signal values were converted to contrast agent concentrations using software developed by the author. The author proof read, commented on and approved the final abstract.

Asrress KN, Williams R, Lockie T, Biglands JD, Chiribiri A, Radjenovic A, Jogiya R, De Silva K, Kozerke S, Chowienczyk P, Nagel E, Marber M, Redwood S, Plein S. Increased endocardial to epicardial flow ratio present at rest disappears during exercise stress perfusion CMR in normal volunteers – a potential mechanism for exercise induced subendocardial ischaemia. *Journal of Cardiovascular Magnetic Resonance*. 2012; 14 (Suppl 1):P226. MBF estimates were derived using software developed by the author. The author proof read, commented on and approved the final abstract.

Larghat AM, Biglands J, Greenwood JP, Fairbain TA, Maredia N, Radjenovic A, Ball S, Plein S. Myocardial blood flow in patients with Type 2 Diabetes Mellitus and normal coronary angiography. *Journal of Cardiovascular Magnetic Resonance*. 2011;13(Suppl 1):P275. MBF estimates were derived using software developed by the author. The author proof read, commented on and approved the final abstract.

Maredia N, Plein S, Younger JF, Brown JM, Nixon J, Everett CC, Ridgway JP, Radjenovic A, Dickinson CJ, Biglands JD, Larghat AM, Ball SG, Greenwood JP. Detection of triple vessel coronary artery disease by visual and quantitative first pass CMR myocardial perfusion imaging in the CE-MARC study. *Journal of Cardiovascular Magnetic Resonance*. 2011;13(Suppl 1):O29. MBF estimates were derived using software developed by the author. The author proof read, commented on and approved the final abstract.

Larghat AM, Radjenovic A, Maredia N, Biglands J, Greenwood J, Plein S. Reproducibility of first pass perfusion CMR at rest and during hyperaemia for estimation of myocardial perfusion. *Journal of Cardiovascular Magnetic Resonance*. 2010;12(Suppl 1):P228. MBF estimates were derived using software developed by the author. The author proof read, commented on and approved the final abstract.

Larghat AM, Radjenovic A, Maredia N, Biglands J, Greenwood JP, Jerosch-Herold M, Plein S. Subendocardial to subepicardial absolute myocardial blood flow at rest and hyperaemia determined by first pass CMR and Fermi deconvolution modelling. *Journal of Cardiovascular Magnetic Resonance*. 2010;12(Suppl 1):P223. MBF estimates were derived using software developed by the author. The author proof read, commented on and approved the final abstract.

Johnstone R, Ridgway J, Biglands J, Greenwood J, Radjenovic A. Assessment of cardiac oedema in patients with acute myocardial infarction by manual planimetry and computerised segmentation of triple inversion recovery prepared turbo spin echo images. *Journal of Cardiovascular Magnetic Resonance*. 2009;11(Suppl 1):51. The author assisted in the development of software to process the images for this study. The author proof read, commented on and approved the final abstract.

International society of magnetic resonance imaging (ISMRM) meeting

Biglands JD, Larghat A, Plein S, Magee DR, Boyle R, Radjenovic A, Myocardial contour error distance metric evaluators do not correlate with myocardial blood flow estimates from DCE-MRI cardiac perfusion, *In Proceedings of the International Society of Magnetic Resonance Imaging*, 2011 Montreal. The author carried out the perfusion analysis, computational modelling, statistical analysis, software development, generated all the results and wrote the final abstract.

Biglands JD, Larghat A, Plein S, Magee DR, Boyle R, Radjenovic A. The effect of myocardial contour errors on myocardial blood flow estimates in cardiac DCE-MRI perfusion, *In Proceedings of the International Society of Magnetic Resonance Imaging*, 2011 Montreal. The author carried out the perfusion analysis, computational modelling, statistical analysis, software development, generated all the results and wrote the final abstract.

Biglands JD, Larghat A, Plein S, Buckley DL, Jerosch-Herold M, Magee D, Boyle R, Radjenovic A. Saturation correction of dynamic contrast enhanced MRI uptake curves for quantitative myocardial blood flow measurements using an assumed T_1 for blood. *In Proceedings of the International Society of Magnetic Resonance.* 2010, Stockholm. The author carried out the perfusion analysis, computational modelling, statistical analysis, software development, generated all the results and wrote the final abstract.

Buckley DL, Biglands JD, Larghat A, Sourbron SP, Radjenovic A, Greenwood JP, Plein S. Myocardial microvascular function at rest and under adenosine stress measured with dynamic contrast-enhanced MRI. *In Proceedings of the International Society of Magnetic Resonance Imaging*, 2011 Montreal. Signal values were converted to contrast agent concentrations using software developed by the author. The author proof read, commented on and approved the final abstract.

Radjenovic A, Biglabnds JD, Larghat A, Greenwood JP, Jerosch-Herold M, Plein S. Comparison of systolic and diastolic perfusion by dynamic contrast enhanced MRI. *In Proceedings of the International Society of Magnetic Resonance*. 2010 Stockholm. The author assisted in the development of software to process the images for this study. The author proof read, commented on and approved the final abstract.

American heart association (AHA) meeting

Larghat A, Biglands J, Greenwood J, Fairbain TA, Maredia N, Radjenovic A, Ball SG, Plein S. Myocardial blood flow in angiographically normal patients with type 2 Diabetes mellitus, prediabetes and normal controls – A cardiovascular magnetic resonance perfusion study. *Circulation*. In AHA scientific Sessions, 124, 2011: A15128. MBF estimates were derived using software developed by the author. The author proof read, commented on and approved the final abstract.

Fairbairn A, Motwani M, Mather AN, Biglands JD, Larghat AM, Greenwood JP, Plein S. Myocardial blood flow changes during cold pressor testing for the assessment of endothelial function. A Cardiovascular Magnetic Resonance study. *Circulation*. In AHA scientific Sessions, 124(21), 2011: A1496. MBF estimates were derived using software developed by the author. The author proof read, commented on and approved the final abstract.

Acknowledgements

Sincere thanks go to my supervisors Dr. Sasha Radjenovic, Dr. Derek Magee, and Prof. Roger Boyle (who retired during the period of this research). Beyond their considerable academic expertise they have displayed enthusiasm and a much needed sense of humour, which have made supervision meetings as enjoyable as they have been educational.

In addition I am immensely grateful to Dr. Steven Sourbron, Prof. David Buckley and Dr. John Ridgway who have been tremendously generous with their time in helping me to understand DCE-MRI physics and to Prof. Sven Plein and Dr. John Greenwood for clinical discussions.

I would like to thank Dr. Neil Maredia, Dr. Adam Mather, Dr. Tim Fairbairn, Dr. Abdulghani Larghat, Dr. Akhlaque Uddin, Dr. Manish Motwani and Dr. Ananth Kidambi for their interest in this research and for enabling it to be applied in so many clinical contexts. I am indebted to the Leeds cardiac MR radiographers Margaret Saysell, Gavin Bainbridge and Caroline Richmond for scanning the patients and volunteers. My heartfelt thanks go to my fellow PhD student sufferers Constantine Zakharov and Owen Richardson for much needed moral support and coffee!

I thank my mother and sister for supporting me in every way they knew how and Les Goldstraw for teaching me to love knowledge wherever it lies. I reserve my biggest thankyous for my wife Jenny and my two children Ellie and Josiah (who was born during this PhD). Jenny has believed in me more than I believed in myself and, in these last months, has made monumental sacrifices to enable me to spend the time I needed to complete this thesis. Ellie and Josiah are a constant source of joy to me. My family makes me richer than I ever expected to be and I thank God for them as I thank him for the gift of my own life and the dreams that I have been able to chase in the time that I have been given.

Abstract

The assessment of myocardial perfusion using dynamic contrast enhanced magnetic resonance imaging (DCE-MRI) is a powerful tool for diagnosing myocardial ischaemia due to coronary heart disease, which affects nearly 2.7 million people in the UK and for which there is an effective treatment. Although visual analysis of DCE-MRI data performs well diagnostically, a quantitative estimate of myocardial blood flow (MBF) makes the diagnosis objective and could increase diagnostic performance. Obtaining MBF estimates from DCE-MRI data is a multi-step process requiring:

- the localisation of the myocardium and arterial input function (AIF) to generate signal intensity vs. time curves;
- the conversion of signal intensity data to contrast agent concentration values;
- the application of a perfusion model to generate a quantitative MBF estimate;
- the interpretation of MBF estimates to make a diagnostic assessment of myocardial ischaemia.

There are a range of approaches for solving each of these problems. The aim of the work presented in this thesis has been to provide clinically relevant evidence for choosing between these approaches. Myocardial localisation contour error tolerance levels are suggested based on simulations using a volunteer dataset. A non-linear signal intensity to contrast agent concentration conversion method is presented and tested using simulations and phantom data. An investigation into the best way to interpret quantitative MBF estimates is then presented. Finally a comparison of four, widely applied, perfusion models is conducted.

Where possible, methods have been compared on a sizeable patient dataset in terms of diagnostic performance rather than MBF estimate accuracy. This provides evidence suitable for informing clinical decisions on the best methodology for quantitative perfusion. Such evidence could contribute to a standard methodology for quantitative cardiac MR perfusion. This is necessary for large clinical trials, which are essential before quantitative MBF estimates can be accepted into routine clinical practice.

Table of Contents

List of Tables

List of Figures

List of abbreviations

2CXM – Two Compartment eXchange Model

AHA – American Heart Association.

AIF – Arterial Input Function

ANOVA – Analysis Of Variance

AUC – Area Under Curve

BAT – Bolus Arrival Time

bSSFP – Balanced Steady State Free Precession

CA – Contrast Agent

CABG - Coronary Artery Bypass Graft

CAD – Coronary Artery Disease

CE-MARC – Clinical Evaluation of MAgnetic Resonance imaging in Coronary heart disease.

CER – Contrast Enhancement Ratio

CFR – Coronary Flow Reserve

CHD – Coronary Heart Disease

CMR – Cardiac Magnetic Resonance

CNR – Contrast to Noise Ratio

CT – Computed Tomography

DCE – Dynamic Contrast Enhanced

DRA – Dark Rim Artifact

DSC – Dice’s Similarity Coefficient

DTPA - Diethylene Triamine Pentaacetic Acid

EBCT – Electron Beam CT

ECG – Electrocardiogram

EES – Extracellular, Extravascular Space

ETL – Echo Train Length

ETM – Extended Tofts Model

EPI – Echo Planar Imaging

FAS – Flip Angle Sweep

FFE – Fast Field Echo

FFR – Fractional Flow Reserve

FT – Fourier Transform

Gd - Gadolinium

GRE – Gradient Recalled Echo

GUI – Graphical User Interface

Hct – Hematocrit

HD – Haussdorff Distance

HU – Hounsfield Units

IHD – Ischaemic Heart Disease

IR – Inversion Recovery

IRSE – Inversion Recovery Spin Echo

LA – Left Atrium

LAD – Left Anterior Descending artery

LCX – Left CircumfleX artery

LGE – Late Gadolinium Enhanced

LMS – Left Main Stem

LV – Left Ventricle

MBF – Myocardial Blood Flow

MD – Maximum Deviation

MIBI - MethoxyIsoButylIsonitrile

ModI – Model Independent

MOLLI – Modified Look-Locker Inversion Recovery

MPI – Myocardial Perfusion Imaging

MPR – Myocardial Perfusion Reserve

MRI - Magnetic Resonance Imaging

MW – Myocardial Width

NSF - Nephrogenic Systemic Fibrosis

OneCP – One ComPartment model

PCI – Percutaneous Coronary Intervention

PET – Positron Emission Tomography

PTCA- Percutaneous Transluminal Coronary Angioplasty

QCA – Quantitative Coronary Angiography

RA – Right Atrium

RCA – Right Coronary Artery

ROC – Receiver Operator Curve

ROI – Region of Interest

RF – RadioFrequency

rFOV - rectangular Field Of View

RV – Right Ventricle

SA - SinoAtrial

SD – Standard Deviation

SE – Spin Echo

SENSE – SENSitivity Encoding

SI – Signal Intensity

SNR – Signal to Noise Ratio

SPECT – Single Photon Emission Computed Tomography

SR – Saturation Recovery

SVD – Singular Value Decomposition

^{99m} Tc – Technetium (A metastable isomer of Technetium-99)

T_1 – longitudinal, spin-lattice, relaxation time

T_2 – transverse, spin-spin, relaxation time

TD – Trigger Delay

TFE – Turbo Field Echo

TE – Echo Time

TI – Inversion Time

TR – Repetition Time

TS – Saturation Time

TSVD – Truncated Singular Value Decomposition

1. Introduction

1.1. Background

Coronary heart disease (CHD) is the formation of plaque in the coronary arteries that supply blood to the heart. The resulting arterial narrowing can reduce blood flow to the heart causing myocardial ischaemia leading to painful angina symptoms. Complete obstruction, most commonly through thrombus formation on a vulnerable plaque, may result in myocardial infarction (cardiac cell death), know as a heart attack. CHD affects 2.7 million people in the UK (1) but, if a patient is diagnosed, there is an effective treatment by coronary angioplasty or coronary bypass grafting (see section 3.3).

The methods for diagnosing CHD and myocardial ischaemia are many and varied (see section 3.4). However, the role of magnetic resonance imaging (MRI) in the assessment of myocardial perfusion is becoming more and more recognised within the cardiology community. At the time of writing two of the largest clinical trials for cardiac MR perfusion have shown that the cardiac dynamic contrast enhanced (DCE)-MRI perfusion test is as specific and more sensitive than the current standard assessment, nuclear medicine, in diagnosing CHD (2,3). Furthermore, there is reason to hope that these figures will improve in the future as subendocardial defects become more easily detectable with ever increasing image resolution and signal to noise ratio (SNR) capabilities in MRI.

These assessments were performed using a visual analysis of the MR data. Corresponding large scale diagnostic performance studies using quantitative myocardial blood flow (MBF) estimates based on cardiac DCE-MRI data are lacking. Such studies would show whether quantitation can improve diagnosis of CHD. Of particular interest is the impact on diagnosing three vessel disease, where stenoses in all three coronary vessels can confound visual detection as there is no healthy myocardium to compare against. Apart from the extra complexity and time-consuming nature of many aspects of quantitative image acquisition and analysis, a further obstacle to researchers seeking to undertake such trials is the lack of consensus on the analysis method.

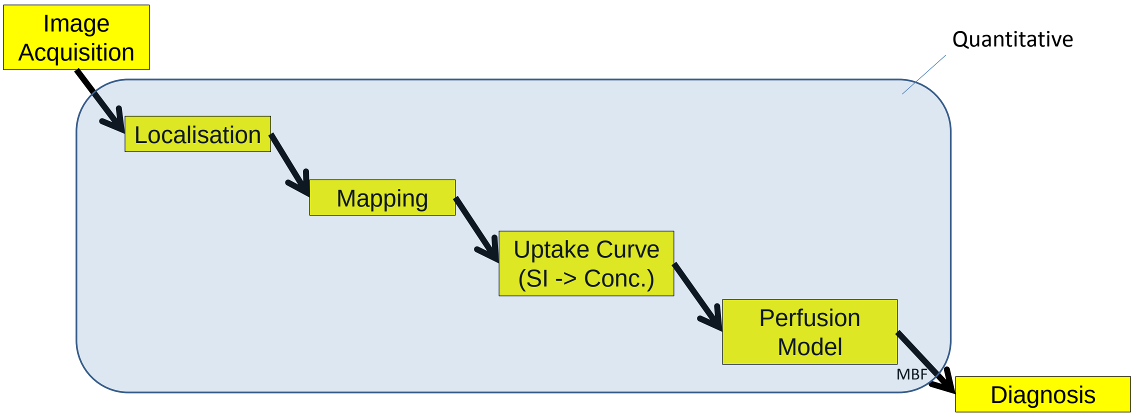

Figure 1-1 – Flow diagram depicting the analysis pathway for quantitative DCE-MRI cardiac perfusion. After the DCE-MRI dataset has been acquired the myocardium and blood pool arterial input function (AIF) must be identified on every image frame (*localisation*). Typically the myocardium is then subdivided into regions related to different coronary arteries (*mapping*). Signal intensity (SI) vs. time *uptake curves* must then be generated from each frame and then converted to contrast agent concentrations. A *perfusion model* is then applied to the two uptake curves in order to generate a quantitative estimate of myocardial blood flow (MBF). This MBF value must then be interpreted in order to make a *diagnosis* as to whether the myocardial region is ischaemic or not. Only quantitative, or semi-quantitative, analysis requires the steps within the box.

The analysis pathway for quantitative perfusion is outlined in Figure 1-1. Each of the steps in Figure 1-1 has been the subject of substantial research effort and, as a result, there are a variety of techniques available to tackle each one and each solution has its own set of advantages and disadvantages. This leaves the research community with a vast array of options for performing quantitative analysis. The lack of a standardised consensus approach for quantifying MBF limits the generalisability of any trial using quantitative MBF values, as any differences in methodology could feasibly affect the results. What evidence is there upon which to formulate a consensus methodology? Validation of each new innovation has been in terms of the measured MBF, either using animal studies, or an independent measurement in humans such as PET. One comparison of quantitative perfusion models on the same dataset has been performed showing good agreement of MBF values between perfusion models (4). However, differences in MBF between different studies can be quite profound. For example compare the results of (5) and (6) rest MBF 0.52 ± 0.11 ml/g/min to 0.88 ± 0.28 ml/g/min and stress MBF 1.78 ± 0.53 ml/g/min to 2.32 ± 0.46 ml/g/min. Both of these studies were performed in healthy volunteers having previously reported good correlations with PET.

The ultimate purpose of the MBF measurement is to diagnose ischaemia. Therefore, the most powerful evidence base for a consensus opinion on quantitative analysis is a comparison of diagnostic performance between methods on real-world clinical data. Differences observed in terms of diagnostic performance will have a more profound influence on clinical choices, and real-world clinical datasets differ from healthy volunteer studies. Clinical datasets are more prone to patient dependent problems, such as poor breath-holding and unreliable ECG data, and of course include perfusion defects and lower MBF values. Therefore, when attempting to distinguish methods for clinical use, it is important to use data that includes patients suffering from CHD. Furthermore, in the context of imperfect, real-world imaging it may be that the distinguishing factor between methods is not the accuracy of the measurement but the robustness to imperfections in the datasets enabling application to a wider cohort of patients.

1.2. Aims

The primary aim of this research was to compare quantitative perfusion models in terms of diagnostic performance. This involved providing a method for non-linear conversion of the MR signal to contrast agent concentration values and automated methods for processing large volumes of DCE-MRI data. A comparison of methodologies for obtaining a diagnosis from MBF estimates has also been performed. The aims of this research are related to the methodological steps outlined in Figure 1-1 as follows:

Aim 1 – To compare quantitative perfusion models in terms of diagnostic performance (perfusion model).

Aim 2 – To compare methodologies for interpreting regional quantitative MBF estimates in terms of diagnostic performance (mapping).

Aim 3 – To provide myocardial contour error tolerance levels for quantitative perfusion purposes (localisation).

Aim 4 – To provide a methodology for converting MR signal values to concentrations, specific to the pulse sequence used in this research (uptake curve).

Aim 5 – To provide fully automated quantitative perfusion uptake curve processing algorithms.

1.3. Overview

Chapter 2 provides a description of the basic physics of MRI before describing the imaging pulse sequences applied to cardiac perfusion imaging. The choices and compromises that must be made when designing a perfusion imaging sequence are then described taking into account the extra considerations pertinent to quantitative imaging.

Chapter 3 gives a brief description of cardiac anatomy and physiology before describing coronary heart disease and its treatment. A review of medical imaging modalities for diagnosing CHD and myocardial ischaemia is given before a more detailed discussion is made of the advantages and disadvantages of cardiac perfusion MRI including a review of the diagnostic performance literature.

Chapter 4 provides an explanation of the models used to make estimates of MBF. Semi-quantitative methods are described briefly before a detailed mathematical description of the quantitative methods used in this thesis is given.

Most of the research presented in this thesis is based on two datasets. Chapter 5 describes in detail the acquisition protocol for the dual-phase study and the CE-MARC trial. The original purposes of the investigations are given along with the pulse sequence parameters. A description of the manual contouring methodology applied in all cases is then provided. The automated methods used for uptake curve pre-processing (prior to quantitative analysis) are then described and tested qualitatively.

Chapter 6 explains the method used to convert signal intensity values into contrast agent concentrations. The pulse sequence for the acquisition of the perfusion DCE-MRI data is represented as a mathematical model. The assumptions of this model are then tested using computer simulations. The model is then further tested using images acquired of a T_1-gel phantom using the perfusion imaging sequence.

Chapter 7 describes a novel method used to derive tolerance limits for myocardial contours. In order to assess the affect of myocardial contour errors on MBF estimates, contour errors are simulated on manual contours applied to a dataset of healthy volunteers. These simulations are used to describe the relationship between contour errors and MBF errors. This relationship is then used to provide a basis for setting an allowable error rate in the context of global and regional perfusion analysis.

Chapter 8 describes the subset of patients taken from the CE-MARC trial before describing the exclusion process for this dataset. The dataset is then used to investigate whether the non-linear concentration conversion described in chapter 6 improves diagnostic power. Separate investigations are then performed to attempt to find the best way to use regional MBF estimates for diagnosing myocardial ischaemia. The use of separate MPR cut-offs for each of the coronary arteries is investigated. An investigation into whether the mean or minimum regional MPR value should be used is conducted. Finally the comparative power of using only the middle imaging slice, as opposed to all three slices, is carried out and the diagnostic performance when global analysis is used instead of regional analysis is evaluated.

In chapter 9 four quantitative perfusion methods are compared in terms of diagnostic performance. Model-independent deconvolution, Fermi-constrained deconvolution, the uptake model and the one-compartment model are implemented on the entire CE-MARC subset. The diagnostic performance of these four models is then compared using the methods derived in chapter 8.

Chapter 10 draws general conclusions from the research described in this thesis, details the limitations of the research and provides recommendations for future work.

2. Background: perfusion MRI physics

2.1. Introduction

Although the basics of MRI have been described many times in the literature this thesis will have cause to analyse the evolution of longitudinal magnetization M_z in detail and so would not be complete without a description of this concept. Numerous MRI texts have described the basics of magnetic resonance with reference to spin-up and spin-down energy eigenstates. However, other authors argue that this has led to confusion and that the classical description is adequate for understanding magnetic resonance imaging (7,8). For this reason the description given in this thesis follows that of Levitt (8), and is an entirely classical description. After describing the origins of the MR signal, the basic gradient recalled echo sequence is described. A brief description of the extensions to this sequence that are most commonly applied in cardiac perfusion imaging is then presented. A discussion of the multiple factors that must be taken into account when designing a perfusion sequence and the inevitable compromises that must be struck between competing demands on the resulting image is then given. This latter part is based on sections of a review paper recently published in JCMR (9), written by the author of this thesis.

2.2. The origin of the MR signal

Nucleons possess a magnetic moment and an angular momentum by virtue of an intrinsic property called ‘spin’. The spin angular momentum $\boldsymbol{S}$ and magnetic moment $\boldsymbol{\mu}$ are proportional to each other and are oriented either parallel or anti-parallel to each other dependent on the sign of the gyromagnetic ratio $\boldsymbol{\gamma}$**:**

$$\boldsymbol{\mu} = \gamma \boldsymbol{S}$$

Equation 2-1

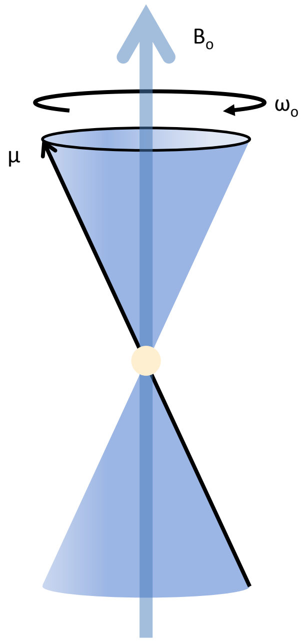

Figure 2-1 - In the presence of an external magnetic field, B_o, the spin magnetic moment μ precesses around B_o at an angular frequency ω describing a cone shape.

The spin angular momentum is a vector which can point in any direction in three-dimensional space, thus the magnetic moment can also point in any direction. In the presence of an external magnetic field, B_o, the combination of the angular and magnetic moments of the spin causes it to precess around the external magnetic field describing a cone, keeping a constant angle between the spin magnetic moment and B_o (Figure 2-1). The frequency of precession is known as the Larmor frequency, ω_o, and is given by the Larmor equation:

$$\omega_o = -\gamma B_o$$

Equation 2-2

2.3. Longitudinal recovery

By virtue of the fact that the spins are initially randomly orientated the net magnetization over any macroscopic sample is zero. Once placed into an external magnetic field the spins all precess at the same angular frequency (assuming a completely homogeneous B_o) but this has no affect on the net magnetization due to the arbitrary phase of each precessing spin. However the molecules that carry the protons are in constant motion. This in itself has no effect on the orientations of the spins, which maintain their orientation independent of molecular orientation. However each molecule possesses small localised magnetic fields. The magnetic field at a given time is the sum of B_o and contributions from the immediate molecular neighbourhood. Thus, each spin experiences small fluctuations in magnetic field strength which lead to small changes in the cone angle between $\boldsymbol{\mu}$ and B_o. Over time the magnetic moment wanders over the complete range of possible cone orientations.

The magnetic energy between two magnetic moments is at a minimum when those two moments are parallel. At finite temperatures it is slightly more probable that each spin is driven to an orientation with low magnetic energy than to a high magnetic energy (8). Thus, as the spins wander through cone angles there is a slight preference for alignment with B_o. Over time this leads to a stable state where there is a finite net magnetization parallel with $B_{o.}$ This is denoted M_{eq} as it is the magnetization at thermal equilibrium. At any one time the net magnetization is M_{eq} however the individual spins are still constantly changing orientation and the net magnetization is due to the slight preference in the system toward low energy magnetization orientations.

The transition to thermal equilibrium after exposure to B_o is not instantaneous. The net magnetization in the z-direction at time t, $M_z(t)$, increases exponentially to M_{eq}:

$$M_z(t) = M_{eq}\left(1 - e^{-t/T_1}\right)$$

Equation 2-3

T_1 is the longitudinal relaxation time and describes the rate at which the system arrives at thermal equilibrium. Importantly for magnetic resonance imaging (MRI) T_1 is different for different substances. Fundamentally T_1 depends on the correlation time of the molecular motion, i.e. how fast the molecules move. By acquiring data at different times on the T_1 recovery curve MRI is able to generate images with different M_z values for different tissues and this is one of the sources of image contrast in MRI.

2.4. Transverse magnetization

The longitudinal net magnetization is almost undetectable along the z-axis in the presence of the large B_o field. In an MR experiment, in order to be able to detect the net magnetization, it is flipped into the transverse plane. This is done by applying, for a brief time, a second magnetic field, B_1, which is perpendicular to B_o. The spins, still precessing around B_o, now begin to precess around B_1 resulting in the net magnetization spiralling into the transverse plane. Because the spins are precessing at ω_o the B_1 field must oscillate at the same frequency in order for each spin to experience a constant magnetic field relative to its constantly changing orientation. The rate of oscillation required is in the radiofrequency range of the electromagnetic spectrum (Figure 2-2).

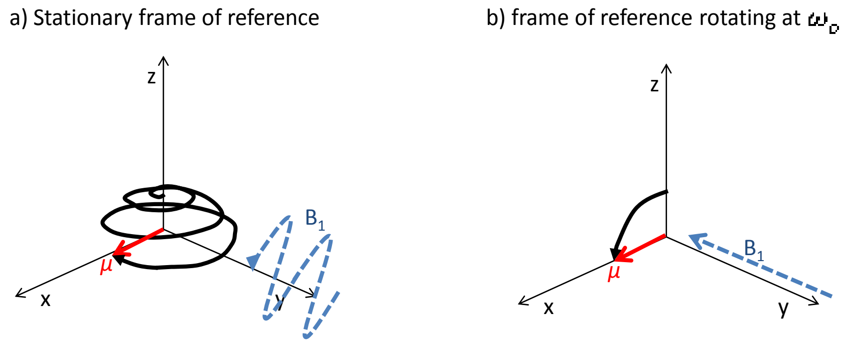
a) Stationary frame of reference

b) frame of reference rotating at ω_o

Figure 2-2 – a) The net magnetization simultaneously precesses about B_o and a second magnetic field oscillating at exactly ω_o causing the net magnetization to spiral into the transverse plane. b) Viewed from a frame of reference rotating at ω_o the oscillations of B_1 are removed and the net magnetization appears to simply flip directly into the xy-plane.

The preference in the spins for alignment with B_o has now been rotated 90^o from the z-axis and manifests as a preference to precess in phase in the xy-plane. The net magnetization now rotates around the z-axis with an angular frequency ω_o. Once in the xy-plane the net magnetization can be measured by the strength of electric signal it induces in a wire coil placed near the sample and this is the basis for all MR measurements. The net magnetization will return to align with B_o at a rate dictated by T_1 as described in section 2.3.

However, the transverse magnetization decays by a separate mechanism. Directly after the B_1 field has been switched off the spins start to dephase and the transverse net magnetization rapidly deteriorates. Fluctuations in the microscopic magnetic field that each spin experiences cause small changes in precessional frequency which lead to dephasing and deterioration of the net transverse magnetization. In real-world MR experiments spatial inhomogeneities in the generated B_o field are also responsible for dephasing. The transverse magnetization, $M_{xy}(t)$, decays exponentially according to the transverse relaxation time constant T_2 (or T_2^* when B_o inhomogeneities are not corrected for) according to:

$$M_{xy}(t) = M_{eq}e^{-t/T_2}$$

Equation 2-4

2.5. Generating an image: localisation

The process described so far leads only to the measurement of an oscillating electric signal in a conducting coil placed near the substance. How can these signals be interpreted to generate an image? Almost all image localisation in MRI is performed using temporally variable magnetic gradients[1]. These are generated by additional coils positioned inside the bore of the main superconducting magnet, which generate small gradient magnetic fields that add and subtract from the main B_o field.

Selective excitation (slice selection)

If a magnetic field gradient is applied across the object of interest the precessional frequencies vary spatially with the gradient. As described in section 2.4 the B_1 field must be at the Larmor frequency for spins to rotate into the transverse plane. By limiting the radiofrequency bandwidth of the B_1 pulse whilst the gradient is applied the B_1 field is limited to only effect spins in a finite spatial area (Figure 2-3).

---

[1] In parallel imaging the position of the multiple coils is also used as part of the image generation process.

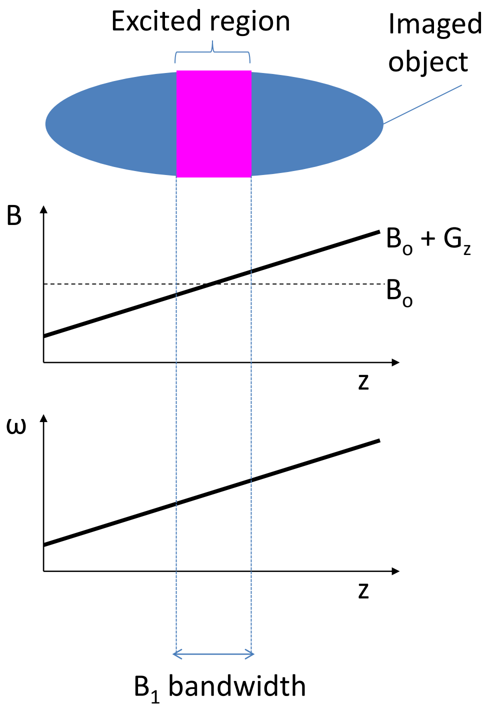

Figure 2-3 – By applying an additional gradient, G_z, whilst exposing the object only to a limited bandwidth of B_1 frequencies only spins in a finite slice are excited.

Localisation within the excited slab is performed by exploiting the Fourier transform (FT), which transforms time domain signals into the frequency domain and vice versa. Applying a frequency encoding magnetic field gradient in the x direction causes spins at higher field strengths to precess at higher frequencies. In other words frequency has become a function of x:

$$\omega(x) = -\gamma(B_o + G_x x)$$

Equation 2-5

Where $\omega(x)$ is the precessional frequency at a position *x* along the x-axis and G_x is the gradient strength *dB/dx*. The time domain signal will consist of signal from all the spin frequencies from the entire excited slab. However, the Fourier transform converts this time domain signal onto a frequency axis. As the signals have been encoded such that frequency is synonymous with position the frequency axis can be reinterpreted as spatial position (Figure 2-4).

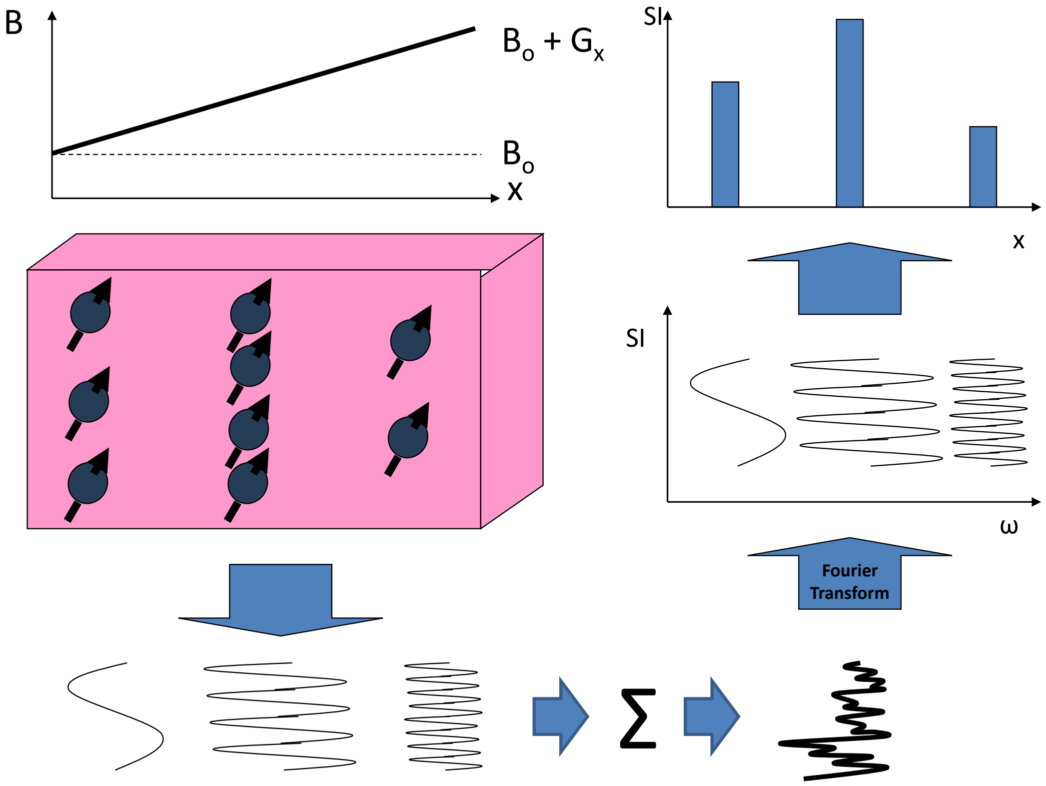

Figure 2-4 – Precessional frequency increases with x due to the magnetic field gradient G_x. The measured signal is the sum of all spin frequencies and amplitudes. The Fourier transform represents these on a frequency axis. As frequency is synonymous with spatial position, by virtue of the frequency encoding gradient G_x, the frequency axis can be reinterpreted as position along the x direction[2].

The final spatial dimension is encoded in terms of the phase of the spins. Prior to frequency encoding a phase encoding magnetic field gradient is applied, orthogonal to the frequency encoding direction, which varies the spin frequency for a short interval before the phase encoding gradient is turned off (Figure 2-4). In this case *phase* is encoded with distance *y*:

$$\Delta\phi(y) = \gamma \int_0^T y G_y(t)\,dt$$

Equation 2-6

---

[2] The final amplitudes in Figure 2-4 have been drawn to reflect proton density (the number of spins at a given frequency). In most MR images the signal strength is dominated by T_1 and T_2 contrast.

Where $\Delta\phi(y)$, is the change in phase at position *y*, T is time for which the phase encoding pulse is applied and G_y is the phase encoding gradient $G_y = dB/dy$.

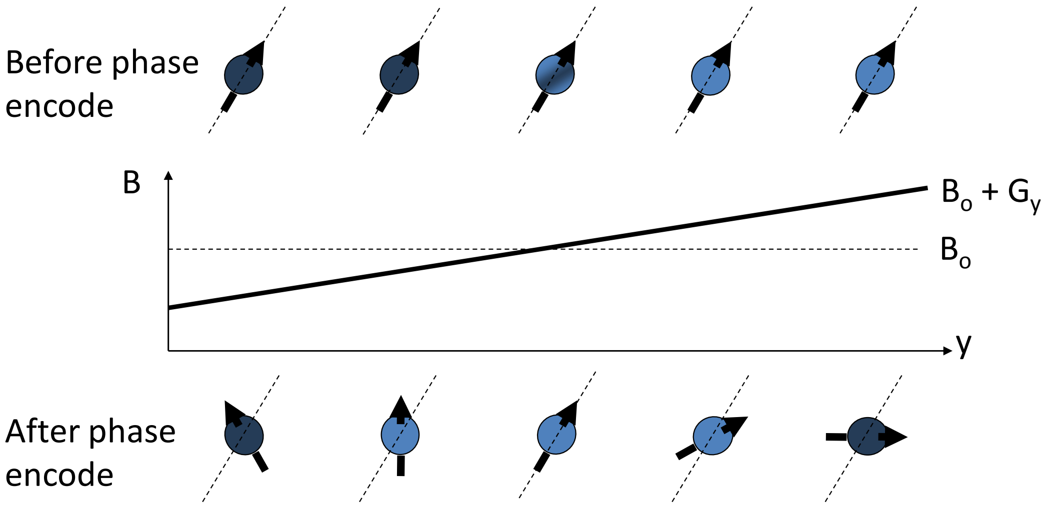

Figure 2-5 – After the application of a phase encoding gradient for a short time in the y direction the spin's phase is a function of distance along y.

The Fourier transform can only analyse time variant signals and so cannot decode a single phase encoding step. Therefore, the process is repeated over a range of phase encoding gradients. The signals from each phase encoding step are arranged in order of phase encoding gradient amplitude in a matrix known as k-space. In the frequency encoding direction the data represents time variant changes in signal whose Fourier transforms are frequencies, which have been encoded to represent position along x. In the phase encoding direction the data represents the rate of change of phase at each position in the object over all of the phase encoding steps. The rate of change of phase will be higher at the outer edges of the object where the gradient changes were most extreme. The Fourier transform in this direction will represent rate of change of phase as simply another frequency, which has been encoded to represent distance along the y direction. Thus, by representing the data in this way and performing a 2D Fourier transform an image of the MR signal is produced.

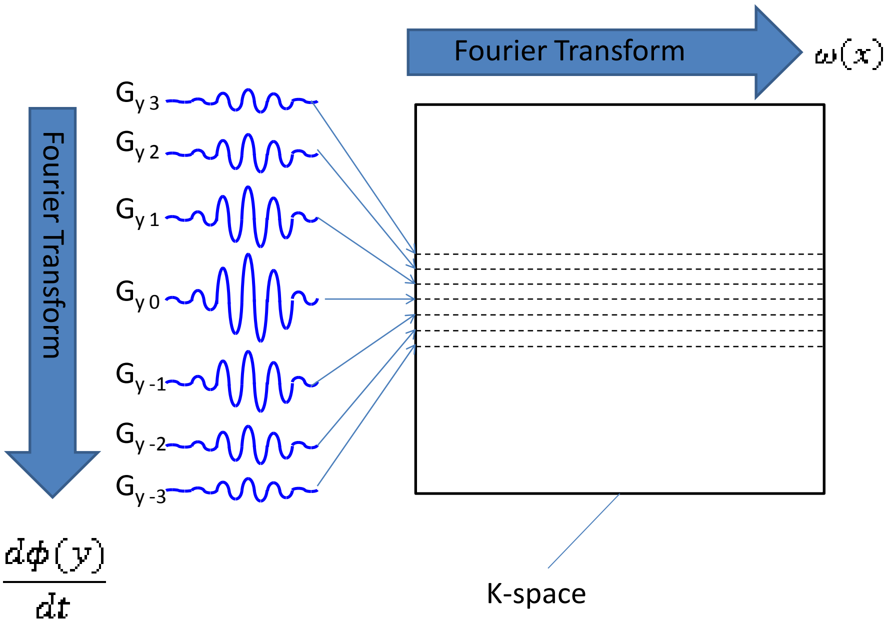

Figure 2-6 – Signal acquisitions acquired with increasing phase encoding gradient strength are arranged sequentially in a matrix called k-space. In the frequency encoding direction the FT transforms the data onto a frequency axis $\boldsymbol{\omega(x)}$. In the phase encoding direction the FT transforms the data to a rate of change of phase axis $\boldsymbol{\frac{d\phi(y)}{dt}}$.

2.6. Pulse sequences

2.6.1. Gradient recalled echo (GRE)

The MR pulse sequence, of which there are an enormous variety, refers to the particular series of RF pulses and gradients, with associated timings, used to generate the image. Here the description is limited only to sequences that are used in myocardial perfusion DCE-MRI. The pulse sequence diagram for gradient recalled echo (GRE) is shown in Figure 2-7. In an MR acquisition, before each line of k-space is acquired a time TR (the relaxation time) must be left to allow the longitudinal magnetization to recover sufficiently before applying the next RF pulse. This parameter controls the degree to which T_1 differences between substances effect the image contrast. To generate a T_1-weighted image after a 90^o RF pulse TR needs to be of the order of a few hundred milliseconds making the acquisition time for the full k-space long. By using a flip angle $\alpha < 90^o$ much shorter TRs can be used, albeit with poorer image contrast. The top line of the pulse sequence diagram in Figure 2-7 depicts the α^o RF pulse in conjunction with a gradient in the slice selection direction. The application of any gradient causes dephasing of the spins, which is an undesirable loss of signal coherence in this instance, and so an immediate rephasing pulse is applied in the opposite direction to undo the dephasing in the slice selection direction. This is followed by the phase encoding gradient G_p, which causes dephasing necessary for the image formation. Simultaneously, a dephasing gradient is applied in the frequency encoding direction prior to the frequency encoding gradient. The frequency encoding gradient then immediately rephases and then continues to dephase the signal whilst the acquisition is made. This results in the generation of a symmetric echo with a peak signal strength at the centre of k-space. The centre of k-space contains the low spatial frequency information, which is the most critical for image contrast. The time between the RF pulse and the centre of the read-out signal is the echo time (TE) and controls the strength of the effect of T_2* contrast on the image.

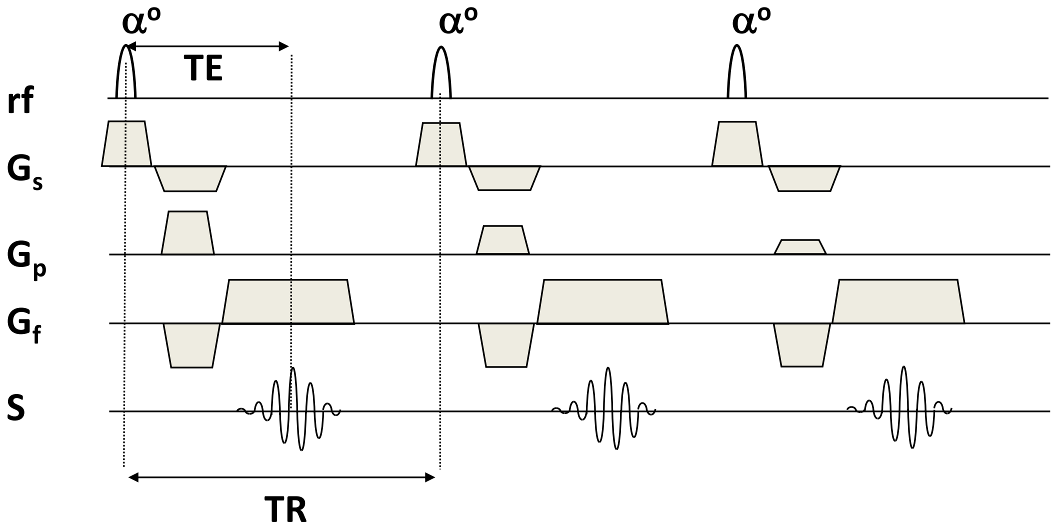

Figure 2-7 – Gradient recalled echo. The α^o RF pulse is applied in conjunction with the slice selection gradient G_s, followed by a rephasing gradient. The phase encoding gradient ,G_p, is applied in conjunction with the a dephasing gradient G_f, after which the signal is acquired during the frequency rephasing gradient.

2.6.2. Fast sequences

At very low flip angles TR can be set so low that the transverse signal has not completely dephased by the onset of subsequent RF pulses, leading to image artifacts. Spoiled gradient echo uses a spoiler gradient to dephase transverse magnetization to destroy transverse magnetization prior to the next RF pulse. Conversely, balanced steady state free precession (bSSFP) ‘rewinds’ the signal dephased by the applied gradients by applying additional balancing gradients to rephase the MR signal before each subsequent RF pulse. The remnant transverse magnetization is then superimposed onto the magnetization generated by subsequent RF pulses generating high signal. Echo planar imaging (EPI) uses rapidly alternating frequency encoding gradients, interspersed by phase encoding pulses, to refocus multiple gradient echoes following a single RF pulse. Single-shot EPI acquires all of the echoes required to fill k-space in a single echo train, however T_2* decay throughout the echo train causes the images to be heavily T_2*-weighted resulting in relatively poor image quality. For cardiac perfusion imaging a hybrid-EPI (also known as segmented EPI) approach is typically employed where a number of shorter echo trains are acquired by applying multiple RF pulses. This reduces the detrimental effect of T_2* weighting, improving the image quality while maintaining some of the speed advantage provided by the EPI technique (Figure 2-8).

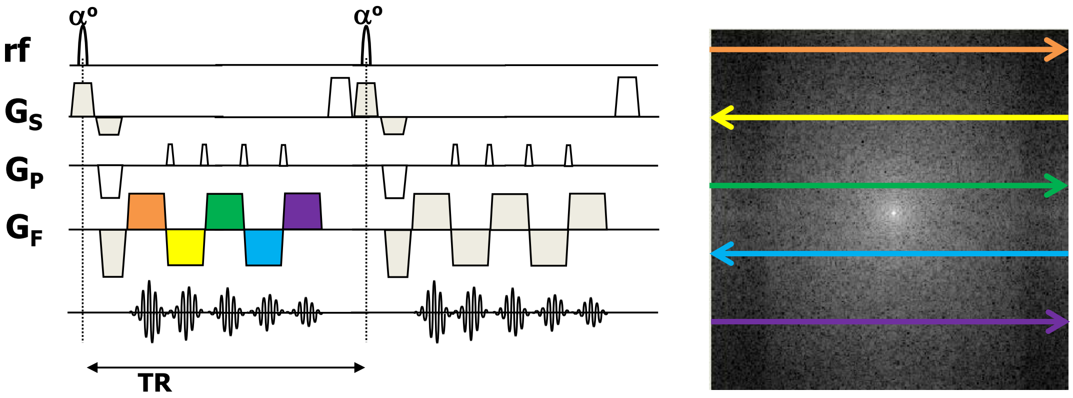

Figure 2-8 - Hybrid Echo Planar Imaging (hybrid-EPI). The slope of the frequency encoding gradient is rapidly alternated, generating a train of gradient echoes following a single RF excitation pulse. Phase encoding gradients are applied between each frequency encoding gradient to ensure each gradient echo fills a different line of k-space. In hybrid-EPI multiple RF pulses are used, each followed by an echo train. (ETL = 5 in this case).

2.6.3. The preparation pulse

To reduce acquisition time the perfusion sequences described above employ small flip angles and very short TRs resulting in poor T_1-contrast. For this reason a preparation pulse can be applied prior to the read-out pulse sequence with a sufficiently long saturation time (TS) to establish a high T_1-contrast before the read-out sequence is employed. For instance a spoiled gradient echo read-out sequence uses small flip angle RF pulses so that M_z is only partially decreased, and full recovery occurs earlier after the read-out. This enables short repetition times (TR), but also limits the changes in contrast between substances (Figure 2-9a). If a 90^o preparation-pulse is applied with a long delay before the read-out then the image contrast is increased (Figure 2-9b), before the fast read-out sequence is applied. The time between the preparation pulses and the central, contrast defining, line of k-space, k_o, is known as the saturation time (TS).

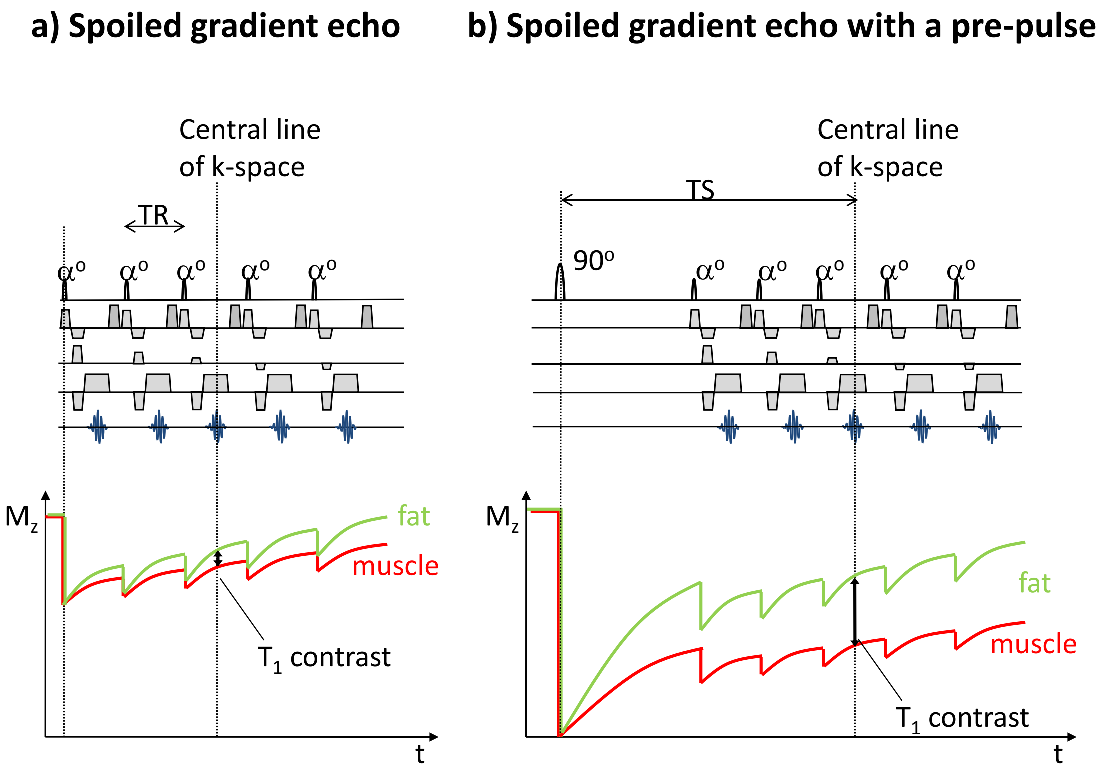

Figure 2-9 – a) small flip angles and short TRs in spoiled gradient echo creates poor T_1 image contrast. b) The use of a 90^o saturation pulse and a long saturation time (TS) establishes strong T_1 contrast before applying the spoiled gradient echo read-out.

2.7. MR contrast agents

MR contrast agents enhance MR signal by modifying tissue T_1 and T_2 relaxation times. The most commonly used contrast agents exploit the strong paramagnetic properties of the lanthanide ion gadolinium (Gd). Local field interactions between the seven unpaired electrons of the Gd ion and the hydrogen nuclei within adjacent water molecules cause a reduction in both the T_1 and T_2 of the surrounding tissue. The Gd ion is bound, or chelated, to a larger electron-donating molecule or ligand to render it safe for in-vivo human use, except in cases of impaired renal function (10–12). The ability of a given contrast agent to influence relaxation rates is expressed in terms of its *relaxivity* which is the change in relaxation rate per unit concentration expressed in $mM^{-1} \cdot s^{-1}$. If the concentration in mM of contrast agent is C and the T_1 relaxivity is r_1 then the observed relaxation rate of the tissue $T_{1\ (observed)}$ can be related to its native relaxation rate $T_{1(native)}$ as follows (13):

$$1/T_{1\ (observed)} = 1/T_{1\ (native)} + r_1 \cdot C$$

Equation 2-7

There is a corresponding expression for the observed T_2 relaxation rate of the substance $T_{2\ (observed)}$ as follows:

$$1/T_{2\ (observed)} = 1/T_{2(native)} + r_2 \cdot C$$

Equation 2-8

Where r_2 is the T_2 relaxivity and $T_{2(native)}$ is the native relaxation rate. Relating $T_{1(observed)}$ to the final image signal intensity (SI) value is more complicated. SI is dependent on T_1, T_2, proton density, the MR imaging sequence and its parameters. Figure 2-10 shows a plot of SI versus contrast agent concentration. At low concentrations T_1 shortening is the dominant effect of the contrast agent so that the SI increases with concentration. However at higher concentrations the T_2 shortening effect becomes dominant and SI begins to fall. If the images are to be used for quantitative analysis then the contrast-induced changes in SI must directly reflect changes in Gd concentration. At low concentrations this assumption holds because the relationship between SI and Gd concentration is approximately linear. At higher concentrations this relationship becomes non-linear and quantitation of concentration based on uncorrected SI values will yield erroneous results. At still higher values the signal becomes saturated and it is no longer possible to derive a single concentration from the measured SI value because the relationship between SI and CA concentration ceases to be monotonic.

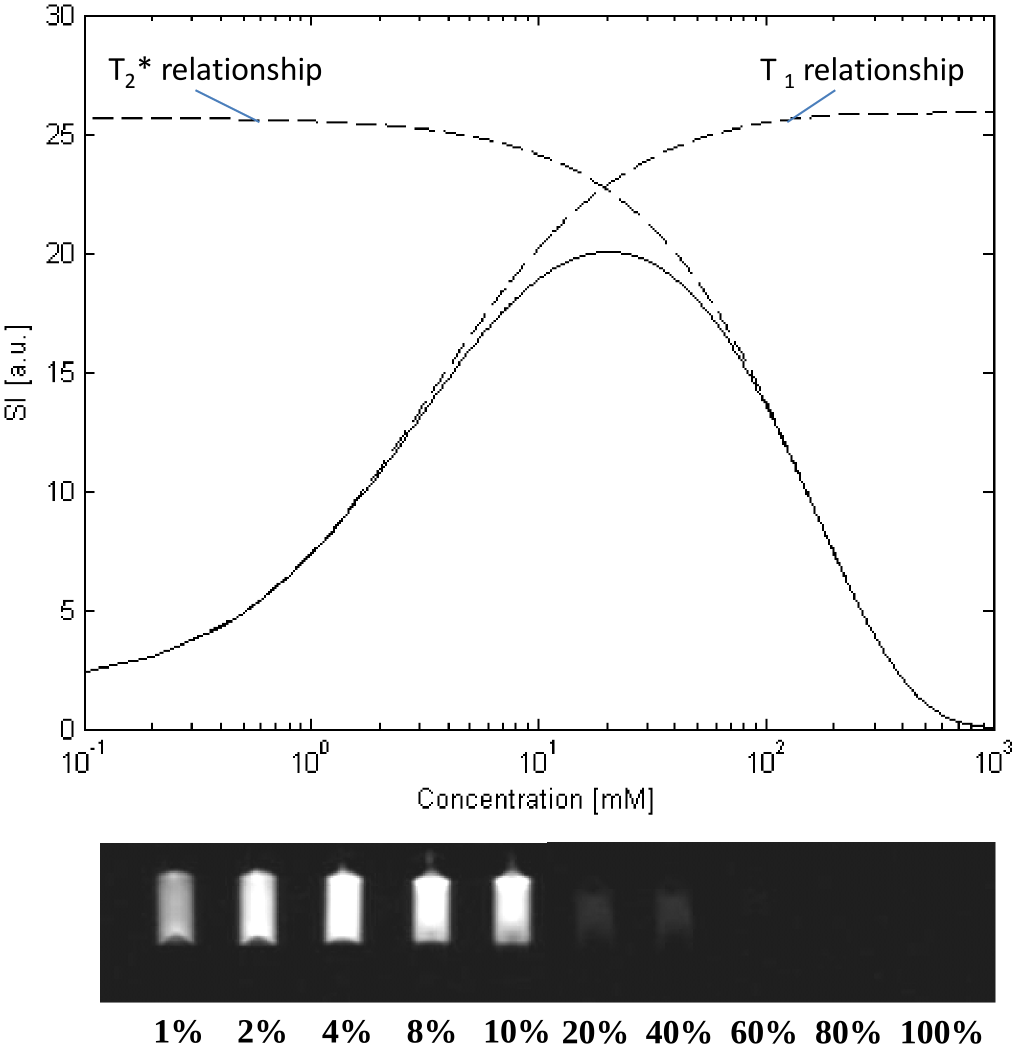

Figure 2-10 - Signal intensity values over a range of concentrations for a spoiled gradient echo pulse sequence. The solid line shows the combined effect of T_1 and T_2* on signal intensity. The two dashed curves show the separate dependencies of the signal behaviour for T_1 or T_2* alone. At low concentrations the effect of T_1 shortening is dominant, while at higher concentrations the T_2* shortening dominates. A series of samples imaged with increasing percentage concentrations of Gadolinium are shown underneath the plot as a visual demonstration of the effect.

Extra-vascular, extra-cellular contrast agents are the most commonly used in clinical practice. These agents are small enough to leak through the capillaries from the vascular space into the extra-vascular, extra-cellular space but not through cell membranes. It is this property of the contrast agent that enables late gadolinium enhancement of myocardial infarcts where the extravascular, extracellular space is enlarged. Intravascular contrast agents, which stay within the vascular space, are less commonly used but may be preferable for quantitative perfusion imaging as they allow simpler mathematical models to be used for flow quantification as no account needs to be taken of leakage from the vascular space (14).

2.8. Dynamic contrast enhanced magnetic resonance imaging (DCE-MRI) myocardial perfusion[3]

In order to assess myocardial perfusion, blood passing into the myocardium needs to alter image signal intensity so that areas of reduced perfusion can be detected. This is typically achieved using a signal enhancing contrast agent. The contrast agent is injected intravenously whilst multiple images of the heart in the same anatomical position and the same cardiac phase are acquired in successive heart beats (Figure 2-11). Typically short-axis images are acquired but a long-axis image is also sometimes additionally acquired in order to cover the apex of the heart. The acquisition protocol needs to take into account the trade-off between spatial requirements (i.e. coverage, resolution) and the temporal resolution.

---

[3] This section is based on a previously published review paper, Biglands, 2012 (9).

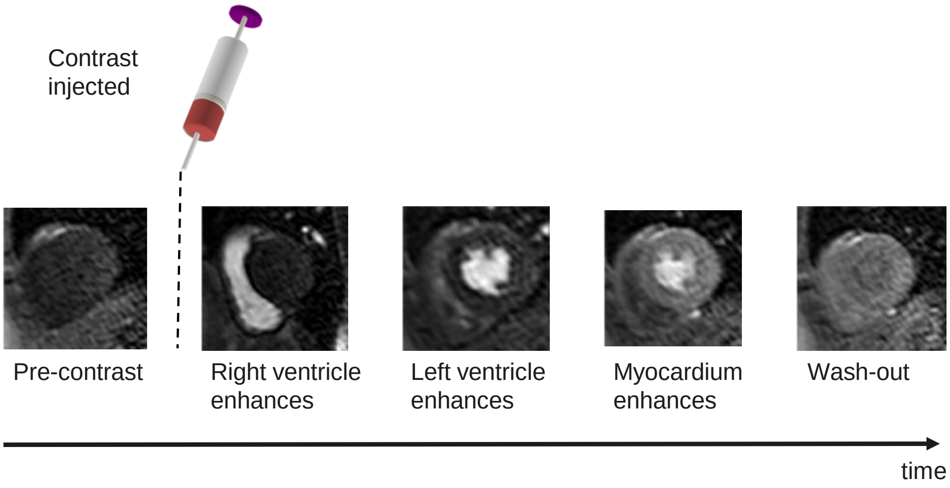

Figure 2-11 - Contrast agent is injected intravenously whilst multiple images of the heart are acquired to create a dynamic series showing the contrast agent passing through the heart. Contrast agent can be seen as signal enhancement in the right ventricle (RV) followed by the left ventricle (LV) and more gradually in the myocardium, before finally washing out.

The essential requirements of a DCE-MRI cardiac perfusion imaging sequence can be summarised as follows: All data for multiple images must be acquired within a single heart beat and the effects of cardiac and respiratory motion must be minimised. In addition the image contrast must be T_1-weighted to maximise the effect of the contrast agent on image signal intensity. In order to fulfil these requirements, the choice of pulse sequence, method of contrast generation and approaches to minimise motion effects must be carefully considered.

2.8.1. The perfusion pulse sequence: read-out sequence

In DCE-MRI the image appearance changes significantly between contiguous frames due to the passage of the contrast agent through the heart so multi-shot k-space imaging strategies that fill k-space over multiple cardiac cycles are not applicable. Therefore, in order to acquire images quickly, DCE-MRI perfusion imaging is generally performed as a single shot technique with a fast (or turbo) spoiled gradient echo (FGE), balanced steady state free precession (bSSFP), or echo planar imaging (EPI) pulse sequence. Despite numerous comparison studies there is still no consensus on the optimal data acquisition pulse sequence for perfusion imaging. Objective measures of pulse sequence performance include the speed of acquisition, the level of artifact and the signal-to-noise ratio (SNR) and contrast-to-noise ratio (CNR). SNR is the ratio of the signal intensity of a particular tissue to the background image intensity in an area where signal is absent, while CNR is the ratio of the signal *difference* between two particular tissues and the background image intensity. As FGE uses a RF pulse per read-out line it is less susceptible to fluctuations in k-space, which should theoretically make it less susceptible to ghosting artifacts.

Nevertheless, hybrid EPI has been shown practically to be less artifact prone than FGE (15). Hybrid-EPI is also faster, allowing increases in coverage and resolution. By maintaining steady state transverse magnetization bSSFP sequences generate the greatest signal of the three methods (16). The higher SNR of bSSFP images allow a much higher bandwidth to be selected leading to shorter TE and TR making bSSFP a faster sequence than FGE and SSFP has been shown to have better sensitivity for detecting perfusion defects (17), also due to its high image SNR and CNR.

However, of the three sequences SSFP is the most prone to artifacts (18) caused by off resonance magnetization. It has a greater occurrence of susceptibility artifact and ghosting and is prone to truncation artifact in the endocardium due to the increased difference in signal intensity between the blood and the myocardium (19). Due to the large number of causes of artifacts with bSSFP it tends to be the least robust sequence, being both capable of producing high quality images but prone to significant image artifacts.

2.8.2. The perfusion pulse sequence: T_1-weighting and TS

DCE-MR images should be T_1-weighted in order to maximise the effect of the contrast agent on signal intensity. This is achieved using a preparation pulse (section 2.6), with the amount of T_1 weighting controlled by the saturation time (TS) (Figure 2-12). Perfusion imaging is usually carried out using a saturation recovery preparation pulse as inversion recovery increases the total scan time, and is more vulnerable to RR variation (18). For visual analysis of perfusion defects the T_1 weighting can be optimised to maximise T_1 contrast using a long TS. However, unnecessarily long TS values take up too much of the RR-interval and limit coverage and spatial resolution. Furthermore, if the images are to be used for quantitative imaging, shorter TS values are preferable to minimise the non-linearity in the relationship between CA concentration and signal intensity.

2.8.3. The perfusion pulse sequence: trigger delay (TD)

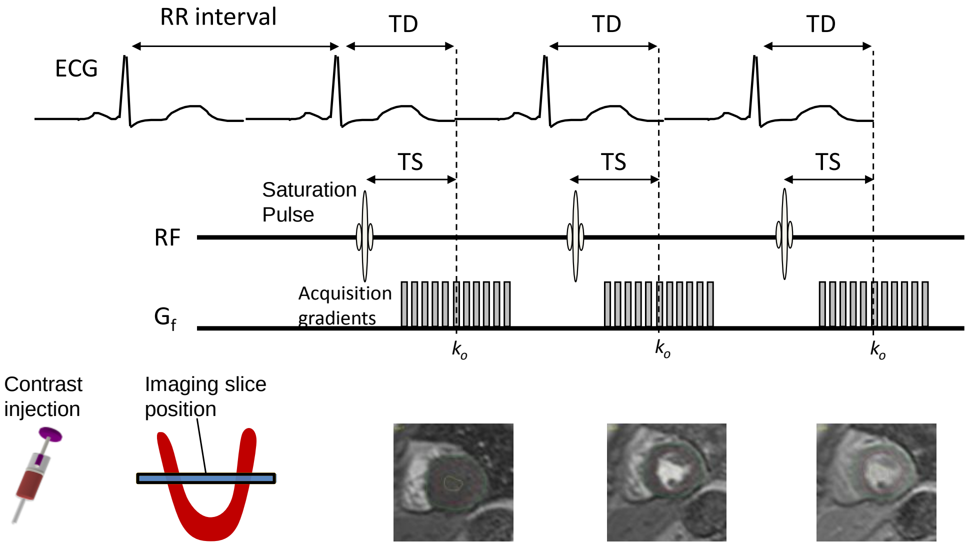

Figure 2-12 - The trigger delay (TD) sets the point at which the centre of k-space, k_0, is acquired within each RR-interval. The saturation time (TS) determines the time between the saturation pulse and the centre of k-space, thereby controlling the T_1-weighted contrast of the image for a particular image slice.

In perfusion imaging each single-shot image acquisition is acquired quickly enough to avoid the detrimental effect of cardiac motion. The use of ECG triggering serves only to determine at what phase of the cardiac cycle the heart will be imaged. This is set by the trigger delay (TD), which is the time from the ECG R-wave to the time of the acquisition of the central line of k-space, k_o, (Figure 2-12). In a single slice acquisition this can be set to any point of the cardiac cycle. TD does not change with RR interval so if the heart rate increases during imaging the cardiac phase of the image will change during imaging. The fastest heart motion is during systole and early diastole, thus imaging at mid-diastole should minimise motion artifacts. Conversely there is a preference for imaging in systole if quantitative analysis is foreseen, as the thicker myocardial wall in systole allows larger ROIs within the myocardium and subsequently improved SNR in contrast uptake curves.

2.8.4. Coverage and resolution

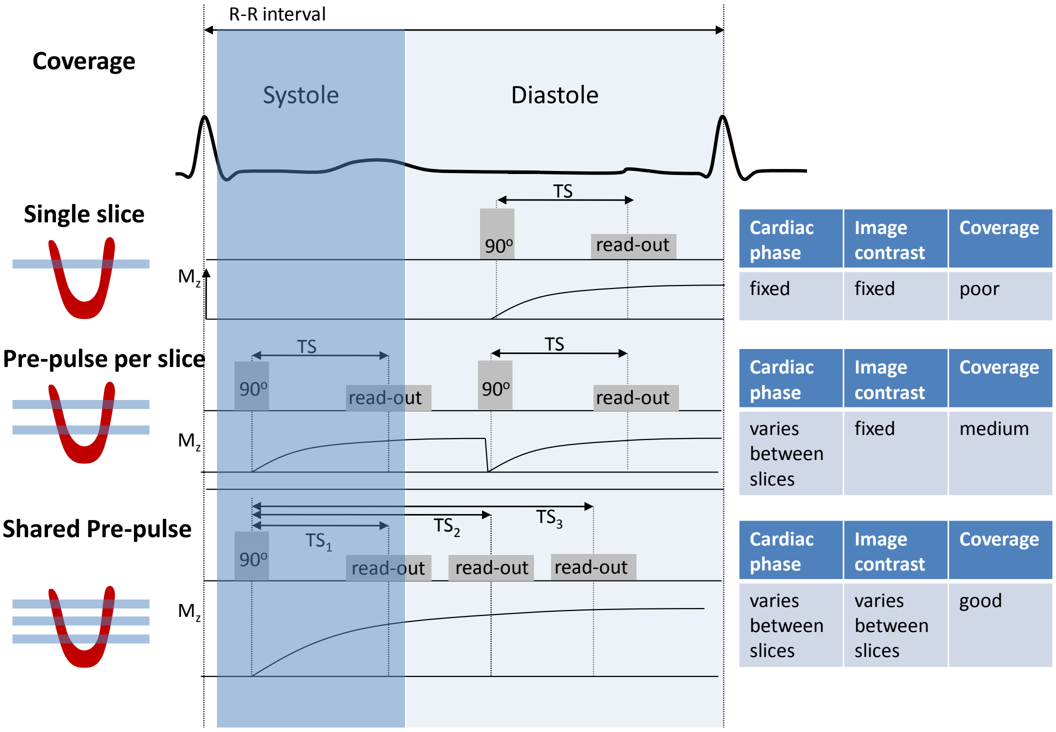

Figure 2-13 - With a single slice acquisition per RR interval (top) there is flexible choice for the optimal cardiac phase and T_1-weighted image contrast, but poor coverage of the LV. For multiple slice acquisitions, the use of a separate preparation pulse for each slice (centre) allows the same image contrast for each slice (fixed TS) but the two slices are acquired at different cardiac phases due to their different trigger delays and the number of slices is limited. Using a pre-pulse shared by all the slice acquisitions (bottom) potentially allows more slices to be acquired, but leads to each slice having both a different T_1-contrast behaviour, and a different cardiac phase.

For the detection of sub-endocardial perfusion defects there is a requirement to maximise spatial resolution but this increases the acquisition time for each slice which renders the acquisition more prone to cardiac motion and limits the number of slices that can be acquired within a heartbeat, thus limiting coverage. However, endocardial perfusion defects may occur at any point in the left ventricular wall and so maximising the coverage of the left ventricle is also important. The AHA recommend that three short-axis slices are acquired to cover basal, mid and apical regions of the left ventricle (20) and that a spatial resolution of at least 2.5mm (21,22) is necessary to be able to reliably detect sub-endocardial defects. The achievement of all of these requirements within a single RR-interval is challenging. One approach to increase coverage along the long-axis of the left ventricle is to acquire an increased number of slices over 2

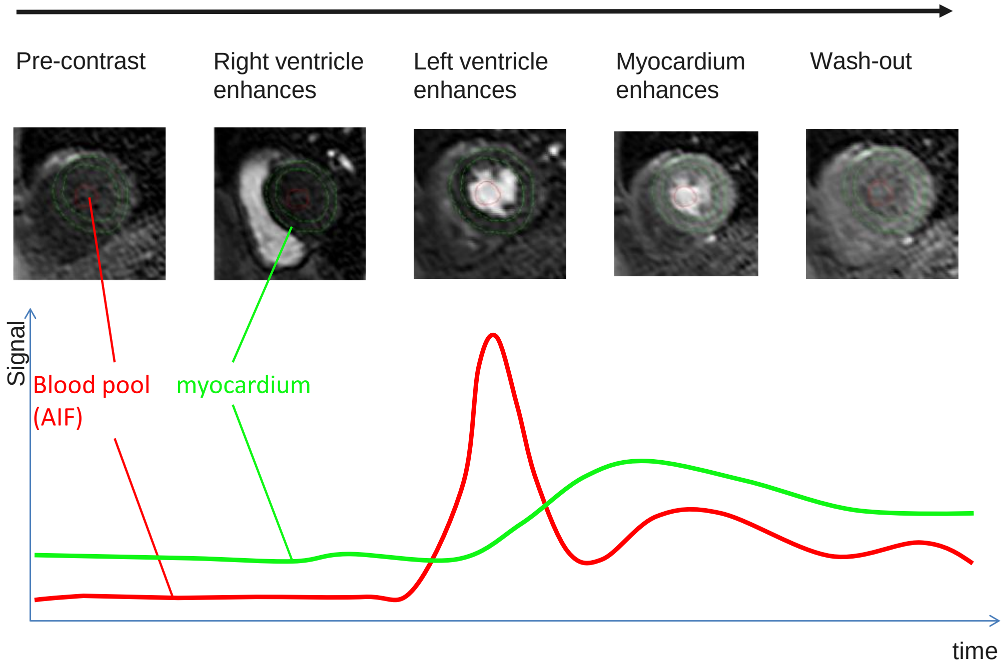

Figure 2-14 - For every image in the dynamic sequence contours describing the myocardium and a region in the blood pool are drawn. The average signal intensity from within each region is plotted for each time point to generate plots of signal intensity versus time that show the increase in signal intensity in both the myocardium (green) and the blood pool (red).

RR-intervals, which has the effect of decreasing the temporal resolution of the dynamic series. This is a less desirable option if a quantitative assessment of perfusion is required (18,21). A further alternative is to abandon the requirement that each read-out pulse has a separate preparation pulse (23). The delay following the saturation pulse, TS, is the longest time delay in the sequence and so the use of a shared saturation pulse applied to all three slices, followed by three slice data acquisitions reduces the acquisition time significantly (Figure 2-13). However, this approach results in a different image contrast for each slice, with the longer TS slices less suited to quantitative analysis.

2.8.5. Factors relevant to quantitation of myocardial blood flow

In order to quantify myocardial blood flow (MBF) signal vs. time uptake curves must be obtained. Regions of interest (ROIs) are drawn on each frame of the dynamic series of images to define the myocardium and an area within the left ventricular blood pool. Signal intensities for each of these regions are then plotted at each time point to generate dynamic uptake curves. The blood pool curve is taken to represent the contrast agent passing into the myocardium or the arterial input function (AIF) and the myocardial region represents the contrast agent remaining within the myocardium (Figure 2-14). These curves can be analysed to obtain semi-quantitative or quantitative estimates of MBF.

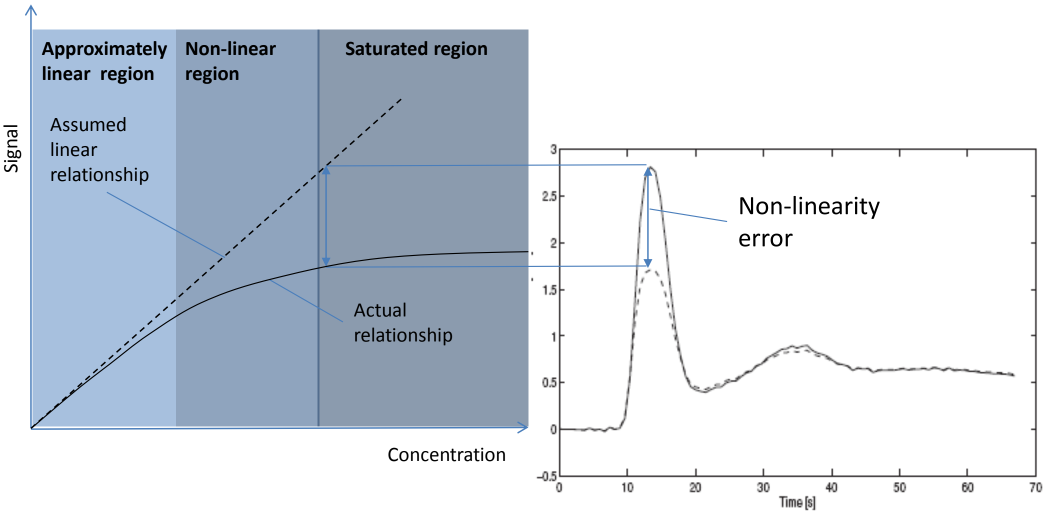

Figure 2-15 - The left hand graph shows the difference between the assumed linear relationship between signal intensity and Gd concentration (dotted line) and the true relationship (solid line). The right hand graph shows how the non-linear relationship at higher concentrations can propagate into a peak height error in the measured blood pool curve (the arterial input function or AIF) causing an overestimate in MBF.

2.8.6. Non-linearity effects at high gadolinium concentrations

If perfusion data are to be used for MBF quantitation then an extra consideration becomes relevant in terms of the MR acquisition. The non-linearity in the relationship between gadolinium concentration and signal intensity (SI) must be minimised. Typically for perfusion measurements contrast agent doses do not exceed 0.1mmol/kg and so the SI to concentration curve has negligible influence from T_2^* shortening (Figure 2-10). Figure 2-15 illustrates how the non-linearity in the relationship between signal intensity and Gd concentration causes blunting of the AIF peak yielding overestimates in MBF. The degree of non-linearity depends on the dose and injection rate of the administered contrast agent, the type of MR pulse sequence (EPI, FFE, SSFP) and the saturation time (TS). Acquisition protocols for quantitative perfusion imaging attempt to optimise these factors to ameliorate the effect of this non-linearity on the MBF estimate.

The simplest method is to administer a low dose of contrast agent so that the relationship between MR signal intensity and Gd concentration is in the approximately linear region (Figure 2-15). Contrast agent doses need to be around 0.01 mmol/kg to ensure linearity in the blood pool (24). These low doses reduce the CNR and SNR of the images rendering visual analysis (still the main-stay of clinical reporting) difficult. The myocardial curve enhances less dramatically than the AIF due to the lower concentration within the myocardium and such low administered doses can reduce the change in signal in the myocardium to such an extent that MBF estimates become significantly affected by image noise, compromising the precision of the MBF estimate.

To tackle these issues dual-bolus strategies have been proposed that employ two contrast injections. Firstly a low dose bolus is injected from which the AIF will be acquired but the poor CNR myocardial data will be discarded. This is followed by a higher dose bolus from which only the myocardial curves will be used. The method is practically challenging as it requires the patient to undergo a total of four contrast injections (if they are to be imaged under rest and stress conditions), but has shown good agreement with PET MBF values (5). However the increased accuracy of the dual-bolus technique has not been shown to increase its diagnostic value over single bolus (25). This might be explained by the introduction of extra noise from the separate pre-bolus analysis.

An alternative approach is to reduce non-linearities by altering sequence parameters. The dual-sequence strategy uses a sequence with very short TS (~10ms) and low image resolution followed by a more typical TS (~100ms) acquisition (26). The short TS images exhibit a more linear SI to concentration relationship and are used to generate the AIF curve, whereas the longer TS images are used for the myocardial enhancement curve. Acquiring two acquisitions for each heart position requires a corresponding reduction in coverage and, as with dual-bolus, the AIF images will suffer from lower CNR than the myocardial images.

Non-linearity correction attempts to convert the SI vs. time curve to a concentration vs. time curve post hoc. (27,28). In this approach the MR imaging sequence equation is used to convert each SI value into a T_1 value (using prior knowledge of the imaging parameters) (29–31). If the native tissue T_1 has been measured prior to the perfusion scan then the contrast enhanced T_1 values can be converted to concentrations. If the SI value lies in the approximately linear, or non-linear region (Figure 2-15) then it should be possible to convert it to CA concentration. However, if the curve has passed into the plateau region then the solution to the pulse sequence equation will become error prone and the correction becomes useless. Such conversions are also susceptible to errors in the native T_1 measurement and errors in the pulse sequence parameters.

2.9. The dark rim artifact (DRA)

All MR images are susceptible to image artifacts. However in cardiac perfusion imaging the dark rim artifact (DRA) is particularly problematic as it mimics the very perfusion defects that the investigation is designed to show. DRAs manifest as transient signal voids at the endocardial boundary and can be mistaken for genuine sub-endocardial perfusion defects. They differ from genuine hypoperfusion events in that they typically last only a few heart beats (32) and they can cause the myocardial signal intensity to drop below the baseline (pre-contrast) signal value (33). A number of comparison studies have been conducted to investigate which sequences are most prone to DRAs (16,17,34) showing that bSSFP is the acquisition sequence most affected. The cause of a given DRA is difficult to pinpoint as multiple factors have been shown to contribute. Motion during image acquisition can generate abrupt discontinuities in k-space which translate into banding artifacts at tissue boundaries in the image (35). Magnetic susceptibility effects may also cause DRA due to increased magnetic field distortions around boundaries in the image and temporal changes in magnetic susceptibility on the arrival of contrast agent (17,33). This effect is most prominent in bSSFP due to its higher sensitivity to changes in magnetic susceptibility which cause local changes to the Larmor frequency. These off-resonance effects become worse at stronger concentrations of contrast agent. The presence of truncation artifact at the high contrast boundary between the blood pool and myocardium is another potential cause of DRA (22). This is caused by an insufficient content of high spatial frequency data in k-space which means that the Fourier transform is unable to accurately represent true high contrast boundaries in the image. This causes signal variations adjacent to these boundaries that appear as bright and dark bands. This effect becomes worse at higher contrast levels such as with higher bolus concentrations and injection rates, and when using bSSFP as the acquisition sequence.

2.10. Summary

The basics of MRI, including the origin of the MR signal and basic pulse sequences, have been described with a focus on the imaging methods used in CMR perfusion imaging. The demanding imaging requirements for CMR perfusion imaging have been described and the options and compromises as to how these demands are to be met have been discussed. The next chapter will discuss coronary heart disease and myocardial ischaemia, explaining the role that these CMR perfusion techniques play in its diagnosis.

3. Background: ischaemia and myocardial perfusion

3.1. Introduction

MRI is by no means the only method for diagnosing coronary heart disease (CHD). Most medical imaging modalities have methods for detecting the disease with their own sets of advantages and disadvantages. After a discussion of basic cardiac anatomy and function, CHD and its treatments are briefly described in this chapter. An overview of the main methods for diagnosis of these conditions is then given considering the methods used, the associated advantages and disadvantages and the diagnostic performance of each test. As befitting a thesis on MR perfusion, a more detailed description of the performance of MR is given considering the impact of visual, semi-quantitative and fully quantitative analysis on diagnostic performance as reported in the cardiac MR literature.

3.2. Cardiac anatomy

The human heart consists of four chambers: the right and left atria and the right and left ventricles. The right side of the heart is dedicated to reoxygenating the blood via the lungs, whereas the left side pumps oxygenated blood to the rest of the body. This gives the left side of the heart a higher workload than the right, which is why the left ventricular muscle wall is thicker than that of the right ventricle. This process is illustrated schematically in Figure 3-1 a). For such an active organ as the heart sufficient nutrients could not diffuse quickly enough through the heart wall to supply all the myocardial cells. Instead, the coronary arteries, branching directly from the ascending aorta, encircle the heart and provide the heart with blood (Figure 3-1 b). The finer details of the coronary circulation vary between individuals, with a major distinction being drawn between left and right dominant circulations dependant on which artery provides blood to the posterior descending artery, which supplies blood to the posterior third of the interventricular septum (the wall between the ventricles).

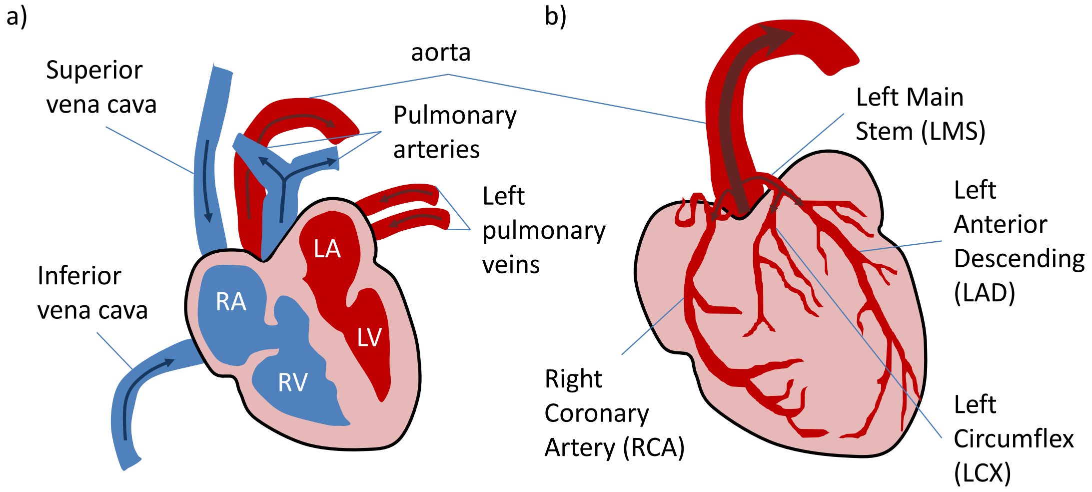

Figure 3-1 – a) Oxygenated blood from the pulmonary veins enters the left atrium (LA) and is pumped into the left ventricle (LV), which pumps oxygenated blood to the rest of the body. The deoxygenated blood returns via the inferior and superior vena cavae into the right atrium where it passes into the right ventricle to be pumped to the lungs for reoxygenation via the pulmonary arteries. b) The right coronary artery (RCA) and left main stem (LMS) branch directly from the ascending aorta. The LMS bifurcates into the left anterior descending artery (LAD) and the left circumflex (LCX).

The coronary circulation also contains multiple *anastomoses*, where two or more arteries interconnect. These interconnections provide alternative routes for blood and can allow myocardial perfusion to persist when single arteries become blocked. These complications make the mapping of an ischaemic blood vessel to the corresponding myocardial region in a medical image difficult. The process is further confounded by the possibility for coronary collateralization, where microscopic cardiac collateral vessels widen their lumen in order to preserve blood flow to ischaemic regions of the myocardium.

3.3. Coronary heart disease (CHD)

Coronary heart disease affects nearly 2.7 million people in the UK (1). Ischaemic heart disease (IHD) occurs when the cardiac blood supply is reduced, typically due to the narrowing of one or more coronary arteries by atherosclerotic plaques (coronary artery disease (CAD)). The reduced blood supply causes hypoxia (reduced oxygen supply) in the myocardium, especially under stress conditions. Chronic hypoxia causes cells to enter a ‘hibernation’ state, where function is dramatically reduced and the patient may experience pain (angina pectoris). However the cells are still viable and if the oxygen supply is re-established they will recover. Complete and acute obstruction of blood flow, most commonly through thrombus formation on a vulnerable plaque, may result in myocardial infarction (commonly called a heart attack). Here the cells in the affected region of the heart die and are replaced by non-contractile scar tissue. If the sufferer survives the event the scar tissue can manifest as abnormal contractile function in the heart.

Lifestyle changes (exercise, stopping smoking and diet improvements) can slow the progression of ischaemia. Cholesterol lowering agents stabilise the plaque, making it less susceptible to attracting blood clots. Beta blockers reduce the heart rate thus reducing oxygen demand and reducing hypoxia, whilst nitrates increase blood supply by vasodilation (widening of the blood vessels). Medical therapy typically consists of a combination of these approaches whereas mechanical interventions involve physically restoring the blood flow to the heart.

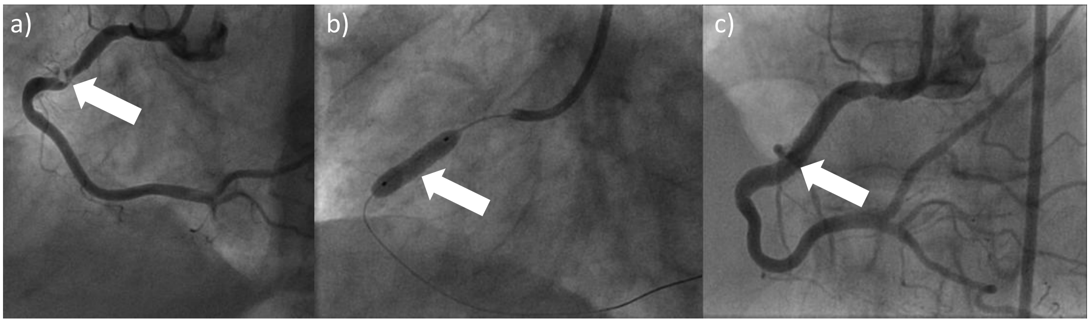

Figure 3-2 – PTCA. a) X-ray with iodinated contrast agent of right coronary artery showing a significant stenosis. b) X-ray without contrast agent showing balloon angioplasty and the radio-opaque catheter guidewire. c) X-ray with contrast agent showing the opened artery post angioplasty and stent placement[4]

Percutaneous transluminal coronary angioplasty (PTCA), also known as percutaneous coronary intervention (PCI) involves the insertion of a catheter

---

[4] Images provided by Andy Davies, University of Leeds.

into an artery in the arm or leg. The catheter is then fed to the stenotic site, under X-ray guidance, and a balloon is inflated to squash the plaque against the artery wall. Because 30-50% of PTCA re-opened arteries restenose within six months of the procedure a stent (resembling a small spring) is then deployed in the artery to keep the artery open (Figure 3-2).

A *Coronary artery bypass graft (CABG)* uses a section of artery or vein from another part of the body (typically the chest wall for arterial grafts and the leg for venous grafts) to connect the aorta directly to a region downstream from the stenosis. This effectively bypasses the problem area and allows blood to flow beyond the diseased artery.

Revascularisation aims to restore blood supply to living but hypo-perfused tissue. However if the tissue is infarcted (cell death) then revascularization will have no benefit. There is a small but significant risk to the patient undergoing arterial catheterization and so it is important to avoid the procedure when it will be of no benefit to the patient. MR viability imaging provides imaging of myocardial scar. Images are acquired 5-15 minutes post contrast injection. In scar tissue cell walls break down increasing the extravascular space and the wash-in and wash-out characteristics of this space are slower (36) thus the scar manifests as a bright, contrast filled zone, on late gadolinium enhanced (LGE) images. These images provide important diagnostic information about whether or not a given patients prognosis will be improved by revascularization (37).

3.4. Diagnosing coronary heart disease

3.4.1. The cascade of ischaemia

The cascade of ischaemia (38) describes the order in which detectable events occur in response to ischaemia. Initially only subendocardial perfusion defects are detectable (39). More severe stenosis leads to transmural hypoperfusion followed by diastolic (relaxed heart), and then systolic (contracted heart), wall motion abnormalities. Finally electrocardiogram (ECG) (See section 3.4.4) changes become detectable and angina symptoms may manifest. Therefore, imaging modalities which can detect subendocardial perfusion defects have the potential to be the most powerful test for early detection of myocardial ischaemia.

The argument may be made, and in many cases may be quite valid, that an even earlier test for ischaemia is possible by imaging the coronary artery stenosis itself, as is routinely performed in X-ray angiography. However, the relationship between coronary artery stenosis and myocardial ischaemia is not straightforward. It has been widely demonstrated that an anatomical assessment alone is unreliable in predicting the functional significance of a coronary stenosis. Multiple other physiological processes determine the functional relevance of an epicardial stenosis. A perfusion defect demonstrates a mismatch between blood demand and blood supply at a specific myocardial site. Syndrome-X patients manifest such defects without exhibiting any coronary stenosis (40), whereas other patients with significant coronary stenosis have been found to have no myocardial ischaemia due to collateral flow maintaining myocardial blood flow. Thus a reliable method for detecting subendocardial hypo-perfusion has the potential to be the most direct and diagnostically powerful test for detecting ischaemic heart disease.

3.4.2. Stress testing

Auto-regulation maintains myocardial blood flow in the heart even in the presence of ischaemia until the degree of stenosis becomes critical. For this reason it is necessary to perform tests under stress conditions in order to reveal myocardial ischaemia in a diagnostic test. In ECG based tests, where the patient’s mobility is not limited, stress is simply induced by requiring the patient to exercise, either on a treadmill or an exercise bike. With investigations that limit patient movement due to the constraints of the imaging apparatus, stress is typically induced pharmacologically using an infusion of either a positive inotropic agent such as dobutamine or a vasodilator like adenosine. Dobutamine increases the heart rate and contractility actually inducing ischaemia in patients, whereas adenosine dilates the coronary arteries to their maximum, increasing myocardial blood flow without inducing ischameia. Whether the differences between maximal vasodilation, induced ischameia and physical stress are relevant in terms of diagnosing CHD from perfusion imaging is yet to be established.

3.4.3. Myocardial perfusion reserve (MPR)

Diagnostic studies using quantitative or semi-quantitative myocardial blood flow (MBF) estimates often express their results in terms of the myocardial perfusion reserve (MPR). The MPR is the ratio of the stress and resting myocardial blood flows:

$$MPR = \frac{Stress\ MBF}{Rest\ MBF}$$

Equation 3-1

The rationale for expressing perfusion measures in this way goes back to the concept of coronary flow reserve (CFR) (41). The ultimate effect of a given stenosis depends on the ability of the coronary circulation to compensate for the increased impedance to blood flow by vasodilation. To make a CFR measurement rest and stress coronary flow measurements are made downstream from a given stenosis, with the stress measurement made under adenosine induced, maximal vasodilation. The ratio of the stress and rest measurements can be taken as a measure of the ability of the system to maintain flow in the face of a given stenosis i.e. its reserve of possible flow increase before maximal vasodilation occurs. The concept is illustrated in Figure 3-3, which is reproduced from (41). Stress and resting coronary flow rates are shown at a range of stenosis levels. The CFR measures the ratio between the vasodilated and rest flows. The coronary pressure (being the pressure gradient that drives blood down the artery) reduces non-linearly with the degree of stenosis, giving a corresponding reduction in CFR. Autoregularory reserve is exhausted between 85% and 90% stenosis, with 90% stenosis giving slight reductions in flow even under resting conditions.

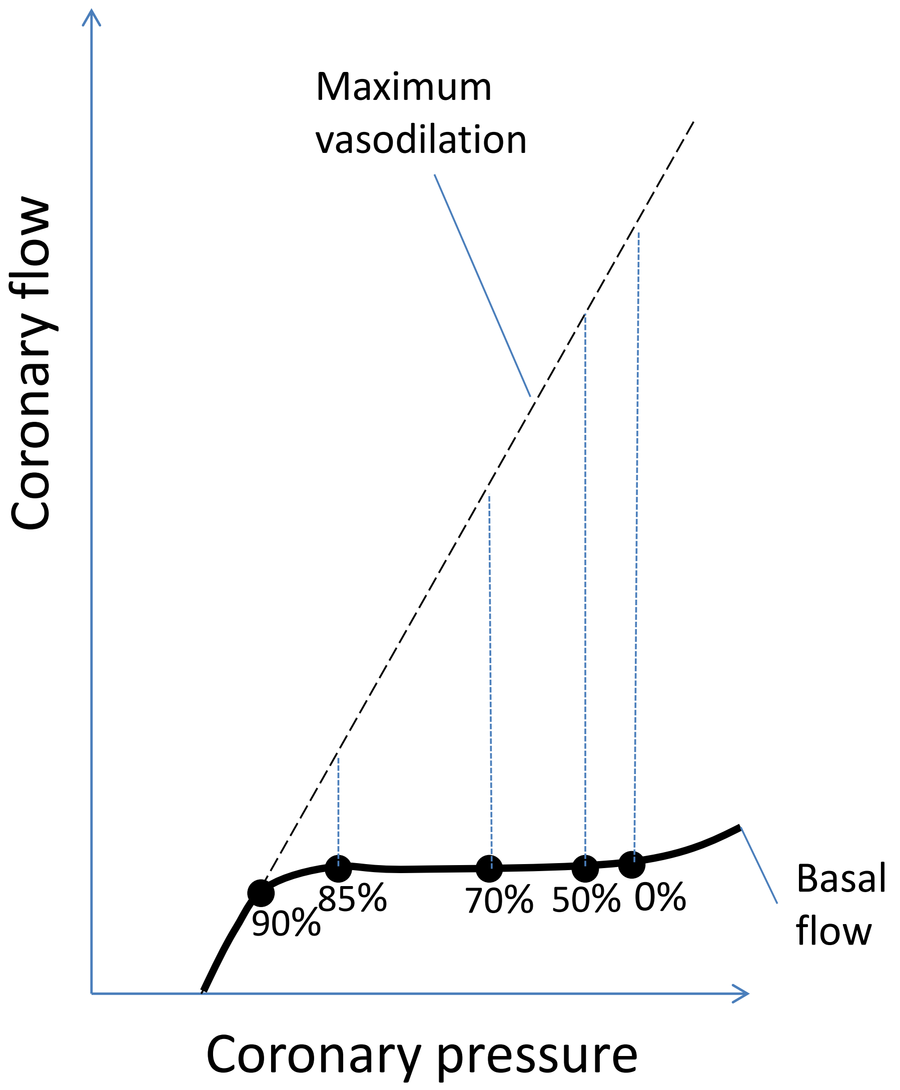

Figure 3-3 – Coronary Flow Reserve. The dotted line describes the coronary flow at maximal vasodilation and the solid line the flow at rest. Each solid circle corresponds to a different percentage degree of coronary stenosis. Reproduced from (41)

The MPR is an analogous measure to CFR based on MBF measurements made in the myocardium itself. The relationship between coronary stenosis and MBF is more complicated than that for coronary flow, due to the high interconnectivity of the arterial pathways and the possibilities for collateralization. However MPR can be taken as a measure of the ability of the entire coronary and myocardial system to maintain blood flow in the event of coronary stenosis and has been shown to be a good measure of the presence of CAD (Table 3-1).

3.4.4. Electrocardiogram (ECG)

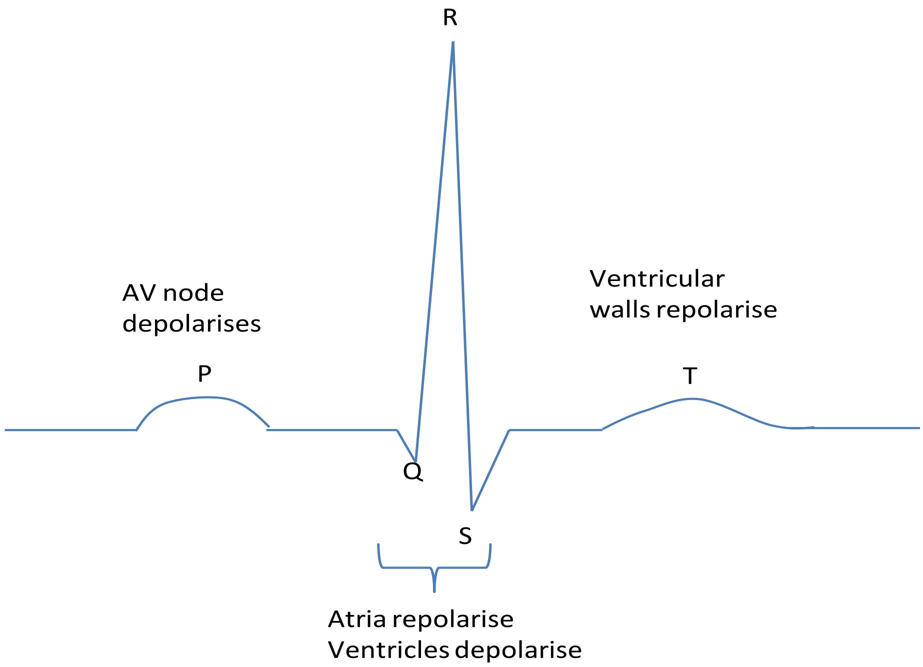

Figure 3-4 – Normal ECG plot. The P wave corresponds to the depolarisation of the AV node and atrial contraction. The QRS complex corresponds to the simultaneous repolarisation of the atria and depolarisation and contraction of the ventricles (systole). The T wave corresponds to repolarisation of the ventricles.

The pacing of heart contraction is controlled by a network of specialised fibres; the autorythmic fibres. An electrical action potential initiated by the sinoatrial (SA) node is conducted down the heart, through the atria (causing them to contract first) and finally to the Purkinje fibres which rapidly conduct the potential from the apex of the heart upward causing ventricular contraction. The passage of these potentials through the heart generates current that can be detected by electrodes placed on the surface of the body. The resulting plot is known as the electrocardiogram (ECG) and has peaks and troughs corresponding to the electrical stimuli that cause the heart to beat. Abnormalities in the ECG trace can be correlated with a range of cardiac abnormalities. Under stress conditions cardiac depression of the ST segment (below baseline) is an indicator of ischaemia. The ST segment represents the time when the ventricular fibres are depolarized and is depressed when the heart is receiving insufficient oxygen. The ECG test is easy to perform and is often the first test performed when patients present with chest pain but has limited diagnostic accuracy for ischaemic heart disease (sensitivity 73-90%, specificity 50-74%) (42).

3.4.5. X-ray angiography

X-ray angiography obtains images of the coronary artery tree and enables direct visualisation of coronary stenosis rather than the resulting perfusion defect. In the operating theatre a radio-opaque catheter is inserted into an artery in the leg or arm and guided through the vascular system to the ostia of the coronary arteries in the ascending aorta. The procedure is done under the guidance of fluoroscopy X-ray. A relatively low dose (thus low image quality), X-ray movie is displayed to enable the cardiologist to navigate the catheter to the correct place. A short bolus of iodine based X-ray contrast agent (e.g Ultravist at around 370 mg/ml Iodine) is then injected into either the right or left coronary artery whilst a higher dose, high quality X-ray movie is recorded for several heart beats. The resulting movie can then be assessed to give a qualitative or quantitative assessment of the degree of stenosis. An example of a stenosis imaged in this way is shown in Figure 3-2 a). The coronary arteries bifurcate multiple times and the artery routes are tortuous. Therefore, a single planar X-ray view may miss stenoses if they happen to be obscured by other arteries at a given imaging angle or if the stenosis does not manifest around the complete circumference of the artery wall. For this reason multiple views of the coronary tree are taken ideally, using repeated contrast boluses or multi-detector systems. Alternatively three-dimensional views of the coronary arteries can be acquired using a computed tomography (CT) angiogram. Acquiring X-ray images from a range of imaging angles around the patient during the infusion of a radio-opaque contrast agent yields high resolution, 3D images of the coronary arteries.

Routinely a visual, qualitative analysis of the degree of stenosis is made from the X-ray angiogram, expressed as the percentage narrowing relative to the adjacent, healthy lumen size. Quantitative coronary angiography (QCA) makes a measurement or the degree of stenosis using semi-automated software (e.g. QCAPlus software, Sanders Data Systems, Palo Alto, California, USA). A line is drawn manually along the artery through the stenotic region. The software then expresses the narrowest part of the defined region as a percentage of the healthy artery lumen, calculated from the outer portions of the selected artery length.

X-ray angiography is the gold-standard assessment for the diagnosis of coronary artery disease and the presence and severity of coronary stenosis. In clinical practice, angiographic stenosis severity is often also assumed to correlate with myocardial ischaemia. However, there are a number of important limitations, which should be understood. Firstly there are problems regarding the acquisition and interpretation of the data. Qualitative analysis of X-ray angiography is associated with significant observer variability (43,44). The variability can be improved by using quantitative analysis (45), however significant variability has also been found between QCA software implementations (46). QCA is also susceptible to errors when there is diffuse disease as the ‘normal’, unstenosed lumen diameter is difficult to locate (47). Furthermore the assumption that arterial flow reduction is correlated with stenotic diameter is too simplistic. Models taking into account stenosis size and length and allowing for the additive value of multiple stenoses have been validated but these are complicated and difficult to introduce into routine clinical practice (48). These limitations can be overcome by measuring the fractional flow reserve (FFR) across the stenosis. To make this measurement a sensor on the tip of the wire is used to measure pressure and flow before and after the stenosis giving a direct measurement of the impact of the stenosis on coronary blood flow. FFR measurements are becoming more common in research studies using angiography as the gold-standard.

Secondly, the assumption that a reduction in arterial flow is directly linked to a resultant and proportional reduction in myocardial blood flow (MBF) is too simplistic. The ability of the cardiac system to utilise collateral arteries in the presence of stenoses means that some stenoses may not manifestly reduce MBF at all. Conversely there are cases of patients exhibiting the symptoms of ischaemic heart disease, including myocardial perfusion defects, with no detectable coronary stenoses; the so called ‘Syndrome X’ (40).

Finally, it is important to recognise the risks associated with X-ray angiography. The investigation has a small but significant morbidity and mortality at ~0.5% for procedural death, myocardial infarction or stroke. Furthermore, it involves ionising radiation with the subsequent risk of developing a solid tumour estimated at 1 in 2500 (49,50).

3.4.6. Single photon emission computed tomography (SPECT)

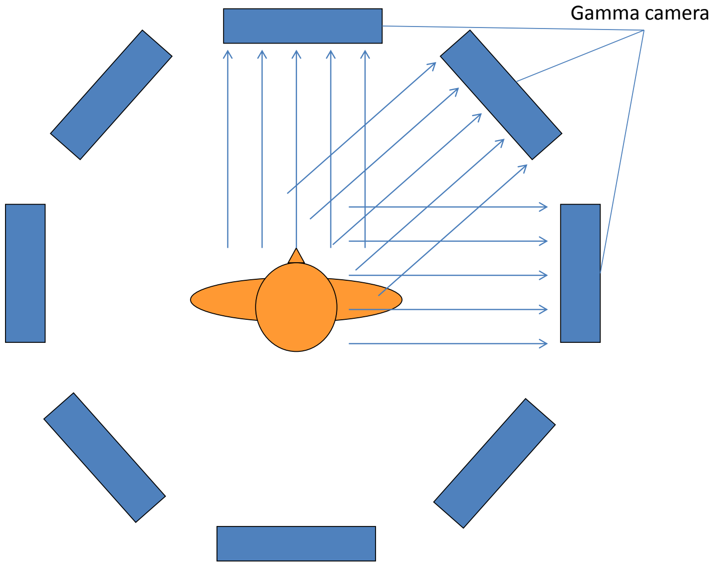

Figure 3-5 – SPECT – Multiple planar gamma camera images are taken at a range of viewing angles which can be reconstructed to generate a transaxial view of the distribution of radioactive tracer in the myocardium.

Nuclear medicine based techniques use a radioactive tracer that is injected into the patient. This can then be imaged using radiosensitive imaging equipment. Single photon computed tomography (SPECT) uses a gamma camera, mounted on a rotating gantry to acquire planar images representing the distribution of radioactive tracer within the patient at multiple viewing angles (Figure 3-5). These planar views can then be reconstructed into cross-sectional views of the heart, typically using a filtered back-projection, or an iterative reconstruction method. Unlike MRI perfusion, SPECT perfusion imaging does not image the passage of contrast agent through the myocardium. Rather the tracer builds up in the myocardial tissue over time with underperfused regions showing as a relative shortage of tracer and appearing as ‘cold spots’ on the resulting image (Figure 3-6).

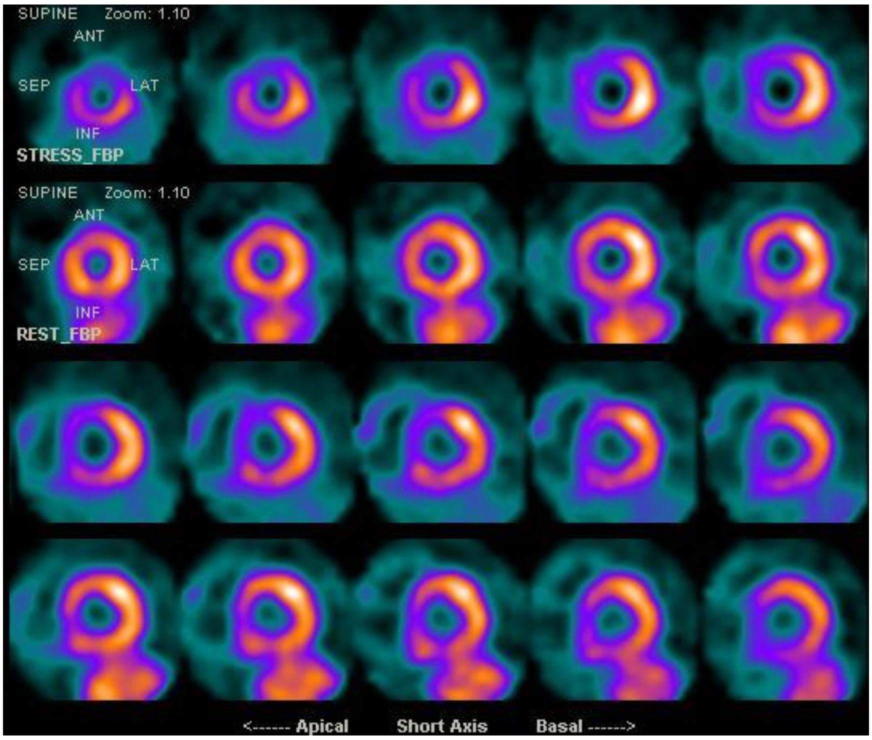

Figure 3-6 – Transaxial SPECT images acquired at stress (rows 1 & 3) and rest (rows 2 & 4) in 10 slices through the heart. A reversible perfusion defect in the anterior wall manifests as an under-perfused area at stress with normal perfusion rest.[5]

Typical radio-tracers are Thallium-201, Tc^{99m} methoxyisobutylisonitrile (MIBI) or Tc^{99m} tetrafosmin, which are taken up by the myocytes. All have shown similar sensitivities and specificities for detecting CAD, with Thallium-201 having worse image quality due to its lower energy gamma rays (51,52). Stress can be achieved with physical exercise (using a treadmill or bicycle prior to imaging), but is commonly pharmaceutically induced with adenosise or dypridamole, achieving comparable diagnostic accuracies to exercise (53,54).

---

[5] Images provided by Dr Penny Thorley, Leeds Teaching hospitals

Myocardial SPECT imaging is susceptible to artifacts due to cardiac motion and tissue attenuation. Heart wall motion can lead to underestimates in regional uptake and so acquisitions should be ECG-gated (55) as illustrated in Figure 3-7.

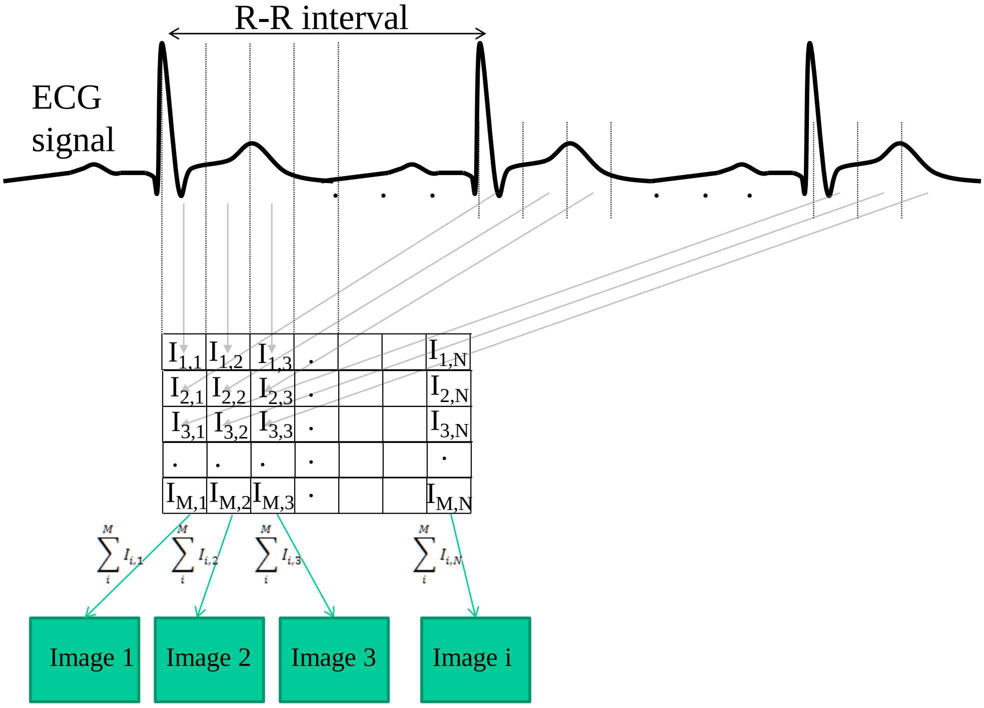

Figure 3-7 – Cardiac SPECT ECG gating. The ECG RR interval is broken down into N temporal bins. Data acquired during each temporal bin from multiple RR-intervals is averaged to create a series of images representing one heart beat.

In order for gamma-photons to be detected they must pass from the heart through the body of the patient to the gamma camera. Attenuation within the patient is a well recognised problem leading to poor image quality and, in some cases, mimics the appearance of perfusion defects. In order to ameliorate attenuation artifacts CT imaging can be used. The CT image, which represents the tissue densities of the image in Hounsfield units (HU), can be incorporated into the SPECT reconstruction to correct for tissue attenuation and significantly ameliorate attenuation artifacts. Attenuation corrected SPECT data have been shown to improve agreement with PET studies (56) and to improve the specificity and sensitivity of the diagnostic test (57).

Cardiac SPECT images can be reported visually by simply locating ‘cold-spots’ on the images. However, semi-quantitative analysis of cardiac SPECT images is possible. Typically multiple slices are represented as a single polar plot by dividing each slice into radial regions and taking the maximum pixel value. These polar plots are then normalised and compared to a database of pixel values from normal healthy patients and the difference used to automatically classify a given region as unhealthy or not. Such methods have been shown to improve the detection of CAD from cardiac SPECT data (58–60).

Cardiac SPECT is a well accepted and well validated technique. However its resolution is relatively poor and subendocardial artifacts, visible in MRI, are not detectable. It also exposes the patient to a radiation dose, which can be avoided with other modalities.

3.4.7. Positron emission tomography (PET)

In order to obtain an image that represents a planar transmission of gamma rays from the source distribution within the patient gamma cameras use parallel hole lead collimators. The collimator successfully limits detection events to rays travelling perpendicular to the gamma camera but also reduces the count sensitivity of the system. Positron emission tomography (PET) overcomes this fundamental limitation of the gamma camera by using coincidence detection. Radioactive tracers that decay by positron emission are used on PET imaging. After travelling a few millimetres an emitted positron annihilates with an electron creating two 511KeV gamma-rays travelling in opposite directions. The PET scanner consists of a ring of detectors surrounding the patient. When two detection events occur within the same temporal detection window (6-12ns) they are assumed to originate from the same annihilation event (Figure 3-8). The finite temporal window is necessary to allow for the different transit times of the two gamma rays. The source of the annihilation event must lie along the line connecting the coincidence detectors. A reconstruction algorithm is used to deduce the original radioactive source distribution from multiple lines of coincidence detected during a PET acquisition.

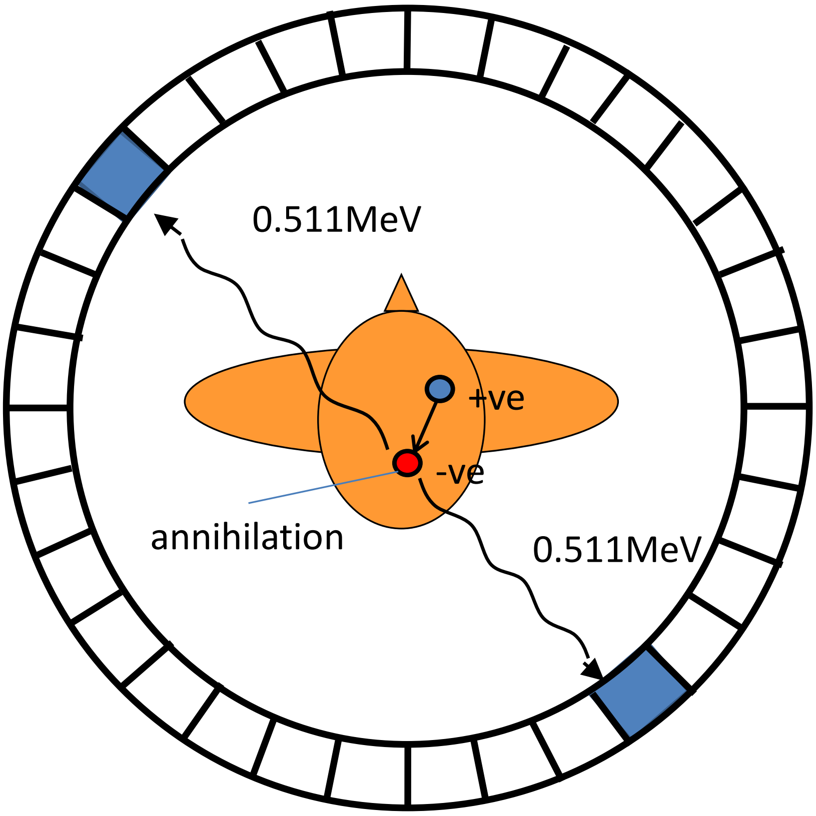

Figure 3-8 – Coincidence detection in PET. A positron travels a small distance before annihilating with an electron to produce two 180° opposed gamma-rays which are detected within a small temporal window at two points in the PET detector ring. The line connecting the two detectors is the line along which the annihilation event must have occurred.

For quantitative myocardial perfusion PET imaging an intravenous injection is made of one of a variety of positron emitting tracers such as ^{82}Rb, ^{13}N-Ammonia, ^{15}O-Water. Like SPECT tracers these cross the capillary walls and are taken up by the myocardial cells (myocytes). Unlike SPECT however dynamic imaging is possible in PET, albeit with an inferior temporal resolution to MRI (~5s as opposed to ~1s in MRI). The ability of PET to obtain dynamic transaxial views of the heart means that radioactivity counts vs. time plots can be generated. Based on these tracer-kinetic models such as those described in chapter 4 can be used to calculate quantitative estimates of myocardial blood flow. As with SPECT, attenuation is a significant factor and has to be corrected for using pre-PET CT scanning, or an equivalent transmission imaging technique (61). Data must be corrected for radioactive decay and detector dead-time. With the exception of ^{15}O PET tracers the extraction of tracer from the blood into the myocardium is reduced as the perfusion is increased. The relationship between extraction and flow is non-linear and, if it cannot be corrected for using mathematical models, it leads to an underestimate in the estimated MBF (62). Image resolution, though superior to SPECT, is still lower than MRI techniques and partial volume effects must be corrected for when trying to obtain separate arterial input function (AIF) and myocardial uptake curves from regions of interest (ROIs) placed on PET images. PET is associated with a significant radiation dose (especially with the accompanying CT scan), which is a cause for concern, especially if repeated scans are necessary.

PET measurements have been validated against microsphere blood measurements in animal studies (63–67). In a recent meta-analysis investigating the diagnostic accuracies of SPECT, PET and MRI, PET was found to achieve the highest diagnostic performance (AUC analysis), although CMR had the highest sensitivity at 89% (68) and other studies have shown comparable performances (69). On the basis of such evidence quantitative PET MBF values have been used as a reference standard against which to compare MR MBF estimates. In the absence of more absolute measurements of MBF in humans this is a strong reference measure for justifying any MRI methodology. However, care should be taken in the interpretation of PET measurements. PET based diagnostic accuracy studies have found that the optimal hyperaemic MBF cut-off values for diagnosing CAD is dependent on PET methodology and tracer (62,70,71). This suggests that PET MBF estimates are strongly correlated with CAD, but not absolute measures of the true MBF. The same argument is true for quantitative CMR measurements and so this is not an argument for the superiority of MRI, but care should be taken when ‘validating’ any MBF estimate against PET. A set of MBF measurements that reflect disease status but do not fall in the same MBF range as the PET measurements should not be classed as incorrect on that basis.

3.4.8. Echocardiography

Echocardiography refers to the application of ultrasound imaging to the heart.

Ultrasound generates images using a transducer that generates and records high frequency sound signals. Sound waves, travelling at different speeds in different tissues reflect from tissue interfaces and are recorded by the transducer. These recorded echoes are used to build up images of the tissue surfaces. Perfusion measurements with echocardiography have been made possible through the development of ultrasound contrast agents. These consist of microbubbles which are highly reflective to ultrasound signals. These contrast agents have been used in dogs to show that measurements of the transit times of the bubbles through the myocardium can reflect MBF in dogs with artificially occluded arteries (72). The method was later shown to have a comparable diagnostic performance to SPECT in humans (73). As a non-ionising imaging alternative the method shows promise, however, to date the method is in use in research studies only and larger clinical trials are required before it can to be accepted into clinical practice.

3.4.9. Computed tomography (CT)

By far the most common use of CT in the context of myocardial ischaemia is CT angiography, described briefly in section 3.4.5. However, CT based quantitative myocardial perfusion estimates are also possible, though rarely performed, using iodine based contrast agents and electron beam CT (EBCT), also known as ultrafast CT. Conventional CT mechanically moves the X-ray tube around the patient in order to rapidly generate multiple viewing angles. In EBCT electromagnetic coils are used to direct a beam of electrons onto any given point on a ring shaped tungsten target surrounding the patient. It is the impact of the electrons onto this circular target which generates the X-rays for imaging. The reduction in mechanical moving parts involved in EBCT enables images to be acquired much more quickly and makes the temporal resolution necessary for CT based perfusion imaging possible. An iodine based contrast agent is injected into the patient and dynamic images are acquired. MBFs can be quantified using similar models to those described in chapter 4. The method has been validated in animal studies against radioactive microspheres (74) and in humans against SPECT (75,76) with promising results. However the method does underestimate MBF at high flow rates. Although EBCT systems are the fastest CT scanners they are expensive and there are comparatively few imaging systems in use. This fact, combined with the significant radiation dose associated with dynamic CT, makes the future of CT based cardiac perfusion measurements uncertain.

3.4.10. Magnetic resonance imaging (MRI)

Perfusion imaging in MRI uses a gadolinium based MR signal enhancing contrast agent. Dynamic images, captured every RR-interval, show the passage of the contrast agent bolus through the heart. For quantitative analysis regions of interest (ROIs) drawn over the myocardium and within the blood pool are used to generate signal vs. time uptake plots. These data are analysed to generate estimates of blood flow. The imaging process is described in greater detail in section 2.8 and a description of the models used to estimate MBF is given in chapter 4.

Many studies have correlated quantitative and semi-quantitative analyses of MR perfusion estimates with microsphere measurements in animals (5,77–81) and against PET measurements in humans (5,29,80,82). One of the reasons for so many validation studies is due to the lack of standardization in the MR approach. The choice of imaging sequence, contrast agent injection scheme and analysis methodology for MBF estimation may all affect the final result. One of the aims of this thesis is to provide evidence for standardisation in MR perfusion analysis schemes. The reproducibility of MR derived perfusion measurements has also been evaluated (83–86). The results are not excellent, with only good to moderate reproducibility, but this performance is no worse than PET reproducibility values (87,88).

Ref	No. patients	MR assessment method	X-ray assessment method	Sensitivity	Specificity
(89)	42	Visual	≥ 50% stenosis	0.85	0.67
(90)	79	Visual	≥ 50% stenosis	0.91	0.62
(91)	30	Visual	≥ 50% stenosis	0.79	0.83
(3)	**533**	Visual	≥ 50% stenosis	0.67	0.61
(92)	136	Visual	≥ 70% stenosis	0.85	0.88
(93)	104	Visual	≥ 70% stenosis	0.90	0.85
(94)	75	Visual	≥ 70% stenosis	0.93	0.75
(95)	40	Visual	≥ 70% stenosis	0.81	0.68
(96)	101	Visual	≥ 70%, (≥ 50% LMS)	0.91	0.94
(2)	**752**	Visual	≥ 70%, (≥ 50% LMS)	0.86	0.83
Visual analysis average values				**0.81**	**0.76**
(97)	44	Semi-quantitative	≥ 50% stenosis	0.93	0.75
(98)	43	Semi-quantitative	≥ 50% stenosis	0.88	0.90
(99)	48	Semi-quantitative	≥ 50% stenosis	0.88	0.85
(100)	92	Semi-quantitative	≥ 70% stenosis	0.88	0.82
(101)	20	Semi-quantitative	≥ 75% stenosis	0.90	0.83
(102)	84	Semi-quantitative	≥ 75% stenosis	0.88	0.90
(103)	31	Semi-quantitative	FFR distinguish in range 50% - 75%	0.88	0.87
Semi-quantitative average values				**0.89**	**0.85**
(91)	30	Quantitative	≥ 50% stenosis	0.88	0.67
(104)	37	Quantitative	≥ 50% stenosis	0.85	0.49
(103)	31	Quantitative	FFR distinguish in range 50% - 75%	0.77	0.86
Quantitative average values				**0.83**	**0.66**

Table 3-1 – Table summarising diagnostic performance studies for CMR against X-ray angiography. Averages, weighted for study population, are shown for studies with visual, semi-quantitative and quantitative CMR data analysis.

The diagnostic accuracy of MR perfusion measurements has been assessed in a number of investigations summarized in Table 3-1. The studies are grouped in terms of whether the CMR analysis was performed using visual, semi-quantitative or quantitative analyses. It is difficult to say whether this data represents an improved diagnostic performance with semi-quantitative and quantitative methods over visual analysis. Indeed the fully quantitative scores reported here appear to have a lower diagnostic accuracy. One of the motivating factors for pursuing quantitative over semi-quantitative methods is due to the reported non-linearity of semi-quantitative MBF estimates with increasing MBF. In a comparison of semi-quantitative and quantitative perfusion methods Christian et al. found that, whereas quantitative MBF measurements agreed well with microsphere measurements in animals, semi-quantitative measurements substantially underestimated hyperaemic MBFs (77). However, these reported improvements in the quantitative approach have not propagated into an improvement in diagnostic accuracy detectable in the studies presented in Table 3-1.

There is still no consensus on an ideal protocol for acquiring DCE-MRI data for quantitative perfusion and imperfect data may be one reason for a lack of improvement with quantitation. For instance, of the three quantitative studies in Table 3-1, two studies (103,104) use a contrast dose that has been shown to lead to non-linearity effects and overestimates of MBF (105), without attempting to apply a correction. One of the motivations for quantitation is the detection of triple-vessel disease where the entire myocardium is similarly under-perfused. In this case visual detection of a perfusion defect is difficult whereas, quantitative analysis has been shown to be able to detect triple-vessel disease and to distinguish the increased ischaemic burden between single and triple vessel disease (91). As the incidence of 3 vessel disease is relatively small, another reason for the lack of a detectable improvement may be that the studies are underpowered to show such differences, particularly given the variety of acquisition protocols used.

Two large trials assessing the diagnostic performance of CMR with respect to SPECT, using X-ray angiography as the reference standard have recently been published. The MR-IMPACT II trial (3) assessed 533 patients and achieved a sensitivity of 0.67 and 0.61, with CMR achieving a superior sensitivity but inferior specificity to the SPECT performance in that trial. The CE-MARC trial (described in detail in section 5.2.1) is the largest clinical CMR trial to date and recruited 752 patients. CMR achieved a sensitivity and specificity of 0.86 (0.82, 0.90) and 0.83 (0.79, 0.87) respectively, outperforming SPECT sensitivity but not specificity. These trials provide much needed, large patient cohort evidence supporting the wider use of CMR in the clinical investigation of CHD. However, both trials evaluated the CMR data with visual analysis only. A well conducted quantitative analysis of a trial of this size would provide more persuasive evidence as to the impact of quantitation on diagnostic accuracy.

3.4.11. The AHA mapping

In 2002 Cerquieira et al (106) published recommendations for a standardized myocardial segmentation and nomenclature for tomographic imaging of the heart, which has been widely applied in the cardiac imaging community. For imaging modalities that represent myocardial perfusion a segmentation model is recommended that subdivides the imaged myocardium into 17 separate segments (Figure 3-9). The 17th segment corresponds to the apical cap, which is frequently discarded from investigations as it requires a separate long-axis acquisition (with associated scanning time) and is often too thin to provide any meaningful information. A diagnosis of ischaemia can be made by simply considering whether the MBF in any of the segments falls below a certain value, or visually appears hypoperfused. However the AHA mapping associates each of the 17 segments with one of the three coronary arteries (Figure 3-9 c) meaning that in principle a separate diagnosis for each coronary artery could be made or the perfusion image could be used to deduce the location of the coronary stenosis. In fact the coronary architecture varies from patient to patient and so the validity of this mapping will depend on the patient in each case, with the greatest variability at the apical cap which can in fact be supplied by any of the three arteries. Nevertheless, in the absence of separate images of the coronary arteries registered to the perfusion dataset the AHA mapping is the closest approximation to knowing which artery provides each territory.

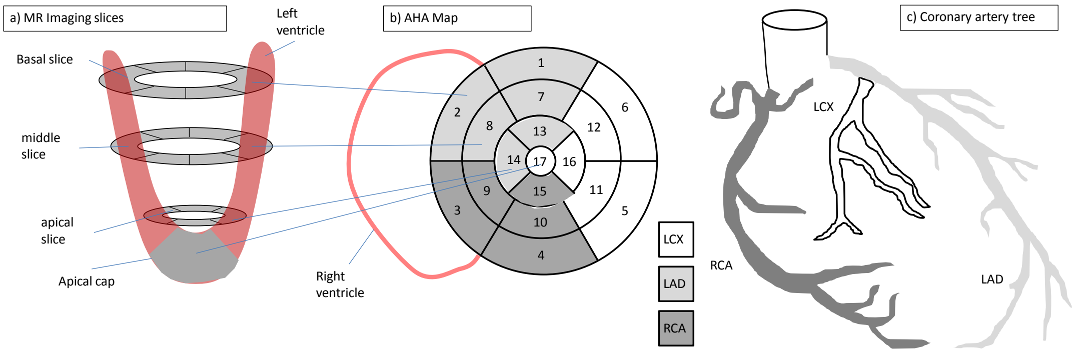

Figure 3-9 – The AHA segmentation model. Three transaxial imaging slices and a long-axis view (a) are subdivided into a 17 segment bulls-eye view (b). This can be used to each territory to the corresponding coronary artery (c).

3.4.12. The role of CMR in diagnosing myocardial ischaemia

MR perfusion imaging is now proven to be as good as SPECT (the most commonly used test) in diagnosing ischaemic heart disease, with the largest current clinical trial reporting an improvement in diagnostic sensitivity (2). There is reason to believe that CMR should out-perform nuclear medicine techniques due to its superior image resolution. Typically image resolution for SPECT is 10mm, with PET achieving 6mm. CMR achieves 3mm as standard with studies incorporating techniques such as temporal under-sampling achieving 1.5mm image resolution (107). This gives MR the ability to detect subendocardial defects, which has the potential to increase its sensitivity for detection of CAD (108). A significant advantage of the MRI investigation, which can often be overlooked when making direct comparisons of diagnostic performance, is the versatility of investigations that can be performed in a single imaging session. In a one hour CMR investigation images for investigating cardiac perfusion, wall-motion abnormalities, tissue viability and MR angiography images of the coronary arteries themselves can be obtained without the patient moving from the investigation couch (109,110). This so called ‘one-stop’, comprehensive investigation is more convenient for the patient and has the potential to be more cost-effective. The lack of ionising radiation exposure with MR is also a significant advantage, and enables longitudinal measurements to be made without concerns of increasing radiation exposure.

There are however disadvantages with MR. Patients with non MR safe implants are contraindicated and the recent concerns over the link between gadolinium contrast agents and nephrogenic systemic fibrosis (NSF) mean that renally impaired patients are contraindicated for gadolinium based contrast agents (111–114). Due to the nature of the image acquisition MR is prone to image artifacts that are often not intuitive and can obscure images entirely, rendering them unfit for diagnostic purposes. Peculiar to DCE-MRI cardiac perfusion imaging is the dark rim artifact (DRA) which mimics the appearance of a perfusion defect, although experienced observers can distinguish the two. There are a number of potential causes of the artifact (see section 2.9) but they are reduced with increasing resolution (107) and the continuing improvements in this area have the potential to reduce their impact substantially. Finally, MRI is an expensive investigation to perform. However, due to the number investigations it can perform in a single visit, it may still be a cost-effective alternative to other perfusion assessment methods.

3.5. Summary

Coronary heart disease and myocardial ischaemia have been described along with the current treatments and interventions for these conditions. The techniques for diagnosing CHD and ischaemia have been described and the advantages and disadvantages of each modality have been discussed. An analysis of the diagnostic accuracy of cardiac perfusion DCE-MRI has been presented in terms of visual analysis as well as considering semi-quantitative and quantitative analysis methods. The methods for estimating myocardial blood flow using semi-quantitative and quantitative analysis of cardiac DCE-MRI perfusion data is the subject of the next chapter.

4. Quantitative myocardial perfusion

4.1. Introduction

Previous sections have described how the MRI dataset of the contrast agent passing through the heart is acquired and how the resulting data series is processed to generate an uptake curve (chapter 2). This section provides a background to understanding some of the methods employed to estimate myocardial blood flow (MBF) based on this uptake curve. After a brief description of semi-quantitative methods a description of deconvolution approaches is given. A description of tracer kinetic model based MBF measurements is then given including a description of each of the methods compared in chapter 9.

4.2. Semi-quantitative analysis

Semi-quantitative methods do not attempt to make absolute measurements of myocardial blood flow (MBF). Rather they measure some property of the uptake curve that is thought to correlate with MBF. Figure 4-1 illustrates some of the key curve parameters. These have been interpreted as semi-quantitative measures of MBF in a variety of ways, some of which are described below:

Contrast enhancement ratio (CER) is expressed as:

$$CER = \frac{SI_{pk\_myo} - SI_{bl\_myo}}{SI_{bl\_myo}}$$

Equation 4-1

Where SI_{pk_myo} is the peak of the myocardial uptake curve and SI_{bl_myo} is the pre-contrast baseline. This is a measure of peak enhancement, i.e. the maximum effect of the contrast agent on signal intensity, after accounting for the native signal intensity. Consequently CER is a measure of the accumulation of contrast agent but takes no account of the rate of delivery or clearance of contrast agent, and so should not be expected to correlate well with MBF.

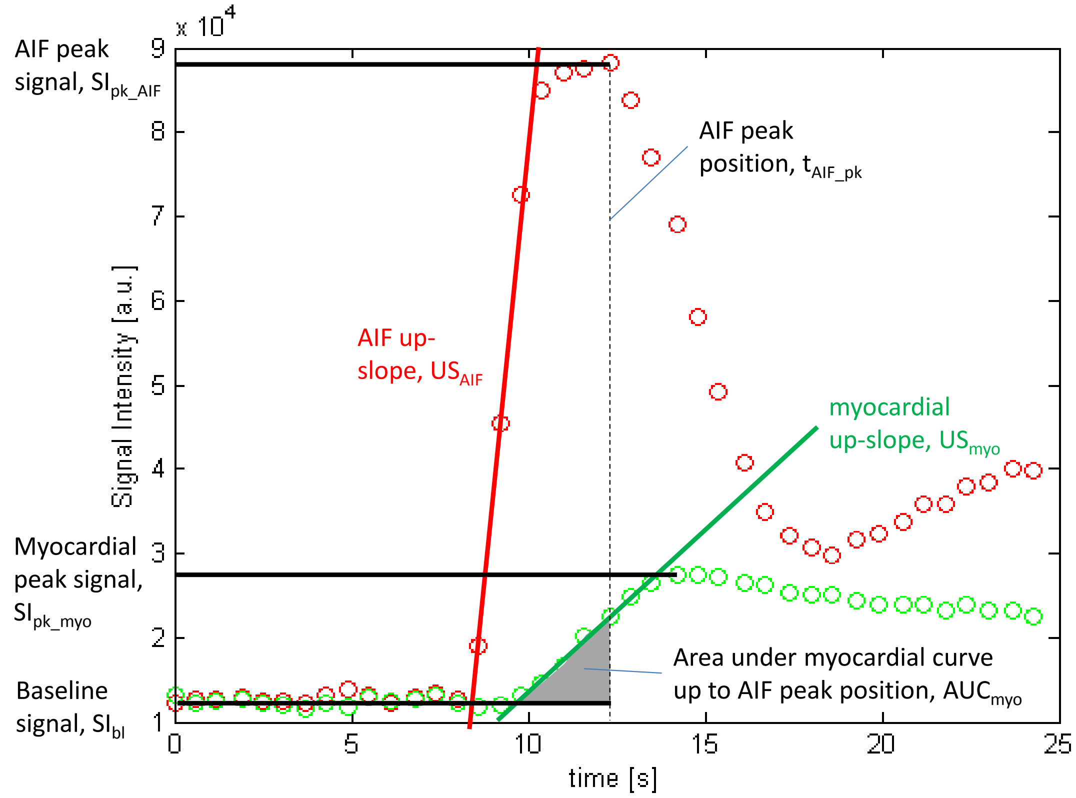

Figure 4-1 – Semi-quantitative analysis parameters. Diagram showing the baseline (SI_{bl}) and peak height SI values for the AIF (SI_{pk_AIF}) and myocardium (SI_{pk_myo}) as well as the AIF (US_{AIF}) and myocardial (US_{myo}) up-slopes and the area under the myocardial curve up to the AIF peak position (AIF_{myo}).

Upslope Index is the ratio of the AIF and myocardial up-slopes i.e. US_{myo}/US_{AIF}.

The individual up-slopes are calculated by a ‘sliding window’ method. A straight line is fitted to *n* contiguous time points from t_1 to t_n and the gradient measured. The procedure is then repeated for time points t_i to t_{i+n} for *i=1:Nt-n*, where *Nt* is the number of time points in the sequence. The maximum calculated straight line gradient is then taken as the up-slope. The up-slope of the myocardial curve is intuitively linked to flow. As the rate of flow increases the rate of change of signal due to contrast agent will increase. However, the shape of the myocardial uptake curve, and therefore its up-slope, depends on the shape of the AIF. In an attempt to factor this in to the perfusion measurement the myocardial up-slope measurements are normalised by dividing by the AIF up-slopes. The problem is that the up-slope is an obviously limited measure of the full curve shape. The relationship between AIF and myocardial curves can only be fully accounted for using fully quantitative, deconvolution based methods.

Area under the curve (AUC) measures the area under the myocardial uptake curve from the bolus arrival time (BAT) to the point corresponding to the peak enhancement in the AIF, t_{AIF_pk}. The AUC will be more sensitive to different aspects of the uptake curve shape than the up-slope method, however it incorporates no measurement of the AIF and is therefore susceptible to changes in AIF which depend on a range of factors other than MBF, such as injection rate, bolus volume, and the degree of dispersion within the vasculature prior to reaching the heart.

The AUC method has been correlated with quantitative MBF measurements in animals (115) and the up-slope index has been shown to be a diagnostically sensitive measure of CAD in humans (see Table 3-1). However in a comparison of semi-quantitative and quantitative methods significant non-linearities between semi-quantitative measurements and microsphere measurements were found in dogs (77). In general the semi-quantitative measures began to underestimate MBF at higher flow rates. This plateauing occurred at around 1ml/min/g with CER, 2ml/min/g with upslope index and 3ml/g/min with AUC. This was reflected in the linear correlation scores, CER (r=0.75), upslope index (r=0.69) and AUC (r=0.89). However, the corresponding quantitative Fermi deconvolution based correlation was excellent at r=0.95. The study illustrates how semi-quantitative measures can achieve a strong diagnostic performance in clinical trials, by virtue of their significant correlation with flow, without achieving an absolute quantification of MBF.

4.3. Quantitative analysis

4.3.1. The central volume principle

The fundamental measurement on which quantitative perfusion estimates are based is the signal intensity at a given time *t* in the myocardium. This is related to contrast agent concentration (see section 2.7) so that we have an estimate of the quantity of contrast agent in the myocardium at time *t*, $C_{myo}(t)$. For the most simple perfusion analysis the myocardium is represented as a single compartment with an arterial input of concentration $C_a(t)$ at time *t*, and venous output $C_v(t)$. Such a representation is *model-independent* in the sense that no functional tissue structure is specified. If the system is closed and stationary (

Figure 4-2) then, from the principle of mass balance the amount of tracer within the compartment is simply the difference between the amount of tracer washed into the compartment and that washed out:

$$\frac{dC_{myo}(t)}{dt} = F_p . C_a(t) - F_p . C_v(t)$$

Equation 4-2

The contrast agent resides in the blood plasma and cannot penetrate the red blood cells in the blood. C_a and C_v are *plasma* concentrations, as opposed to blood concentrations, that can be related to the concentration in the blood, C_b, via the hematocrit (Hct) which is a measure of the percentage volume of red blood cells in the blood:

$$C_b = (1 - Hct)C_a$$

Equation 4-3

F is the flow rate of blood plasma through the compartment.

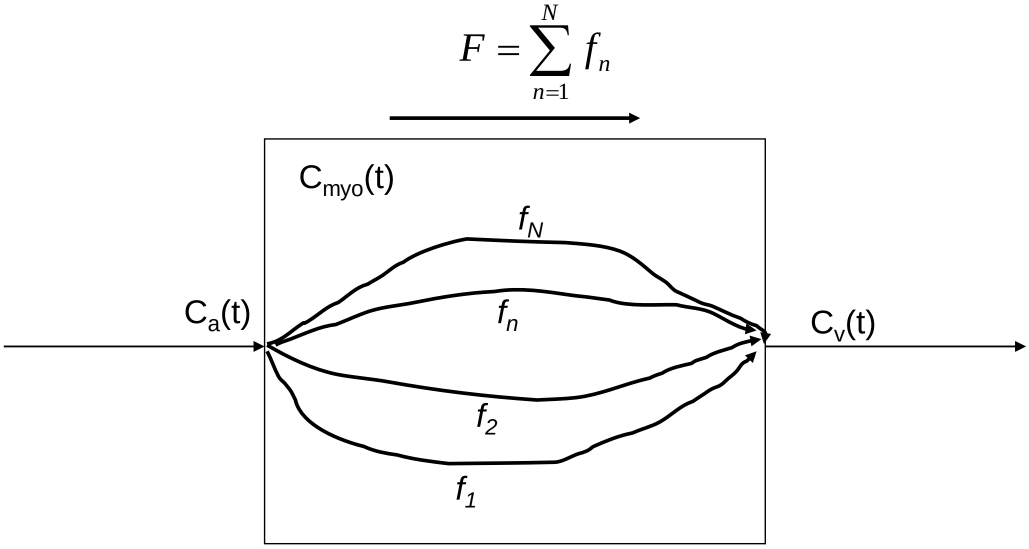

Figure 4-2 - A single compartment model. It is a *closed* system in that it has a single input $C_a(t)$ and output $C_v(t)$. The system is *stationary* if the distribution of flows $f_{1:N}$ remains constant over the duration of the measurement. The system is *linear* if the response of the myocardial tissue to an injected dose is linearly proportional to that injected dose.

For any linear and stationary system the outflow concentration can also be expressed as a convolution of the inflow concentration with transfer function *h(t)* (116,117):

$$C_v(t) = \int_0^t C_a(s)\, h(t-s) ds$$

$$C_v(t) = C_a(t) * h(t)$$

Equation 4-4

The symbol '*' represents the convolution operation. The transfer function *h(t)* represents the frequency distribution of transit times in the compartment, i.e. the distribution of times taken for CA molecules to traverse the compartment. By substituting this expression for $C_v(t)$ into Equation 4-2 an expression for $C_{myo}(t)$ that is independent of $C_v(t)$ (which we cannot measure) can be written:

$$C_{myo}(t) = F_p \int_0^t [C_a(s) - C_a(s) * h(s)] ds$$

$$\boldsymbol{C_{myo}(t) = F_p \int_0^t C_a(s) * [(\delta(s) - h(s))]ds}$$

As $\int_0^t (f(s) * g(s))ds = \left(\int_0^t f(s)ds\right) * g(t) = f(t) * \left(\int_0^t g(s)ds\right)$

$$C_{myo}(t) = F_p\left(C_a(t) * \int_0^t \delta(s)ds - C_a(t) * \int_0^t h(s)\, ds\right)$$

$$C_{myo}(t) = F_p\left(C_a(t) * \left[1 - \int_0^t h(s)ds\right]\right)$$

Equation 4-5

Introducing the flow weighted impulse response function *$R_f(t)$:*

$$R_f(t) = F_p\left[1 - \int_0^t h(s)ds\right] = F_p\, R(t)$$

Equation 4-6

Equation 4-4 becomes:

$$C_{myo}(t) = R_f(t) * C_a(t)$$

Equation 4-7

R(t) is the tissue response function which represents the fraction of contrast agent that remains in the compartment at time *t*, where *t=0* corresponds to the time of injection. By this definition, at time zero, it has value one (R(t=0) = 1) signifying that no tracer can instantaneously traverse the ROI. Therefore from Equation 4-6 R_f(t=0) = F. This means that if Equation 4-7 can be solved for $R_f(t)$ then it is possible to estimate the flow by evaluating R_f(t=0).

4.3.2. Deconvolution

If estimates for $C_{myo}(t)$ and $C_a(t)$ are obtained from ROIs placed over the myocardium and the left ventricular blood pool in the dynamic image series then it might be expected that it would be possible to solve Equation 4-7 by performing deconvolution. However, deconvolution is a mathematically ill-posed problem. This means that there are multiple solutions for $R_f(t)$ that give a good fit to the same data set. In practice this means that very small changes in $C_a(t)$ or $C_{myo}(t)$ yield large changes in the resulting $R_f(t)$. It is easier to understand why this is so if one considers the Fourier convolution method for performing deconvolution in the Fourier domain. The Fourier convolution theorem states that convolution in the time domain is equivalent to point-wise multiplication of the Fourier transforms of the two quantities in the convolution integral:

$$C_{myo}(t) = R_f(t) * \ C_a(t)$$

$$\mathcal{F}\{C_{myo}(t)\} = \mathcal{F}\{R_f(t)\}\mathcal{F}\{C_a(t)\}$$

Equation 4-8

Where $\mathcal{F}\{x\}$ represents the Fourier transform of *x*. Thus the flow weighted response function can be calculated as follows:

$$R_f(t) = \mathcal{F}^{-1}\left\{\frac{\mathcal{F}\{C_{myo}(t)\}}{\mathcal{F}\{C_a(t)\}}\right\}$$

Equation 4-9

As $C_a(t)$ will be a smoothly varying function $\mathcal{F}\{C_a(t)\}$ will contain some frequencies with zero, or very small amplitude, giving infinite, or very large, corresponding values in $R_f(t)$ (118). Hence the solution described in Equation 4-9 is unstable.

4.3.3. Fermi-constrained deconvolution

In cardiac perfusion the most widely accepted method for constraining Equation 4-7 is to represent $R_f(t)$ as a Fermi function, which is a three parameter monotonically decaying curve (119,120):

$$R_f(t) = \frac{A}{1 + e^{-\frac{(t-\varpi)}{\tau}}}$$

Equation 4-10

Once the form for $R_f(t)$ has been defined like this the deconvolution problem becomes a matter of finding the parameters for Equation 4-10 that best fit the given $C_{myo}(t)$ after convolution (Equation 4-7). Thus the deconvolution process is reduced to a three parameter fit, which can be approached robustly with linear least squares fitting techniques. The Fermi function is a decreasing exponential with a shoulder near t=0. The early flattening of the curve allows for the initial filling stage of the compartment and the later exponential fall off is due to the decreasing fraction of CA left in the compartment with increasing time. Fermi-constrained deconvolution can be described as *parametric* deconvolution, as it provides a parametrisation of the response function which is not based on an underlying model of the tissue structure. The choice of the Fermi-function to constrain the data is empirical, not theoretical. It has a shape that resembles response functions derived using detailed models of the vasculature or those derived using model-independent methods (section 4.3.4), but it is not based on a theory of indicator passage through the myocardium. In practice Fermi-constrained deconvolution only performs comparably with other models if the data is limited to the first-pass only. Failure to reduce the data before fitting this way results in a 25% overestimate in blood flow with the Fermi model (4).

4.3.4. Model independent analysis

M*odel-independent* deconvolution methods perform deconvolution without inherently assuming a structure for $R_f(t)$. Rather than imposing a theoretical model or a given parameterisation on the response function these models only impose general side constraints on the solution to Equation 4-7. This can be done by posing the problem as a matrix inversion problem and adding an additional side constraint. Expressing the convolution in Equation 4-7 as the convolution integral:

$$C_{myo}(t) = \int_0^t C_a(t-s)R_f(s)ds$$

Equation 4-11

Adopting the convention that the value of a vector R_f at the *i*th time point is R_{fi}, Equation 4-11 can be discretised as follows:

$$C_{myo}(t_i) = C_{myo\,i} = \sum_{j=1}^{i} C_a(t_i - t_j)\, R_f(t_j)\ \Delta\mathrm{t} = \sum_{j=1}^{i} A_{i,j}.R_{f\,j}$$

Equation 4-12

Where *A* is a matrix constructed of the *N* elements of *C*$_a$*(t)* such that matrix multiplication with A performs convolution with *C*$_a$*(t)*:

$$A = \begin{bmatrix} C_{a1} & 0 & \dots & 0 \\ C_{a2} & C_{a1} & \dots & 0 \\ \vdots & \vdots & \ddots & \vdots \\ C_{aN} & C_{aN-1} & \dots & C_{a1} \end{bmatrix} \Delta\mathrm{t}$$

Equation 4-13

Thus:

$$C_{myo} = A.R_f$$

Equation 4-14

And the solution for *R*$_f$*(t)* can in principle be obtained by inverting *A*:

$$R_f = A^{-1}.C_{myo}$$

Equation 4-15

Again this is an ill-posed problem and Equation 4-15 yields unstable solutions for *R*$_f$*(t)*. Posed as a matrix inversion problem, singular value decomposition (SVD) can be used to find the best solution to Equation 4-15 in the least squares sense. We seek the response function that minimises:

$$min\left\{\left\|A.R_f - C_{myo}\right\|^2\right\}$$

Equation 4-16

Equation 4-16 is in the correct form to apply the SVD to find *R*$_f$*(t)* (121)(122) :

$$U.\Sigma.V^T = SVD(A)$$

$$R_f(t) = \sum_{i=1}^{N_s} \left(\frac{u_i^T.C_{myo}(t)}{\sigma_i}\right).v_i$$

Equation 4-17

where u_i and v_i represent the i^{th} columns of the output matrices from the SVD algorithm U and V respectively and σ_i represents the i^{th} value along the leading diagonal of Σ, of length s, that is the i^{th} singular value. Equation 4-17 gives the closest solution to Equation 4-16 in the least squares sense. However if there are small singular values in σ then very large values will be generated in the R_f and the solution will show large spurious oscillations (81). The problem can be tackled using truncated SVD where only singular values up to a certain cut off ($N_s < N$) are included in Equation 4-17.

An alternative method for regularizing the solution, frequently utilised in the cardiac perfusion literature (81,123), is that of Tikhonov regularization (121), which incorporates an additional side constraint into Equation 4-16. The matrix L applied to R_f incorporates an additional constraint, dependent on the response function, into minimisation:

$$min\left\{\left\|A.R_f(t) - C_{myo}(t)\right\|^2 - \lambda^2\left\|LR_f(t)\right\|^2\right\}$$

Equation 4-18

Typically L is the identity matrix, but the first order differential matrix can also be used, in which case the solution is constrained by the temporal gradient of the response function which forces the solution to be smooth to a degree dictated by the value in the coefficient λ.

Truncated SVD and Tikhonov regularization both provide a framework for a generalised, model-independent solution to Equation 4-17. However they are both critically dependent on a single parameter (the cut-off point N_s for TSVD and the parameter λ in Tikhonov regularization). A common approach for finding the optimal value for these parameters is L-curve analyses (121) which is described in the context of Tikhonov regularization as follows. The technique plots the two components of Equation 4-18 over a range of values of λ, on a log scale. When the smoothness constraint is dominant there is a large change in $\left\|LR_f(t)\right\|$ as λ changes. Conversely when the unconstrained solution is dominant $\left\|A.R_f(t) - C_{myo}(t)\right\|$ change rapidly with λ . The resulting plot has an 'L' shape, hence 'L-curve' analysis (Figure 4-3), with the optimal value for λ at the corner of the ‘L’, i.e. at the maximum point of curvature.

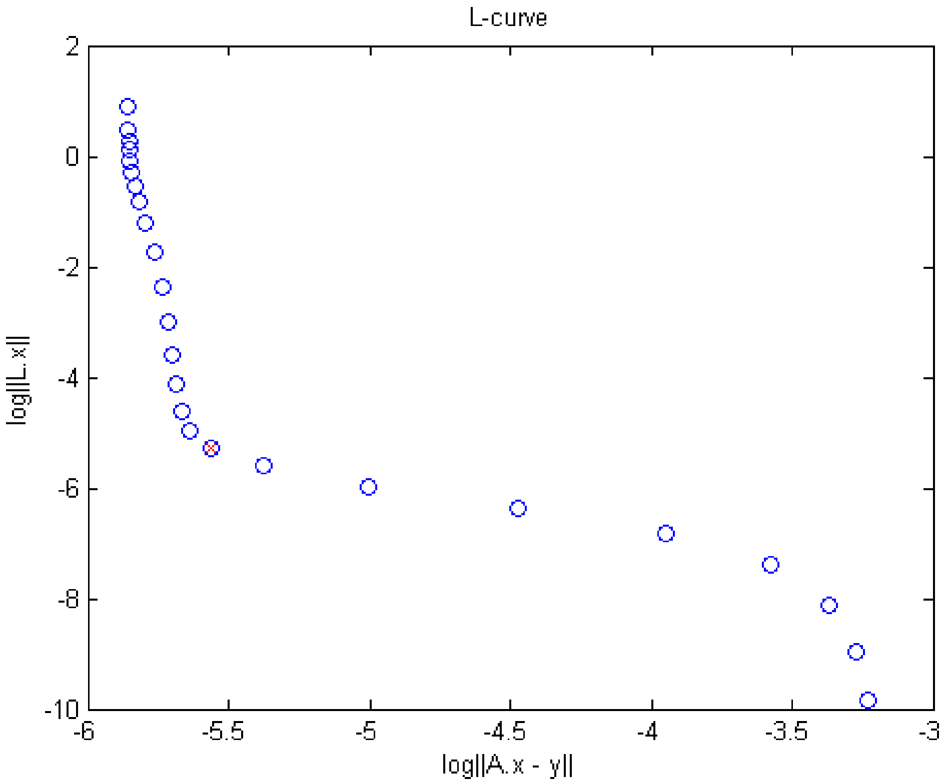

Figure 4-3 – L-curve analysis - the y-axis (log||Lx||) shows the smoothness constraint alone, whilst the x-axis plots only the unconstrained solution log||Ax-y||. The ‘x’ marks the optimal λ value where neither component is dominant.

Model-independent analysis is completely model free, in that the response function can take any form. Therefore the entire dataset (as opposed to just the first-pass in Fermi-analysis) can be incorporated into the analysis. However, the lack of any constraint, apart from smoothness, on the response function means that unphysiological response functions (that create good fits but extreme MBF estimates) can be generated. The method described here has been validated in human volunteers (6). Previous validation against radioactive microsphere measurements in pigs was performed using a similar model-independent strategy that represented the response function as a sum of B-splines before applying Tikhonov regularization (81).

4.3.5. Tracer-kinetic modelling

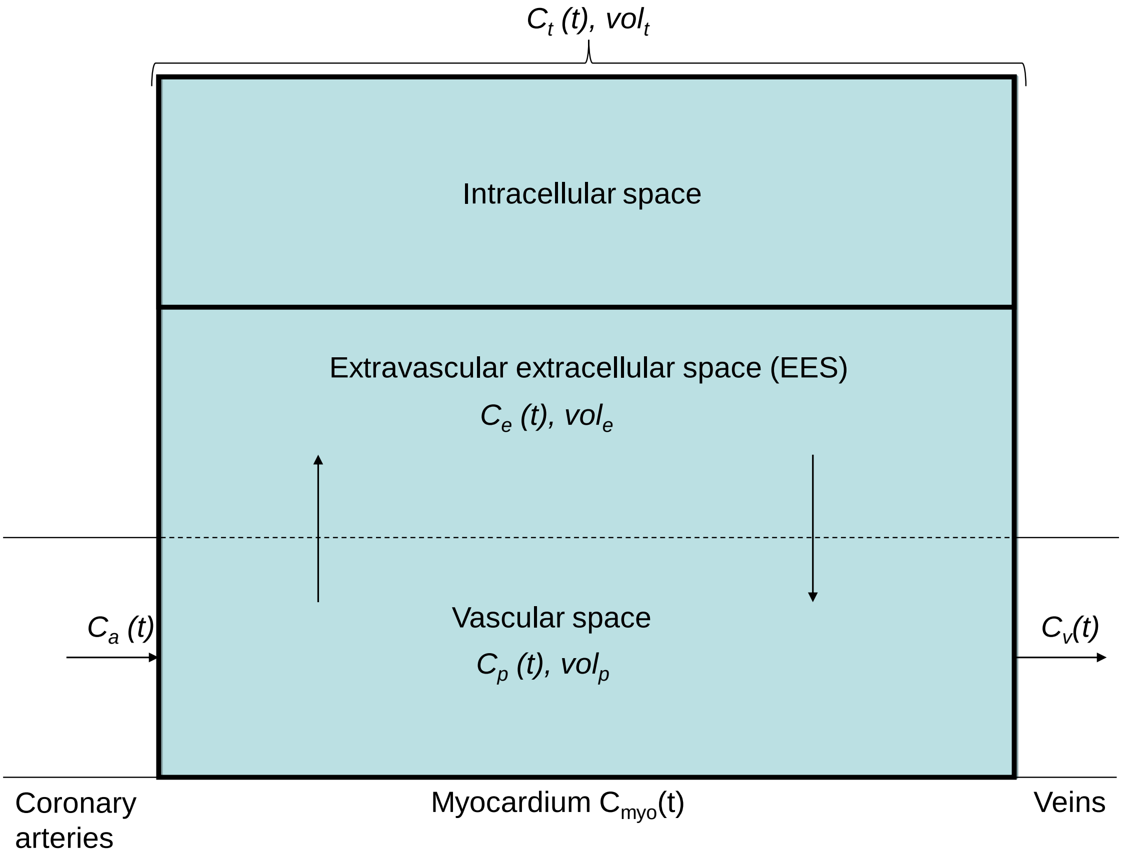

Figure 4-4 – Contrast agent enters through a single input with concentration C_a(t) and leaves with concentration C_v(t). Contrast agent flows across the capillary membrane from the vascular space to the extravsacular, extracellular space (EES). Contrast agent cannot pass through cell membranes into the intracellular space.

Parametric deconvolution methods (such as Fermi) and model-independent techniques attempt to find a response function to relate C_a and C_{myo} without any theoretical consideration of the form of the response function. Tracer-kinetic modelling approaches pose an analytic form for the response function based on a set of assumptions about the tracer-kinetic properties of the tissues (124). Depending on the complexity of the model they can generate other physiological parameters describing the nature of the perfused tissue, such as the volumes of the vascular and extravascular spaces. However care must be taken that the assumptions made in the derivation of the model hold true in all cases of application and that the data is of sufficient quality to derive robust measurements of the parameters, as more complex models can over-fit data and generate results which are physiologically non representative.

Gd-DTPA is an extravascular contrast agent and as such leaks from the vascular space (inside capillaries and arteries) into the extravascular, extracellular space (the tissue space outside the vasculature also known as the interstitium) but not through cell membranes into cells (the intracellular space), except in necrotic cells. Figure 4-4 illustrates these spaces and denotes the CA concentrations and volumes of each of the spaces accordingly. The process can be modelled using the two compartment exchange model (2CXM) illustrated in Figure 4-5.

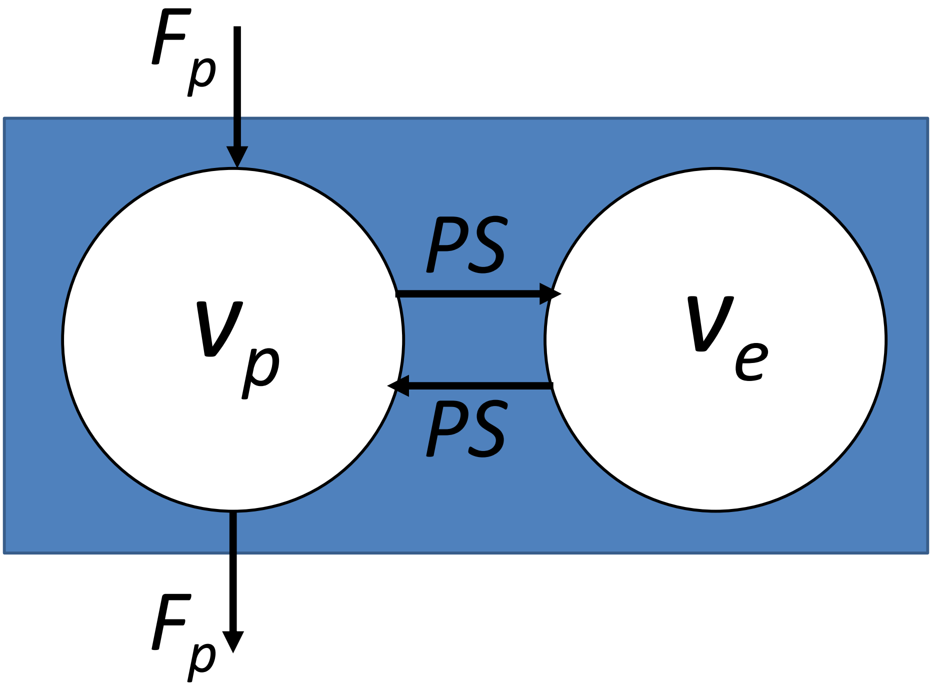

Figure 4-5 – The two compartment exchange model. Contrast agent flows at a rate F_p into the vascular space of volume fraction v_p. Indicator leaks between the vascular space and the EES (volume fraction v_e) at a rate dictated by the product of the capillary surface area S and permeability P.

Plasma flows at a rate F_p into the vascular space and out at the same rate. Whilst in the vascular space, indicator passes through capillary walls at a rate dictated by the product of the capillary surface area *S* and the capillary permeability *P*. The volume fraction of the vascular space and EES are defined relative to the volume of the tissue region:

$$v_p = \frac{vol_p}{vol_t}$$

$$v_e = \frac{vol_e}{vol_t}$$

In the previous discussion a compartment was a space across which indicator could traverse with a distribution of transit times. In this context the definition of a *compartment* becomes a well mixed space into which contrast agent instantaneously and homogeneously mixes. Once this has been established systems of equations defining the rate of change of indicator in each compartment can be constructed by employing conservation of indicator mass which states that no indicator is created or destroyed inside the tissue. Hence the rate of change of indicator for a given compartment must be the difference between the influx and outflux from the compartment. The outflux from any compartment is equal to concentration of CA in that compartment multiplied by the flow rate. Applying these principles to Figure 4-5:

$$v_p \frac{C_p(t)}{dt} = F_p C_a(t) + PS\, C_e(t) - F_p C_p(t) - PS\, C_p(t)$$

Equation 4-19

$$v_e \frac{C_e(t)}{dt} = PS\, C_p(t) - PS\, C_e(t)$$

Equation 4-20

The two compartment model has a bi-exponential impulse response function (125) and can be used for uptake curve fitting. However in general, and particularly in the heart, much simpler models are used.

4.3.6. One compartment ($PS = \infty$)

Capillary permeability in the myocardium is high. If permeability is high enough the two compartment model becomes flow limited and it is not possible to derive permeability figures from the model because effectively all indicator that arrives permeates the capillaries immediately. In this case the vascular space and EES become one compartment with a concentration C_{myo}:

$$C_{myo}(t) = v_p C_p(t) + v_e C_e(t)$$

Equation 4-21

If we assume that the indicator is instantaneously and well mixed, and that there is only a single compartment then the venous output concentration will be equivalent:

$$C_v(t) = C_p(t) = C_e(t)$$

Equation 4-22

$$C_v(t) = \frac{C_{myo}(t)}{v_p + v_e}$$

Equation 4-23

Now utilising the original equation for the one compartment model Equation 4-2:

$$\frac{dC_{myo}(t)}{dt} = F_p C_a(t) - F_p \frac{C_{myo}(t)}{v_p + v_e}$$

Equation 4-24

Equation 4-24 is an inhomogeneous, first-order linear differential equation with constant coefficient, for which an equation of the form:

$$\frac{dx}{dt} = -a\, x(t) + y(t)$$

Has the solution:

$$x(t) = e^{-at} * y(t) + e^{-at}\, x(0)$$

Therefore, setting $C_{myo}(0) = 0$, Equation 4-24 has the solution:

$$C_{myo}(t) = F_p C_a(t) * e^{-\frac{F_p}{v_p + v_e}t}$$

Equation 4-25

4.3.7. The uptake model

The model can be simplified even further by removing the venous outflow from the model such that:

$$\frac{dC_{myo}(t)}{dt} = F_p C_a(t)$$

Equation 4-26

This model only holds in the early stages of contrast uptake in the myocardium when the finite transit time of the myocardium means that CA is entering but not leaving the compartment. From Equation 4-26 it follows that:

$$C_{myo}(t) = F_p \int_0^t C_a(s)ds$$

Equation 4-27

So that F_p can be measured plotting the integral of the AIF up to t against the myocardial concentration at t and taking the slope of the straight line fit to the data points.

This is a very simple analysis method to perform. The difficulty is in deciding at which time point the no venous output assumption ceases to hold. This can be done by establishing the data set for which the best fit to the straight line is achieved (126). A more pragmatic approach is to simply choose the peak of the AIF as the cut-off point (123).

4.4. Summary

This chapter has provided a description of some of the methods used for estimating myocardial blood flow in the heart. Most of these methods are also used in other anatomies and imaging modalities. However the emphasis here has been on the application of these methods to measure myocardial blood flow from cardiac perfusion DCE-MRI datasets only. The chapter provides the underlying theory for the quantitative methods used in later chapters of this thesis. In particular the models that are compared in chapter 9 have been described in detail.

5. General methods

5.1. Overview

The research in this thesis is primarily based on data from two studies; the dual-phase study and the CE-MARC trial and the following chapters will refer to these datasets repeatedly. The full methodologies and primary purposes of these two studies are outlined in section 5.2 in order to avoid unnecessary repetition in subsequent chapters. In order to generate quantitative MBF estimates from these datasets contours depicting the myocardium, and a region within the left ventricular blood pool depicting the AIF, must be drawn. The contouring protocol used in this thesis is described in detail in section 5.3. All of the quantitative MBF estimates presented in this thesis were generated using automated curve pre-processing. The algorithms used to automate pre-processing are described in section 5.4 and are tested for failures as assessed by human observation in section 5.5.

5.2. Datasets

5.2.1. CE-MARC

Purpose

The CE-MARC trial (2,23) was designed to establish the accuracy of a multi-parametric cardiovascular magnetic resonance (CMR) protocol for diagnosing coronary heart disease against a reference standard of X-ray coronary angiography. The trial also compared the diagnostic capabilities of CMR and nuclear medicine SPECT. 752 patients with suspected angina were assigned to the trial and 628 patients completed with assessable and available results in all three modalities (CMR, SPECT and X-ray angiography). The trial concluded that CMR had a sensitivity of 86.5% and specificity of 83.4% and found a significant improvement in the sensitivity of CMR over SPECT in diagnosing CHD (2).

Method

Out of 4065 consecutive patients presenting at Pinderfields General Hospital or Leeds Teaching Hospitals with suspected angina pectoris 752 were recruited to the trial. Exclusion criteria were; previous coronary artery bypass surgery, crescendo angina, acute coronary syndrome or contraindication to CMR, adenosine or gadolinium based contrast agent. 628 patients completed CMR, SPECT and X-ray angiography investigations and were included in the final analysis.

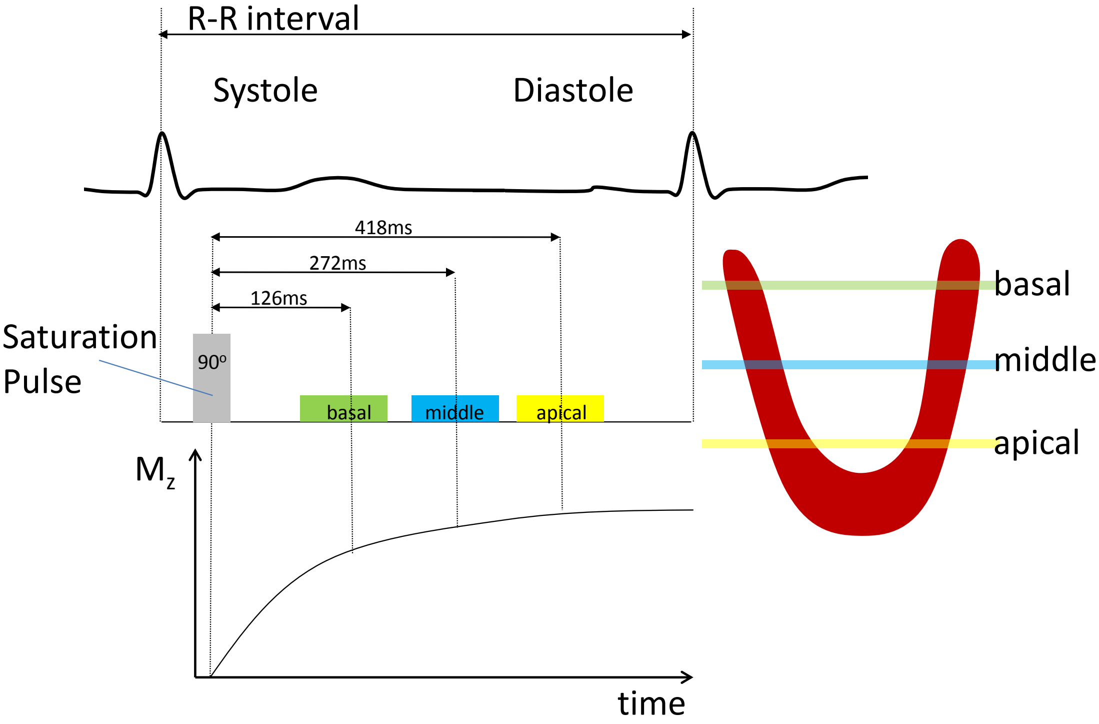

Figure 5-1 – CE-MARC perfusion pulse sequence. A single, shared 90^o saturation pulse is used giving saturation times (TS) for the basal, middle and apical cardiac slices of 126ms, 272ms and 418ms respectively and resulting in different T_1-weighting and cardiac phase for each of the three slices.

Cardiac MRI

For the MRI investigation patients were positioned supine on a dedicated cardiac research scanner (1.5T, Intera CV, Philips, Best, The Netherlands) equipped with ‘Master’ gradients (30mT/m peak gradients and 150mT/m/ms slew rate). Signals were received with a 5 element cardiac phased-array RF coil and ECG gating and triggering was performed. For the perfusion investigation patients were imaged using aT_1-weighted saturation recovery turbo field echo (SR-TFE) imaging sequence. Three slices were acquired with a single shared saturation pulse in order to fit the three image acquisitions in a single RR-interval. Images were acquired with a linear k-space ordering, with the central line of k-space acquired at 126ms for the basal slice, 272ms for the middle slice and 418ms for the apical slice. Using a shared pre-pulse results in a different image contrast for each imaging slice as well as different cardiac phases for each slice. The basal slice will be more systolic (and less T_1-weighted) whereas the apical slice will have a stronger T_1-weighting and will be imaged in the diastolic phase (See Figure 5-1).

No. lines of k-space in FAS	12
Central line of k-space	21
Partial Fourier	0.67
TR/TE	2.7ms / 1.0ms
Alpha (after FAS)	15^o
TS	Basal 126ms, middle 272ms, apical 418ms (from 90^o pulse to central line of k-space)
SENSE	Factor 2
FOV	320mm – 460mm
Typical matrix size	144x144 (reconstructed to 256x256 by zero filling before reconstruction)
Slice thickness	10mm

Table 5-1 – Scan parameters for the CE-MARC perfusion imaging sequence

The three slices were positioned according to the "3 of 5" technique (127). Pulse sequence parameters: TE 1.0 ms, TR 2.7 ms, flip angle 15°, SENSE factor 2, matrix 144 × 144, field of view 320–460 mm, slice thickness 10 mm partial Fourier 0.67, resulting in a single slice acquisition time of 130ms (summarized in Table 5-1). Imaging was carried out whilst a bolus intravenous injection of 0.05 mmol/kg dimeglumine gadopentetate (Magnevist®, Schering AG, West Sussex, UK) followed by a 15 ml saline flush was delivered through an arm vein at 5 ml/s using a power injector (Spectris®, Medrad, Pittsburgh, Pennsylvania). The patient held their breath at end expiration timed to coincide with the first-pass of the bolus through the heart. The patient was then directed to hold their breath for imaging for as long as possible thereafter and then to commence gentle breathing to minimise breathing motion as much as possible in subsequent image frames. Stress was pharmacologically induced using an intravenous injection of adenosine administered at a dose of 140 mcg/kg/min. The patient's blood pressure was recorded every two minutes and the heart rhythm monitored on the vector-ECG. The perfusion study commenced approximately 4 minutes into the adenosine infusion. A rest perfusion study was performed approximately 15 minutes after the stress investigation.

Nuclear Medicine

The nuclear medicine investigation was conducted using SPECT (Single Photon Emission Computed Tomography) gamma camera imaging. As with the MR investigation patients were imaged under rest and stress conditions, with stress induced using 140 mcg/kg/min of adenosine for 4 minutes so that the techniques for SPECT and CMR were directly comparable. Patients were injected with the radioisotope tracer 99^{m}Tc tetrofosmin (Myoview) using a standard dose of 400 MBq for each examination, adjusted for weight to a maximum of 600 MBq per examination. SPECT images were acquired with the patients in the supine position. Eight ECG gated frames per cardiac cycle were acquired using 64, 40s long projections at 3^{o} over a 180^{o} orbit using a 64 x64 matrix size. Transaxial slices of 6mm were reconstructed using filtered back projection using a Butterworth filter with a cut-off frequency of 0.4 Nyquist and order of 6. Transaxial slices were reorientated to the cardiac axes for analysis. Semi-quantitative analysis of the perfusion data including summed stress and rest scores was performed. Based on visual comparison of rest and stress SPECT perfusion scans, each SPECT dataset was summarized as having fixed or inducible defects in the anterior, lateral, septal or inferior positions.

X-ray Reference Standard

Invasive X-ray angiography using a radio-opaque dye was performed on all of the patients after CMR and SPECT. A quantitative estimate of the degree of coronary stenosis (expressed as a percentage reduction in vessel lumen) was made for each identified stenosis. Coronary artery stenoses were then mapped to myocardial segments using the AHA recommended mapping (106) (see section 3.4.11).

5.2.2. Dual phase

Purpose

The dual-phase study was designed to acquire DCE-MRI cardiac perfusion time series with identical scan parameters at systole and diastole. The primary purpose of this dataset was to identify differences in MBF between systole and diastole (128). For this reason the pulse sequence was designed to optimize image quality in a single 2D slice and allow this slice to be scanned using identical preparation and read-out settings at two separate time points in the cardiac cycle.

Method

Seventeen healthy volunteers (9 male, 8 female, mean age 34 years age range 24–48 years) with no history of heart disease, diabetes, hyperlipidaemia or chronic illness were recruited into the study. All volunteers had normal blood pressures and showed normal left ventricular mass as assessed by planimetry in short-axis left ventricle stack images. Informed consent was taken from all volunteers in accordance with a study protocol approved by the regional ethics committee. All volunteers were instructed to refrain from caffeine for 24 h prior to the examination. Volunteers underwent myocardial perfusion DCE-MR imaging on a 1.5T whole body imaging system (Phillips Medical Intera systems, Best, The Netherlands). Volunteers were positioned supine with a flexible five element cardiac phased array receiver coil placed on their chest. Images were acquired during an intravenous injection of contrast (Magnevist, Schering, Berlin, Germany) at a dose of 0.05mmol/kg Gd-DTPA at a rate of 5ml/s followed by a 20ml saline flush via an automated infusion pump (Medrad Spectris Solaris,Medrad, Indianola, PA,USA). Volunteers were initially imaged under stress, which was pharmaceutically induced by an intravenous infusion of adenosine over 4 min at 140 µgmin^{-1} kg^{-1}. A rest scan was acquired approximately 15 min later. Mid-ventricular short-axis DCE-MRI series were acquired at mid-systole and mid-diastole. Images were acquired using a saturation recovery prepared single-shot gradient echo pulse sequence, (see Figure 5-2).

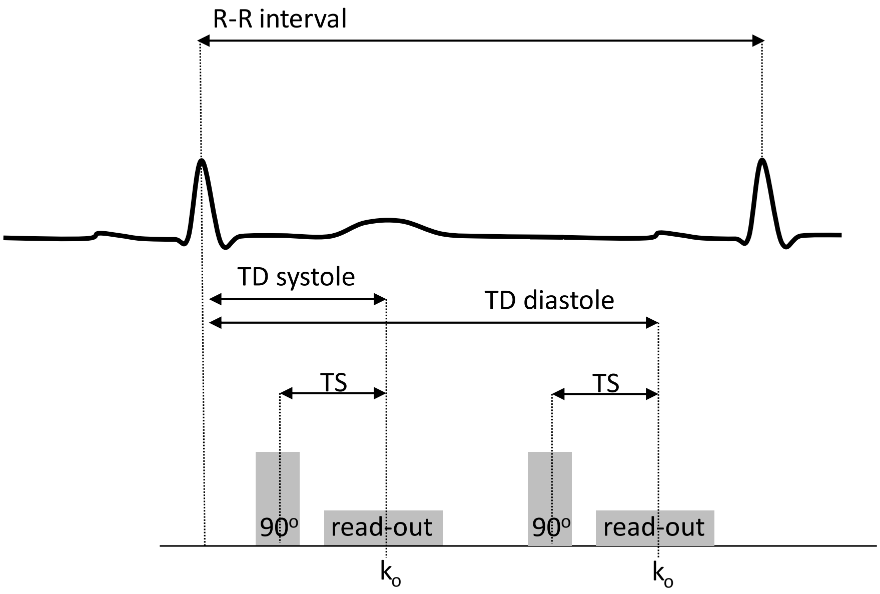

Figure 5-2 – The dual-phase imaging sequence. In a single RR-interval two SR-GRE images are acquired with equal saturation times (TS) from the 90^o pulse to the central line of k-space (k_o) and different trigger delays (TD) to place the two images in mid-systole and mid-diastole.

The pulse sequence parameters are described in Table 5-2, including the number of lines of k-space involved in the flip angle sweep and the position of the central line of k-space (k_o), which were ascertained using the Phillips Pulse Programming Environment (PPE). The slice thickness was 10mm and the mean FOV was 332 mm × 284 mm (range: 290 mm × 245 mm to 410 mm × 338 mm). The mean scan pixel size was 2.27 mm × 1.95 mm (range: 2.08 mm × 1.70 mm to 2.64 mm × 2.35 mm). All images were reconstructed to a 256 × 256 matrix size giving a mean reconstructed pixel size in the image of 1.30 mm × 1.11 mm (range: 1.13 mm × 0.96 mm to 1.60 mm × 1.32 mm). Each dynamic image was obtained after an ECG triggering timed to image the heart in systole or diastole. Volunteers were instructed to hold their breath at end expiration, timed to coincide with the arrival of contrast into the heart, for as long as they were capable and then to resort to gentle breathing thereafter. This breath-holding strategy minimizes motion during the first-pass of contrast agent through the myocardium, which is the data used for MBF estimation in this study. A total of 60 dynamic frames were acquired in each DCE-MRI set. Slice positioning and the timing of acquisition were designed to image the same single mid-ventricular short-axis slice at systole and diastole. The position of the end-systolic slice was

No. lines of k-space in FAS	12
Central line of k-space	21
Partial Fourier	0.67
TR/TE	2.7ms / 1.0ms
Alpha (after FAS)	15^o
TS	150ms (from 90^o pulse to central line of k-space)
SENSE	Factor 2
Typical matrix size	160x160 (reconstructed to 256x256 by zero filling before reconstruction)
Slice thickness	10mm
rFOV	80%

Table 5-2 – Pulse sequence parameters for the dual-phase imaging protocol.

planned using a cine series (two-chamber and four- chamber view, 30 phases) so that it was located in the mid-ventricular position. Because of the longitudinal lengthening of the heart from systole to diastole, the myocardium at the mid-ventricular level in systole moves toward the base of the heart in diastole. To allow for this movement the diastolic slice position was planned immediately above the middle slice, nearer to the base of the heart, and its position was verified in the chosen diastolic frame. Finally, the trigger delay for each slice of the DCE-MRI readout was selected from the cine images so that slice 1 was acquired in end-systole, followed by the slice 2, which was acquired mid-diastole (see Figure 5-2).

5.3. Manual contouring of myocardial perfusion imaging

For all of the datasets described in this thesis endocardial and epicardial contours were manually drawn by an expert user for every frame and every slice of the cardiac DCE-MRI dynamic series using dedicated cardiac image analysis software (Mass 7.0, Medis, Leiden University, Leiden, The Netherlands). A further contour was drawn within the left ventricular blood pool, avoiding the papillary muscles to sample the blood pool (see Figure 5-3). In order to subdivide the myocardium into the circumferentially equidistant regions recommended by the AHA (106) a reliable marker is required to ensure that the myocardium is divided with respect to the same reference point. For the dual-phase dataset this was taken to be the anterior insertion point (where the right ventricular wall meets the left ventricular myocardium). For the CE-MARC dataset it was found that the corresponding posterior junction (where the right ventricular wall meets the left ventricular myocardium) was easier to identify, thus a more reproducible marker, and so this was used as the marker in that dataset.

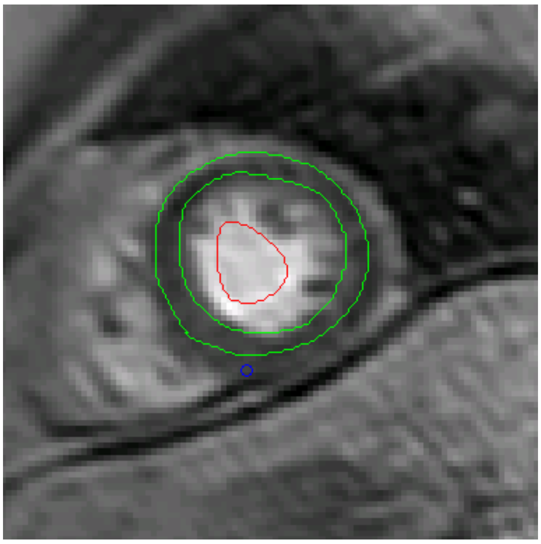

Figure 5-3 – Contour example from the CE-MARC dataset. Myocardial contours (green), a contour within the left ventricular blood pool representing the AIF (red) and the reference point marker (blue).

In a given dynamic series the image exhibiting maximum contrast between the myocardium and surrounding tissues was used to draw the contours. These contours were then copied to the full time series and manually translated to compensate for breathing motion. This contouring methodology inherently assumes that the cardiac motion in the dynamic series consists of rigid translations only. In fact rotational motion and some non-rigid deformity is also present in these datasets. This must be accepted as a limitation to the contours used in these investigations. However, it is important to note that breath-holding for these acquisitions was timed to coincide with the first-pass of contrast agent through the myocardium, being the most important data for quantifying perfusion. Throughout breath-holding the ‘rigid translation only’ assumption is reasonable. An alternative contouring strategy would be to draw separate contours for every individual frame. Besides the substantial increase in time and effort that using such a strategy would entail, it is not certain that the resulting contours would be a better representation of the true myocardial uptake curves. It is very difficult to identify the myocardium in the low image contrast images before and after the main bolus and the contour errors generated due to poor image contrast in these frames may well exceed those generated by allowing rigid translation only (see Figure 5-4). The ideal contouring methodology would consist of propagating the maximal contrast contours to the rest of the dataset via a non-linear registration algorithm. However image registration algorithms can also be unreliable (especially in the presence of image artifacts). Suffice to say that, although the contouring strategy used here will generate errors, there is not an alternative strategy that would be guaranteed to yield more accurate results. Furthermore, the protocol used here is commonly employed, and thus the conclusions of the work in this thesis should be generally applicable across centres applying similar contouring strategies.

Figure 5-4 – Example of poor image contrast pre contrast bolus making accurate myocardial contouring difficult. (Taken from the same patient as Figure 5-3).

5.4. Automated analysis of perfusion curves

Introduction

Quantitative analysis of myocardial perfusion uptake curves requires pre-processing of the curves. Both AIF and myocardial uptake curves must be baseline corrected so that the native tissue has a concentration value of zero. For Fermi-constrained deconvolution the post first-pass data must be cropped from the curves to avoid significant overestimates in MBF (4). For analysis of large datasets, especially when the myocardium is subdivided into multiple regions, manual pre-processing becomes prohibitively time-consuming and one of the multiple obstacles to the acceptance of quantitative MBF estimates into clinical practice. This section describes methods for full automation of myocardial perfusion uptake curve pre-processing before evaluating the performance of these methods by visual verification.

Methods

5.4.1. Measuring the baseline

Quantitative perfusion methods model the passage of a contrast agent bolus through the heart. The pre-contrast signal intensity should therefore be zero, corresponding to zero contrast agent in the tissue. If the signal values from the imaging system are converted to CA concentration before analysis then the resulting pre-contrast CA concentration will be zero by definition, but the conversion process requires a measurement of the pre-contrast baseline signal intensity in any case. For the rest dataset, remnant contrast agent will be present from the stress study and so a second baseline subtraction step will be required to remove remnant contrast agent.

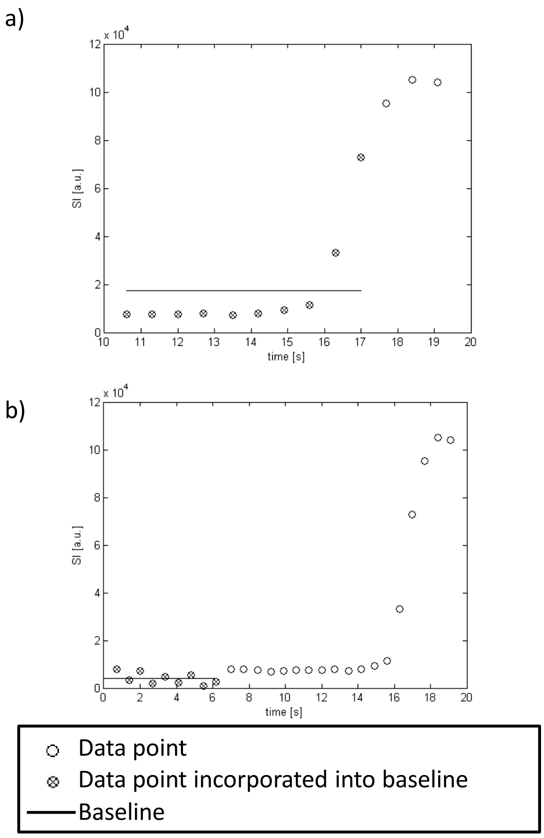

Figure 5-5 – Diagram illustrating two problems with using a simple baseline based on first *n*=10 data points. a) An unusually short pre-bolus time incorporates some contrast enhanced points erroneously raising the baseline. b) Noise in the early points generates errors in the baseline that would have been avoided had *n* been longer.

A simple automated approach to baseline measurement would be to take the first *n* data-points of the data series and average them. However the choice of *n* is clearly critical to this method. If *n* is too large the method runs the risk of encountering a data series with an earlier injection time, thus the baseline will incorporate contrast enhanced data points and be set too high (Figure 5-5 a). Conversely if *n* is too small the susceptibility to noise is increased (Figure 5-5 b). High levels of noise are common in the early data points as image contrast is poor, making contours difficult to choose (Figure 5-4). In reality a large dataset will contain both types of problem. The ideal solution is to have a bespoke, case specific baseline region that maximises the available data in each case. The method adopted for this study uses a piecewise linear-linear continuous regression model to fit two conjoined straight lines to the uptake curve. The method was originally suggested as a way of estimating bolus arrival time (129). After cropping the uptake curve of all data points following the point where the curve reaches half the peak height the curve is assumed to approximate to a linear-linear piecewise continuous function:

$$\boldsymbol{C}(\boldsymbol{t}[\boldsymbol{i}]) = \begin{Bmatrix} \boldsymbol{\beta_o} & \boldsymbol{t}[\boldsymbol{i}] \leq \boldsymbol{t}[\boldsymbol{k}] \\ \boldsymbol{\beta_o} + \boldsymbol{m}(\boldsymbol{t}[\boldsymbol{i}] - \boldsymbol{t}[\boldsymbol{k}]) & \boldsymbol{t}[\boldsymbol{i}] > \boldsymbol{t}[\boldsymbol{k}] \end{Bmatrix}$$

Equation 5-1

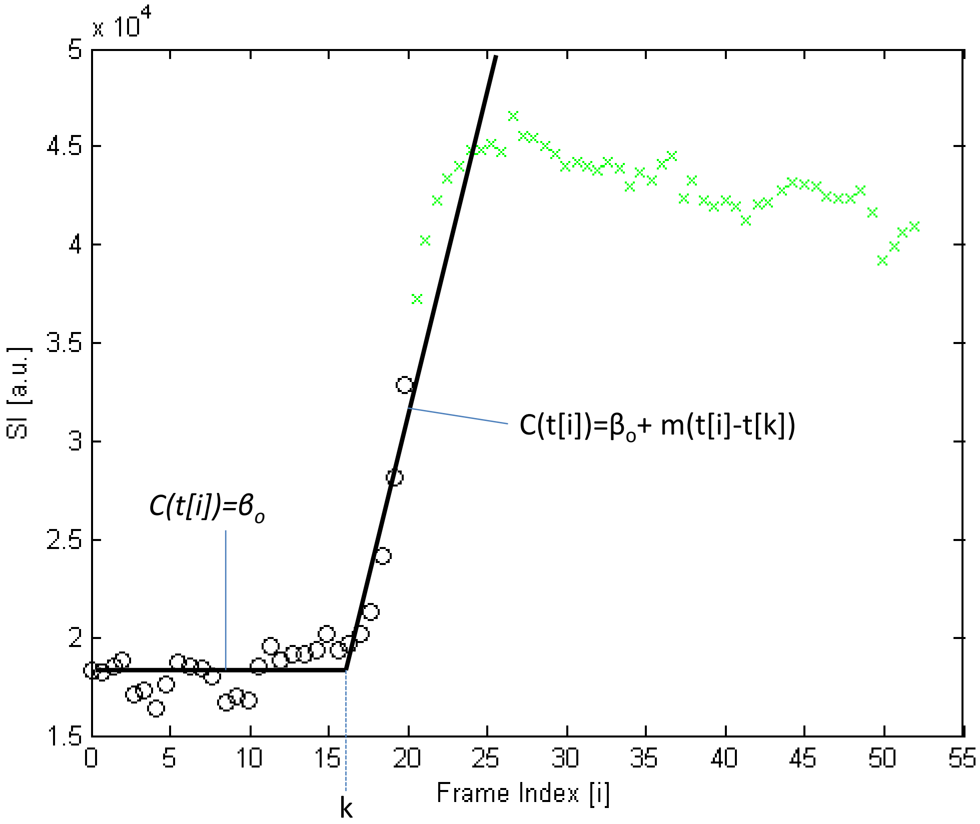

Figure 5-6 – Illustration of the method for finding the end of the baseline *k*. All data points after the curve has risen to half peak (x) are excluded. The piecewise linear-linear continuous regression fits a horizontal line of amplitude β_o to data points before *k* and a straight line of gradient *m* and intercept β_o to points following k. The solid line is the fit through the included point (o).

Equation 5-1 represents the fitting of a horizontal line with amplitude β_o to the data preceding the bolus arrival time *k* and a straight line of gradient *m* and intercept β_o to all data points following k. The fit is repeated with k set to every data point in the series and the value of k producing the best fit to the data is the bolus arrival time. Figure 5-6 illustrates the function fitted to an example uptake curve.

5.4.2. Identifying the end of the first pass

Tracer kinetic models that derive a tissue response function theoretically should be able to model enhancement curves wherever the assumptions of that model are valid. Thus model independent methods (section 4.3.4) and the one compartment model (section 4.3.6) can be applied to full datasets. The use of the Fermi function to represent the response function is not based on a theoretical tracer-kinetic model. It is rather a pragmatic choice based on the appearance of empirical response functions. This may account for the importance of limiting data sets to the first-pass when using Fermi-constrained deconvolution to avoid poor fits and significant overestimates in MBF estimate (4).

The automated method used to find the end of the first-pass is illustrated in Figure 5-7. After smoothing the AIF using a spline function in order to reduce the impact of high frequency oscillations, due to noise and frame specific contouring errors, the AIF is differentiated to generate a plot of dSI/dt against time. The minimum dSI/dt corresponds to the downslope of the first pass peak. The next point where dSI/dt crosses the line dSI/dt=0 corresponds to the valley immediately following the first-pass peak, i.e. the end of the first-pass. All data subsequent to this point in the original uptake curve is then cropped to generate a first-pass only uptake curve.

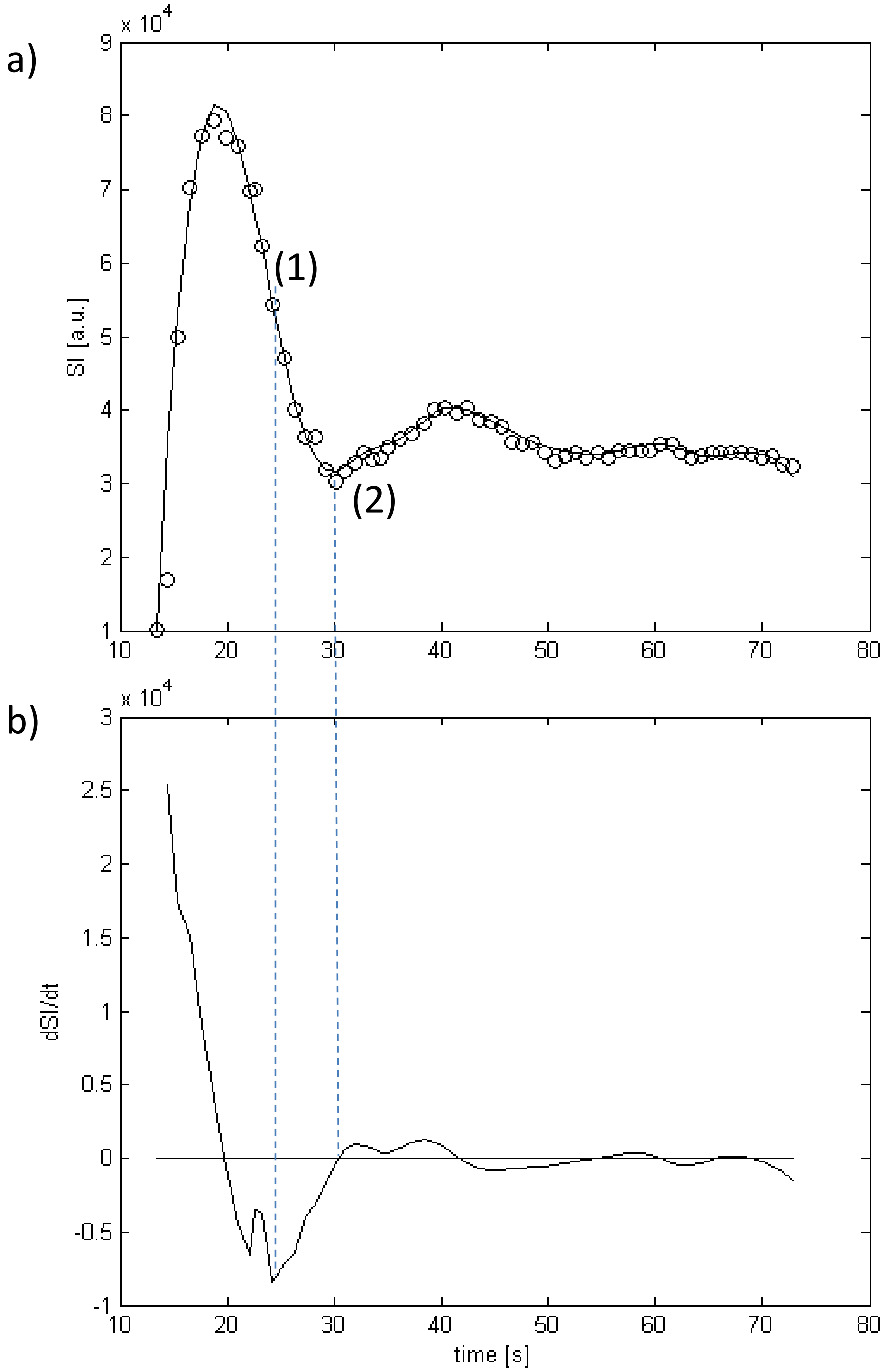

Figure 5-7 – The AIF data points (o) are smoothed by fitting with a spline function (a). The differential of the smoothed function (dSI/dt) is then calculated (b). The minimum dSI/dt value corresponds to the downslope of the first-pass (1). The point where dSI/dt next crosses the line dSI/dt=0 is the end of the first-pass (2).

5.4.3. Calculating the delay time

It is not possible to gain a reliable arterial input function from the coronary arteries themselves. The current limitations in image resolution and the large amount of movement would generate very noisy AIFs. Some authors have used a separate imaging slice in the aorta to gain an input function as close as possible to the input function that enters the myocardial tissue (31). However this requires dedicating an imaging slice to the aorta alone, thereby losing a myocardial slice and decreasing the cardiac coverage. For this reason many studies, including all the myocardial perfusion studies presented in this thesis opt to take the AIF from the left ventricular blood pool. Here a large ROI can be used to obtain a high SNR AIF. However the contrast bolus generating this AIF must then pass through the aortic valve, into the aorta, through the coronary arteries and into the myocardium. For this reason there is a significant time delay (*dt*) between the arrival of the contrast agent bolus in the left ventricle and in the myocardium. This manifests as a translational shift along the time axis between the AIF and the myocardial uptake curve. Uncorrected, this time delay causes an underestimate in the MBF. There are a variety of ways of determining *dt*. Some investigations require a human observer to set *dt* manually (120). This becomes impractical when large numbers of datasets are to be analysed. Furthermore it is often not clear what the optimal *dt* is from visually inspecting the curves and so this method may introduce errors into the quantitation. An automated bolus arrival time finding algorithm has been described (129) but this will be susceptible to the same ambiguities in the curves that reduce the accuracy of the manual method. Alternatively *dt* can be incorporated into the fitting procedure as an extra parameter in the fit. Although this increases the degrees of freedom in the fitting procedure, and may increase the likelihood finding local minima, it is a fully automated method and has been widely applied in the literature (123). Alternatively, for the studies in this thesis, *dt* was determined by performing model fitting multiple times over a range of *n* values of *dt*. The delay-time was implemented by zero padding before the AIF. The optimal *dt* value was then chosen as that which achieved the best fit to the data. This method is more computationally expensive than incorporating *dt* into the model fit (by factor *n*), however it reduces the likelihood of local minima. In our experience we have found this to be a more reliable method than those previously mentioned, although we have not conducted formal investigations to verify this quantitatively. A disadvantage of this method is that it inherently limits the delay time to the temporal resolution of the dynamic acquisition, whereas fitting can set *dt* to any value. To ameliorate this problem all data sets were interpolated by a factor of 4 to increase the apparent temporal resolution of the dynamic series. In order to achieve this a piecewise cubic hermite interpolating polynomial (130), MATLAB® *pchip,* was used to preserve the local shape of the curve.

5.5. Qualitative evaluation of automated curve pre-processing for quantitative myocardial perfusion.

5.5.1. Introduction

The automated curve pre-processing algorithms described in section 5.4 were used in all of the MBF estimates used in this thesis. Although an absolute gold-standard for these parameters was not available the performance of these algorithms was tested against human observer opinion as to the correct values. In this section the performance of the automated algorithms was checked by human observers and the number of failures and the reasons for failure are discussed.

5.5.2. Method

The automated pre-processing algorithms described in section 5.4 were applied to all of the uptake curves in the CE-MARC subset (described in section 5.2.1). This amounted to 4800 (50 patients x 2 rest/stress states x 3 slices x 16 regions) myocardial uptake curves and 1600 AIFs (as AIFs were taken from the basal slice only). Each curve was visualised using the *Perfusion* graphical user interface (GUI). This GUI is described in detail in chapter 8. It enabled rapid visual assessment of the automated pre-processing algorithms by displaying MR images, contours and uptake curves pre and post automated processing, with the baseline and first-pass cut-off points overlaid on the plots (Figure 5-8). Wherever it was deemed necessary the automated pre-processing parameters were adjusted for later analysis and the parameter adjustment, and reasons for it were noted. Parameter adjustment was deemed necessary if it would give a more accurate representation of the parameter in question. This is obviously a subjective criterion, but it is clear from the examples given in section 5.5.4 that the need for manual intervention was usually obvious.

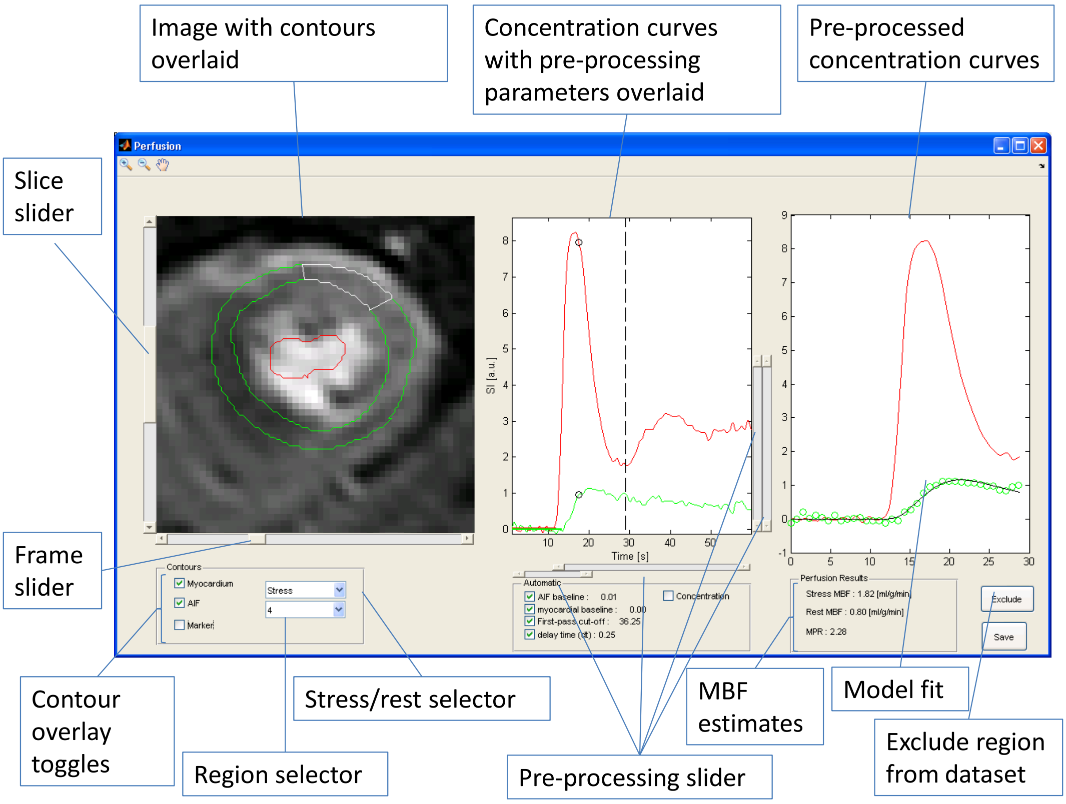

☑ Myocardium
☑ AIF
☐ Marker
Stress
4

☑ AIF baseline : 0.01
☑ myocardial baseline : 0.00
☑ First-pass cut-off : 36.25
☑ delay time (dt) : 0.25
☐ Concentration

Stress MBF : 1.82 [ml/g/min]
Rest MBF : 0.80 [ml/g/min]
MPR : 2.28

Figure 5-8 - GUI allowing simultaneous viewing of stress and rest images, contrast uptake curves and estimated MBFs as well as manual adjustment of pre-processing parameters and an exclusion button to exclude the region if necessary. The black circles depict the time on the curve that the dynamic image shown corresponds to (see section 8.3).

5.5.3. Results

The number of regions (and percentage regions) that required manual adjustment are shown in Table 5-3.

Manual Intervention adjusted	AIF Baseline	Myocardial Baseline	First-pass cut-off	Bolus arrival delay time	Total
No. regions affected	0 (0%)	32 (0.6%)	32 (0.6%)	0 (0%)	64
No. Cases affected	0 (0%)	3 (0.06%)	2 (2%)	0 (0%)	5

Table 5-3 – Summary of cases where manual intervention was deemed necessary expressed as the number of individual regions and as a percentage in brackets. The number of individual patients affected by these adjustments is also shown.

5.5.4. Discussion

Of the 4800 segments considered (50 patients at rest and stress over three slices divided into 16 regions) 64 regions required manual intervention. Of these 32 required adjustment of the myocardial baseline and 32 were affected by adjustment of the first-pass cut-off. Almost all the myocardial baseline adjustments were due to a single patient (30 regions adjusted at rest and stress). The first-pass cut-off adjustments were due to 2 AIFs, which affected all regions. No corrections were required in the AIF baseline or the bolus arrival time delay. It is to be expected that automated baseline calculation would be more difficult in the myocardium than the LV blood pool as a single myocardial region is typically smaller (and less dramatically enhanced) than the LV blood region making it more susceptible to noise.

The myocardial baseline corrections required were actually due to problems with the myocardial contours. In the patient concerned poor contour placement in the pre-contrast frames incorporated high signal in the myocardial baseline (Figure 5-9 a). At the onset of contrast the contours were shifted (Figure 5-9 b) generating a dip in the myocardial curve. The true baseline value should be at the base of this dip as the preceding baseline was contaminated by non-myocardial signal.

a)

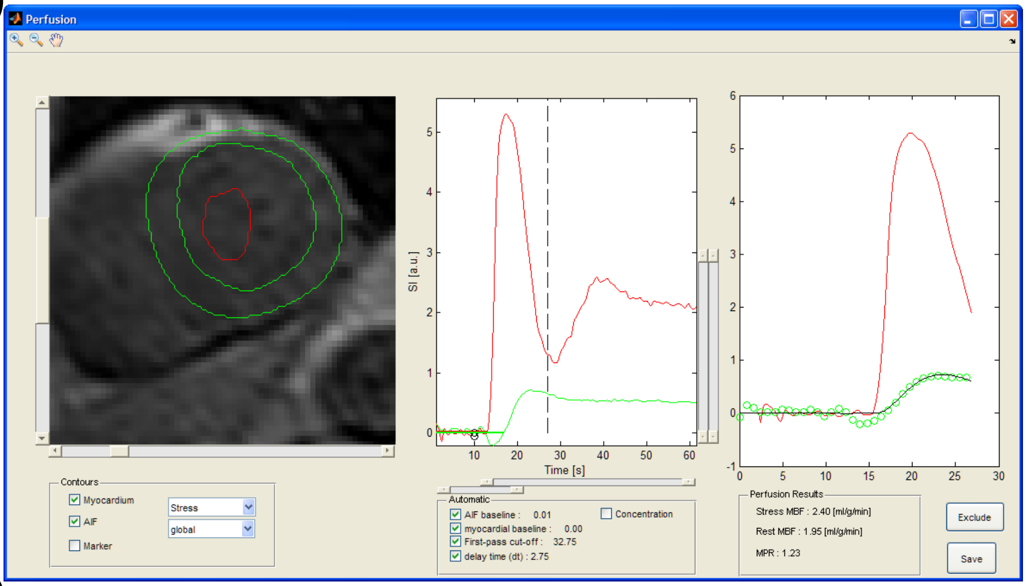

Contours
☑ Myocardium — Stress
☑ AIF — global
☐ Marker

Automatic
☑ AIF baseline : 0.01
☑ myocardial baseline : 0.00
☑ First-pass cut-off : 32.75
☑ delay time (dt) : 2.75
☐ Concentration

Perfusion Results
Stress MBF : 2.40 [ml/g/min]
Rest MBF : 1.95 [ml/g/min]
MPR : 1.23

b)

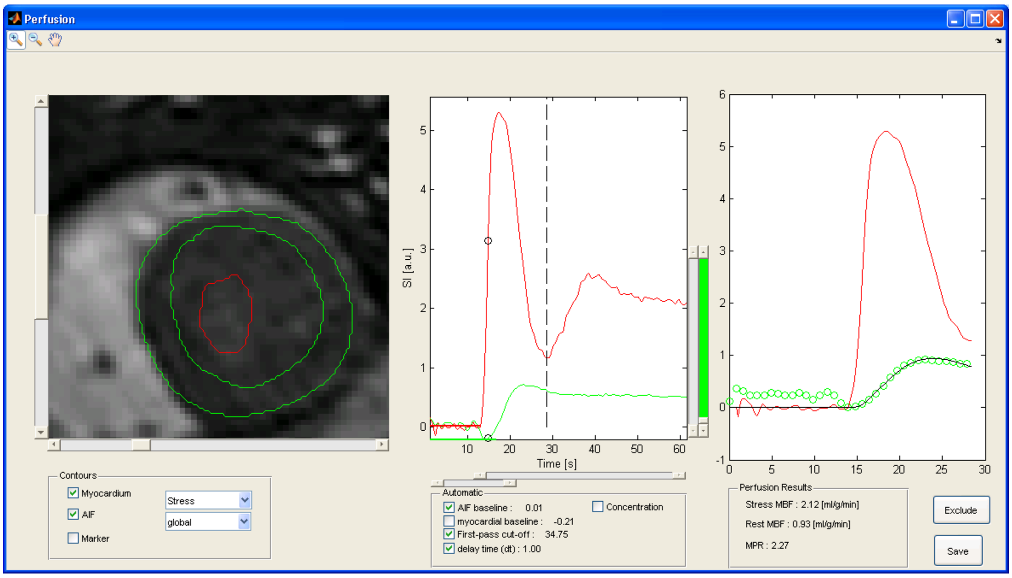

Contours
☑ Myocardium — Stress
☑ AIF — global
☐ Marker

Automatic
☑ AIF baseline : 0.01
☐ myocardial baseline : -0.21
☑ First-pass cut-off : 34.75
☑ delay time (dt) : 1.00
☐ Concentration

Perfusion Results
Stress MBF : 2.12 [ml/g/min]
Rest MBF : 0.93 [ml/g/min]
MPR : 2.27

Figure 5-9 – Myocardial baseline correction was required due to problems with the myocardial contours. Pre-contrast contours incorporated signal from surrounding structures increasing the baseline signal value (panel a). At contrast enhancement the contour was shifted so as not to include these structures (panel b).

The errors in the first-pass cut-off occurred in two patients only. It is important to note that the first-pass cut-off was based on the AIF of the basal slice, which was used for all regions. Therefore, a single failure of the algorithm on this AIF affected all regions for that case. Figure 5-10 shows one of the AIFs that caused a failure in this study. The valley at the peak of the AIF is difficult to explain. The AIF ROI is close to some interior dark structure in the LV cavity and movement of the ROI into this region at the peak of the AIF may explain the signal loss at this point. Another explanation is signal loss due to T_2* effects but that is unlikely with this protocol (see section 6.3.1). The cut-off algorithm searches for the first valley after the AIF peak, which it has found in this case, but it is evident that this valley is not the end of the first-pass in this case, hence the need for manual intervention.

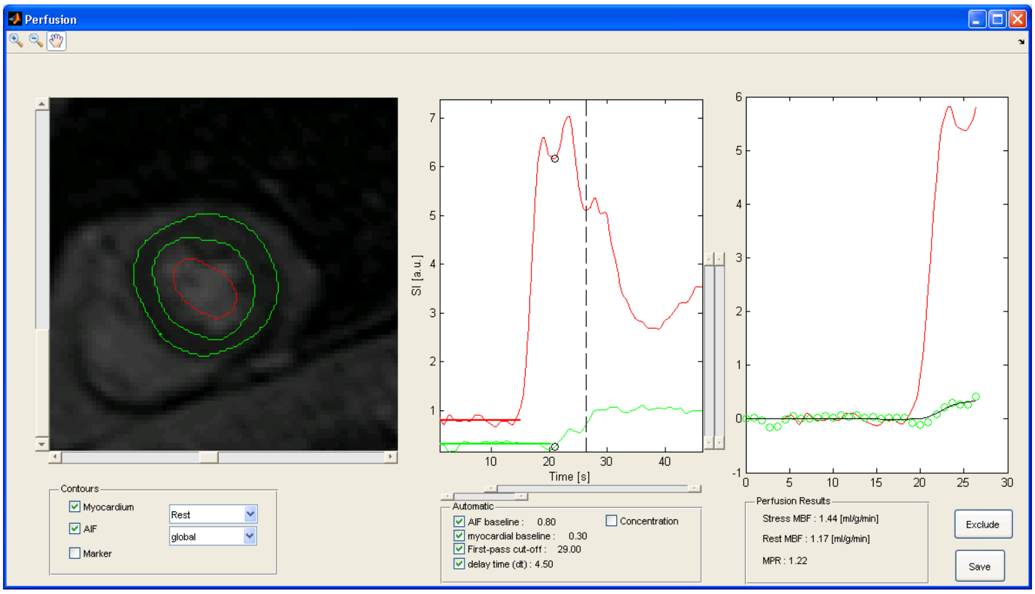

☑ Myocardium
☑ AIF
☐ Marker
Rest
global

☑ AIF baseline : 0.80
☑ myocardial baseline : 0.30
☑ First-pass cut-off : 29.00
☑ delay time (dt) : 4.50
☐ Concentration

Stress MBF : 1.44 [ml/g/min]
Rest MBF : 1.17 [ml/g/min]
MPR : 1.22

Figure 5-10 – Failure in end of first-pass finding algorithm due to a valley in the AIF peak.

5.5.5. Conclusion

The results show that the automated pre-processing algorithms are robust and reliable. No interventions were required in the AIF baseline and the bolus arrival time delay parameters, meaning that complete automation for these two parameters has performed as well as visual analysis. The failures of the myocardial baseline and first-pass cut-off algorithms have been explained in terms of contouring errors. Although these cases required genuine manual intervention, the automated algorithms could not be expected to perform well due to contouring errors generating anomalous uptake curves. In conclusion the automated pre-processing algorithms have proved to be robust in practice although manual checks on curves are still advisable because of the possibility of contour error induced anomalies in the uptake curves.

5.5.6. Limitations

The reference standard in this investigation was visual assessment. This is a subjective measure and it is possible that errors in the automated algorithms may have been missed as a result. This is particularly possible in the case of the bolus arrival delay time which is difficult to assess visually. However, the author is aware of no superior, more objective, standard against which the curves could be compared in the context of genuine patient datasets. To the author’s knowledge visual assessment represents the best reference standard available. This assessment shows that the automated solutions are at least as good as manual methods.

5.6. Summary

This chapter has described in detail the datasets and methods that are used throughout the remainder of the thesis. A subset of the CE-MARC dataset (section 5.2.1) is the basis upon which the comparison of methods (chapter 8) and the comparison of perfusion models (chapter 9) were performed. The dual-phase dataset (section 5.2.2) was used in the evaluation of contour errors (chapter 7) and was used in the patient data based simulations in chapter 6. The contouring protocol described in section 5.3 has been used on all the datasets described in this thesis. The automated analysis methods described in section 5.4 and qualitatively validated in section 5.5

have been used to generate all of the MBF estimates presented in this research.

6. Signal intensity to concentration conversion in magnetic resonance imaging for quantitative myocardial perfusion

6.1. Overview

In order to justify the assumption that the signal measured from the MR image is linearly proportional to the concentration of contrast agent in the ROI, quantitative blood flow MRI investigations in the heart are usually carried out using either a low dose single bolus injection or, more recently, a dual-bolus protocol (see section 2.8.6). In the single bolus case the price for using a small enough dose for this assumption to hold true is poor SNR in the resulting images. This has an adverse affect on the contrast uptake curves and reduces the accuracy of visual reporting. Dual-bolus injection protocols aim to avoid this issue by using separate, dedicated bolus concentrations for the AIF and myocardial tissue curves. However administration of two boluses makes the investigation complicated, requiring three injection pumps (two contrast agent (CA) boluses plus saline) or a member of staff in the investigation room to swap syringes mid scan (131). Adequate separation between pre-bolus and bolus injections is difficult to time correctly and bolus time courses can become contaminated by the pre-bolus. An alternative approach is to convert the signal intensity (SI) values into CA concentrations by modelling the non-linear relationship between SI and CA concentration. This allows simple, single-bolus acquisitions, with good SNR, to be used in quantitative analysis.

The aim of this chapter was to derive and validate a method for converting signal values derived from DCE-MRI cardiac perfusion into CA concentrations. The mathematical model of the pulse sequence is described in detail (section 6.2.1) and is then refined to incorporate a simulation of the flip-angle sweep used on Philips systems to reduce image artifacts (section 6.2.3). Simulation experiments are then used to defend potential criticisms of the model. The use of an assumed blood T_1 is shown to be unlikely to cause significant errors in MPR (section 6.3.7), the assumption that the effect of T_2^* on signal intensity will be small is validated and the effect of flip angle sweep on MPR is also shown to be small (section 6.3.2). The model is then validated using a T_1-gel phantom showing excellent fits of the model to the phantom (section 6.4). The phantom is also used to investigate the effect of flip angle errors on the conversion. In-vivo tests of the model were not carried out due to concerns over the dual-bolus dataset on which this was to be performed. These concerns were based on the significant discrepancy between pre-bolus and dual-bolus MBF estimates in these datasets. These discrepancies are reported and preliminary investigations into what has caused them are described.

6.2. A method for converting signal intensities to concentrations in myocardial perfusion imaging

In order to use cardiac MRI perfusion data for quantitative MBF measurements the measured signal intensities should be linearly proportional to the concentration of contrast agent in the ROI. Section 2.8.6 explains this requirement in detail and outlines the main proposed methods for dealing with it. In this section an approach is described to convert each signal intensity value to its corresponding T_1 value using the mathematical description of the imaging pulse sequence. The method was first described by Fritz-Hansen et al and Larsson et al. (30,31) for an inversion recovery FFE (IR-FFE) pulse sequence. In the heart it is reasonable to assume a mono-exponential T_1 recovery, i.e. that there is a fast rate of exchange between tissue compartments (132). Therefore, the change in longitudinal relaxation rate T_1 due to a given concentration c(t) of contrast agent at time t can be related as follows (13):

$$\frac{1}{T_1(t)} - \frac{1}{T_{1o}} = r_1 c(t)$$

Equation 6-1

where T_{1o} is the native relaxation time without CA, $T_1(t)$ is the relaxation time at time t with the CA and r_1 is the CA relaxivity. Thus, the concentration $c(t)$ of CA at time t can be expressed as:

$$c(t) = \frac{\Delta R_1(t)}{r_1} \text{; with } \Delta R_1(t) = \left(\frac{1}{T_1(t)} - \frac{1}{T_{1o}} \right)$$

Equation 6-2

Therefore, CA concentration can be derived from the R_1 in a given ROI provided that the native R_1 of the tissue is known. The problem then becomes one of relating a given signal intensity to R_1. The relationship between signal intensity and R_1 can be written as:

$$SI = \Psi \cdot f(R_1)$$

Equation 6-3

SI is the signal intensity measured from a given region, $f(R_1)$ is an abbreviation for the full pulse sequence equation, described later in this chapter (sections 6.2.1 and 6.2.3), for which R_1 is the only unknown parameter. Ψ is a calibration factor, which is constant over the DCE-MRI experiment. For this derivation ψ comprises the receiver gain factor Ω, the net magnetization vector M_o, $\sin(\alpha)$, and the factor for T_2* decay e^{-TE/T_2^*}

$$\psi = \Omega . \mathrm{M_{eq}} . \sin\alpha \, . \, e^{-TE/T_2^*}$$

Equation 6-4

Considering the left ventricular ROI containing blood only, the blood calibration factor ψ_b can be calculated using the pre-contrast (baseline) signal intensities (SI_{bo}) and the native R_1 value for blood (R_{1bo}):

$$\Psi_b = \frac{SI_{bo}}{f(R_{1bo})}$$

Equation 6-5

Once obtained ψ_b can be used to derive $R_{1b}(t)$ for every time point in the perfusion series assuming $f(R_1)$ is invertible:

$$f(R_{1b})(t) = \frac{SI_b(t)}{\Psi_b}$$

Equation 6-6

$$R_{1b}(t) = f^{-1}\left(\frac{SI_b(t)}{\psi_b}\right)$$

Equation 6-7

Ideally R_{1bo} would be measured on a patient by patient basis. However, these measurements can be time-consuming and error prone and are not available in all perfusion studies. An alternative is to assume a value from measurements published in the cardiac MRI literature. This is the approach adopted in this chapter.

The above method should also be applied to the myocardial ROI. Using a measured or assumed value for normal myocardial R_1 is not practical in ischaemic patients whose native myocardial R_1 will be modified by their disease. An alternative is to assume that the calibration constant is the same for the blood and the myocardium ($\psi_b = \psi_m$), so that:

$$R_{1m}(t) = f^{-1}\left(\frac{SI_m(t)}{\psi_m}\right)$$

Equation 6-8

SI_m and R_{1m} are the myocardial signal and R_1 values respectively. This is a reasonable assumption within an imaging slice as one would not expect large changes in coil sensitivity between adjacent areas within the same slice. Furthermore, most perfusion acquisition protocols will use parallel imaging techniques which should improve within slice B_1 homogeneity.

In order to generate a myocardial perfusion reserve (MPR) cardiac perfusion imaging is carried out under rest and stress conditions with a separate contrast bolus in each case. Typically rest perfusion is conducted 10 – 15 minutes after stress perfusion, after which time remnant CA is still present in the blood and myocardium (Figure 6-1). For this reason it is not possible to generate a separate calibration factor for the rest acquisition. Therefore a further assumption has to be made that the calibration factor does not change between the stress and rest acquisitions ($\psi_{stress}=\psi_{rest}$) and the stress calibration factor is applied to the entire dataset. This assumption is also reasonable as the same location is being imaged in both cases.

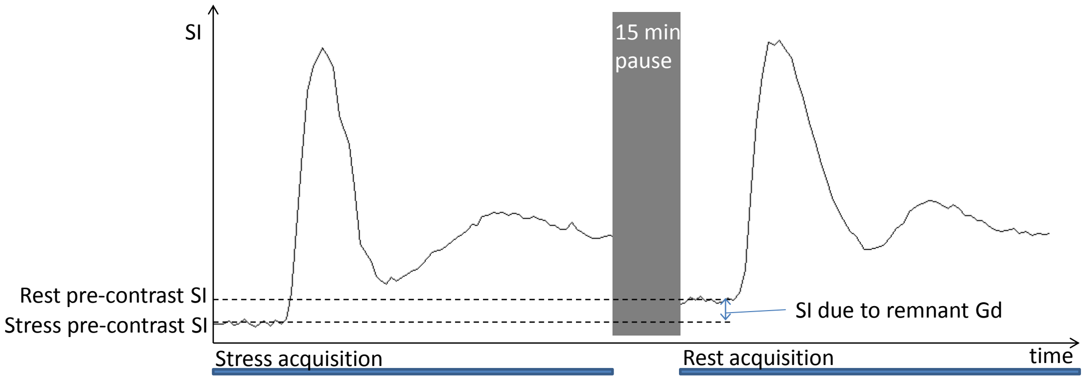

Figure 6-1: Signal intensity vs. time plot showing stress and rest data. The precontrast (baseline) signal intensity for the rest scan is higher than the native tissue signal intensity due to remnant CA in the tissue from the stress scan. The calibration factor should be derived from the stress pre-contrast data only.

For the CE-MARC imaging sequence (section 5.2.1) a shared pre-pulse (section 2.8.4) was used resulting in different saturation times for each imaging slice. For this reason the AIF was taken from the basal slice (corresponding to the shortest saturation time) for all slices, whereas the myocardial uptake curve was taken from each individual slice. The coil gain within the imaging slice is reasonably homogeneous, justifying the assumption used above that the myocardial curve can be converted using the blood calibration factor ($\psi_b= \psi_m$). However, the same assumption cannot be made when the AIF and myocardial uptake curves are taken from different imaging slices. For this reason each myocardial uptake curve was converted using a calibration factor derived from the baseline blood signal from its own slice, even though the AIF was always taken from the basal slice.

6.2.1. Derivation of the SR-TFE pulse sequence equation

The SR-TFE sequence consists of an initial 90^o saturation pulse followed by a TFE read-out consisting of multiple low flip angle (α) RF pulses separated by short relaxation times (TR) (see section 2.6). The recovery of the longitudinal magnetization M_z after the initial 90^o RF pulse is given by:

$$M_z(TS) = M_{eq}\left(1 - e^{-TS/T_1}\right)$$

Equation 6-9

Where TS is the saturation time between the 90^o RF pulse and the first TFE read-out RF pulse and M_{eq} is the equilibrium magnetization of the fully relaxed system. The magnetization at any point in the readout pulse can be determined by considering the affect of each RF pulse on M_z. Recovery towards M_{eq} from an arbitrary initial magnetization $M_z(0)$ is described by:

$$M_z(t) = M_z(0) + \left(M_{eq} - M_z(0)\right)\left(1 - e^{-t/T_1}\right)$$

$$M_z(t) = M_z(0)e^{-t/T_1} + M_{eq}\left(1 - e^{-t/T_1}\right)$$

Equation 6-10

The magnetization after the first RF pulse of the TFE read-out train $M_1(+)$ is related to the magnetization before the RF pulse $M_1(-)$ *by*:

$$M_1(+) = M_1(-)\cos\alpha$$

Equation 6-11

corresponding to point B in Figure 6-2. Inserting this expression into Equation 6-10, following recovery over TR, the magnetization immediately prior to the next RF pulse is:

$$M_2(-) = \mathrm{M}_1(-)\cos\alpha e^{-TR/T_1} + M_{eq}\left(1 - e^{-TR/T_1}\right)$$

Which reduces to:

$$M_2(-) = M_1(-)A + M_{eq}B$$

Equation 6-12

Where $A = \cos\alpha e^{-TR/T_1}$ and $B = \left(1 - e^{-TR/T_1}\right)$, which corresponds to point C in Figure 6-2. In general the expression for the n^th RF pulse can be written as:

$$M_n(-) = A^{n-1}M_1(-) + \left(\frac{1 - A^{n-1}}{1 - A}\right)M_{eq}B$$

Equation 6-13

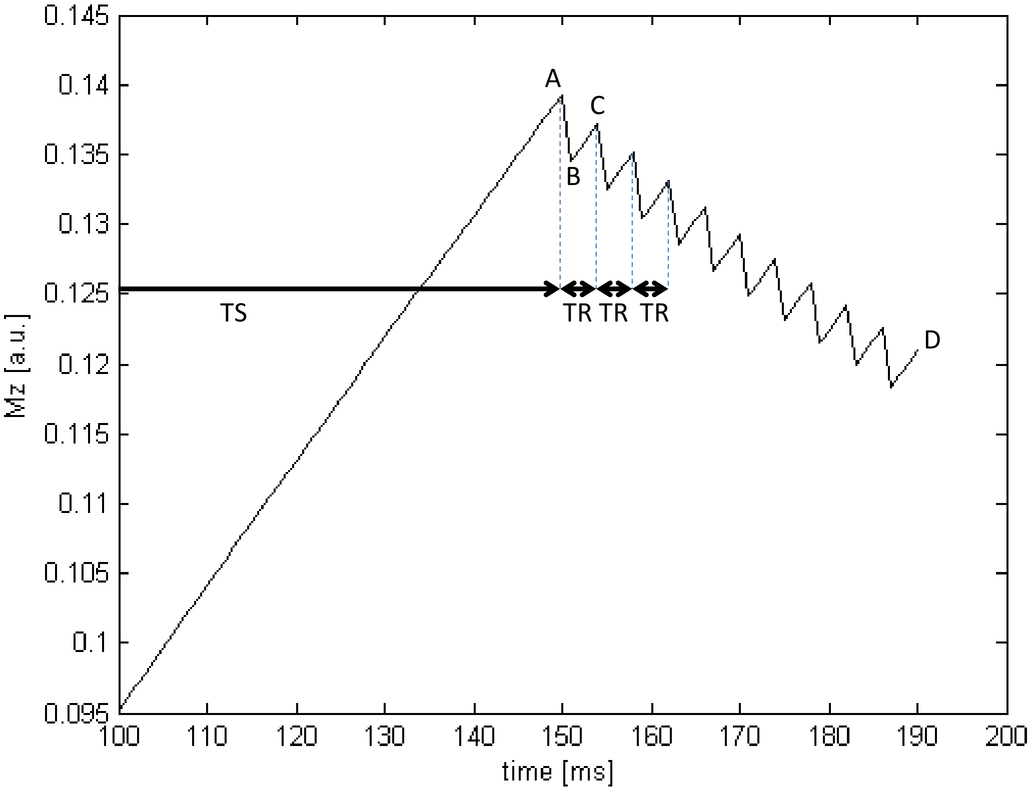

Figure 6-2 – Illustration of longitudinal magnetization, M_z, recovery in the SR-TFE pulse sequence. Initially the magnetization recovers from $M_z(0)$ over TS to point A. The initial read out flip angle then reduces M_z to point B followed by recovery over TR to point C. The magnetization after n TR readout pulses is D.

Utilizing the identity: $(1 + x + x^2 + \cdots + x^{n-1}) = \frac{1-x^n}{1-x}$. $M_n(-)$ corresponds to point D in Figure 6-2 if *n*=10.

Finally incorporating, Equation 6-9:

$$M_n(-)\frac{1}{M_{eq}} = A^{n-1}\left(1 - e^{-TS/T_1}\right) + \left(\frac{1 - A^{n-1}}{1 - A}\right)B$$

Equation 6-14

6.2.2. SR-TFE with flip angle sweep

The derivation described in section 6.2.1 assumes a constant flip angle *α* throughout the TFE read-out sequence. On Philips imaging systems the SR-TFE pulse sequence incorporates a steadily increasing flip angle scheme or flip-angle sweep (FAS) at the commencement of the sequence in order to reduce oscillations in the evolution of the longitudinal magnetization which can cause ghost artifacts. If the flip angle sweep evolves over *N* lines of k-space then the flip angle used for the n^{th} line is given by (133):

$$\alpha_n = \frac{n\left(2N - n\right)}{N^2}\alpha$$

Equation 6-15

In order to validate Equation 6-15 the Philips PPE environment was used to measure the RF pulse magnitudes for each k-space line of the acquisition. (Figure 6-3).

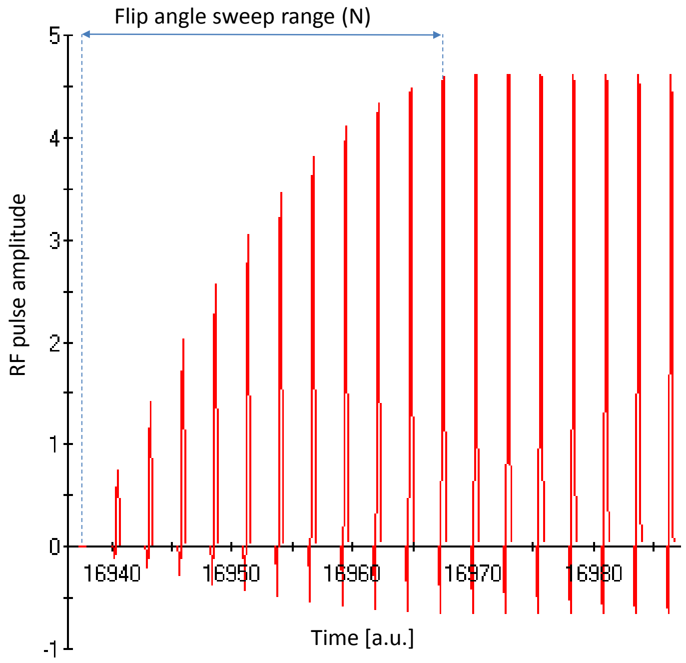

Figure 6-3 – RF pulse amplitudes displayed in the Philips PPE environment showing flip angle evolution over the initial 12 lines of k-space (rf-pulse durations are constant hence amplitude is proportional to flip angle).

The PPE measurement tool was then used to measure the maximum amplitude of the RF pulse for each k-space line. Equation 6-15 was used to generate angles with N=12 normalised to the maximum RF amplitude measured and plotted on the same scale. The signal evolution trends were compared and shown to match well with differences of less than 1% between the measured and calculated RF pulse amplitude for each individual point (Figure 6-4).

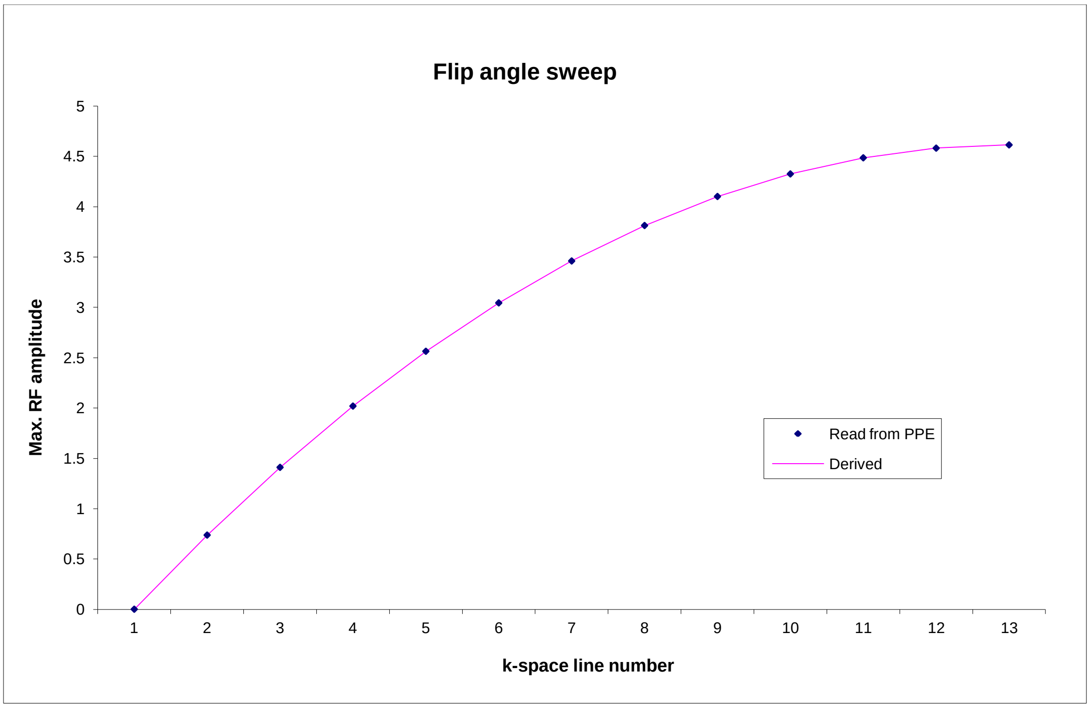

Figure 6-4 – Measured RF amplitudes (points) and calculated values using Equation 6-15.

6.2.3. Derivation of the SR-TFE signal intensity equation incorporating flip angle sweep

The influence of variations in the flip angle can be modelled mathematically in a similar manner to section 6.2.1 as follows; The magnetization after the first RF pulse of the TFE read-out train $M_1(+)$ is related to the magnetization before the RF pulse $M_1(-)$ *by*:

$$M_1(+) = M_1(-)\cos\alpha_1$$

Where α_1 is the 1st flip angle in the TFE sequence. Using Equation 6-10, following recovery over TR, the magnetization immediately prior to the second RF pulse is:

$$M_2(-) = \mathrm{M}_1(-)\cos\alpha_1\, e^{-TR/T_1} + M_{eq}\left(1 - e^{-TR/T_1}\right)$$

Which reduces to:

$$M_2(-) = CM_1(-)\cos\alpha_1 + D$$

Where $C = e^{-TR/T_1}$ and $D = M_{eq}\left(1 - e^{-TR/T_1}\right)$.

Iterating to the 3rd RF pulse:

$$M_3(-) = CM_2(-)\cos\alpha_2 + D$$

Substituting in $M_2(-)$

$$M_3(-) = C^2M_1(-)\cos\alpha_1\cos\alpha_2 + CD\cos\alpha_2 + D$$

Similarly for the 4th and RF pulse:

$$M_4(-) = C^3M_1(-)\cos\alpha_1\cos\alpha_2\cos\alpha_3 + C^2D\cos\alpha_2\cos\alpha_3 + CD\cos\alpha_3 + D$$

And in general:

$$M_n(-) = \left(\prod_{i=1}^{n-1}\cos\alpha_i\right).\left(M_{eq}\left(1 - e^{-TS/T_1}\right)C^{n-1}\right) + \sum_{j=2}^{n-1}\left[\prod_{i=j}^{n-1}(\cos\alpha_i).DC^{n-j}\right] + D$$

Equation 6-16

6.2.4. Minimization

In order to use Equation 6-14 and Equation 6-16 for converting signal values to concentrations these equations must be solved for T_1. An analytical solution for T_1 is not possible therefore T_1 must be found by minimization techniques. For all of the implementations in this thesis this was done using a single-variable non-linear zero finding algorithm (fzero.m MATLAB7 R2009b) (134)

6.3. Simulation Studies

6.3.1. T_2* effects

Introduction

The models described in section 6.2 do not incorporate T_2* effects into the pulse sequence equations, i.e. they assume that the change in the measured signal due to T_2* effects is small due to the short TE used in the pulse sequence. The aim of this section was to ascertain whether T_2* effects are indeed small enough to be discarded from the model for the pulse sequences used in the following studies.

Theory

Equation 6-1 relates contrast induced change in T_1 to concentration via the T_1 relaxivity. A similar relationship exists for T_2* relaxivity:

$$R_2^*(t) - R_{2o}^* = r_2^*.c(t)$$

Equation 6-17

Equation 6-3 can be modified to incorporate T_2* decay as follows:

$$S = \Psi' f\big(R_1(t)\big)e^{-TE.R_2^*(t)}$$

Equation 6-18

The calibration factor is now denoted ψ' to emphasies the fact that its value is different to that in previous simulations, which effectively assumed a constant T_2* decay for all contrast concentrations. Substituting Equation 6-1 and Equation 6-17 into Equation 6-18:

$$S = \psi' f(r_1.c(t) + R_{1o})\exp\left(-TE(r_2^* c(t) + R_{2o}^*)\right)$$

$$S = \psi'' f(r_1.c(t) - R_{1o})e^{-TE.r_2^* c(t)}$$

Equation 6-19

Where the constant $e^{-TE.R_{2o}^*}$ has been incorporated into a new calibration constant ψ'':

$$\Psi'' = \Psi' e^{-TE.R_{2o}^{*}}$$

Equation 6-20

Method

Using Equation 6-19 signal vs. concentration curves were generated. Based on previous observations, using a similar injection protocol, the peak concentration in AIF was expected to be around 3mM and to not exceed 5mM (30). Signal vs. concentration curves were plotted with and without T_2* effects and the percentage difference due to T_2* effects was calculated at each TS. The simulations were implemented in MATLAB (The Mathworks, Natick, MA) using a calibration factor of one (Ψ=1). The simulation was run using the range of saturation times (TS) used in the experiments in this thesis (TS=126ms, 150ms, 272ms, 418ms). An assumed value of T_1 commensurate with the literature for blood in the left ventricle (1393ms) was used, derived from an average (weighted for study population) of the measurements published in (135–138). A T_1 relaxivity for Magnevist in blood plasma of 4.1 L mmol^{-1} s^{-1} (13) was used and a T_2* relaxivity of 7.6 L mmol^{-1} s^{-1} (139).

Results

Figure 6-5 shows signal intensity vs. concentration plots for the four saturation times. The percentage errors at 5mM and the predicted peak AIF concentration (3mM) are shown in Table 6-1.

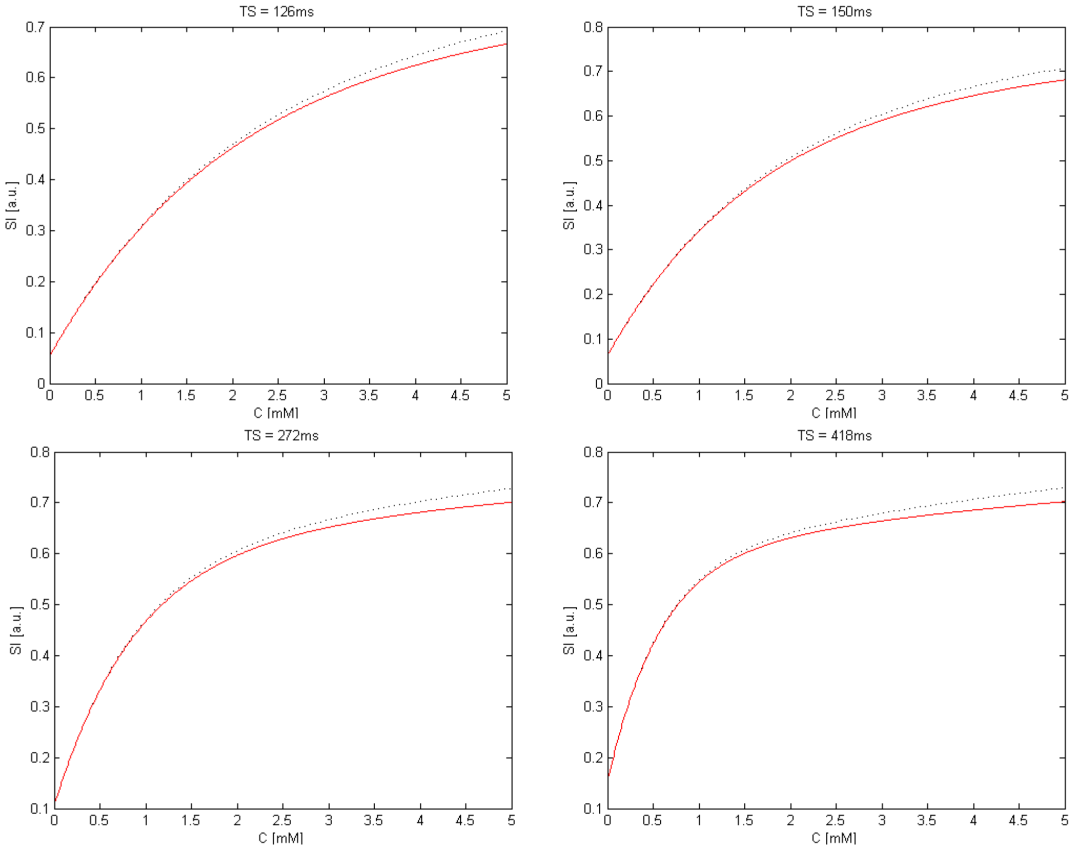

Figure 6-5 – Signal Intensity (S) vs. concentration (C) as simulated with T_2* effects (solid line) and without T_2* effects (dotted line).

TS	126ms	150ms	272ms	418ms
Percentage difference at 3mM	2.9%	3.3%	4.0%	4.1%
Percentage difference at 5mM	7.0%	7.3%	7.8%	7.8%

Table 6-1 – Percentage errors between the T_2* model and the non T_2* model at 3mM and 5mM.

Discussion

The differences in signal intensity due to T_2* effects at the concentrations expected in cardiac perfusion imaging are small for this pulse sequence (~3.5% at 3mM and ~7.5% at 5mM). This difference is unlikely to have a significant effect on diagnosis as it will be of a similar magnitude and direction for both rest and stress scans thus having a negligible effect on MPR. The representation of the data in terms of signal errors is perhaps not ideal and the fact that these simulations have not been used to show the degree of MBF error due to T_2* effects is a limitation of this study. However, the results presented here in terms of signal imply that the changes in MBF will be small.

6.3.2. Comparing SR-TFE equations with and without flip angle sweep

Introduction

Philips MR imaging systems use a flip angle sweep (FAS) in the Cardiac perfusion pulse sequence. The aim of this study was to ascertain the effect of the FAS on MR signal intensity, and the subsequent effect of neglecting FAS when converting signal intensities to concentration on quantitative MBF estimates and MPRs was then assessed.

6.3.3. Method

Pulse sequence simulations

In order to allow a visual comparison of the signal evolution for the two models signal intensities were simulated using the no FAS model (Equation 6-13) and the FAS model (Equation 6-15 and Equation 6-16). The mathematical models were implemented in MATLAB (The Mathworks, Natick, MA) using a calibration factor of one (Ψ=1). The simulation was run once using an assumed value of T_1 commensurate with the literature for blood in the left ventricle (1393ms) and once with an estimate of the T_1 expected at the peak of the AIF in the myocardial perfusion investigation (50ms). The native blood T_1 was derived from an average (weighted for study population) of the measurements published in (135–138). Experiments using a bolus dose of 0.1 mmol/kg (30,31) have presented enhancement curves with AIF peaks not exceeding 3mM. Using our assumed blood T_1 of 1393ms and a relaxivity for Magnevist in blood plasma of 4.1 L $mmol^{-1}$ s^{-1} (13), Equation 6-2 yields a T_1 of approximately 40ms. Noting that this study uses a half dose of 0.05 mmol/kg we can be confident that our T_1 values will not fall below this value thus our expected blood T_1 at the peak of the AIF was estimated to be around 50ms and no shorter than 40ms.

To investigate variations between the models over a realistic range of T_1 values SI values from the two models were generated using T_1s ranging from 10ms to 2000ms. Absolute and percentage differences between the FAS and no FAS models were then plotted against T_1.

Perfusion Analysis

The dual-phase dataset, described in detail in section 5.2.2, was used to make the comparison. Manual contours depicting the myocardium and an area within the left ventricular pool avoiding papillary muscles were drawn for both rest and stress datasets on each volunteer as described in section 5.3. The signal uptake curves derived from the image contours were then converted into concentration curves using the method described in section 6.2 using mathematical models incorporating FAS (section 6.2.3) and neglecting FAS (section 6.2.1). Myocardial blood flow (MBF) values were then derived from both sets of curves using fully automated curve preparation (section 5.4) and Fermi-constrained deconvolution (section 4.3.3). Myocardial perfusion reserves (MPR) were calculated as the ratio of stress to rest MBFs. Significant differences in stress and rest MBF values and MPR from the two pulse sequence models were assessed using a paired t-test.

6.3.4. Results

Figure 6-6 shows the evolution of signal to the central line of k-space (k_o) with and without FAS incorporated into the simulation. The percentage difference in signal at k_o (difference in SI at k_o / average of the two SIs at k_o)

was 8.6% with native T_1 and 4.1% at the peak of the AIF (T_1=50ms).
Figure 6-7 relates the k_o SI for the two models to T_1 and shows the absolute and percentage differences at each T_1 value. The largest absolute difference in SI occurred at T_1=90ms, corresponding to a 6% difference in SI values.

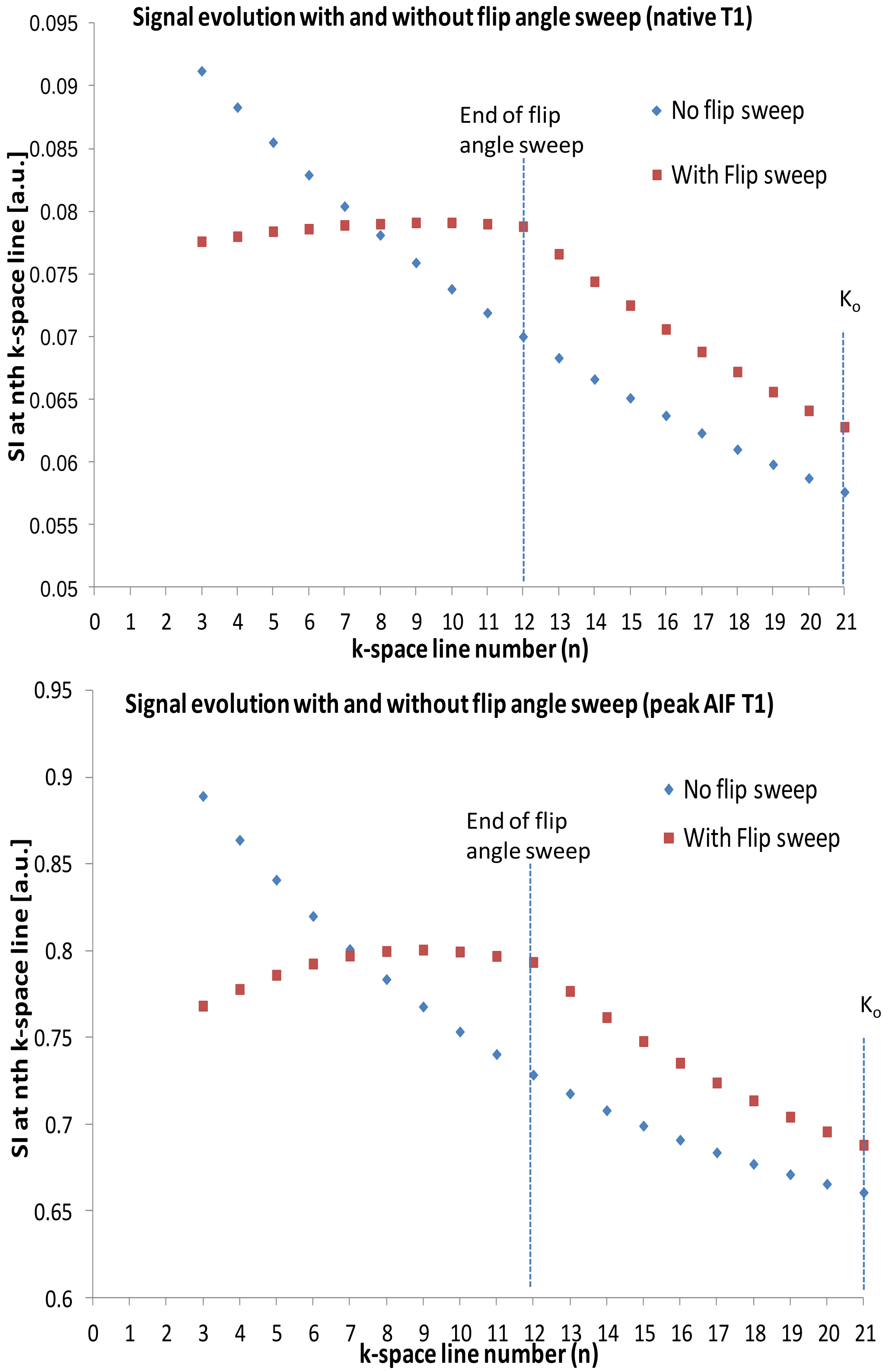

Figure 6-6 - Evolution of signal intensity (M_z) simulated with and without incorporating FAS. The central line of k-space is denoted k_o. [left pane] simulation with native T_1=1393ms. [right pane] simulation with T_1 estimate at peak of AIF (T_1=50ms).

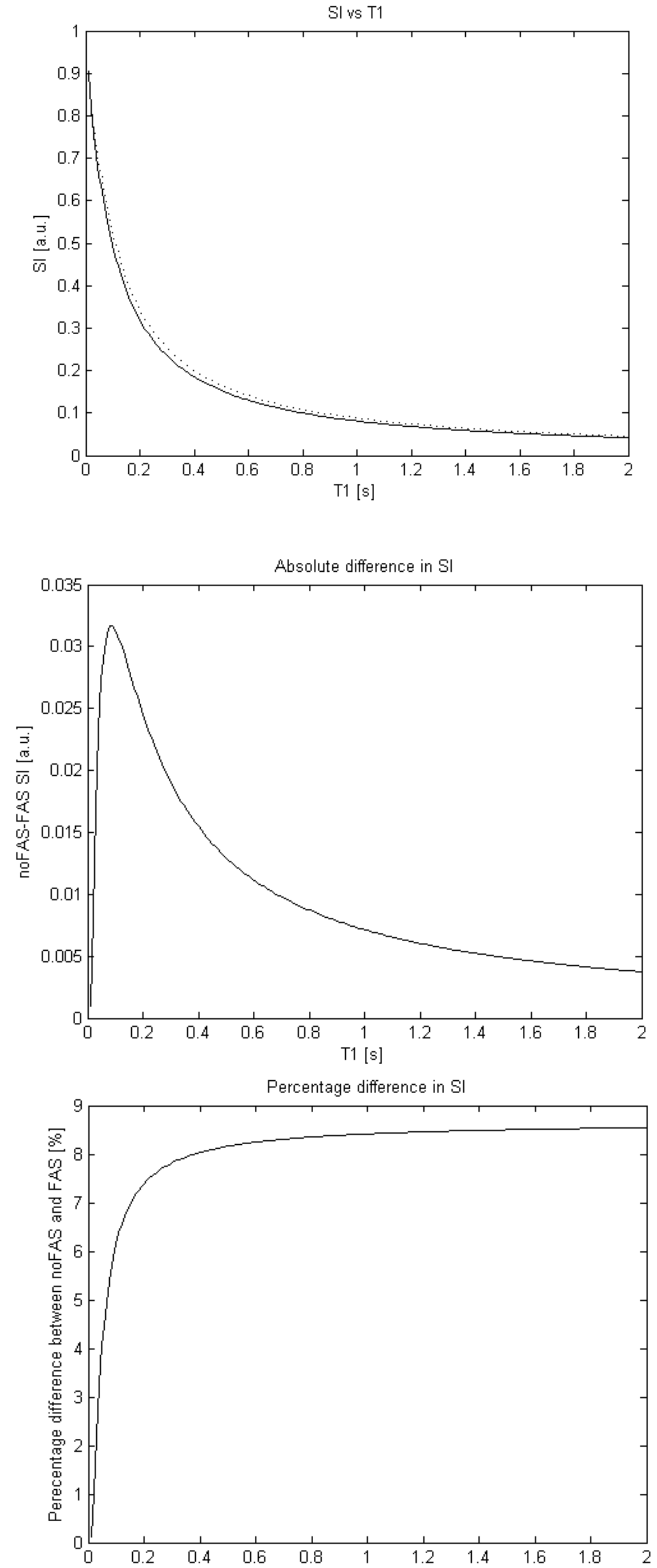

Figure 6-7 – Signal intensity vs. T_1 curves for SR-TFE ignoring (solid line) and including (dotted line) FAS [top panel]. Absolute [central panel] and percentage [bottom panel] differences between the models.

MBF values

The conversion algorithm successfully generated concentration curves for all the volunteers. One volunteer was excluded because their concentration conversion yielded very high peak AIF concentrations which could not be representative of the true concentration. The curve in question had a peak concentration 35 mM with a T_1 value of 7ms. This was due to an unusually small pre-contrast AIF SI value. This yielded a small calibration factor ψ and correspondingly small R_1 values yielding high concentrations. The anomalous curve was detected visually but could have been detected by testing curve parameters, such as testing that the peak AIF concentration did not exceed 10mM or that the peak T_1 was not less than 20ms, or by setting a limit on the ratio between the pre-contrast baseline and AIF peak SI values. The reasons for the particularly low pre-contrast baseline in this volunteer are unknown. Signal reduction could be caused by poor contouring (incorporating low signal voxels in the lung for example) or by image artifacts but neither of these were visually noticeable on the dataset.

The no FAS vs. FAS MBF estimates at stress and rest (mean±sd) were 2.27±0.68 vs. 1.97±0.71 and 0.81±0.28 vs. 0.72±0.30 respectively with MPR values of 2.9±0.62 vs. 2.83±0.78. The difference in MBFs between concentration curves incorporating FAS and no FAS was significant at stress ($p<0.0001$) and rest ($p<0.0001$) with average differences of 0.3ml/g/min and 0.08ml/g/min. In each case the MBF was overestimated when FAS was not incorporated into the conversion. These differences did not propagate to significant differences in MPR ($p=0.32$) with MPR differences approximately normally distributed around a mean positive bias of 0.07 (Figure 6-8).

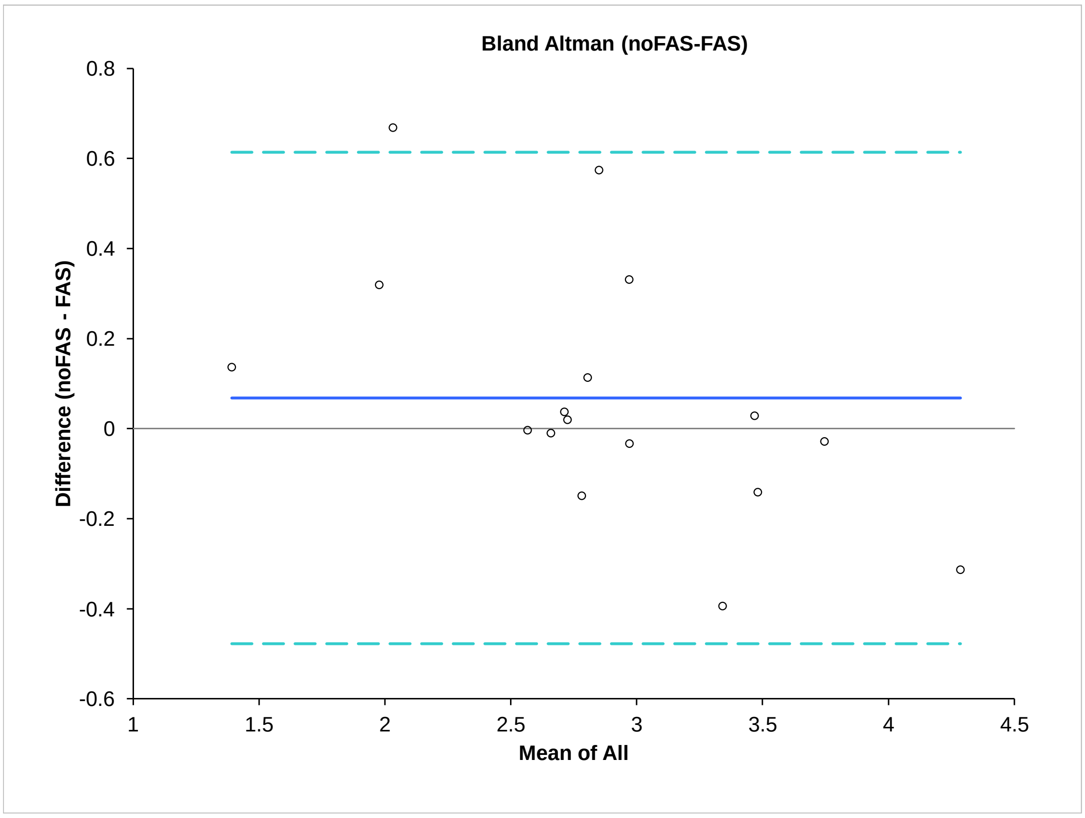

Figure 6-8 – Bland Altman comparison of MPR values generated using signal to concentration conversions incorporating and not incorporating FAS.

6.3.5. Discussion

The SI vs. k-space line number plots in Figure 6-6 illustrate well the differences between the evolution of SI in the two models, with the no FAS model decreasing monotonically, whilst the FAS model increases over the flip angle sweep before entering a monotonic descent once the flip angle becomes constant. At the central line of k-space (k_o) this manifests as an increased SI value with the FAS model. The magnitude of this error is more profound at the AIF peak (0.03 [a.u.]) than the native blood (0.005 [a.u.]). However, expressed proportionally to the SI the larger percentage error is in the non-contrast tissue (8.5% for native blood and 4% at the AIF peak). These errors are illustrated by Figure 6-7, which shows the difference between the models over a range of T_1 values. The maximum absolute difference (pane b) occurs at TI=90ms (corresponding to a 6% error) but the larger percentage errors occur at larger T_1 values (pane c) due to the generally lower SI at these T_1s (pane a). Both of these errors have the potential to affect MBF estimates. Clearly a change in the peak of the AIF will be reflected in the MBF measured, but errors in the pre-contrast baseline concentration will also indirectly affect the MBF measurement through the baseline correction, although it is likely that at these lower SIs noise will be a more profound cause of error then the small systematic shift between pulse sequence models described here.

Considering the volunteer study, a failure to incorporate FAS in the concentration conversions yielded a small (~10%) but systematic and therefore statistically significant difference in MBF value. These differences did not propagate to a significant change in MPR. This is to be expected as a similar ~10% increase in MBF at both stress and rest should not alter MPR=stress MBF/rest MBF.

6.3.6. Conclusion

The error induced in concentration conversion due to neglecting FAS effects is small but systematic. Absolute differences are most significant at T_1s close to the peak of the AIF (which has most effect on MBF estimates) but percentage differences are more profound at native tissue T_1 values. Neglecting FAS in the conversion has a moderately small but significant systematic effect on MBF estimates, however this effect does not significantly affect MPR measurements.

Small but significant improvements in the accuracy of MBF estimates from cardiac myocardial perfusion datasets can be made by incorporating FAS into the mathematical model of the imaging pulse sequence. However these improvements will not significantly impact MPR estimates. Where possible FAS should be incorporated into future studies where Philips sequences that incorporate FAS are used but the effects are small enough to be able to accept results of studies that did not incorporate FAS into their modelling with confidence.

6.3.7. The effect of errors in the assumed blood T_1[1]

Introduction

The method for converting SI values to concentration described in section 6.2 is dependent on the native T_1 of blood. This can be obtained by measurement prior to the perfusion scan (31). However, T_1 measurement is time consuming (both in terms of scanning time and off-line analysis) and of limited accuracy, especially when applied to the left ventricular blood pool where the native T_1 is long (requiring long TIs) and flow effects may create signal changes that are difficult to compensate for. Accepting then that the baseline T_1 (whether it is assumed or measured) will have some error associated with it the aim of this study was to establish how robust the non-linear conversion to concentration is to errors in T_1 as expressed in the final MBF estimate.

Method

The dual-phase data set described in section 5.2.2 was used in the study. A weighted average of the native cardiac blood values taken from (135–138) gave a mean ± standard deviation (SD) T_1 value of 1393 ± 126ms, giving a 95% confidence interval of 1141 ms to 1645 ms. Signal to concentration conversion was carried out using the method described in section 6.2 and 6.2.3 (incorporating FAS) using a range of assumed T_1 values encompassing this confidence interval. The resulting curves were used to estimate MBF using Fermi-constrained deconvolution with automated curve pre-processing (section 5.4). Box plots of the MBF for each assumed T_1 value were plotted for comparison.

Results

The mean MBFs (± SD) using the reference T_1 (1393ms) at stress and rest

---

[1] This study was previously published with a smaller volunteer dataset (158)

were 3.14 ± 0.70 ml/g/min and 1.09 ± 0.36 ml/g/min respectively. Using the reference blood T_1 to derive the calibration factor ψ, the mean myocardial T_1 derived from the myocardial baseline using the reference blood T_1 was 1195 ± 266ms. Figure 6-9 shows the distribution of stress and rest MBFs and MPRs over the volunteers for each assumed T_1 value. With respect to the reference T_1, the largest mean difference in MBF occurred at T_1=1141ms, which gave an absolute mean difference in MBF at stress of 0.73 ml/g/min and at rest 0.29 ml/g/min, giving percentage differences of 22% and 28% respectively. This corresponded to a change in the MPR ratio of 0.16 (5%). The largest shift in MBF in a single measurement due to changing T_1 was 1.6 ml/g/min at stress and 0.53 at rest, both observed with a T_1 of 1141ms. The largest individual increase in MPR was 1.58.

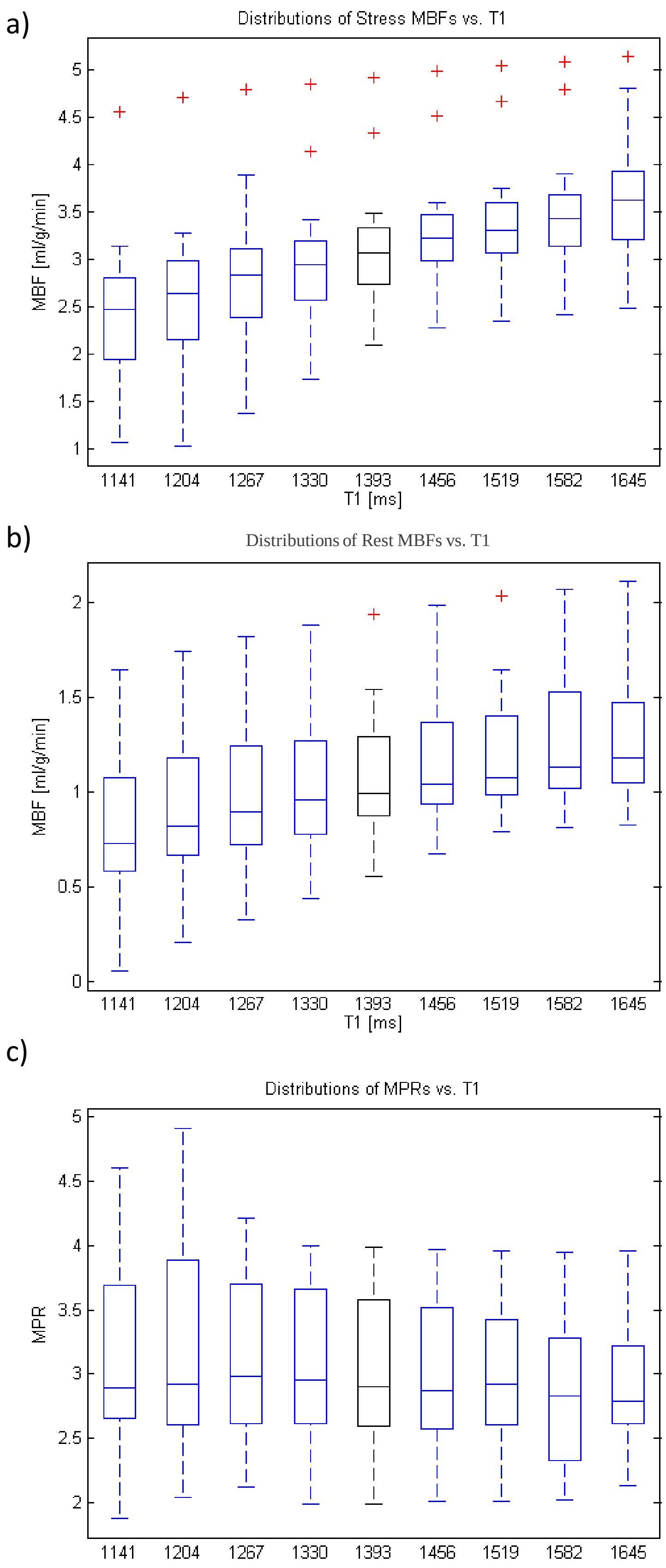

Figure 6-9 – Boxplots showing the distribution of stress MBF values for each assumed T_1 value (a), the corresponding distributions for REST MBF values (b) and MPRs (c).

Discussion

None of the median MBFs in Figure 6-9 fall outside of the inter-quartile range of the MBFs estimated assuming the reference T_1, suggesting that the variation in MBF induced by varying T_1 is less pronounced than the experimental variation of MBFs within the reference (T_1 = 1393ms) dataset. It could be postulated that a larger dataset than this, using data not requiring correction, or corrected using measured T_1 values, might exhibit a narrower variation in MBF. However, the weighted mean of resting MBF measurements taken from studies (6,29,126,140), which satisfied these criteria, was 0.85 ± 0.32 ml/g/min. The resting MBFs for all T_1 values in this study maintained a standard deviation comparable with this suggesting that the variability in this dataset is not abnormal. The mean derived myocardial T_1 in the experimental data (1195 ± 266ms) was higher than a weighted mean of myocardial T_1 values taken from (135–138), 944 ± 87ms, although still within one standard deviation of the literature value. The effect of changing the assumed blood T_1 on MPR values is smaller than that for MBF (5% maximum change in the mean MPR) due to the fact that a change in assumed T_1 affects both rest and stress MBF in the same direction (increase or decrease) so resulting changes in the ratio between the measurements are small.

In conclusion, errors in assumed T_1 can have a substantial impact on individual MBF estimates. However, the variation in MBF induced by errors in the assumed T_1 of blood is less pronounced than the experimental variation in MBF estimates and is therefore unlikely to affect diagnosis decisions within a single patient cohort.

6.4. Phantom experiments

6.4.1. Introduction

Section 6.2 described the method for converting SI values to concentrations theoretically. This section attempts to validate the theoretical models using phantom data. The purpose of this study was to establish whether Equation 6-16 correctly models the relationship between T_1 and signal intensity for a given calibration factor ψ using T_1-gel phantoms.

6.4.2. Method

A phantom consisting of tubes containing gels doped with different concentrations of gadolinium was imaged using an inversion recovery spin echo (IRSE) pulse sequence with TI: (50, 100, 200, 400, 800, 1600, 3200)ms. An additional spin echo image without an inversion pulse was acquired in order to normalise the recovery curves to the fully relaxed magnetization M_o. The phantom was then imaged with the pulse sequence used for perfusion imaging in the CE-MARC study (section 5.2.1). Regions of interest were drawn on each IRSE image for each tube over all the inversion times in order to obtain mean signal intensity values from each tube over time. The IRSE signal intensities for each tube were normalised by dividing by the corresponding value from the spin echo image acquired without the inversion pulse. The T_1 value for each vial was calculated by fitting a mono-exponential recovery curve to the normalized mean signal value (S) from each tube over time with three free parameters A, B and T_1:

$$S = A - Be^{\frac{-TI}{T_1}}$$

Equation 6-21

with A~1 and B~2 post-normalization giving the standard inversion recovery T_1 relaxation equation:

$$S = 1 - 2e^{\frac{-TI}{T_1}}$$

Equation 6-22

Regions of interest were then drawn within each tube in the perfusion images and mean signal intensities were plotted against the measured T_1 for each vial. The equation describing the signal intensity of the pulse sequence, given $R_1=1/T_1$, was then fitted to the data allowing the calibration factor ψ as a free parameter:

$$SI = \Psi \cdot f(R_1)$$

Equation 6-23

where $f(R_1)$ is shorthand for Equation 6-16, which is a function of R_1.

The parameter most likely to be susceptible to inaccuracies in the model is the flip angle, α. For this reason the investigation was repeated allowing both ψ and α as free parameters in the model to see what improvements to the fit could be made by varying α. The results of this study showed lower flip angles than those set at the MR console. Therefore the experiment was repeated with administered flip angles of (5^o, 10^o, 15^o, 20^o and 30^o) to further investigate how the fitted flip angle related to that reportedly administered by the scanner.

Previous simulations have dealt with the longitudinal magnetization ($M_z(t)$) only. The $\sin \alpha$ term, which takes the transverse component of the magnetization, has been incorporated into the calibration factor, ψ. In order to include α as a fitted parameter this term must be included in the pulse sequence equation. Incorporating this term Equation 6-16 becomes:

$$M_{xy\,n}(-) = \left\{\left(\prod_{i=1}^{n-1} \cos \alpha_i\right) . \left(M_{eq}\left(1 - e^{-TS/T_1}\right) C^{n-1}\right) + \sum_{j=2}^{n-1}\left[\prod_{j}^{n-1}\left(\cos \alpha_j\right). DC^{n-j}\right] + D\right\} \sin \alpha$$

Equation 6-24

With a modified calibration constant:

$$\psi = \Omega.\, \mathrm{M_{eq}}\;\; e^{-TE/T_2^*}$$

Equation 6-25

The vector of flip angles in the read-out pulse α_{j-n-1} must be recalculated for each flip angle value. This was done using the flip angle sweep equation (Equation 6-15) for each instance of α.

6.4.3. Results

The T_1s of the tubes as measured using the IRSE sequence were 54.6, 176, 436, 703, 856, 935, 1058, 1097.3 and 2510.5ms. Figure 6-10 shows the measured signal values from each tube using the perfusion sequence and the fit of the mathematical model to the data. For the apical, middle and basal slices the imaging TS values were 418ms, 272ms, 128ms, the calibration factor values were 307710, 300400, 299890 respectively. The fitted R^2 value was 0.99 for all slices.

Figure 6-11 shows the corresponding plots allowing both ψ and α as free parameters For the apical, middle and basal slices the fitted value for ψ was 339170, 392300 and 500000 with α of 11.15^o, 8.65^o and 6.75^o respectively. The fitted R^2 value was 1.00 for all slices. At a T_1 of 50ms the difference between the ψ only fit and the fit incorporating α as well was 4.18% for the apical slice, 4.61% for the middle slice and 2.59% for the basal slice.

Figure 6-12 shows the fits applied to the data when a range of applied flip angles were administered by the scanner, for the middle slice only. Table 6-2 shows the values of the fitted parameters.

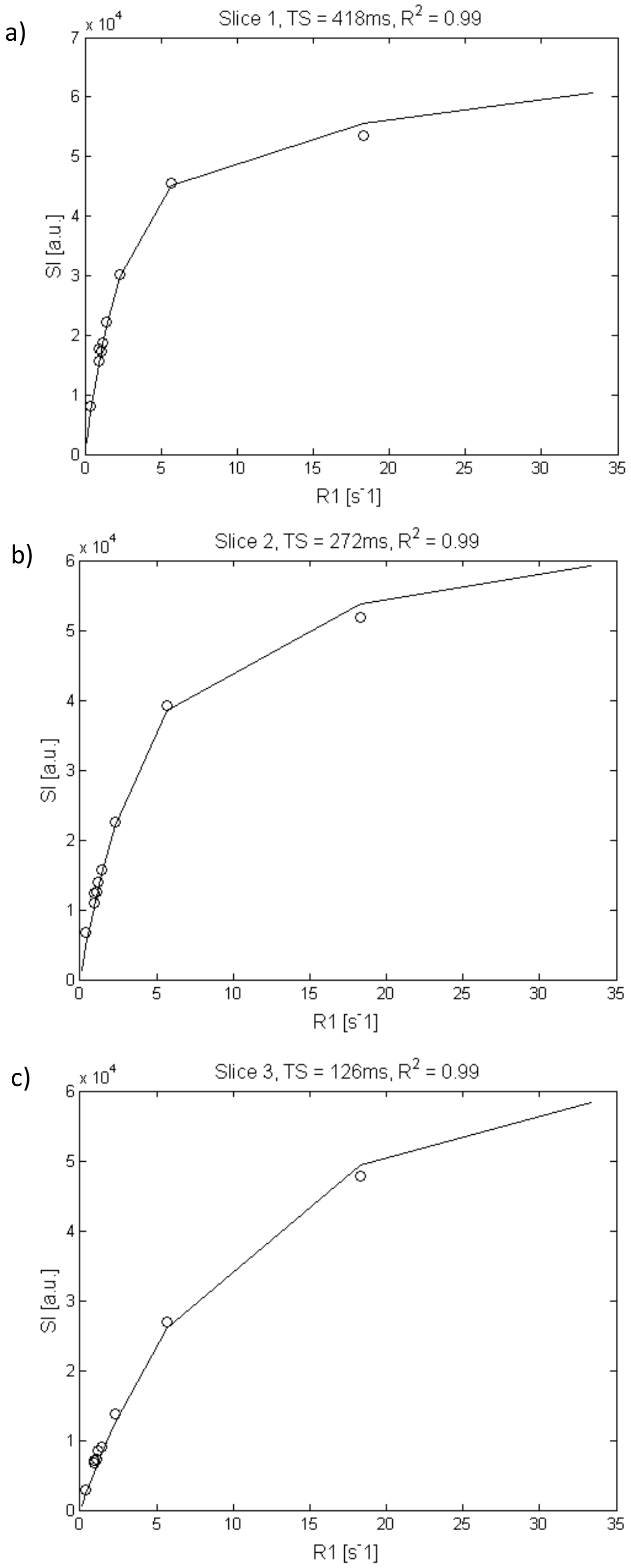

Figure 6-10 – Signal vs. T_1 allowing ψ only as a free parameter. Panels a, b and c correspond to perfusion slice 1 (apical), slice 2 (middle) and slice 3 (basal) with TS 418ms, 272ms and 126ms respectively and were fitted by the model with an R^2 of 0.99 in each case.

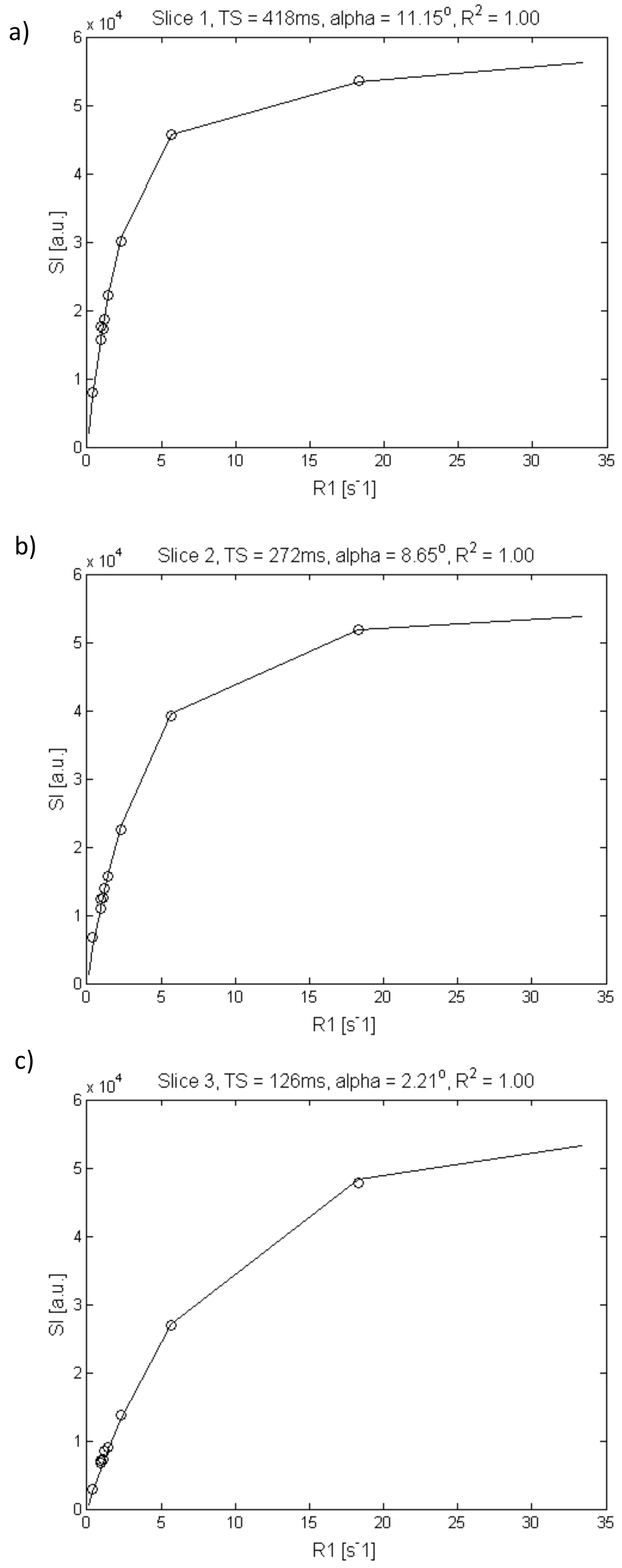

Figure 6-11 - Signal vs. R_1 allowing both ψ and α as free parameters. Panels a, b and c correspond to perfusion slices 1 (apical) ,slice 2 (middle) and slice 3 (basal) respectively and were fitted by the model with an R^2 of 1.0 in each case.

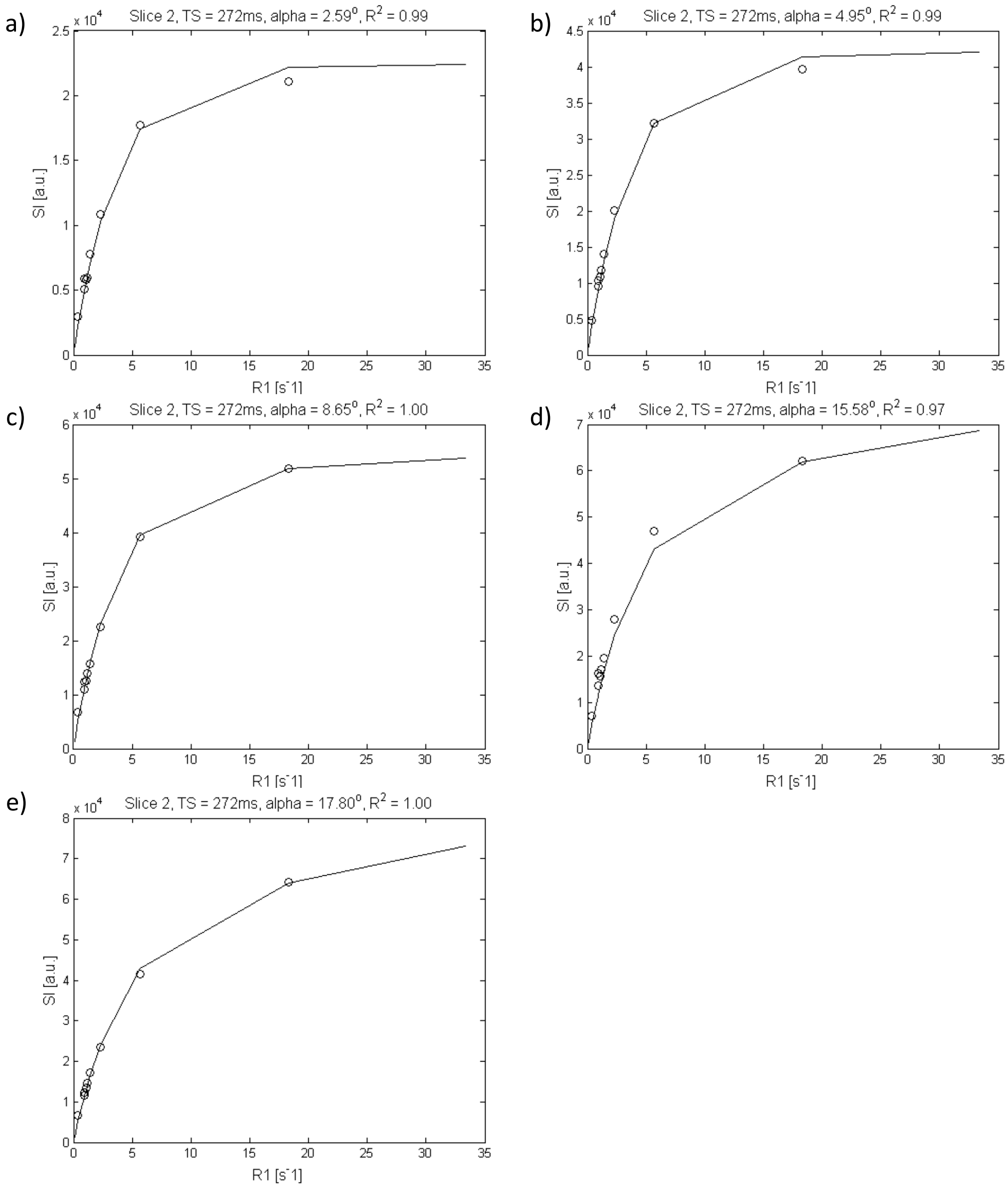

Figure 6-12 – Model fits for the middle slice for data acquired with an administered flip angle of a) 5°, b) 10°, c) 15°, d) 20°, e) 30°.

Panel in Figure 6-12	Administered flip angle	Fitted flip angle	Calibration factor (ψ)
a)	5^o	2.59^o	5×10^5
b)	10^o	4.95^o	5×10^5
c)	15^o	8.65^o	3.9×10^5
d)	20^o	15.58^o	3.3×10^5
e)	30^o	17.80^o	3.3×10^5

Table 6-2 – Administered and fitted flip angles, with corresponding calibration factor values for the plots displayed in Figure 6-12.

6.4.4. Discussion

The initial model, using the reported flip angle from the scanner, fitted the data well with R^2~0.99 for all three slices suggesting that Equation 6-16 is a good representation of the pulse sequence. The calibration factor Ψ was consistent over the three slices with only 2.5% maximum difference between ψ values. The absolute error between the model and the measurement is largest at the shortest T_1~50ms (R_1~20s^{-1}). This T_1 value corresponds to the estimate of T_1 at the AIF peak, which will have the most profound effect on MBF values. The percentage errors between the model and the measured data points for the apical, middle and basal slices at this point are 3.62%, 3.72% and 3.52% respectively.

The flip angle used in the model in Figure 6-10 assumes that the flip angle set in the scanning parameters is delivered fully and homogeneously to the imaged object. This is often not the case and so it is of value to investigate whether allowing α as a free parameter in the model fit generates realistic estimates of the actual flip angle delivered to the phantom. Figure 6-11 shows the improvements to the model fit after allowing α as a free parameter in the model fitting. The fact that the R^2 values improve is expected as there is an extra degree of freedom in the model. The resulting flip angles were all less than the reported administered flip angle of 15^o, which is consistent with the theory that the full flip angle has not been delivered to the phantom. However, the calibration factor, Ψ, varied dramatically between the slices with this model. In fact for the basal slice the unconstrained fit used a very small flip angle (2^o) and a large calibration factor (1400000). It is unlikely that the calibration factor would change so dramatically between slices therefore the model was constrained to an upper limit on ψ of $5x10^5$. After applying this constraint the percentage difference between the two models (ψ only and incorporating α as a free parameter) was less than 5% in all slices. This implies that the effect of errors in administered flip angle on the signal intensity at the AIF peak is small and should not generate large errors in MBF. Furthermore the effect should be similar for rest and stress MBF values and so the effect of flip angle errors on MPR should be minimal.

Figure 6-12 shows the results of the model fit when the actual administered flip angle was varied. The fitted data consistently underestimates the administered flip angle suggesting that the flip angle that the phantom experiences is consistently lower than that administered. When the unconstrained model was fitted to these data the model tended to generate high ψ values and very low ($<1^o$) flip angles. These are unlikely to be representative of the true parameter values. In order to generate Figure 6-12 ψ was again constrained to not exceed $5x10^5$.

The need to constrain Ψ in the model means that the model is unstable with these datasets. For this reason the fitted flip angles cannot be taken as good estimates of the actual administered flip angles. However, in cases where the calibration factor was consistent and the model was stable (e.g. 20^o and 30^o flip angles in Table 6-2) the fitted flip angle was still lower than the reported flip angle. This implies that the administered flip angle is genuinely lower than that reported on the scanner console. In any case, these simulations have shown that the changes in SI due to inaccurate flip angle distribution will be small. This is not surprising as the predominant contribution to signal level will be the recovery time of the saturation pre-pulse (TS).

A limitation of the study is that it has only presented the results in terms of errors in signal intensity. Propagating the errors distributions onto DCE-MRI perfusion datasets and investigating the actual effect on the resulting MBF estimate would strengthen the study but this step has not been implemented in this investigation.

6.4.5. Conclusion

The signal intensity model predicts T_1 phantom data with excellent agreement. Investigations into the differences between the reported and administered flip angles have been inconclusive due to instabilities of the model. However allowing flip angle as a free parameter has shown that the affects of flip angle errors on SI are small for the perfusion sequences considered and thus unlikely to affect MBF.

6.5. In-vivo experiments

6.5.1. Introduction

The next step in assessing the performance of the non-linear correction described in this chapter should be to assess its performance on in-vivo data. In order to assess the non-linearity correction presented here on human data an independent assessment of MBF is required. The dual-bolus approach (section 2.8.6) provides such an alternative. However, the MBF estimates obtained from the dual-bolus datasets acquired for such investigations were much lower than the values expected from the literature. This prompted an investigation into dual-bolus protocol that was used, which is presented in this section

The dual-bolus protocol uses a low dose pre-bolus to obtain an AIF where linearity can be assumed, followed by a normal dose bolus so that adequate SNR can be obtained in the myocardial curve. Practically the process is complicated as it requires three syringes, (two bolus syringes of equal volumes but different concentration, and a saline flush syringe). For this study the protocol recommended by Ishida et al. (131) was adopted, which uses a three-way tap to push the boluses into the injection line (see Figure 6-13). To test this protocol the method of Kostler et al. (141) was used, which compares the MBF acquired using the pre-bolus data alone with that acquired using the dual-bolus analysis. As the linear assumption for SI should hold for both these analyses the results should be comparable, albeit with larger noise values for the pre-bolus myocardial data analysis, as has been shown using early dual-bolus protocols (141).

6.5.2. Method

Volunteer study

Four healthy volunteers were recruited for the study. The study was approved by the national research ethics service (05/Q1205/142) and all volunteers gave written informed consent. Volunteers refrained from caffeine for 24 hours before imaging. Imaging was performed using the CE-MARC study imaging protocol (section 5.2.1) except that the bolus injection protocol described in detail in (131), was used. Two syringes of Gd-DTPA were prepared per perfusion scan (4 in total for rest and stress imaging). The two syringes contained equal volumes but the first syringe contained a 0.005mmol/kg dose, achieved by dilution with saline solution, whereas the second contained 0.05mmol/kg. Prior to imaging the pre-bolus syringe was attached to a 3-way tap in the line between the injector pump and the patient. After the pre-bolus syringe was injected into the line the power injector was used to push 25ml of saline down the line, at a rate of 5ml/s, to force the pre-bolus into the patient. The bolus syringe was then connected to the three way connector and injected into the line. After a delay (~25s) the power injector was then used to push the bolus into the patient with another 25ml of saline. As with the CE-MARC protocol stress imaging was performed first (induced with a 4 minute intravenous infusion of adenosine at 140 mcg/kg/min) followed by rest imaging approximately 15 minutes later.

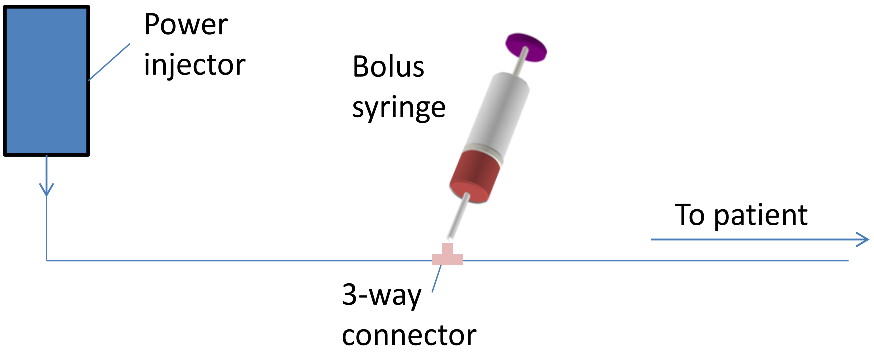

Figure 6-13 – Illustration of the dual-bolus injection method as described by Ishida et al. (131)**. The pre-bolus syringe is connected to the three-way connector and injected into the line before the power injector flushes saline into the patient. After a delay the process is then repeated with the full bolus syringe.**

Analysis

The dual-bolus technique was evaluated by comparing the MBFs obtained using the dual-bolus analysis with the MBF obtained using the pre-bolus data only. For the dual-bolus analysis the pre-bolus AIF was multiplied by a factor of 10 (the bolus concentration ratio) and analysed with the myocardial uptake curve from the main bolus. For the pre-bolus analysis both the AIF and myocardial uptake curves were taken from the pre-bolus. The analysis is illustrated in Figure 6-14. None of the data used in these analyses should exhibit significant non-linearity and so the resulting MBFs should be comparable, as has been shown with other dual-bolus protocols (141), albeit with a larger susceptibility to noise when using the low SNR pre-bolus tissue curve. The MBF values from the two analyses were compared using a paired t-test.

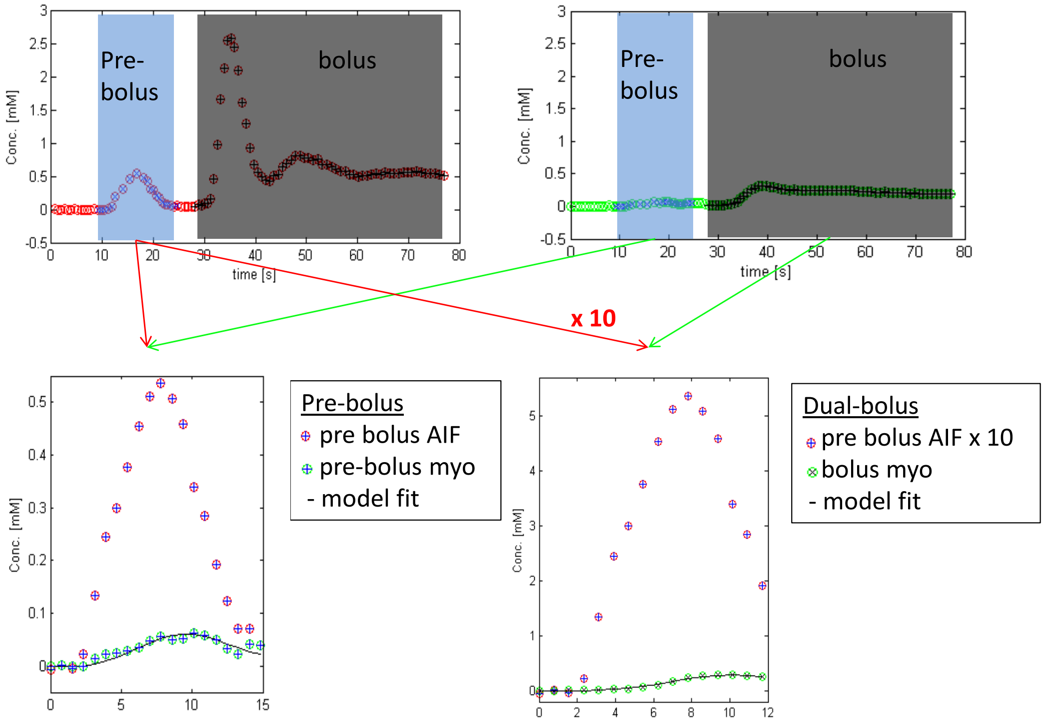

Figure 6-14 – The analysis method for analysing the dual-bolus technique. The pre-bolus MBF is calculated using the AIF and myocardial uptake curve from the pre-bolus injection. The dual-bolus MBF is calculated using the pre-bolus AIF (dose corrected by multiplication by 10) and the bolus myocardial curve. As neither result should exhibit significant non-linearity the resulting MBF values should not be significantly different.

Patient study

As the number of volunteers in the first study was small the investigation was repeated on a ten patient pilot study looking into the effects of rheumatoid arthritis on MBF, that had been conducted using the same dual-bolus injection protocol. Ten patients diagnosed with rheumatoid arthritis gave informed consent in this small study approved by the regional ethics committee (10/H1307/103). The patients underwent stress and rest, dual-bolus DCE-MRI cardiac perfusion imaging using a protocol identical to that described above except that imaging was performed on a 3T magnet and an independent saturation pulse was used for each slice (TS = 100ms), as opposed to the shared pre-pulse used in the CE-MARC protocol. Analysis was identical to that described in the preceding section. In order to reduce the contouring time commitment only the basal slice was contoured for the AIF and the middle slice for myocardium.

6.5.3. Results

Volunteer study

Mean MBF [ml/g/min]	i) Pre-bolus	ii) Bolus	iii) Dual-bolus
Stress	4.77±1.24	3.42±0.68	1.16±0.23
Rest	1.66±0.60	1.50±0.27	0.43±0.09
MPR	3.45±1.02	2.35±0.14	3.16±0.29

Table 6-3 – Stress MBF, rest MBF and MPR averaged over all volunteers and all slices (mean ± standard deviation) analysed using i) pre-bolus (AIF and myocardial uptake curve taken from the pre-bolus), ii) bolus (AIF and myocardium taken from main bolus), iii) dual-bolus (AIF taken from pre-bolus and dose adjusted, myocardium taken from main bolus).

Ratio	i) Pre-bolus / Dual-Bolus	ii) Pre-bolus / Bolus	iii) Bolus / Dual-bolus
Stress	3.66 ± 1.57	1.47 ± 0.61	2.77 ± 0.68
Rest	3.91 ± 1.64	1.14 ±0.47	3.55 ± 0.53
MPR	1.22 ± 0.89	1.68 ± 1.07	0.80 ± 0.25

Table 6-4 –results expressed as ratios between analysis regimens (mean ± standard deviation). i) The ratio of pre-bolus to dual-bolus results, ii) the ratio of pre-bolus to bolus results and iii) the ratio of bolus to dual-bolus results.

Table 6-3 shows the results, averaged over all volunteers and all slices, for stress MBF, rest MBF and MPR. There are three analysis strategies displayed here: i) Pre-bolus – both AIF and myocardial curves are taken from the pre-bolus, ii) Bolus - both AIF and myocardial curves are taken from the main bolus curves, iii) Dual–bolus – the AIF is taken from the pre-bolus and dose corrected (multiplied by 10) whilst the myocardial curve is taken from the main bolus. Table 6-4 represents the results as ratios between the analysis regimens.

Due to the low concentration CA dose used for the pre-bolus, the myocardial uptake curves were particularly prone to noise. Of the 12 (4 volunteers x 3 slices) curves considered, six of the pre-contrast analyses were excluded because the data was too noisy to generate a meaningful fit of the model to the data.

There was a significant difference between the pre-bolus and dual-bolus MBF values at stress ($p=0.001$) and rest ($p=0.003$) but not in the MPR ($p=0.96$). The bolus MBFs were significantly different to the dual-bolus MBFs at stress ($p<0.0001$), rest ($p<0.0001$) and MPR ($p=0.017$).

Patient Study

Mean MBF [ml/g/min]	i) Pre-bolus	ii) Bolus	iii) Dual-bolus
Stress	2.54±0.86	3.70±0.92	1.32±0.33
Rest	1.71±0.67	2.29±0.70	0.62±0.17
MPR	1.81±1.28	1.70±0.44	2.21±0.76

Table 6-5 - Stress MBF, rest MBF and MPR averaged over all patients (mean ± standard deviation) analysed using i) pre-bolus(AIF and myocardial uptake curve taken from the pre-bolus), ii) bolus (AIF and myocardium taken from main bolus), iii) dual-bolus (AIF taken from pre-bolus and dose adjusted, myocardium taken from main bolus).

Ratio	i) Pre-bolus / Dual-Bolus	ii) Pre-bolus / Bolus	iii) Bolus / Dual-bolus
Stress	2.08 ± 0.82	0.69 ± 0.18	2.88 ± 0.61
Rest	2.87 ± 1.11	0.82 ± 0.35	3.74 ± 1.09
MPR	0.94 ± 0.96	1.15 ± 1.0	0.80 ± 0.20

Table 6-6 –Results expressed as ratios between analysis regimens (mean ± standard deviation). i) The ratio of pre-bolus to dual-bolus results, ii) the ratio of pre-bolus to bolus results and iii) the ratio of bolus to dual-bolus results.

Table 6-5 summarizes the MBF results from the larger, patient based data set, with the ratios shown in Table 6-6. Two patients were excluded because the pre-bolus myocardial curves were too noisy to conduct a meaningful analysis. There was a significant difference between the pre-bolus and dual-bolus MBF values at stress ($p=0.02$) and rest ($p=0.002$) but not in the MPR ($p=0.50$). The bolus MBFs were significantly different to the dual-bolus MBFs at stress ($p<0.0001$), rest ($p=0.0001$) and MPR ($p=0.04$).

6.5.4. Discussion

Reference	Pulse Sequence	Quantitative perfusion method	No. of cases	REST		STRESS	
				MBF [ml/g/min]	SD [ml/g/min	MBF [ml/g/min]	SD [ml/g/min
Vallee 1999(140)	SR-FLASH	1-cmpt model	10	0.72	0.22	No data	No data
Kostler 2004(141)	SR-SSFP	Fermi	11	0.75	0.25	No data	No data
Pack 2008(6)	SR-FLASH	Model independent	5	1.09	0.8	3.14	1.69
Pack2009(4)	SR-FLASH	Fermi	14	0.93	0.24	2.84	0.63
		Case weighted average		**0.85**	**0.31**	**2.92**	**0.91**

Table 6-7 - Average of a selection of healthy subject, single-bolus, myocardial perfusion quantitation papers from the literature. All studies were carried out with a single bolus dose of <= 0.02 mmol/kg.

Reference	Pulse Sequence	Bolus dosage pre/main [mmol/kg]	No. of cases	REST		STRESS	
				MBF [ml/g/min]	SD [ml/g/min	MBF [ml/g/min]	SD [ml/g/min]
Hsu 2006(142)	SR-EPI	0.005/0.1	10	1.02	0.22	3.39	0.59
Hsu 2008(27)	SR-SSFP	0.005/0.05	10	0.64	0.1	0.91	0.21
Icihara 2009(126)	SR-TFE (Patlak)	0.005/0.05	10	0.86	0.25	No data	No data
Kostler 2004(141)	SR-SSFP	0.004/0.17*	11	0.73	0.15	No data	No data
Ritter 2006(5)	SR-SSFP	0.004/0.057	12	0.52	0.11	1.78	0.53
Morton 2012(85)	kt turbo GRE	0.0045/0.045	16	0.6	0.1	2.5	0.5
		Case weighted average		**0.71**	**0.15**	**2.17**	**0.47**

***** assuming a patient weight of 70kg

Table 6-8 – Average of a selection of healthy subject, *dual-bolus*, myocardial perfusion quantitation papers from the literature. All quantitative analyses were carried out using Fermi-constrained deconvolution except Icihara 2009, which used Patlak.

Table 6-7 and Table 6-8 give a summary of MBF estimates in the literature for pre-bolus and dual-bolus protocols. Only studies of healthy humans reporting MBF (as opposed to MPR), and without a concentration conversion, were included. Table 6-7 gives average MBFs, weighted for study population, at rest and stress for published *pre-bolus* studies. For the purposes of this analysis a pre-bolus was defined as a single bolus study using a bolus concentration $\leq$0.02 mmol/kg. Table 6-8 gives corresponding average values for *dual-bolus* studies. The results in Table 6-7 and Table 6-8 provide evidence for the validity of the dual-bolus method in general. The average MBFs for rest and stress for the two methods in the literature agree with the standard deviation being larger for the pre-bolus method due to poorer SNR at lower contrast doses, in agreement with the single study results of (141).

Considering the results of the volunteer and patient studies presented in Table 6-3 to Table 6-5 respectively, neither pre-bolus nor dual-bolus results agree well with these literature values. The rest MBFs for the dual-bolus patient dataset do agree with the literature, however the stress MBFs are much lower. This could be due to genuinely lower MBFs in this patient cohort but such a reduction in MBF would be surprising due to rheumatoid arthritis alone. These patients were not known to be suffering from myocardial ischaemia.

The results from the main bolus only should overestimate MBFs due to non-linearity effects. In the patient dataset this holds true and the bolus MBFs are greater than either pre-bolus or dual-bolus results in all cases. However, in the volunteer dataset the pre-bolus results are greater. The volunteer dataset was very small (n=4) and had a significant number of excluded slices due to noisy data in the pre-bolus curves and so this discrepancy is probably due to insufficient numbers.

The philosophy of the dual-bolus method is to only use data where a linear relationship between SI and concentration can be reasonably assumed. It has been shown that this assumption is valid for doses <0.01mmol/kg in the AIF and <0.05mmol/kg in the myocardium (105). Thus the pre-bolus AIF and bolus myocardial uptake curves in this investigation should not be affected by non-linearity effects and should, in principle, generate the same MBF values, as has been shown previously (141) using a different injection scheme. In both the volunteer and the patient study there was a significant difference between dual-pulse and pre-bolus based MBF estimates (see Table 6-4 and Table 6-6). Dual-bolus MBFs were at least 2 times lower than pre-bolus MBFs in all cases. This suggests that there are differences between the pre-bolus and bolus uptake curves other than the planned tenfold change in concentration. No significant difference was found between pre-bolus and dual-bolus MPRs implying that the differences in MBF are constant and proportional.

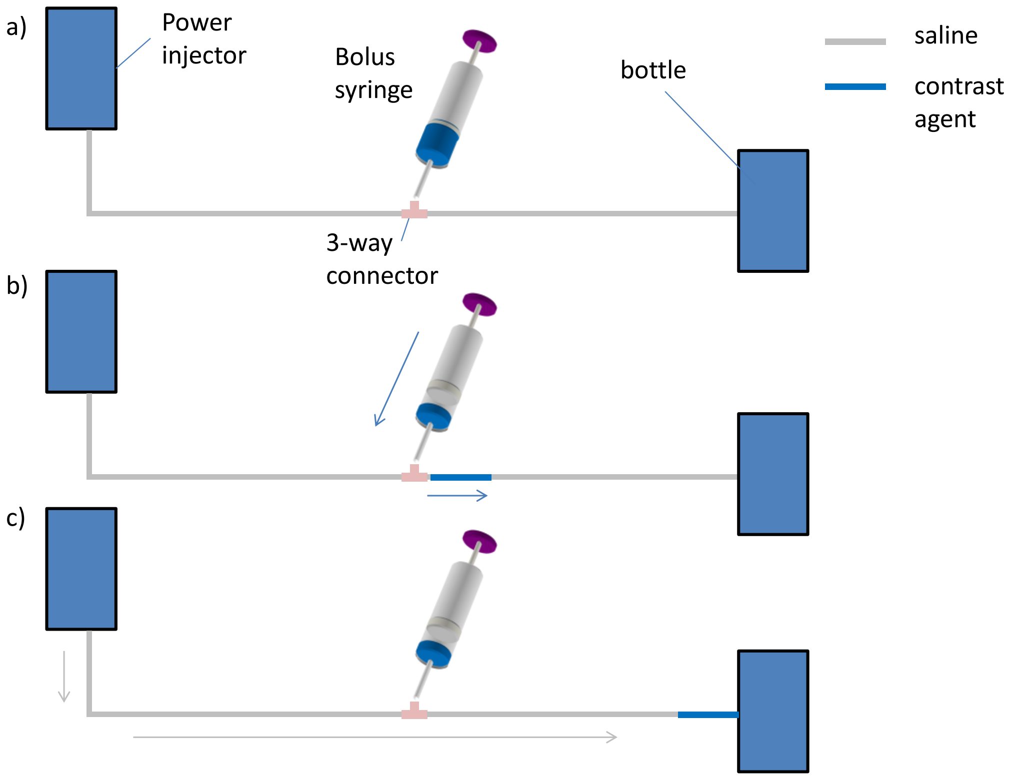

Figure 6-15 – Diagram illustrating the bolus evaluation experiment. The apparatus is set up as for a human study except the line is injected into a plastic bottle. The bolus syringe is dyed using blue food colouring enabling the bolus to be qualitatively assessed visually for dispersion and clearance from the line.

As the results of this study question the 1:10 ratio of bolus concentrations between the pre-bolus and bolus, a small qualitative experiment was conducted in order to assess the transit and clearance of the bolus through the line and into the patient. The saline power injector, lines, 3-way tap and bolus syringe were set up as for patient injection, but the line was injected into a plastic bottle half filled with water. The pre-bolus and bolus syringes were prepared with Gd-DTPA which was dyed with blue food colouring. The dual-bolus injection protocol was carried out as normal but the, now visible, bolus was inspected for dispersion in the line when stationary and for remnants in the line after injection of the saline flush (Figure 6-15).

This qualitative experiment to try and visually assess bolus dispersion and clearance was conducted multiple times. After initial injection the bolus stayed in the line for a few seconds, typically whilst patient breathing instructions or adenosine infusions were being given. Very little dispersion of the bolus could be observed during this interval, which is evidence against the theory that different rates of diffusion (due to different bolus concentrations) in the line might be responsible for the MBF results. During the saline flush the bolus disperses rapidly. After the saline flush there was still a noticeable amount of dye in the line showing that the full bolus had not been injected. This suggested that a larger flush volume should be used. However it was not possible to perceive a difference in the remnant volume left by the pre-bolus compared with that of the bolus, and so this does not explain the mismatch between the pre-bolus and dual-bolus results.

6.5.5. Conclusion

The results of the investigations into the dual-bolus protocol show that the version of the protocol used in these studies is inadequate as a reference standard against which to test the non-linearity correction algorithm presented in this chapter. The reasons for the mismatch between the pre-bolus and dual-bolus MBF estimates have not been found. The mostly likely explanation would be that some aspect of the, relatively new, three-way tap method of administering the two boluses causes extra dispersion or dilution of the second bolus. However, preliminary qualitative experiments using dyed boluses have not produced evidence to support this theory.

6.6. Summary

A method for converting cardiac perfusion DCE-MRI datasets from SI into

CA concentrations has been presented. The method uses the imaging pulse-sequence equation, a pre-contrast signal measurement and an assumed T_1 value for blood to calculate the concentration curve. A detailed mathematical description of the imaging sequence used for studies in this thesis has been presented, incorporating the Philips, flip angle sweep. The errors due to neglecting this flip angle sweep, neglecting T_2* effects and due to errors in the assumed blood T_1 have been investigated using simulations. A T_1 phantom has then been used to assess the accuracy of the model and to investigate the likely magnitude of signal change that can be expected due to flip angle errors. The conversion method has not been validated on in-vivo data, due to concerns about the dual-bolus data intended for this purpose. An investigation into the dual-bolus protocol is presented showing that pre-bolus and dual-bolus MBF estimates do not match. This suggests that differences are present between the pre-bolus and bolus other than the known ten-fold change in concentration. Preliminary investigations into the source of these differences are reported.

6.7. Limitations and future work

The main limitation in this work is that an evidence based conclusion has not been provided to explain why the dual-bolus results do not match the pre-bolus results. This will be an area of further investigation. The experiments to investigate bolus dispersion and clearance were qualitative and superficial. The lack of ability to make quantitative measurements of the remnant dye in the line limits the usefulness of the experiment, particularly as the observed data can only be explained if one bolus concentration is changed by a different amount to the other. The fact that the dye and Gd-DTPA contrast agent are not bound chemically and may have different transit properties is a further limitation. These weaknesses could be overcome by repeating the experiment using radioactively labelled DTPA (Tc^{99m}-DTPA). This would mimic much more closely the properties of Gd-DTPA and quantitative measurements of the remnant tracer in the line could be made using a gamma counter.

The assessment of the plateau region in the SI vs. concentration plots is subjective. A quantitative limit for when this curve plateaus could be achieved by applying simulated noise to these curves and establishing at what point a given SI yields multiple T_1 values. This would be a more objective way of assessing these curves.

Both the volunteer (n=4) and the patient (n=8) dual-bolus studies are small cohorts. The conclusions would be strengthened by larger study numbers.

7. Evaluation of the effect of myocardial segmentation errors on myocardial blood flow estimates from DCE-MRI[1]

7.1. Introduction

To estimate myocardial blood flow (MBF) from dynamic contrast enhanced MRI (DCE-MRI) cardiac perfusion datasets, contours depicting the myocardium and arterial input function (AIF) must be drawn for each frame in the DCE-MRI series (See section 5.3). Manual contour drawing is time consuming and is a significant factor hindering the acceptance of quantitative perfusion into clinical practice (143). Understanding the level of accuracy required in the drawing of these contours is a key step in addressing this problem. How much a given error is likely to affect MBF measurements will dictate how carefully, and thus how quickly, a human contour drawer can perform their task. Such insights are also important in the evaluation of automated segmentation algorithms, which tend to be evaluated with a wide range of segmentation error metrics making it difficult to cross compare algorithm performance, e.g. (144–146). The focus of such algorithms tends to be on the accuracy of segmentation of the myocardial region of interest in high quality datasets, with poorer quality images being discarded as outliers (145). However, poor quality images are a clinical reality and these algorithms may be aiming to achieve an unnecessary level of segmentation accuracy. Given the wide variety of sources of error in MBF estimates, it may be the case that sacrificing segmentation accuracy in order to maintain robustness to poor image quality will have an insignificant effect on MBF estimates. The purpose of this study was to investigate the relationship between geometrical errors in myocardial segmentation and error in MBF by imposing computationally simulated contour errors onto 17 healthy volunteer cardiac perfusion datasets. This relationship will provide a

---

[1] The investigation presented in this chapter has been previously published (159)

basis on which to decide acceptable error limits for myocardial contours, whether manually or automatically generated. It is also important for understanding whether automated segmentation algorithms evaluated in terms of segmentation metrics, e.g. (144), can be meaningfully compared with algorithms evaluated using MBF error, e.g. (146), and may be instructive in deciding how best to evaluate such algorithms in the future.

7.2. Method

7.2.1. Datasets

The study was carried out on the dual-phase data set described in section 5.2.2 and contoured as described in section 5.3. After contouring, the myocardium was divided into six circumferentially equidistant regions according to the model proposed by the American Heart Association (AHA) (106) for the mid ventricular slice. These regions were then further divided circumferentially into endocardial and epicardial compartments resulting in a total of 12 partitions as illustrated in Figure 7-2 (b).

7.2.2. Inter and Intra-observer variability to validate contour error simulations

To ascertain whether the contour errors simulated in this study were representative of human contour errors a subset of 11 patients were contoured a second time by the same person to assess intra-observer variability. A second observer also contoured the dataset to assess inter-observer variability. To measure the error between each contour and the reference contour the Euclidean distance between each point on the reference contour and the nearest point on the contour being investigated was calculated. The distribution of these errors was then compared to the corresponding distribution between the reference contour and the random contour errors simulated in this paper. This was tested using the Kolmogorov–Smirnoff test (147), which calculates the probability that two samples have been drawn from the same underlying continuous population. The inter/intra-observer variability data were analyzed considering stress and rest and endo- and epicontours separately and then finally analyzed considering all cases together.

7.2.3. Random contour errors

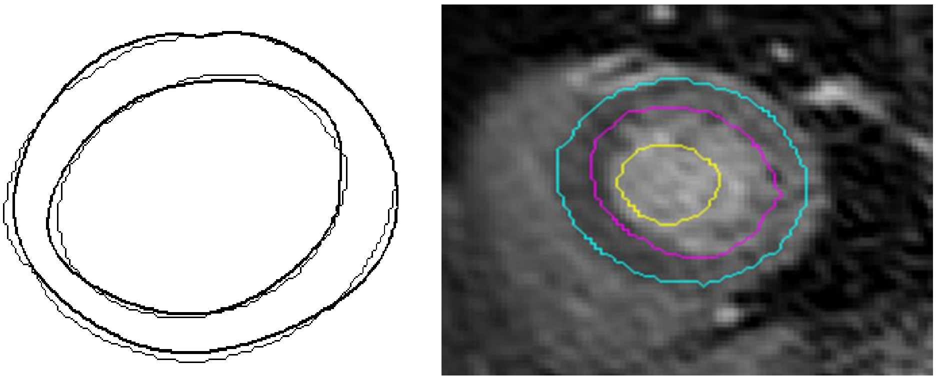

a)

b)

Figure 7-1 - a) Example of generated contour errors. The thin line shows the manual contour and the bold line shows the generated erroneous contour generated with a maximum deviation (MD) of 0.1MW. b) A single frame of a cardiac perfusion sequence showing manual contouring. The left ventricular cavity is filled with Gd-DTPA and appears bright against the surrounding myocardium.

Random contour errors were generated by introducing random radial deviations into the manual contour. The manual contour was represented as a circular spline by automatically placing equally spaced knot points along the defined contour. The knot points of the spline were offset by a random radial displacement allowed to range between ±MD, where MD is the maximum deviation, being the maximum distance the contour may deviate from the 'true' contour. MD was expressed as a fraction of the mean myocardial width (MW) so that the degree of contour error was normalized to the size of the heart. A new contour was generated from these offset knot values to represent the erroneous curve. Figure 7-1 (a) shows an example of a generated erroneous contour with MD = 0.1MW. Ten knot points were chosen to represent the contour to maintain a realistically smooth contour. Each randomly generated set of offset values was applied to contours at all time points in all patients. This process was repeated over 30 iterations of the random offset value generation. The process was repeated using MD =

0.1MW, 0.2MW, 0.3MW, 0.4MW and 0.5MW. F-tests and t-tests between the ‘true’ and erroneous contour datasets were performed to test for significant differences in the variances and means of the distributions respectively.

7.2.4. Systematic contour errors

Systematic underestimates and overestimates of the myocardial region of interest were generated by setting the MD to a constant offset value over all the knot points. For each frame of the cardiac DCE-MRI perfusion dataset the myocardial contours were modified by systematic MD values ranging from −0.5MW to +0.5MW. Figure 7-2 (a) illustrates the directions of positive and negative errors. Differences were calculated, at rest and stress, between the MBFs estimated from modified and unmodified contours and the difference in the means of the resulting distributions was assessed using a statistical *t*-test.

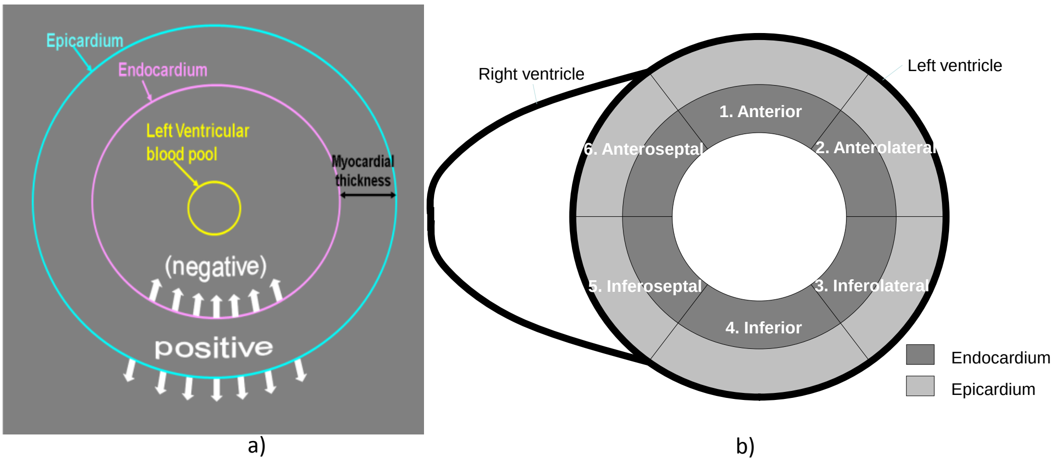

a) b)

Figure 7-2 - (a) A representation of the systematic contour errors illustrating the directions of the positive and negative errors. (b) Partitioning of the myocardial ROI.

7.2.5. Segmentation metrics

Segmentation errors were evaluated with two well recognised geometric segmentation metrics, Hausdorff distance (HD) (148), based on the distance between the two contours and Dice’s similarity coefficient (DSC) (149,150), based on the overlapping areas of the two contours and in terms of error in myocardial blood flow (MBF). Maximum deviation (MD) as defined above was also used as a segmentation metric. Pearson’s correlation between each segmentation metric and the MBF estimate was carried out to test whether the measures were well correlated.

7.2.6. Quantitation of MBF

Both AIF and myocardial uptake signal curves were converted to concentrations using the method described in chapter 6 using an assumed T_1 value of 1393 ms. The conversion from signal intensity to concentration was successful in 16/17 volunteers, with one dataset being excluded because the concentration conversion yielded erroneously high peak AIF concentrations, as described in section 6.3.4. The MBF was quantified from the left ventricular blood pool and myocardial tissue concentration versus time curves using a Fermi-constrained deconvolution method (120), (section 4.3.3). Prior to MBF estimation the curves were interpolated, baseline corrected and temporally shifted for the difference between AIF and myocardial bolus arrival times using the automated methods described in section 5.4.

7.2.7. Units of contour error

The data in this study are expressed in terms of the maximum deviation (MD) that a contour is allowed to deviate from its ‘true’ value. This is no less meaningful a measure of contour error than recognised segmentation metrics as we will show that these do not correlate with MBF error (section 7.3.1). Furthermore, it is consistent with the concept behind our philosophy of simulating contour errors and can be directly interpreted as a contour error tolerance. Expressing MD in terms of voxels would be inadequate because voxel sizes change between MRI acquisitions. Converting results into absolute spatial measures (mm or mm^2) is not appropriate either, as any cohort of cardiac MR images will contain a range of heart sizes; thus, a given absolute contour error will have a more profound effect on a smaller heart than on a large one. For these reasons, contour errors in this study are expressed as a fraction of the mean myocardial width (MW) of the specific heart being considered. Expressing contours this way ensures that a given contour error has the same effect across the entire dataset in terms of its relative geometric change to the myocardial contour with respect to the myocardium.

7.3. Results

Using the manual contours the mean (± standard deviation) MBF at rest was 1.24 ± 0.35 ml g^{-1} min^{-1} and at stress was 3.48 ± 0.67 ml g^{-1} min^{-1}. The mean myocardial width (MW) in the reconstructed images was 5.8 voxels (range: 3.3–8.6 voxels) and 6.9 mm (range: 4.2–10.3 mm).

7.3.1. Segmentation metrics

Table 7-1 shows Pearson's correlation scores between MBF error and maximum deviation (MD), Dice's similarity coefficient (DSC) and Hausdorff distance (HD) for endo- and epicardial modification at rest and stress considered separately and as one dataset. Contour errors were generated using the random contour error simulator. None of the segmentation metrics correlated with MBF error with the most significant correlation at $r = -0.32$.

Contour Error	MD	DSC	HD (mm)
Rest endocardium	0.03	0.03	0.02
Rest epicardium	-0.14	0.15	-0.17
Stress endocardium	0.07	-0.10	0.04
Stress epicardium	-0.22	0.26	-0.32
Rest and stress, endo- and epicontour	-0.08	0.17	-0.13

Table 7-1 - Table of the Pearson's correlation *r*-value between MBF error (ml/g/min) and each of the three segmentation error metrics: maximum deviation (MD) expressed as a fraction of the mean myocardial width (MW), Dice's similarity coefficient (DSC) (no units) and Hausdorff distance (HD) (mm). Results are shown considering errors in rest/stress and endocontour/epicontour separately and finally over all data.

7.3.2. Systematic contour errors

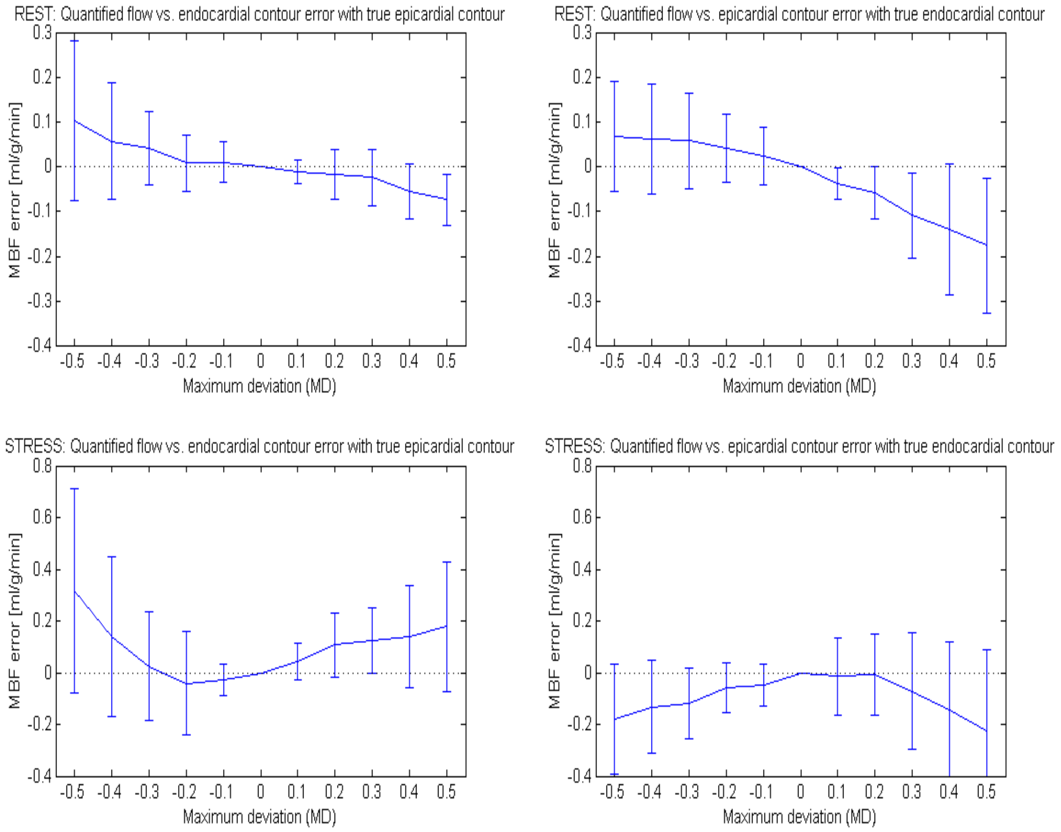

Figure 7-3 - Global MBF errors versus MD (expressed as a fraction of the mean myocardial width) for systematic contour errors in the rest endocardial contour (top left) rest epicardial contour (top right), stress endocardial contour (bottom left) and stress epicardial contour (bottom right). Error bars show the standard deviations.

Figure 7-3 shows the spread of MBF errors for each MD for the endocardium and epicardium at rest and stress over the entire myocardium. Positive MD values correspond to contours modified circumferentially outwards (moving away from the centre of the myocardial circle) and negative contours correspond to contours modified circumferentially inwards (see Figure 7-2 (a)). Errors in MBF were calculated as the difference between the MBF estimated with the modified contours and the MBF estimated with the manual contours. Student's *t*-test between the modified and unmodified MBF error populations yielded non-significant *p*-values for all MD values.

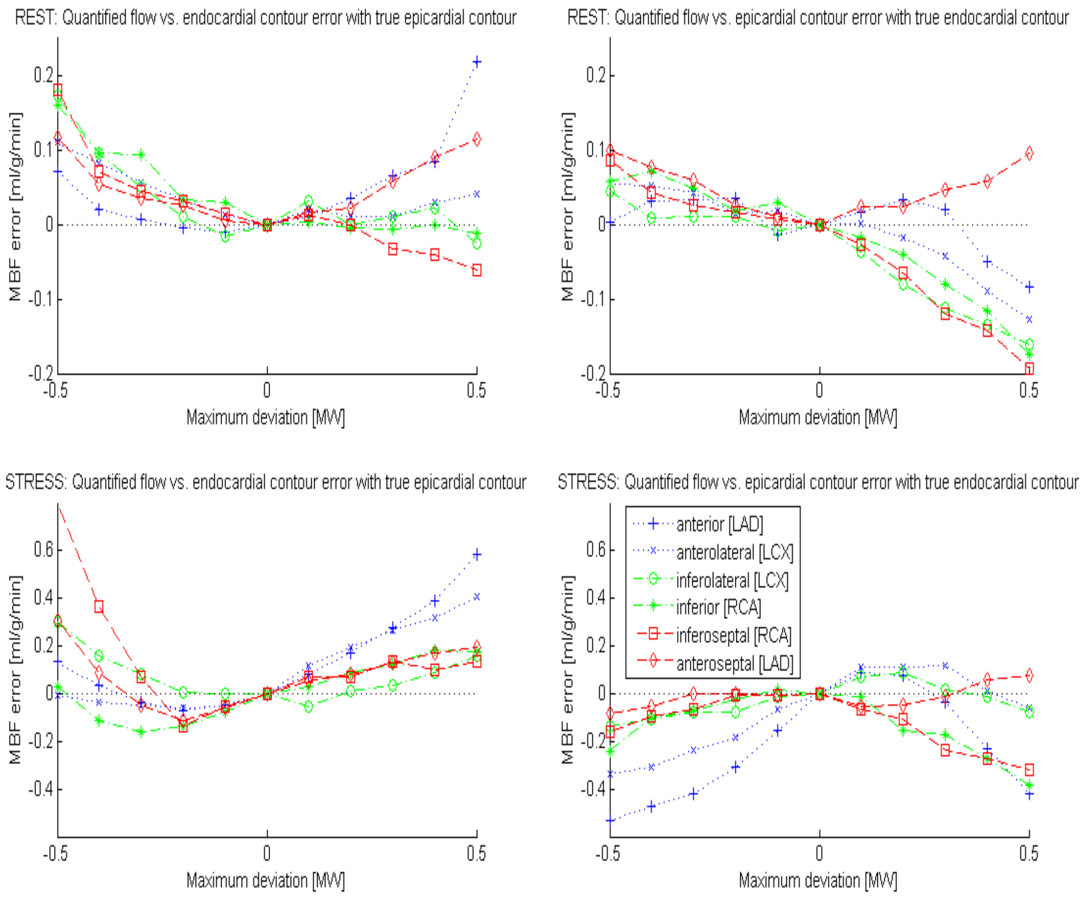

Figure 7-4 - Regional MBF error versus MD (expressed as a fraction of the mean myocardial width) for systematic contour errors in the rest endocardial contour (top left) rest epicardial contour (top right), stress endocardial contour (bottom left) and stress epicardial contour (bottom right).

Figure 7-4 shows the MBF errors for the six separate myocardial regions. Individual *t*-tests for each segment showed no significant difference in mean MBF except for the inferoseptal segment, where a resting epicardial MD of 0.5MW gave (p = 0.05) and a stress endocardial MD of −0.5MW gave (p = 0.02). Figure 7-5 shows the corresponding analysis when the endocardium and epicardium were considered separately. When the epicardial contour is modified only the signal from the epicardium is incorporated in the analysis and when the endocardial contour is modified only the endocardial tissue is considered. The *t*-test for sub-myocardial segments showed generally more statistically significant results than for transmural segments. Significant differences were seen in the endocardial inferospetal segment for MD = −0.5MW at rest ($p < 0.05$) and stress ($p < 0.03$), the epicardial inferoseptal segment at stress for MD = 0.5MW ($p = 0.01$) and MD = 0.4MW ($p = 0.04$), the epicardial inferior segment at rest for MD = 0.5MW ($p = 0.03$), the epicardial anterior segment for MD = 0.5MW at rest ($p = 0.04$) and stress ($p = 0.03$) and in the epicardial inferior segment for MD = 0.5MW at rest ($p = 0.02$) and stress ($p = 0.02$).

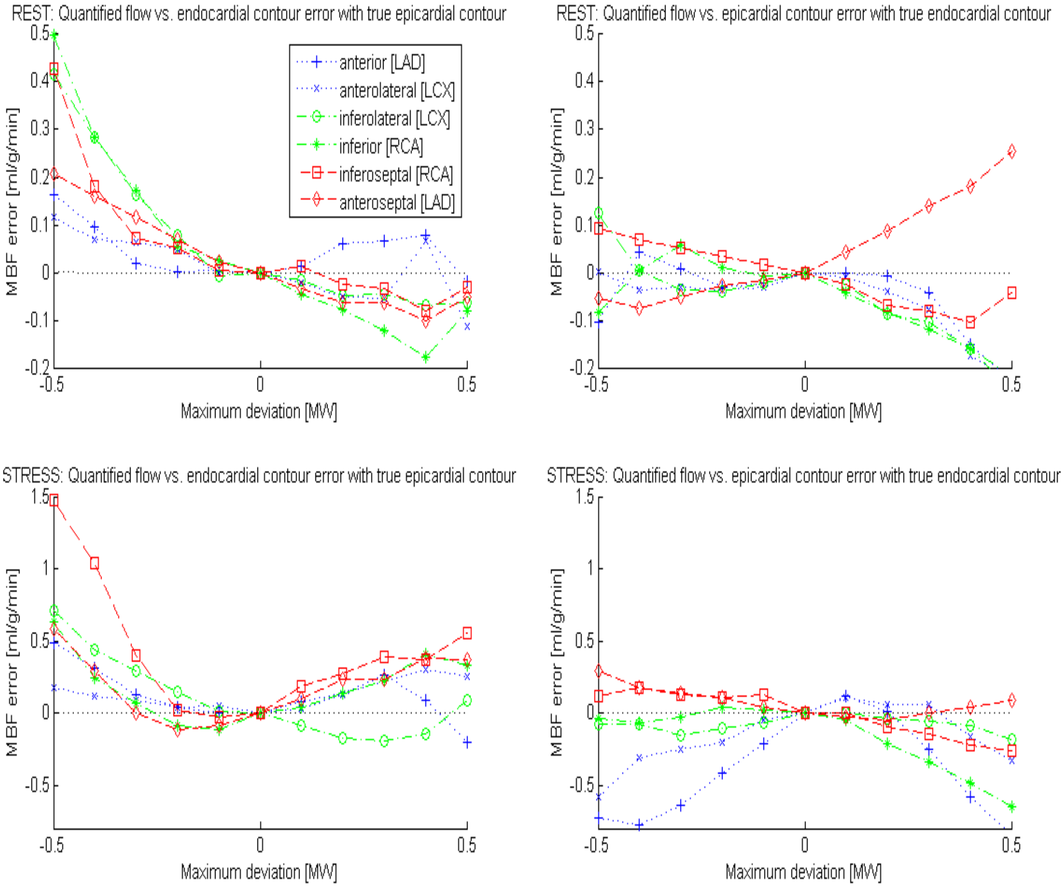

Figure 7-5 - Regional MBF errors divided into endocardial and epicardial segments versus MD (expressed as a fraction of the mean myocardial width) for systematic contour errors in the rest endocardial contour (top left), rest epicardial contour (top right), stress endocardial contour (bottom left) and stress epicardial contour (bottom right).

7.3.3. Random contour errors

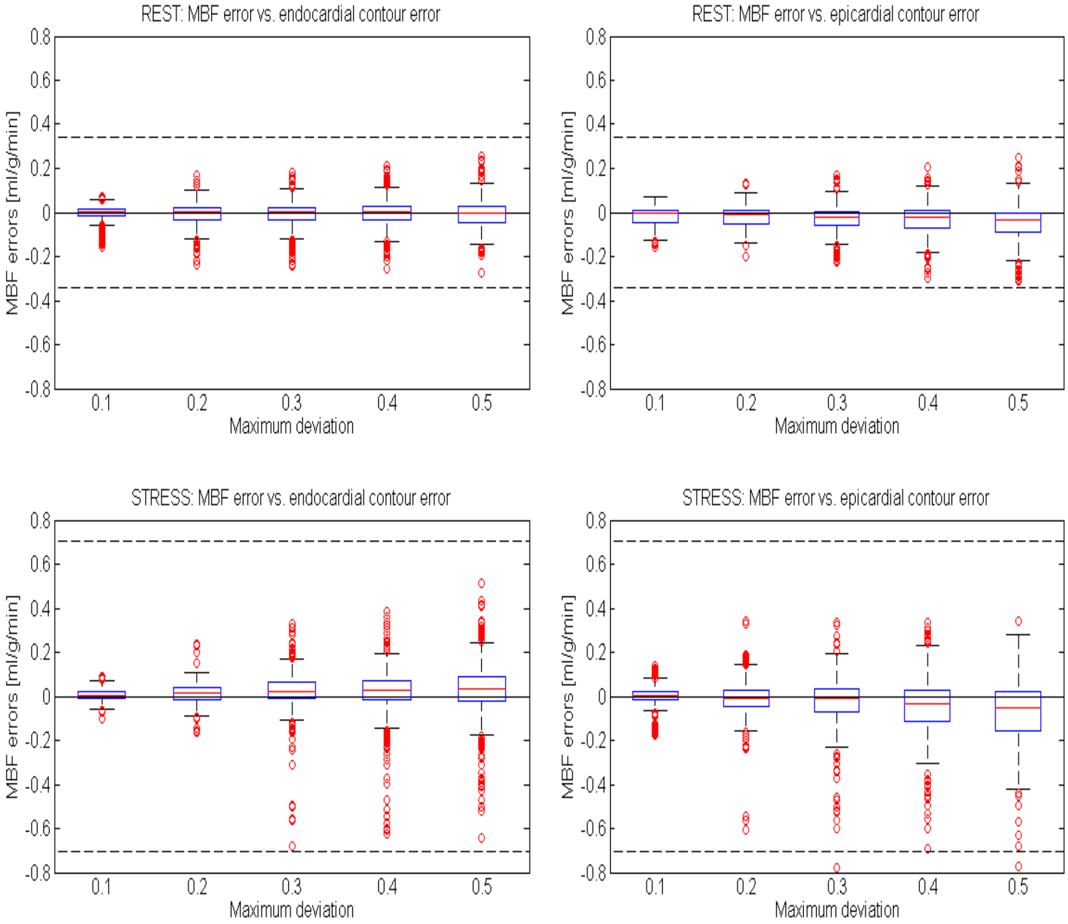

Figure 7-6 - Box-plots of MBF errors versus MD (expressed as a fraction of the mean myocardial width) for random contour errors in the rest endocardial contour (top left), rest epicardial contour (top right), stress endocardial contour (bottom left) and stress epicardial contour (bottom right). Lines, box edges and whiskers of each box-plot correspond to the median, inter-quartile range and 95% percentile range of MBF errors respectively. The dashed black lines depict ± one standard deviation of the MBF values obtained with the manual contours.

Mean myocardium. Figure 7-6 shows the effect of the random contour errors on MBFs estimated over the entire myocardium. Each box-plot represents MBF errors incurred using contours whose random deviations were limited to the given MD on the *x*-axis. The central line, box and whiskers correspond to the median, interquartile range and 95% percentile range respectively. *F*-tests and *t*-test for differences in variance and mean MBF error between manual and modified contours were non-significant *($p > 0.05$)* in all cases except a MD of 0.5MW in the resting epicardium (*t*-test: $p = 0.03$). At stress an MD of 0.5MW in the myocardium approached statistical significance (*t*-test: $p = 0.07$).

Region (corresponding artery)	**Rest / Stress**	**Endo / Epi**	**MD (MW)**	**Test**	**p-value**
Anterior (LAD)	Stress	Endo	0.5	*F-test*	0.04
Anterior (LAD)	Stress	Epi	0.5	*t-test*	0.04
Inferolateral (LCX)	Stress	Endo	0.5	*F-test*	<0.01
Inferior (RCA)	Rest	Endo	0.5	*F-test*	0.05
Inferior (RCA)	Rest	Epi	0.4	*t-test*	0.04
Inferior (RCA)	Stress	Epi	0.5	*t-test*	0.02
Inferoseptal (RCA)	Stress	Epi	0.5	*t-test*	0.02
Anteroseptal (LAD)	Rest	Epi	0.5	*t-test*	0.02
Anteroseptal (LAD)	Rest	Epi	0.2	*F-test*	<0.01

Table 7-2 - Table of statistically significant MBF errors generated by random contour errors considering the six myocardial regions. MD corresponds to the maximum deviation at which MBF errors became significant. Cases where significant *($p < 0.05$)* differences were not observed are not shown.

Regional myocardium. The effects of random contour errors on MBF in the six separate myocardial regions showed similar trends to Figure 7-6, with the spread of MBF errors increasing with MD. Figure 7-7 shows the interquartile ranges for each region at each MD value for all the contours. Statistically significant results are shown in

Table 7-2.

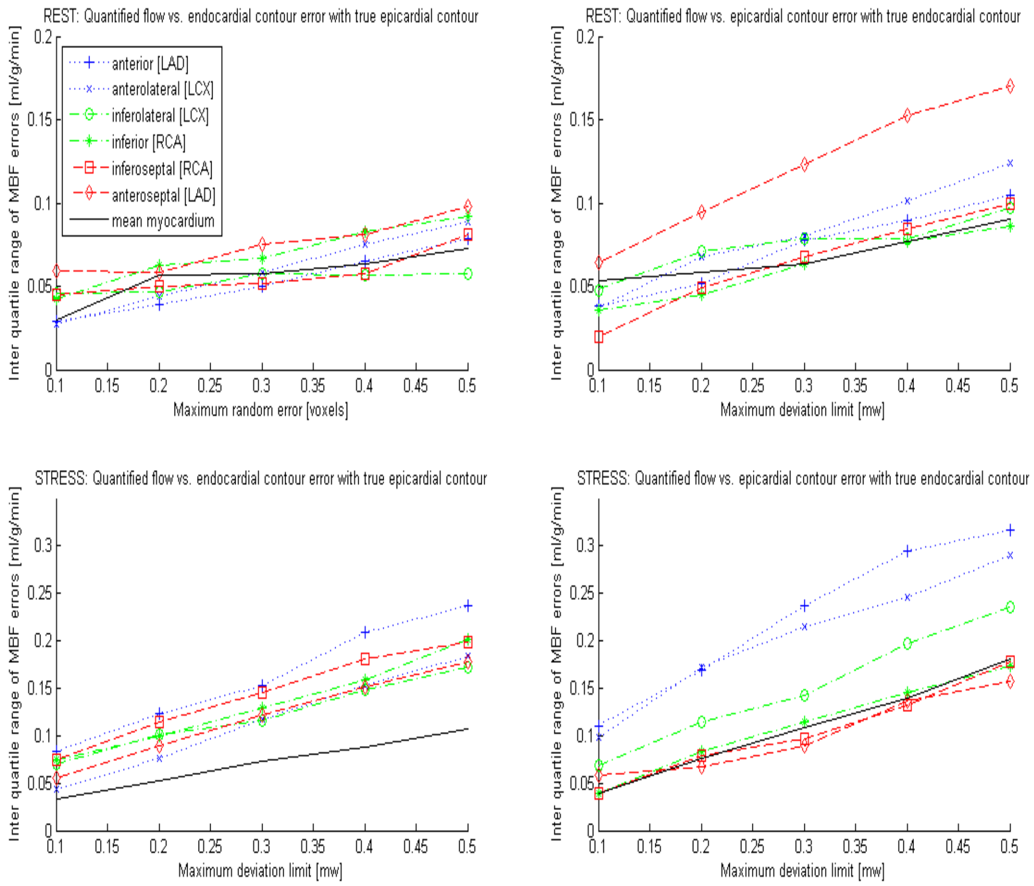

Figure 7-7 – Interquartile range of MBF error for each myocardial region plotted against MD (expressed as a fraction of the mean myocardial width) for random contour errors in the rest endocardial contour (top left), rest epicardial contour (top right), stress endocardial contour (bottom left) and stress epicardial contour (bottom right).

Endo- and epicardium. Considering the endocardium and epicardium as two separate regions showed similar trends with a more dramatic increase in the spread of MBF values with increasing MD. The corresponding interquartile range plots are shown in Figure 7-8 and all statistically significant differences in mean (*t*-test) and variance (*F*-test) of MBF errors are reported in Table 7-3.

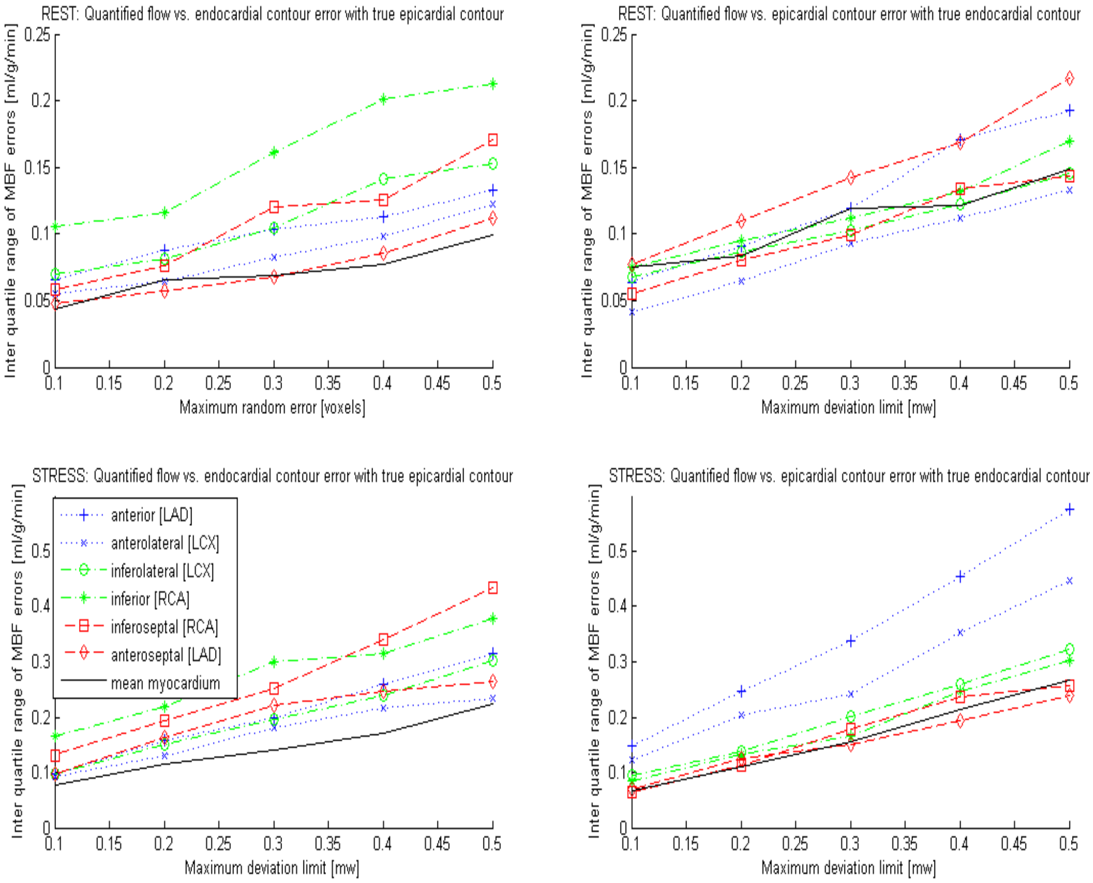

Figure 7-8 - Interquartile range of MBF error for each myocardial region divided into endocardial and epicardial segments versus MD (expressed as a fraction of the mean myocardial width) for random contour errors in the rest endocardial contour (top left), rest epicardial contour (top right), stress endocardial contour (bottom left) and stress epicardial contour (bottom right).

Region	**Rest / Stress**	**Endo / Epi**	**MD (MW)**	**Test**	**p-value**
Anterior(LAD)	Stress	Epi	0.5	*t-test*	<0.01
Anterior(LAD)	Rest	Epi	0.4	*F-test*	0.02
Anterior(LAD)	Stress	Endo	0.4	*F-test*	0.02
Anterior(LAD)	Rest	Endo	0.5	*F-test*	0.03
Anterolateral (LCX)	Rest	Endo	0.4	*F-test*	0.02
Anterolateral (LCX)	Stress	Epi	0.4	*F-test*	0.04
Inferolateral (LCX)	Rest	Endo	0.3	*t-test*	0.04
Inferolateral (LCX)	Rest	Endo	0.3	*F-test*	0.05
Inferolateral (LCX)	Stress	Endo	0.4	*F-test*	<0.01
Inferior (RCA)	Stress	Epi	0.4	*t-test*	0.02
Inferior (RCA)	Rest	Endo	0.5	*t-test*	0.01
Inferior (RCA)	Rest	Epi	0.5	*t-test*	0.05
Inferior (RCA)	Stress	Endo	0.5	*t-test*	0.01
Inferior (RCA)	Stress	Endo	0.4	*F-test*	0.04
Inferior (RCA)	Rest	Endo	0.5	*F-test*	<0.01
Inferoseptal (RCA)	Stress	Endo	0.3	*t-test*	0.05
Inferoseptal (RCA)	Stress	Endo	0.4	*F-test*	0.04
Anteroseptal (LAD)	Rest	Epi	0.2	*t-test*	0.02
Anteroseptal (LAD)	Stress	Endo	0.5	*t-test*	0.01
Anteroseptal (LAD)	Rest	Epi	0.1	*F-test*	0.01
Anteroseptal (LAD)	Stress	Endo	0.3	*F-test*	0.01
Mean	Rest	Epi	0.5	*t-test*	0.03
Mean	Stress	Endo	0.5	*t-test*	0.05
Mean	Stress	Endo	0.4	*F-test*	0.04
Mean	Rest	Endo	0.5	*F-test*	0.01

Table 7-3 - Table of statistically significant MBF errors generated by random contour errors considering the endocardium and epicardium separately. MD corresponds to the maximum deviation at which MBF errors became significant. Cases where significant *(p* $\leq$0.05*)* differences were not observed are not shown.

7.3.4. Inter- and intra-observer variability to validate contour error simulations

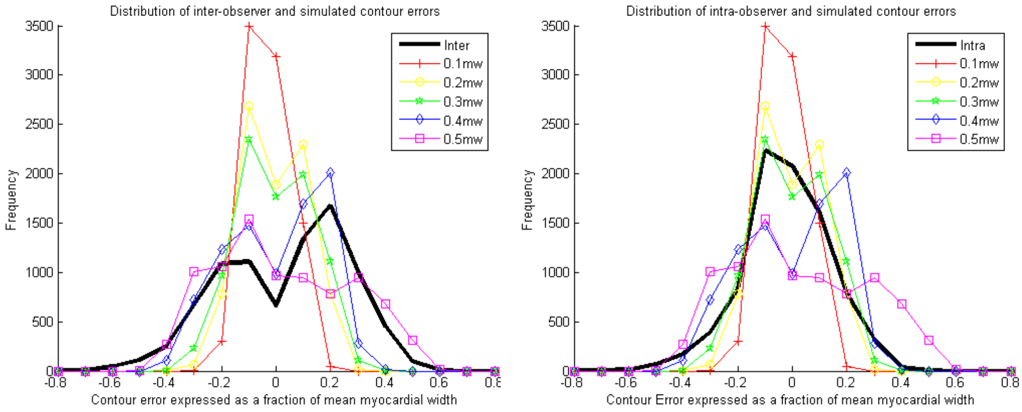

a) b)

Figure 7-9 - Distribution of inter-(a) and intra-(b) observer contour errors (thick black lines). The corresponding distributions of contour errors between manual and simulated contours at each MD setting are also shown (thin coloured lines).

Figure 7-9(a) shows the distribution of contour errors between the manually drawn contours of the first and second observers (inter-observer) and the distribution of random contour errors between the simulated and manual contours for each MD. Kolmogorov–Smirnoff tests between each simulated distribution and the inter-observer distribution yielded the following p-values: 0.1MW($p = 0.01$), 0.2MW($p = 0.08$), 0.3MW($p = 0.08$), 0.4MW($p = 0.38$) and 0.5MW($p = 0.93$). Figure 7-9 (b) shows the corresponding distribution for the repeated manually drawn contours (intra-observer). Kolmogorov–Smirnoff tests between the simulated distributions and the intra-observer distribution yielded the following p-values: 0.1MW($p = 0.03$), 0.2MW($p = 0.19$), 0.3MW($p = 0.19$), 0.4MW($p = 0.67$) and 0.5MW($p = 0.93$). Figure 7-9 includes contour errors from stress and rest, and endo- and epicontours all together. The separate analyses of each of these four cases for inter and intra-observer distributions are shown in Figure 7-10 and Figure 7-11 respectively yielding non-significant ($p < 0.05$) Kolmogorov–Smirnoff tests in all cases.

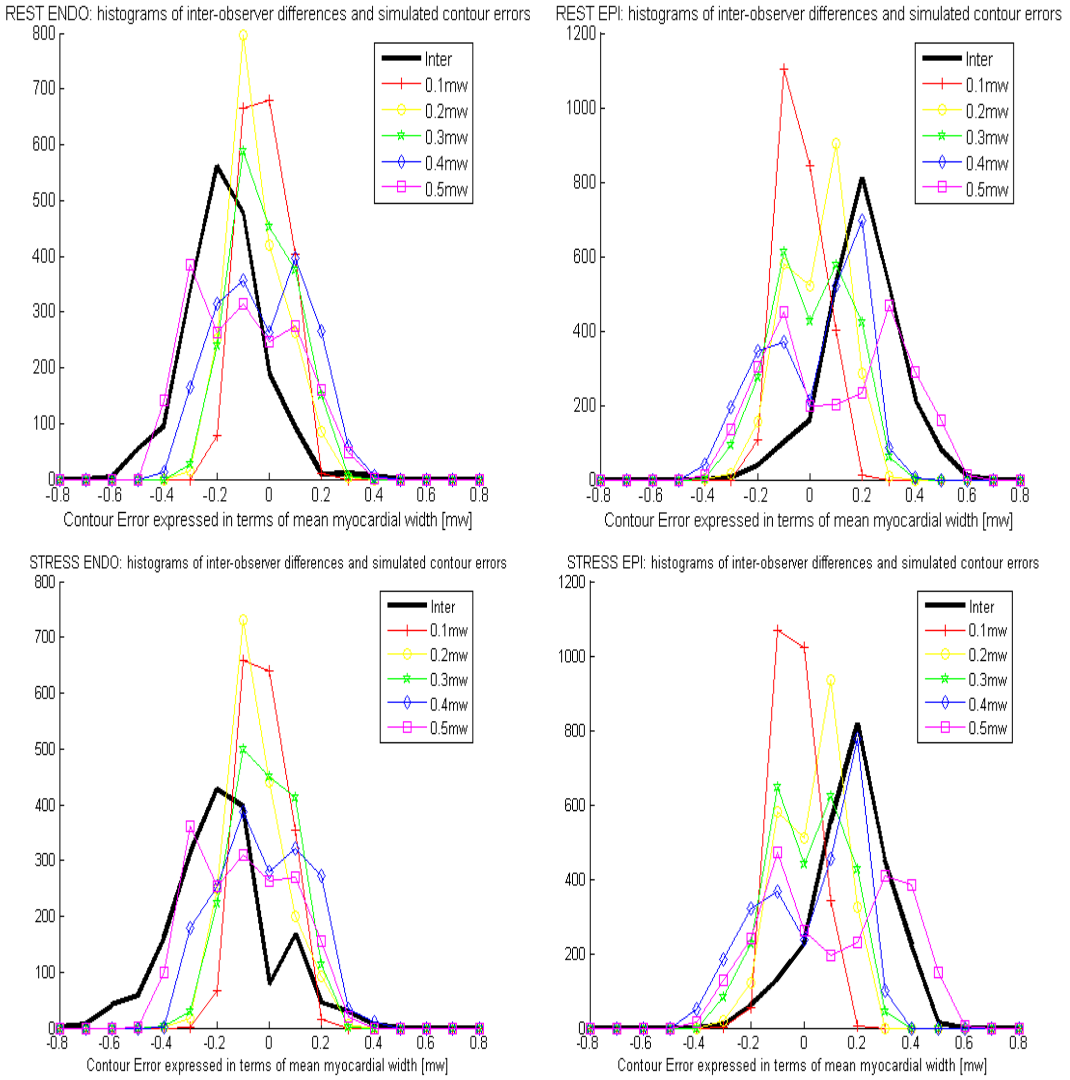

Figure 7-10 - Distribution of inter observer contour errors (thick lines) for the rest endocardial contour (top left), rest epicardial contour (top right), stress endocardial contour (bottom left) and stress epicardial contour (bottom right). The corresponding distributions of contour errors between manual and simulated contours at each MD setting are also shown (thin lines).

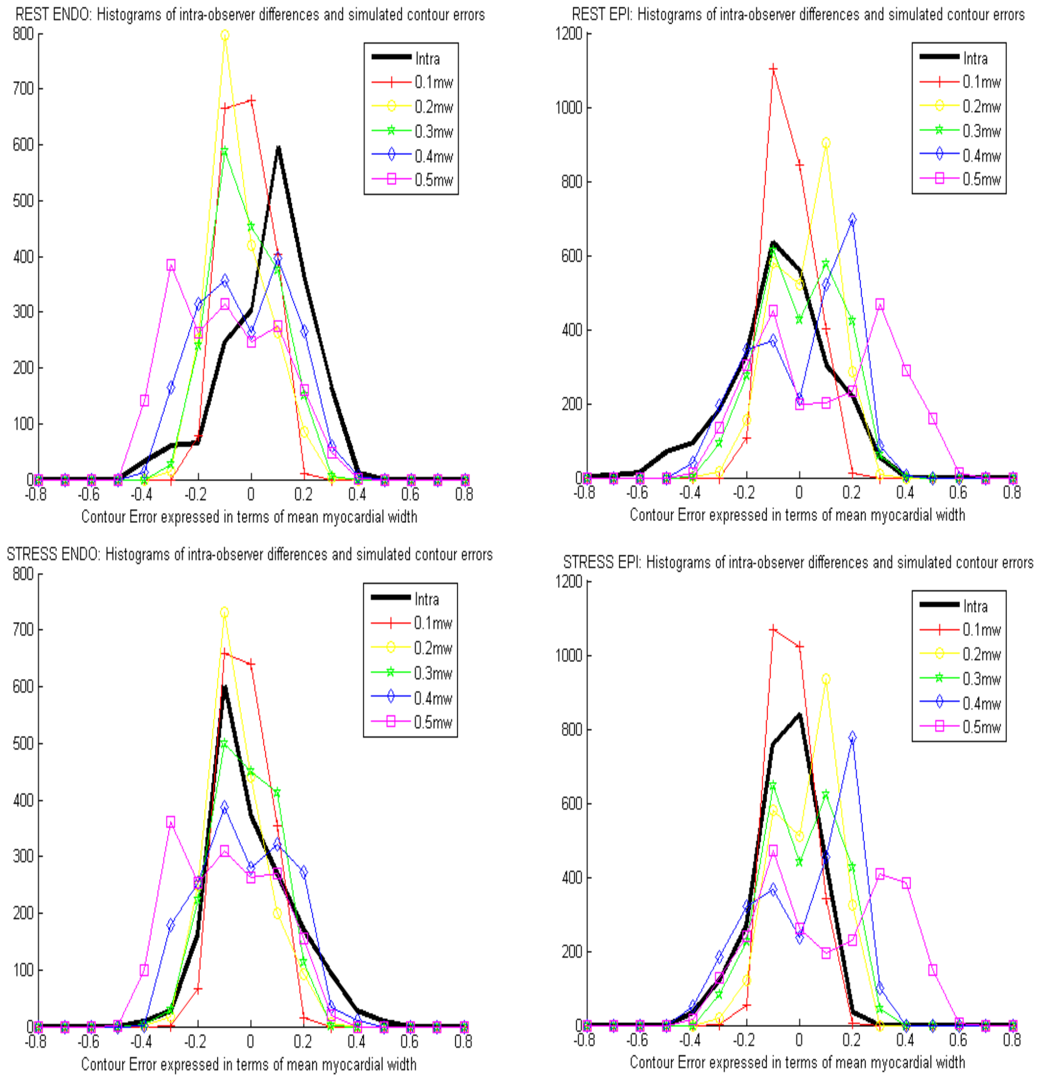

Figure 7-11 - Distribution of intra observer contour errors (thick lines) for the rest endocardial contour (top left), rest epicardial contour (top right), stress endocardial contour (bottom left) and stress epicardial contour (bottom right). The corresponding distributions of contour errors between manual and simulated contours at each MD setting are also shown (thin lines).

7.4. Discussion

Using the manual contours the mean (± standard deviation) MBF at rest was 1.24 ± 0.35 ml/g/min and at stress was 3.48 ± 0.67 ml/g/min, which is consistent with other studies measuring MBF in healthy volunteers, e.g (4).

7.4.1. Segmentation metrics

None of the segmentation metrics considered correlated with MBF error for the random contour error simulation. In the light of the results from the systematic contour error simulations this result is not surprising. A given contour error may correspond to a movement of either the endocardial or epicardial contour into any of a variety of surrounding tissues, depending on the position of the error along the myocardial circumference, with conflicting effects on MBF. The conclusion is that neither MBF error nor segmentation alone is an adequate measure of contour error as there are too many conflicting factors affecting the relationship between these two measures. Thus, if contour errors are random in nature then analysis in terms of MBF error may only show an increase in the variance of the MBF errors, with insignificant changes in the mean MBF. This could lead to misleading claims about the accuracy of an automated algorithm. If the algorithm produces contour errors of a systematic nature then measures of MBF error may be correlated with segmentation error, as described in Figure 7-3. However the relationships between contour error and MBF shown are not linear and it is unlikely that an algorithm would induce systematic errors as uniformly as those simulated here. Therefore, contouring algorithms for DCE-MRI myocardial perfusion should ideally be evaluated by both geometric segmentation metrics and in terms of MBF.

7.4.2. Systematic contour errors

The application of systematic contour errors to the dataset is useful for understanding how MBF errors vary depending on which contour (endocontour/epicontour) has moved and which direction it has moved in. They also serve to simulate systematic conservative or generous contouring. A given contourer may be overly concerned with avoiding non-myocardial voxels or conversely including all myocardial voxels thereby making this type of systematic error. Indeed the inter-observer contour error distribution reported in this study Figure 7-9 (a) suggests a systematic difference in contours between observers of this type. It is conceivable that such global contour errors could occur with automated contouring algorithms as well. For example, active contour-based methods with non-ideal stopping functions may generate consistent global over or underestimates in the contour, and an active appearance model driven method such as (144) will be as conservative as the manual dataset on which it is trained.

Global myocardium, systematic errors

Considering the whole myocardial region systematic contour errors of up to half the mean myocardial width did not yield statistically significant errors in MBF, Figure 7-3. Systematic trends in MBF error were seen as the contours were modified. These trends can be explained in the light of previously observed physiological flow properties of the myocardium. Animal studies have measured the presence of a transmural MBF gradient across the resting myocardium favouring the endocardium, which was no longer observed under stress conditions (77,151,152) and these observations have been confirmed in humans (79) including work based on the dataset used in this study (108). In the light of these observations the trends in Figure 7-3 can be explained as follows:

Variation of endocardial contour at rest. The MBF error increases with negative contour error (as defined in Figure 7-2 a)) as the endocardial contour encroaches on the voxels within the left ventricular blood pool. Rapid signal enhancement in the left ventricular blood pool causes MBF overestimation (i.e. positive MBF error) when blood voxels are incorporated into the myocardial ROI. With positive contour error, endocardial voxels, with high MBF relative to the epicardium are excluded; thus, the relative flow decreases and the MBF error becomes negative.

Variation of epicardial contour at rest. Negative contour errors cause an increase in MBF error as the relatively low MBF epicardial voxels are excluded from the myocardial region. Positive contour errors will incorporate non-myocardial voxels of zero signal enhancement (thus zero MBF) into the region, thus reducing MBF and causing negative MBF errors.

Variation of endocardial contour at stress. As seen at rest the negative contour errors increase the MBF error due to the incorporation of blood voxels into the myocardial ROI. At MD values greater than −0.2MW this effect is not apparent, which may be due to conservative contouring by the manual contourer. There is a clear increase in MBF error with positive endocontour errors which implies a reverse transmural MBF gradient (with the epicardium more highly perfused than the endocardium). As the endocardial contour encroaches on the myocardium, the low MBF voxels in the endocardium are excluded, thus increasing the MBF error.

Variation of the epicardial contour at stress. As at rest positive contour errors reduce MBF error. There is also a reduction in MBF error with negative contour error which is further evidence for a reverse transmural MBF gradient at stress causing negative MBF errors as the higher MBF voxels in the epicardium are excluded.

Whereas the presence of a resting transmural MBF gradient is accepted, there is conflicting evidence for the presence of a transmural flow gradient at stress. Lee et al. (79) observed no such gradient in healthy myocardial tissue at stress, but Christian et al. (77) observed a transmural (epi > endo) gradient at stress that was statistically significant in canines. Such a reverse MBF gradient may be a genuine physiological phenomenon or may be due to measurement errors inherent in the acquisition or analysis. A possible explanation might be the inclusion of endocardial dark rim artifacts in the myocardial region of interest, which could null the endocardial MBF values thereby generating the observed gradient.

Regional myocardium, systematic errors

A measurement of the global MBF is of limited use in investigating coronary artery disease, which induces localized flow defects. The American Heart Association (AHA) model (106) partitions the mid-myocardial slice into six circumferentially equidistant regions that are associated with specific coronary arteries, enabling the link between the perfusion imaging result and the required intervention (see section 8.5). The transmural variation in MBF between endocardial and epicardial tissue has also been shown to be related to arterial stenosis (79); therefore, it is important to consider the effect of contour errors on this further partitioning of the myocardium. For these reasons the myocardial regions were also divided into the 12 partitions illustrated in Figure 7-2(b). In general the six region curves followed the same general trends as those for the whole myocardium with some notable exceptions. At rest positive epicardial contour errors for the anteroseptal segment yielded positive MBF errors, opposing the general trend across the rest of the myocardium of negative errors. This is due to the inclusion of blood voxels in the right ventricle directly adjacent to this myocardial segment, which exhibit rapid signal enhancement. The effect is less apparent on the corresponding stress plot because the relative effect of the right ventricular voxels is reduced with respect to the higher genuine myocardial MBF at stress. At stress, the contour errors pushing the contours inside the myocardium (i.e. negative epicontour errors and positive endocontour errors) appear to effect the anterior segments more profoundly than the remaining segments. There is no reason to expect a stronger transmural gradient in the anterior myocardium so this observation is unexplained. In general, the trends observed in the mean myocardial data are somewhat obscured, either by errors in the measurement process, which is to be expected due to poorer SNR in the smaller segments, or by genuine heterogeneity of MBF gradients around the myocardium. Regional analysis of systematic errors, Figure 7-4, showed non-significant MBF errors except for the inferoseptal segment where a resting epicardial MD of 0.5MW gave ($p = 0.05$) and a stress endocardial MD of −0.5MW gave ($p = 0.02$); thus, a tolerance level of MD = 0.4MW would avoid significant errors in MBF when regional subdivisions are employed.

Endo and epicardium, systematic errors

After further subdivision into endocardial and epicardial layers was made (Figure 7-1 (b)), significant errors in more segments at MD = ±0.5MW were seen. This is due to the greater percentage effect of a given voxel offset on the ROI. A tolerance of MD = 0.3MW was required to avoid all significant MBF errors with the most susceptible region being the epicardial inferior segment at rest which exhibited significant MBF errors at MD = 0.4MW ($p = 0.04$).

Recommendations, systematic errors

These results suggest that systematic errors limited to an MD of 0.3 times the mean myocardial width will not incur a statistically significant MBF error, even with a 12 partition myocardium. Generally, the largest MBF errors were seen when the contours passed outside of the myocardium, either epicardially or endocardially; thus, conservative contouring is preferable to generous contouring for healthy volunteers. Where possible, segmentation algorithms should err on the side of placing the endocardial contour within the myocardium. However, in ischaemic patients with subendocardial abnormalities, the placement of the subendocardial contour may be more critical than these volunteer based results suggest for diagnosing ischaemia.

7.4.3. Random contour errors

Global myocardium, random errors

The box-plots in Figure 7-6 illustrate how the spread of MBF errors increases with MD. For a random contour error applied to a linear MBF error space, one would expect the median MBF error to remain at zero independent of the size of the contour error. However, as the MBF is not linear (Figure 7-3), the median MBF error deviates from zero with increasing MD (Figure 7-6). This did not cause a statistical shift in mean MBF up to contour errors of 0.4MW. The increase in spread of MBF values with contour error is expected but *F*-tests did not show this to be significant even at 0.5 of the mean myocardial width and the 95% confidence interval for MBF errors did not exceed the one standard deviation line of ‘true’ MBFs up to MD = 0.5MW. This shows that the simulated contour errors did not induce a statistically significant change in the distribution of MBFs implying that the variance induced in MBF estimates from the simulated contour errors is not significant compared to the natural variance of MBF within the healthy population. A statistically significant effect was seen for MD = 0.5MW in the resting epicardium (*t*-test: $p = 0.03$). This is predominantly caused by the effect of the epicardial contour bleeding into the right ventricular blood pool as is clarified by the segmental analysis. These results suggest that a safety tolerance of MD = 0.4MW would be acceptable for the analysis of MBF in the global myocardium.

Regional myocardium, random errors

Regional analysis of the myocardium (Figure 7-7) yielded similar trends in the spread of MBF errors to Figure 7-6 with the spread in MBF error increasing more severely with MD than in the mean myocardium due to the more profound effect a given contour error has on smaller ROIs. In general, statistically significant MBF errors were avoided by setting a tolerance of MD $\leq$ 0.3MW (

Table 7-2). The exception was the anteroseptal segment for which statistically significant changes in the variance of the MBF error distributions were seen for the resting epicardium for MD = 0.2MW (*F*-test: $p < 0.01$). Bleeding of the epicardial contour into the right ventricular blood pool incorporates voxels with rapid signal enhancement (due to fast flowing blood in the right ventricle) into the myocardial ROI incurring severe changes in estimated MBF. At stress, the genuinely higher MBF obscures the effect of the right ventricular voxels and a significant effect is not observed. These results suggest that a safety tolerance of MD = 0.3MW would be acceptable for regional analysis of MBF in the healthy myocardium, excluding the anteroseptal segment of the resting epicardium, which requires an accuracy of MD = 0.1MW.

Endo and epicardium, random errors

Considering the endo- and epicardium as separate regions the spread of MBF error increases more rapidly again with increasing MD due to the further decrease in ROI size (Figure 7-8). A tolerance of MD $\leq$ 0.2MW is now required to avoid significant MBF errors, excepting the anteroseptal segment which sees significant effects even at MD = 0.1MW in the resting epicardium (*F*-test $p = 0.01$). Considering the mean endocardium and mean epicardium, a tolerance of MD $\leq$ 0.3MW is sufficient to avoid significant MBF errors.

Recommendations, random errors

For a global analysis a tolerance of 0.4MW is adequate. For regional analysis MD $\leq$ 0.3MW is required and if further subdivision into endocardial and epicardial regions is to be carried out MD $\leq$ 0.2MW is required. For any of the regional analyses the epicardium in the septal regions requires an even higher accuracy ($\leq$0.1MW) and conservative contouring is recommended to avoid the right ventricular blood pool.

7.4.4. Inter- and intra-observer variability to validate contour error simulations

Contour errors were required to be random, in the absence of knowledge of any more systematic form of error population, whilst maintaining a smooth circular form, as one would not expect a manual contourer to deliberately generate sharp corners or high frequency oscillations in the contour. To assess whether the simulated contour errors were representative of human contour errors, the simulated error distributions were compared with inter- and intra-observer contour error distributions as shown in Figure 7-9 (a) and (b) respectively. The simulated distributions of contour errors were similar to both the inter- and intra-observer empirically observed distributions. Visually the 0.4MW and 0.5MW MD simulations best matched the inter-observer variability , with the closest agreement to the intra-observer distribution being the 0.2MW and 0.3MW MD simulations. The Kolmogorov–Smirnoff test results confirmed this observation showing that there is insufficient evidence to reject the null hypothesis that the inter/intra-observer contour errors were drawn from the same underlying distribution as the simulated contour errors for all MD values except in the MD = 0.1MW case. This result was maintained when the separate stress, rest, endocontour and epicontour distributions were analysed (Figure 7-10 and Figure 7-11).

The inter-observer variation in contour errors was broader than that of intra-observer variation. This is unremarkable as one would expect separate observers to disagree more than a single observer reproducing his/her contours. The bimodal shape of the inter-observer contour error distribution was due to one of the observers being consistently more conservative in their contouring. This is evident when the endo- and epicontour distributions are considered separately. Figure 7-10 shows a negative bias in the endocardial inter-observer distribution and a corresponding positive bias in the epicardial distribution, consistent with a systematic difference between the two contourers.

7.4.5. Limitations

This study has been carried out on healthy volunteers only. The inclusion of ischaemic patients, whose MBF is compromised, would incorporate a confounding factor into the data. Contour error limits have been recommended under which healthy MBF estimates do not vary significantly. The effect of such errors on ischaemic patients has not been investigated and the tolerances required there may differ.

MBF varies between systole and diastole (128). To exclude this complicating factor from the study, only systolic images were analyzed. The systolic myocardium is thicker and thus easier to contour, thus providing a more trustworthy contour reference standard. The contour accuracy required for analyzing diastolic data, where the myocardial wall is thinner, may be higher. Thus, strictly speaking, the conclusions of this investigation should only be applied to systolic data. However, the contour errors and recommended tolerances in this study have been expressed as a fraction of the mean myocardial width (MW). There is no reason why such tolerances may not be applied to diastolic data if the distribution of myocardial widths around the myocardial circumference can be assumed to be similar in diastole and systole.

Manual contouring allowed only for rigid translations in the motion correction step, which is consistent with clinical practice at the institution where the data was acquired. The inherent assumption here is that there is no rotational or in-plane motion of the heart, which may not be true during breathing motion. However, as breathing motion has been minimized over the first-pass by the adopted breath-holding strategy, the errors induced due to this assumption should be minimal. The alternative approach of manually contouring each image in the dynamic series is much more time consuming and is difficult in low contrast images, where the myocardium and surrounding tissues can be indistinguishable. There is no reason therefore to suppose that the method used in this study incurs worse errors than a method incorporating an independent contour for each time step.

Contour errors have been simulated by allowing random variations evenly around the contour and it has been shown that these simulations generate a similar distribution of contour errors to inter- and intra-observer variability distributions. It may be the case that contour errors are more likely over certain regions (e.g. where there are more poorly defined edges) than others; thus, an even distribution of random contours is not the best simulation.

The implementation presented here of the method proposed by (30,31) to convert signal intensities to concentrations has two important limitations. Firstly, the method was originally validated for an inversion recovery sequence (29,30). Although the adaptation of the method to a saturation recovery sequence is mathematically simple, the method has not been separately validated for this sequence. Secondly, the method was originally based on measured T_1 values. The use of an assumed T_1 for blood may introduce errors in to the MBF estimation process. Extensive phantom work to validate this method has been undertaken in (chapter 6). However in-vivo validation has not been performed. Nevertheless, as this study is interested in relative changes in MBF due to contour errors it is unlikely that any errors in the conversion to concentration would modify the conclusions of this study.

7.5. Conclusion

Myocardial contour errors have been simulated for estimation of MBF. The relationships between segmentation error and MBF error have been described and explained in terms of cardiac physiology in healthy volunteers. Based on the simulated errors in MBF, contour error tolerance limits have been recommended as guidance limits for manual and automated myocardial contouring protocols.

The contour error evaluation metrics considered did not correlate with random MBF errors; thus, neither measure fully evaluates whether the contours are fit for purpose. Ideally, contouring algorithms for DCE-MRI myocardial perfusion should be evaluated by both geometric segmentation metrics and in terms of MBF error. Comparisons between segmentation algorithms evaluated with segmentation evaluation metrics and those evaluated in terms of MBF error are not possible unless the segmentation errors are systematic in nature.

8. Comparisons of methods for diagnosing coronary artery disease using quantitative perfusion myocardial blood flow estimates

8.1. Introduction

The overarching aim of this thesis is to provide clinically persuasive evidence for a standard methodology for quantitative analysis of cardiac MR perfusion datasets. To this end chapter 9 asks the important question of which perfusion model performs best in terms of diagnosing ischaemic heart disease, and chapter 7 has contributed towards understanding the necessary accuracy of myocardial contours. This chapter is dedicated to the steps between generating the uptake curve and deducing a final diagnosis. These steps are usually simply stated in the methods sections of diagnostic performance CMR papers but the rationale behind them is by no means certain. This chapter aims to provide an evidence base for the analysis protocol utilised in chapter 9.

The dataset used for this and the following chapter is a carefully selected sub-set of the CE-MARC dataset. The rationale behind choosing this sub-set is described in section 8.2. Some uptake curves have been excluded from these investigations. The criteria for exclusion and the characteristics of the excluded cases are described in section 8.3. Non-linearity between signal and contrast concentration is of considerable concern to the DCE-MRI community and a method for correcting for these effects has been presented in this thesis (chapter 6). The impact on diagnostic performance of non-linearity effects is not often reported, although one study has been performed showing no improvement with linear over non-linear data (25). Section 8.4 investigates the effect of the non-linearity correction presented in chapter 6 on diagnostic performance. The correct methodology for interpreting the AHA segmentation described in section 3.4.11 is then considered. Should the AHA myocardial region to coronary artery mapping be used to provide a coronary artery specific diagnosis? What is the best way to summarize multiple regional myocardial territory MBF scores into a single value for the ROC curve? Does regional analysis add to the diagnosis? What diagnostic power is added by considering multiple slices over a single slice investigation? These questions are considered in section 8.5 before final recommendations for the analysis methodology to be used in the next chapter are made in section 8.6.

8.2. The CE-MARC sub dataset

In 2012 Greenwood et al. published the results of the CE-MARC trial (2), which is, at the time of writing, the largest, prospective evaluation of CMR for diagnosis of coronary heart disease. 752 patients underwent stress and rest CMR, as well as SPECT nuclear medicine imaging and X-ray angiography. The following investigations were conducted on a 50 patient subset of the CE-MARC cohort. This cohort was selected to have the same proportion of risk factors and disease states as the full CE-MARC dataset. The identified risk factors were hypertension, diabetes, smoking and age and the disease states were normal, single vessel disease, double vessel disease and triple vessel disease.

The reference standard against which CMR measurements were compared in this study was the consensus diagnosis (ischaemic or healthy) from quantitative X-ray angiography and nuclear medicine. Both of these methods are imperfect (see chapter 3) and there is ambiguity over the ideal cut-off for quantitative X-ray with some publications using a 50% stenosis cut-off (25,104) and others using a higher cut-off value (91,103,153). This generates an ambiguous range of cases (between 50% and 70% stenosis where the true diagnosis is uncertain. Some studies treat these cases as a separate stratification (91,103). These ambiguous cases are part of clinical reality and should be included in any investigation into the diagnostic capabilities of a measurement technique. However the purpose of this investigation was not to report the diagnostic accuracy of quantitative CMR but to compare different diagnostic methodologies. For this reason ambiguities were removed from the dataset to create as pure a reference standard as possible. A vessel was classed as healthy if quantitative X-ray angiography failed to find a stenosis $\geq$50% and the nuclear report was negative for a perfusion defect. A vessel was classified as ischaemic if quantitative X-ray angiography reported a stenosis $\geq$70% and the nuclear report was positive for a defect. Cases where there was disagreement between X-ray and nuclear medicine results and cases were the X-ray score was between 50% and 70% were excluded.

Healthy	No instance of stenosis $\geq$50%	Nuclear report negative for defect
Ischaemic	Any instance of stenosis $\geq$70%	Nuclear report positive for defect

Table 8-1 – Classification criteria for the 50 patient subset

8.3. The exclusion process for the CE-MARC sub-set

8.3.1. Method

The MR acquisition and manual contouring process for the CE-MARC dataset are described in sections 5.2.1 and 5.3 respectively. After manual contouring of the maximum contrast slice the contours were copied to all frames in the dynamic series and manually translated for each frame. Motion correction was limited to rigid translation for pragmatic reasons (in that drawing individual contours on each frame made an already time-consuming task prohibitively so), but also because the difficulty of drawing myocardial contours on the early and late low signal contrast frames may well have generated worse contour errors than those encountered using rigid translation only.

Rigid translation inherently assumes that all motion is in-plane motion, i.e. that there is no component of movement perpendicular to the imaging plane, which would alter the apparent size of the heart. It also assumes that the breathing responsible for the cardiac movement in the image is translational not rotational. Neither of these assumptions are consistently valid in CMR perfusion. These issues were not dealt with by the automated analysis software and in some cases uptake curves were generated that were clearly non-diagnostic, in the sense that the uptake curves were so badly affected by the resulting artifacts that they could not be expected to generate representative MBF values. For this reason every region in the study was viewed manually and uptake curves that were visually assessed to be non-diagnostic were manually excluded. In order to carry out this step a graphical user interface (GUI) called *Perfusion* was developed that enabled the image contours and uptake curve to be simultaneously evaluated and allowed manual adjustment of AIF and myocardial baseline, bolus arrival time and first-pass cut-off when necessary (Figure 8-1).

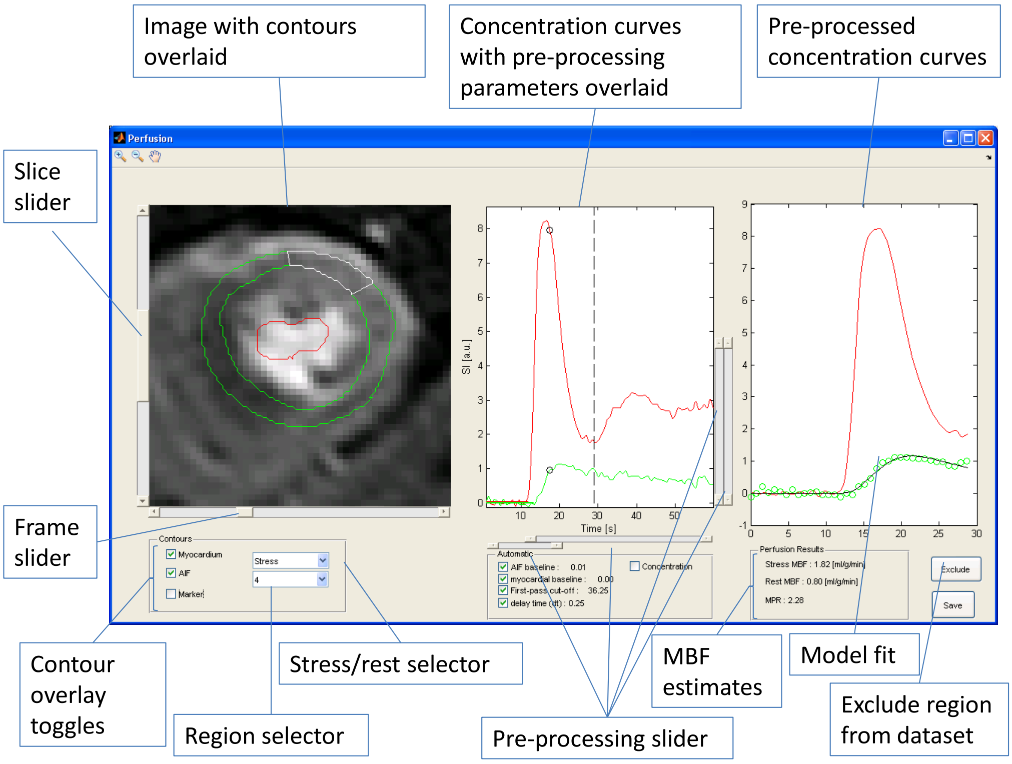

Contours

☑ Myocardium
☑ AIF
☐ Marker

Stress
4

Automatic

☑ AIF baseline : 0.01
☑ myocardial baseline : 0.00
☑ First-pass cut-off : 36.25
☑ delay time (dt) : 0.25
☐ Concentration

Perfusion Results

Stress MBF : 1.82 [ml/g/min]
Rest MBF : 0.80 [ml/g/min]
MPR : 2.28

Figure 8-1 – GUI allowing simultaneous viewing of stress and rest images, contrast uptake curves and estimated MBFs as well as manual adjustment of pre-processing parameters and an exclusion button to exclude the region if necessary

Regions were only excluded where the uptake curves that they generated were clearly non-diagnostic i.e. they could be confidently classified as not representing the uptake of contrast in the myocardium. Exclusions were categorized into the following categories:

- Thin myocardium (Figure 8-2).
- Left ventricular blood pool in the myocardial region (Figure 8-4).

- Right ventricular blood pool in the myocardial region.
- Other tissue (epicardial fat, lung) in the myocardial region (Figure 8-5).
- Severe change in apparent heart slice (Due to ECG-gating failure or breath-hold failure) (Figure 8-3).
- Dark rim artifact (DRA).

After contouring, the myocardium was divided into 16 regions according to the AHA guidelines (106) resulting in 32 regions per patient (rest and stress) giving a total of 1600 uptake curves for analysis in the study. Each of these curves were pre-processed before quantitative analysis was performed. All pre-processing was done using the automated algorithms described in section 5.4.

8.3.2. Results

A total of 164 out of the 1600 regions were excluded (10.3%). The reasons for exclusions are summarized in Table 8-2, classified as thin myocardium, LV in myocardial region, RV in myocardial region, other tissue in myocardial region, severe change in apparent heart size and dark rim artifact. The origins of the excluded regions, in terms of rest and stress scan and which slice are shown in Table 8-3.

Reason	**Thin myo**	**LV in myo region**	**RV in myo region**	**Other tissue in myo region**	**Severe change in apparent heart size**	**Dark rim artifact**	**Total**
No. of regions excluded (%)	97 (6.1%)	32 (2%)	1 (0.06%)	4 (0.25%)	28 (1.8%)	2 (0.1%)	164 (10.3%)

Table 8-2 – Table of reasons for exclusion from the CE-MARC subset

	STRESS			**REST**			**Total**
Slice	**1(apical)**	**2(mid)**	**3(basal)**	**1(apical)**	**2(mid)**	**3(basal)**	
No. of regions excluded (%)	19 (1.2%)	12 (0.75%)	52 (3.25%)	12 (0.75%)	10 (0.6%)	59 (3.7%)	164 (10.3%)

Table 8-3 – Table of exclusion positions from the CE-MARC subset.

8.3.3. Discussion

An exclusion rate of 10% is high, and the necessity for visual assessment of every region is a significant obstacle to the practicality of quantitative perfusion imaging. Considerable effort in the research community has been expended in attempting to automate the steps for quantitative myocardial perfusion, myocardial segmentation, curve pre-processing and tracer-kinetic modelling. This result highlights the need for a further area requiring automation. That of highlighting myocardial regions whose uptake curves are not valid.

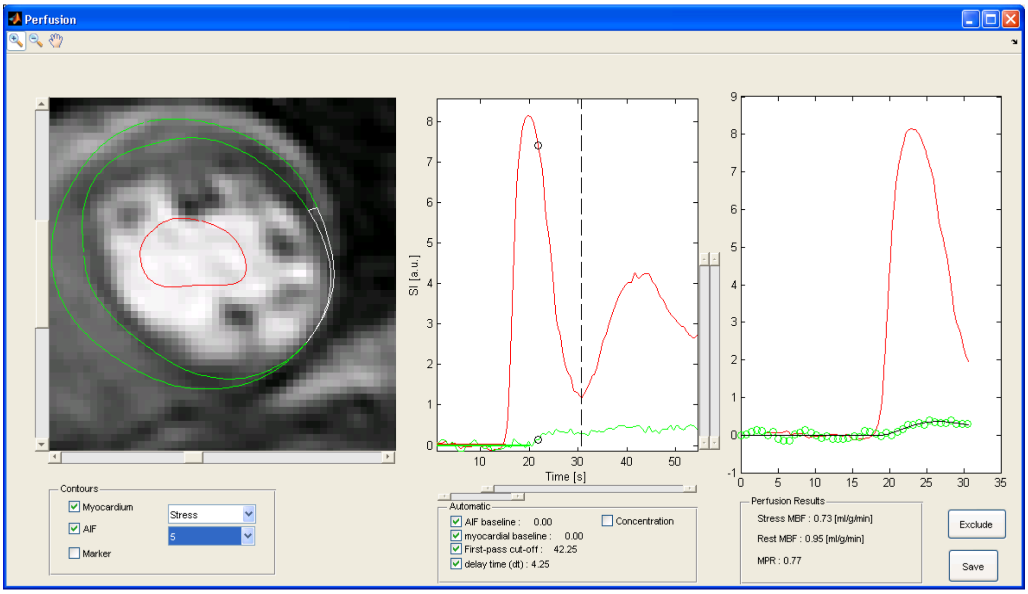

Contours
☑ Myocardium
☑ AIF
☐ Marker
Stress
5

Automatic
☑ AIF baseline : 0.00
☑ myocardial baseline : 0.00
☑ First-pass cut-off : 42.25
☑ delay time (dt) : 4.25
☐ Concentration

Perfusion Results
Stress MBF : 0.73 [ml/g/min]
Rest MBF : 0.95 [ml/g/min]
MPR : 0.77

Figure 8-2 – Example of an exclusion as displayed in the *Perfusion* GUI. Segments 5 (selected in the GUI) and 6 were excluded because the myocardium was so thin that the uptake curves were deemed non-myocardial.

The largest contribution to exclusions was a thin myocardium, which occurred most commonly in the basal slice. This is not surprising as the myocardium thins naturally in the basal region. The high number of exclusions here might be taken as an argument against imaging in the basal region however it is important to note that ~90% of the basal regions were not excluded. Continuing improvements in imaging resolution in myocardial perfusion (154) have the potential to reduce the impact of thin myocardial walls in quantitative perfusion in the future.

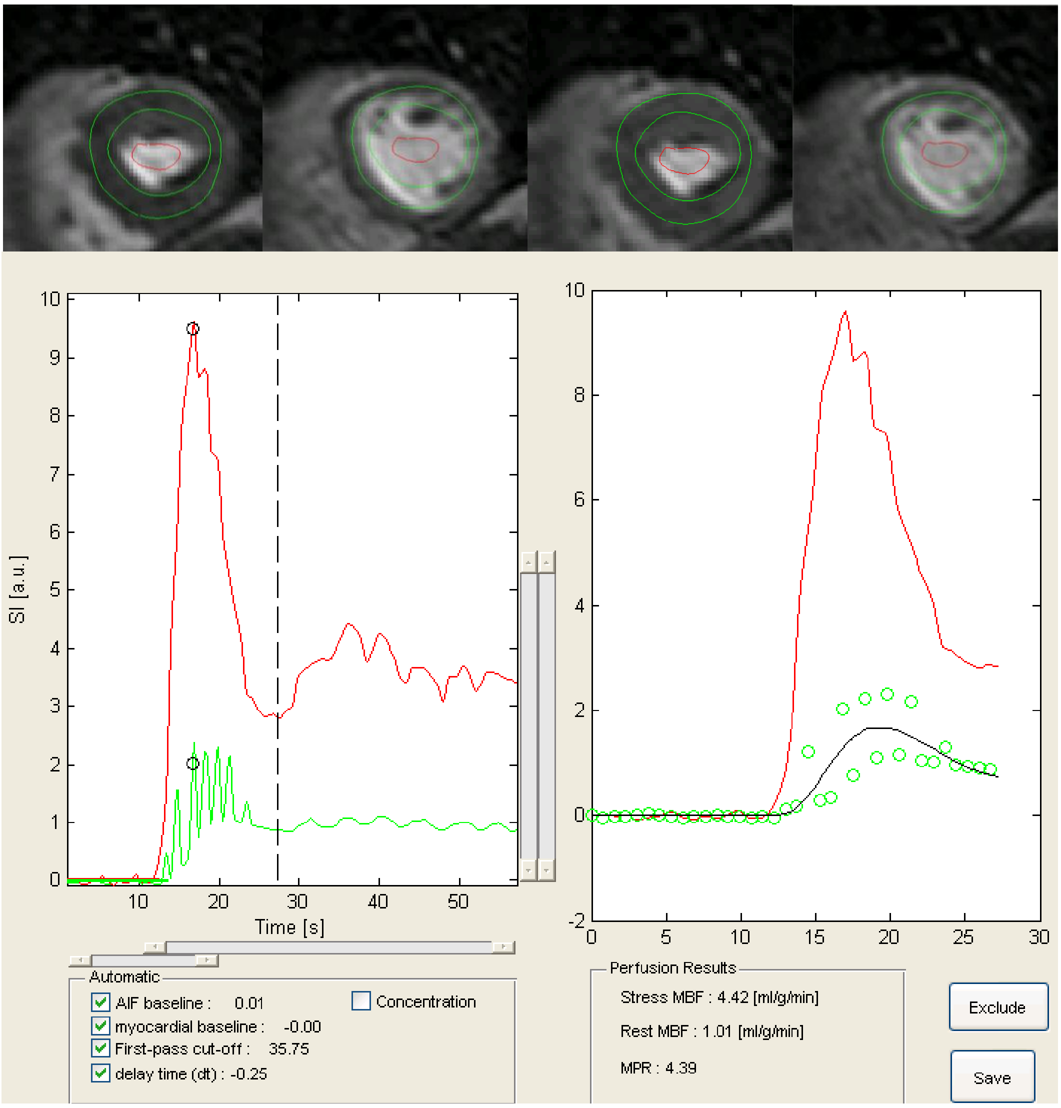

Automatic

☑ AIF baseline : 0.01

☑ myocardial baseline : -0.00

☑ First-pass cut-off : 35.75

☑ delay time (dt) : -0.25

☐ Concentration

Perfusion Results

Stress MBF : 4.42 [ml/g/min]

Rest MBF : 1.01 [ml/g/min]

MPR : 4.39

Figure 8-3 – Example of severe change in apparent heart size. A sequence of four contiguous dynamic frames show that these four images have been imaged at different cardiac phases due to an ECG-gating fault. No contour can satisfactorily be applied to all these images via translation only. The resulting affect on the myocardial uptake curves and perfusion model fit are illustrated below in the *Perfusion* GUI.

The next largest contributions were from LV blood volume bleed into the defined myocardial region and severe change in apparent heart size. Severe changes in apparent heart size are caused either by ECG triggering artifacts or by complete failure of patient breath-holding during the first pass. In the former case the scanning algorithm misreads the R-wave so that the image is acquired in a different cardiac phase and the shape of the heart is radically different. Within the ‘translation only’ contour regimen prescribed this renders it impossible for the contourer to satisfactorily contour the myocardium in every image and a saw tooth pattern emerges in the myocardial uptake curve, which generates significant errors in the model fit (Figure 8-3). In the case of breathing during the first-pass the patient's diaphragm moves relative to the imaging plane so that a different area of the heart is imaged. Similarly to ECG-triggering faults this renders images that are not possible to contour satisfactorily.

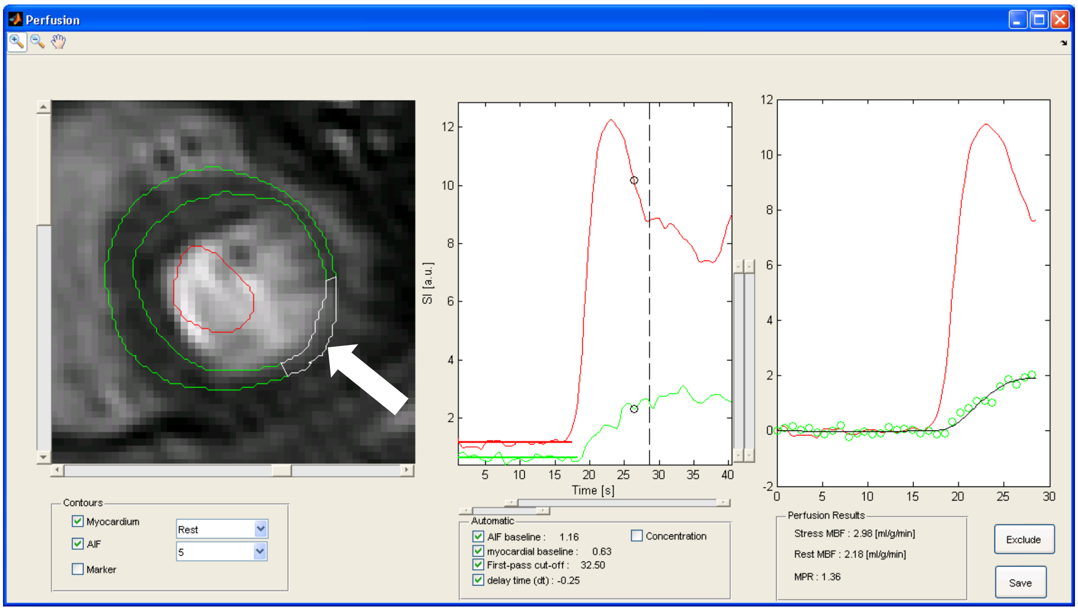

Contours
☑ Myocardium
☑ AIF
☐ Marker
Rest
5

Automatic
☑ AIF baseline : 1.16
☑ myocardial baseline : 0.63
☑ First-pass cut-off : 32.50
☑ delay time (dt) : -0.25
☐ Concentration

Perfusion Results
Stress MBF : 2.98 [ml/g/min]
Rest MBF : 2.18 [ml/g/min]
MPR : 1.36

Figure 8-4 – Example of the LV bleed. The highlighted region in the image shows blood pool enhancement bleeding into the myocardial region. The simultaneous enhancement in the AIF and myocardial uptake curves is unusual (usually AIF enhances first) and is probably due to LV blood in the myocardial region.

LV volume bleed occurs when the contours are allowed to encroach too far into the LV blood pool and the AIF 'bleeds' into the myocardial region. Figure 8-4 shows an example case. In the lateral posterior wall of the heart it is very difficult to distinguish any myocardial wall at all. Instead of allowing a very thin myocardium (as in Figure 8-2) this contourer has encroached on the LV blood pool in order to maintain a significant myocardial region. The resulting region is contaminated by the AIF, as evidenced by the early uptake in the myocardial uptake curve (simultaneous with the AIF enhancement point). Whichever choice the contourer had made this region would need to have been excluded from the study.

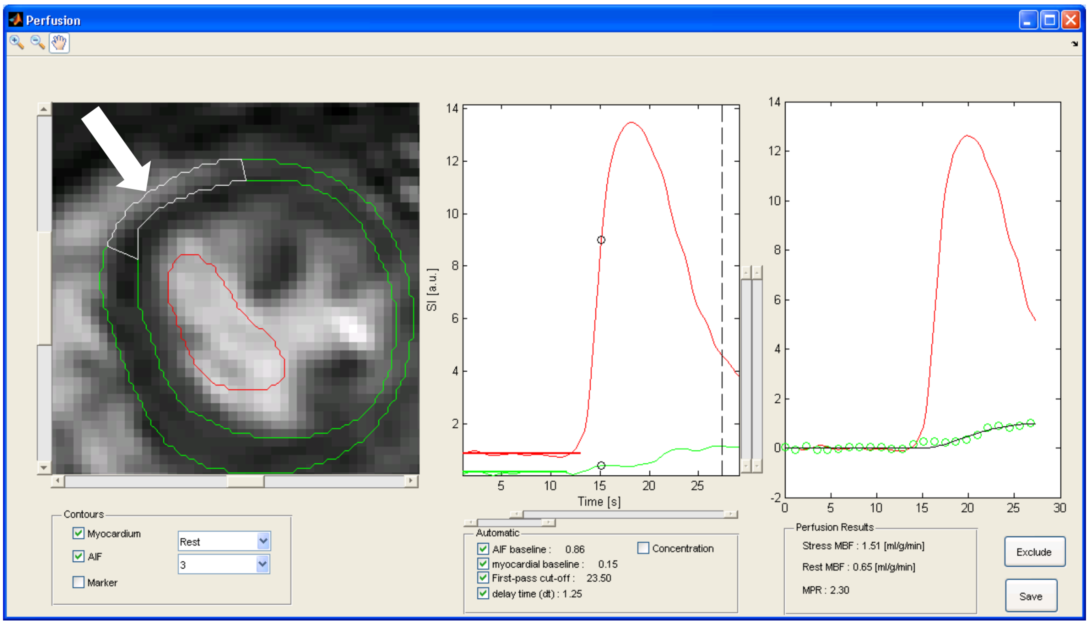

Contours
☑ Myocardium
☑ AIF
☐ Marker
Rest
3

Automatic
☑ AIF baseline : 0.86
☑ myocardial baseline : 0.15
☑ First-pass cut-off : 23.50
☑ delay time (dt) : 1.25
☐ Concentration

Perfusion Results
Stress MBF : 1.51 [ml/g/min]
Rest MBF : 0.65 [ml/g/min]
MPR : 2.30

Figure 8-5 – Poor contouring over the first pass placing segment 3 more in the epicardial fat than the myocardium. This segment did not represent the myocardium and was therefore excluded

Much less common was the inclusion of another tissue such as epicardial fat in the myocardium (Figure 8-5). This was due to contour errors which were generally forced by the contourer having to strike a compromise between the shape of the heart at the beginning and the end of the sequence.

The distribution of exclusions across the three slices was similar at rest and stress implying that there is no fundamental difference in exclusions between rest and stress. The high exclusion rate may be criticised in terms of the manual contouring method used and the qualitative nature of the exclusion process. The contouring method is imperfect in that it does not allow for through plane motion, or in-plane rotation, both of which occur in the dataset. However it is questionable whether a bespoke frame specific contouring would improve the contours, due to poor contrast to noise ratio at points during the dynamic sequence. Furthermore, in some cases it is apparent that, at this resolution, there is no possible contour that would give a meaningful uptake curve (e.g. Figure 8-2).

The qualitative nature of the exclusion method used here may be susceptible to poor reproducibility due to human error. The investigation would be improved if an automated basis for exclusion could be developed. The largest contribution to the exclusions is thin myocardium. This could be objectively calculated from the contours. Automating this exclusion criterion is therefore possible and will be included in future work. Other forms of error are more difficult to address and may be best approached by applying automated segmentation algorithms to reduce contouring error. However, existing segmentation algorithms tend to also present high exclusion rates so applying such algorithms may not ultimately reduce the exclusion rate.

8.4. Diagnostic evaluation of non-linearity correction

8.4.1. Introduction

Chapter 6 describes a method for converting CMR perfusion signal intensity values to concentrations. The CE-MARC sub-set described in section 8.2 provides an opportunity to assess this conversion in terms of the affect it has on the ability of a quantitative myocardial perfusion to diagnose ischaemic heart disease.

8.4.2. Method

Conversion to concentration

For this study the non-linear conversion method described in chapter 6 was compared to a conversion based on an assumed linear relationship between signal intensity and contrast agent concentration. Ignoring the effect of the image read-out RF pulses the signal S for the SR-TFE pulse sequence is:

$$S = \psi(1 - e^{-TS\,R_1})$$

Equation 8-1

Where Ψ is the calibration constant, TS is the saturation time and R_1 is the inverse of the longitudinal relaxation time, T_1, of the tissue. If $TS.R_1$ is small then $(1-e^{-TS.R_1}) \approx TS.R_1$ thus:

$$S = \psi\, TS\, R_1$$

Equation 8-2

The contrast agent concentration at the measurement point *i*, can be calculated from the change in R_1 due to the presence of contrast agent if the relaxivity r_1 is known:

$$C_i = \frac{1}{r_1}\ (R_{1i} - R_{1o})$$

Equation 8-3

Where R_{1o} is the pre-contrast R_1 value and R_{1i} is the value at some measurement point after contrast. Using Equation 8-2 to represent this in terms of MR signal:

$$C_i = \frac{1}{\psi\, TS\, r_1}(S_i - S_o)$$

Equation 8-4

And dividing both sides by S_o:

$$C_i = \frac{R_{1o}}{r_1}\left(\frac{S_i - S_o}{S_o}\right)$$

Equation 8-5

Equation 8-4 holds that $C_i \propto (S_i - S_o)$ so long as the coil gain remains constant, whereas Equation 8-5 holds that $C_i \propto \frac{S_i - S_o}{S_o}$, so long as the native tissue R_{1o} remains constant. In this study AIFs from the basal slice were applied to all three slices in order to avoid more profound non-linearity and longer *TS* values in the other slices. As the coil gain (an element of the constant ψ) may change between slices, Equation 8-5 was used to generate the linear assumption concentration curves. Both rest and stress curves were converted to concentrations using S_o from the stress curve pre-contrast region as the rest curve ‘pre-contrast’ region contains remnant contrast agent from the preceding stress study. After concentration conversion the stress pre-contrast region had C_o=0. However, due to the remnant contrast agent the resting pre-contrast region required further baseline correction using the rest pre-contrast region:

$$C(t) = C(t) - C_o$$

Non-linear conversion to concentration was carried out using the method described in chapter 6 with the same additional baseline subtraction used in the rest curve analysis.

Analysis

Regional quantitative MBF estimates for all patients in the CE-MARC sub-set (section 8.2) were calculated using Fermi-constrained deconvolution, as it is the most widely used method. For every slice the AIF was taken from the basal slice as it exhibits the least non-linearity and is less susceptible to absolute saturation (plateauing). As the CE-MARC acquisition protocol uses a shared pre-pulse each slice has a different saturation time (TS). Therefore each slice has a different T_1-weighting, which effects the enhancement response and thus the MBF. This effect should be corrected for by the non-linear conversion to concentration. To remove this TS factor (which is only relevant for shared pre-pulse sequences) from the comparison, the concentration conversion comparison was carried out on data from the middle slice only. The exclusion protocol is described in section 8.3. Regional MBF values at stress and rest were converted to myocardial perfusion reserve (MPR) scores. The method used for relating each MPR to the coronary artery diagnosis is described in section 8.5. Receiver operator curves (ROC) between the quantitative perfusion results and the reference standard diagnosis were generated. The experiment was carried out twice; once assuming a linear relationship between MR signal intensity and contrast agent concentration and once using the non-linear conversion to concentration described in chapter 6. The ROC curves generated from the two methods were compared using the DeLong DeLong Clarke-Pearson method (155).

8.4.3. Results

The mean (±sd) MBF and MPR at rest and stress and MPR using linear and non-linear concentration conversions are shown in Table 8-4.

Concentration Conversion	Stress MBF (mean + SD) [ml/g/min]	Rest MBF (mean + SD) [ml/g/min]	MPR (mean + SD)
Linear	2.38 + 0.91	1.08 + 0.44	2.36 + 0.95
Non-linear	1.55 + 0.86	0.70 + 0.41	2.33 + 0.88

Table 8-4 – Table showing the mean + SD MBFs at stress and rest and the corresponding MPRs using linear and non-linear correction.

Figure 8-6 shows the ROC curves diagnosis using concentration curves generated using linear and non-linear concentration conversion methods. The area under the curve, with associated confidence interval and the optimal cut-off MPR are shown in Table 8-5.

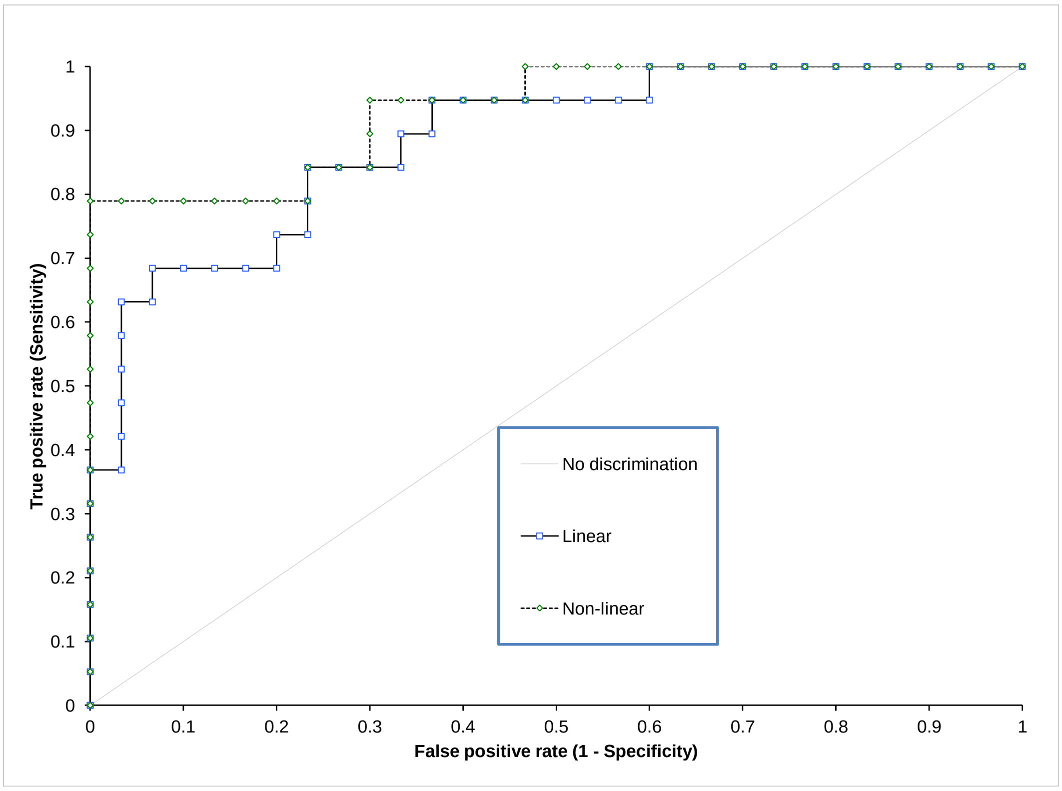

Figure 8-6 - ROC curves for MPRs generated using linear and non-linear concentration conversion regimens p=0.16.

Concentration Conversion	AUC (CI)	Optimal MPR cut-off
Linear	0.88 (0.79, 0.98)	1.58
Non-linear	0.93 (0.86, 1.00)	1.30

Table 8-5 – Area under the curve (and associated confidence interval) for the two concentration conversion methods, with optimal MPR cut-off values derived from the ROC curve.

8.4.4. Discussion

The ROC curves for MPRs generated from concentration curves derived using a linear assumption did not differ significantly from those derived using the non-linear model (p=0.16), thus there is insufficient evidence to favour a non-linear conversion over a linear one. However it is notable that the AUC for the non-linear ROC curve was larger than that for the linear curve (0.93 vs 0.88), and the p-value, though >0.05, is still small and consistent with an 84% probability that the difference between the curves is not a chance observation. The mean MBF values were lower with the non-linear conversion for stress MBF (p<0.001) and rest MBF (p<0.001), Table 8-4. The non-linear conversion resting MBFs were consistent with literature values (See Table 6-7 and Table 6-8). The mean stress MBF with non-linear conversion was lower than literature values, however the literature surveyed in Table 6-7 and Table 6-8 were taken from healthy volunteers and lower stress MBFs from patient data are to be expected. The differences between MBFs acquired using linear and non-linear conversions did not propagate to MPR values, where there was not a significant difference between the two methods (p=0.26). The changes in MBF are consistent with an underestimate in MBF with linear conversion due to non-linearity effects in the AIF. However these effects cancel in the MPR (stress MBF / rest MBF) and become non-significant as has been previously shown (156). This implies that, if the MPR is the final outcome measure used, then non-linearity effects should not prove detrimental to diagnosis. However care should still be taken to avoid saturation (plateauing in the signal vs. concentration plot) in the AIF as this may still impact MPR based results. The coefficient of variation (sd/mean) of the MPR was decreased from 0.40, with the linear conversion, to 0.38, with the non-linear conversion, implying that the non-linear conversion reduced the variability of the MPR measurement by a small degree. Although the non-linear correction did not have statistically significant impact on the diagnostic power of the test the results do suggest some improvement over a linear conversion and some reduction in variability. For these reasons the remaining investigations will use the non-linear concentration conversion method.

8.4.5. Conclusion

The non-linear conversion has been shown to make a significant difference to stress and rest MBF values, but these are cancelled out in the MPR measurement. A small but statistically insignificant improvement in diagnostic power has been shown in the ROC curves when using the non-linear conversion. The non-linear correction has shown a small decrease in the variability of the MPR measurement. For these reasons the non-linearity correction will be used in the remaining sections of this chapter.

8.5. A comparison of approaches for using regional quantitative MPR to diagnose ischaemic heart disease

8.5.1. Introduction

The AHA recommendations for coverage of the heart and assigning myocardial regions to specific coronary arteries is illustrated in Figure 8-7 (c & d) (106). The AHA recommendations are helpful for standardizing analysis methods across imaging modalities. However they do not go so far as to specify how quantitative measurements for each of the regions described in Figure 8-7 should be used to generate a final diagnosis of ischaemic heart disease. In this section the aim is to use the CE-MARC subset to compare and contrast different methods for diagnosing CAD based on quantitative myocardial perfusion estimates. Each of the questions posed in this section must be answered before any researcher can reduce their AHA segmented quantitative MBF measurements to a single diagnosis. They are usually just stated as steps in the methods section, but each choice may have an affect on diagnostic performance. The questions posed are as follows:

1) Does using the AHA mapping to assign regions to separate coronary arteries before analysis improve the diagnostic power of the test?

The assumption that the ischaemic/non-ischaemic cut-off value is equal across the heart may not be valid. Changes in myocardial wall thickness, proximity to coronary arteries and proximity to the right ventricle might all conceivably affect the ‘normal’ MPR. The AHA recommendations provide a method for assigning myocardial regions to coronary arteries. A comparison between coronary artery specific diagnosis (with a coronary specific MPR cut-off) and a whole heart diagnosis (with a global MPR cut-off) was undertaken to assess whether the AHA coronary artery mapping improved the diagnostic power of the test.

2) Is the mean or minimum regional MPR a more powerful diagnostic indicator?

Given a number of regional MPR scores that may or may not correspond to an ischaemic coronary artery what is the best way of grouping the MPR values into a single number for diagnosis? Taking the minimum value could be expected to make the test more sensitive as it only takes a single region to fall below the MPR cut-off value for the diagnosis to become ischaemic. However, the process by which quantitative perfusion estimates are calculated is complicated and each of the analysis steps is associated with a probability of error. MR image artifacts, low SNR, contouring errors, curve pre-processing malfunctions and perfusion model fitting errors may all be responsible for outliers. Taking the minimum of a group of regional MPR scores will be inherently susceptible to such outliers as it discards the majority of the data for the smallest value. The mean MPR may be a better diagnostic measure due to its increased robustness against such outliers. Although a single perfusion defect score would be increased by the surrounding non-ischaemic scores the mean regional MPR will be less susceptible to errors. Fundamentally the choice reduces to one of resolution. Is the presence of erroneous MPR scores sufficient to warrant an effective decrease of the spatial resolution (taking the mean MPR of all regions) or would the resulting reduction in resolution reduce the diagnostic power of the test?

3) What is the power of the test if only the middle slice is used?

As mentioned repeatedly in this thesis the quantitative myocardial perfusion pathway is susceptible to errors. However, some slices are more prone to errors than others. The myocardium in the basal slice is more likely to be too thin for analysis (section 8.3). The apical slice has a smaller diameter (due to the apical narrowing of the heart shape). Therefore it has a smaller number of myocardial regions assigned to it and can also be more difficult to contour, especially in the endocardium in slices where the blood pool can be small. The aim of this investigation was to compare the diagnostic performance of the test when using all slices vs. the middle slice alone. One would hope that the problems were not so severe so as to expect an increase in diagnostic power if only middle slice data were used. However, if the fall in diagnostic power were small then there might be justification for investing the limited MR acquisition time available in increasing image resolution on this middle slice, as opposed to three slice coverage.

4) What is the power of the test using a global MPR?

Following a similar argument to 2), abandoning regional analysis altogether and considering the whole ring of the myocardium as a single region might be a more robust measurement than regional analysis, with a corresponding loss in image resolution. It was the aim of this study to compare global versus regional analysis methods for diagnostic power.

8.5.2. Method

The CE-MARC sub-set (section 8.2) with the exclusions described in section 8.3 was used for all studies. Based on the conclusions of section 8.4 the non-linear conversion to concentration was applied to all of the curves before analysis. Fermi-constrained deconvolution was used to generate the MBF estimates. This choice was not based on any superiority of Fermi over the other models but rather on its widely accepted status in the literature. All analyses were carried out in MATLAB ®, using purpose specific software developed by the author. After exclusions all regions were analysed in a batch file and regional, as well as global, MBFs at stress and rest were stored and converted into MPRs. All of the investigations described below were conducted on this dataset.

1) Does using the AHA mapping to assign regions to separate coronary arteries before analysis improve the diagnostic power of the test?

For whole heart analysis the reference standard was classed as ischaemic if any of the quantitative X-ray regions were >70%. The minimum (see section 8.5.3 part 2) of all the regional MPR values was taken as the MPR measurement for the patient. A single ROC curve was then generated using these MPR and reference standard diagnosis values.

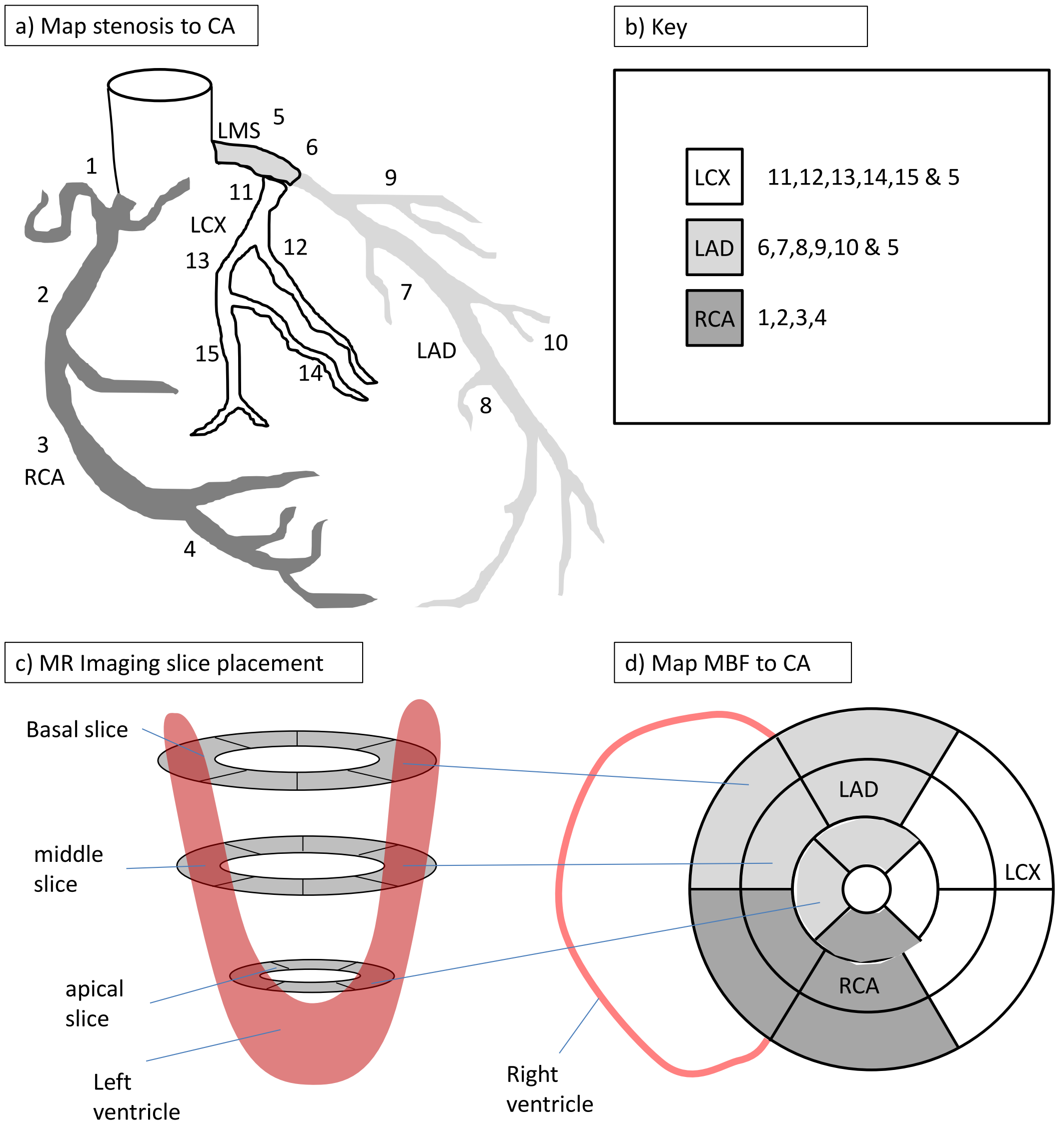

Figure 8-7 – Mapping between coronary artery stenoses and MRI segments. Coronary stenoses were quantified using X-ray angiography at the labelled sites in a). Each artery was classed as ischaemic if any of the sites listed in b) were found to have >70% narrowing. The myocardial slices imaged as illustrated in c) were subdivided and rearranged into the bullseye plot d) where they were assigned to a corresponding coronary artery according to the AHA recommendations.

For coronary artery specific analysis the reference standard for a given coronary artery (LAD, RCA, LCX) was classed as ischaemic if a quantitative X-ray stenosis >70% was identified within that coronary artery. Lesions in the left main stem (LMS) were classed as ischaemia in both LCX and LAD. This generated three sets of diagnoses, one per coronary artery. To generate the corresponding MPR values the AHA mapping was used to assign each myocardial region to a coronary artery. The minimum MPR value for each group was then assigned as the MPR measurement for that patient for that artery. The process is illustrated in Figure 8-7.

ROC curves were generated for each case. The DeLong, DeLong, Clarke-Pearson ROC curve comparison compares curves whose diagnostic outcomes are identical. As the diagnosis for the ROC coronary artery specific and whole heart were different this comparison was not possible. Therefore areas under the curve with confidence intervals were compared in terms of whether their confidence interval overlapped or not.

2) Is the mean or minimum regional MPR a more powerful diagnostic indicator?

The methodology for whole heart analysis in 1) was repeated, but two ROC curves were generated in each case. One generated taking the minimum of all the regions as the MPR value and the other taking the mean. DeLong, DeLong, Clarke-Pearson comparison of ROC curves was used to test for a statistically significant difference between the curves.

3) What is the power of the test if only the middle slice is used?

Analysis limited only to regions from the middle slice for each patient was used to generate a ROC curve. Based on the results of part 2) the minimum MPR was chosen from values generated using non-linear concentration conversion. The resulting ROC curve was compared to the methodology using all the heart regions described in 1) using DeLong, Delong, Clarke-Pearson analysis.

4) What is the power of the test using a global MPR?

ROC curves were generated using the MPRs taken from the whole myocardium from the three slices. The minimum MPR was taken as the value for comparison against the diagnosis to generate a ROC curve. The resulting ROC curve was compared against the whole heart regional analysis described in 1) Using DeLong, DeLong, Clarke-Pearson analysis.

8.5.3. Results

<u>1) Does using the AHA mapping to assign regions to separate coronary arteries before analysis improve the diagnostic power of the test?</u>

Figure 8-8 shows the four ROC curves generated using all regions and using the three separate coronary arteries. The associated area under the curve (AUC), optimal MPR cut-off value and number of ischaemic cases (out of 50) in each case are shown in Table 8-6.

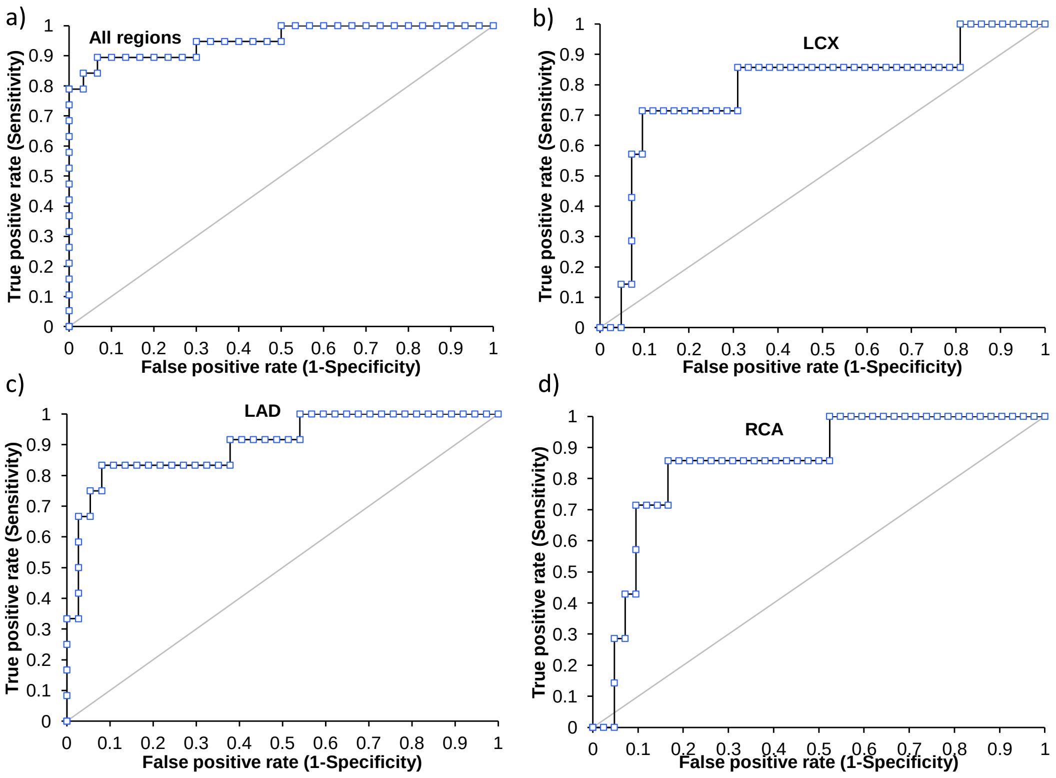

Figure 8-8 – ROC curves for a) all regions and stenoses included in the analysis, b) only LCX stenoses, c) only LAD stenoses, d) only RCA stenoses included in the analysis.

	a) All regions	b) LCX	c) LAD	d) RCA
AUC (CI)	0.95 (0.89, 1.00)	0.79 (0.57, 1.00)	0.90 (0.80, 1.00)	0.85 (0.70, 1.00)
MPR cut-off	1.30	1.30	1.29	1.30
Number of Ischaemic cases	19	7	12	7

Table 8-6 – Table of area under ROC curve (AUC), MPR cut-off values and number of ischaemic cases in dataset for analysis from each coronary artery and when all regions are considered in the analysis.

<u>2) Is the mean or minimum regional MPR a more powerful diagnostic indicator?</u>

Figure 8-9 shows the ROC curves generated when the mean and minimum of all the regions are taken as the MPR for diagnosis. The AUCs were significantly different (p=0.02) with the mean AUC (CI) at 0.85 (0.74, 0.96) and the minimum AUC at 0.95 (0.89, 1.00), with optimal MPR cut-offs at 2.17 and 1.30 respectively.

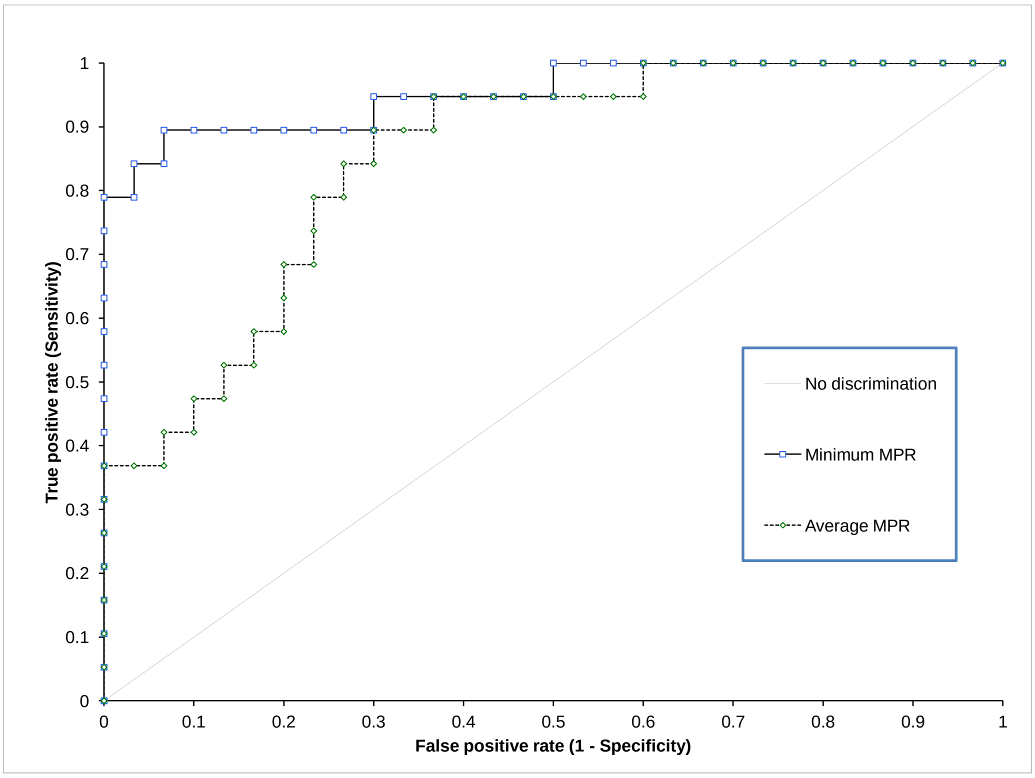

Figure 8-9 – ROC curves generated using the mean and the minimum of all the regions as the MPR for diagnosis.

<u>3) What is the power of the test if slice 2 only is used?</u>

Figure 8-10 shows the ROC curves generated using data from all the slices and that obtained using only MPR data from the middle slice. The AUC values considering all slices was 0.95(0.89, 1.00) and using the mid-slice only was 0.93 (0.86, 1.00). The optimal MPR cut-off was 1.30 in both cases. The curves were not significantly different (p=0.44).

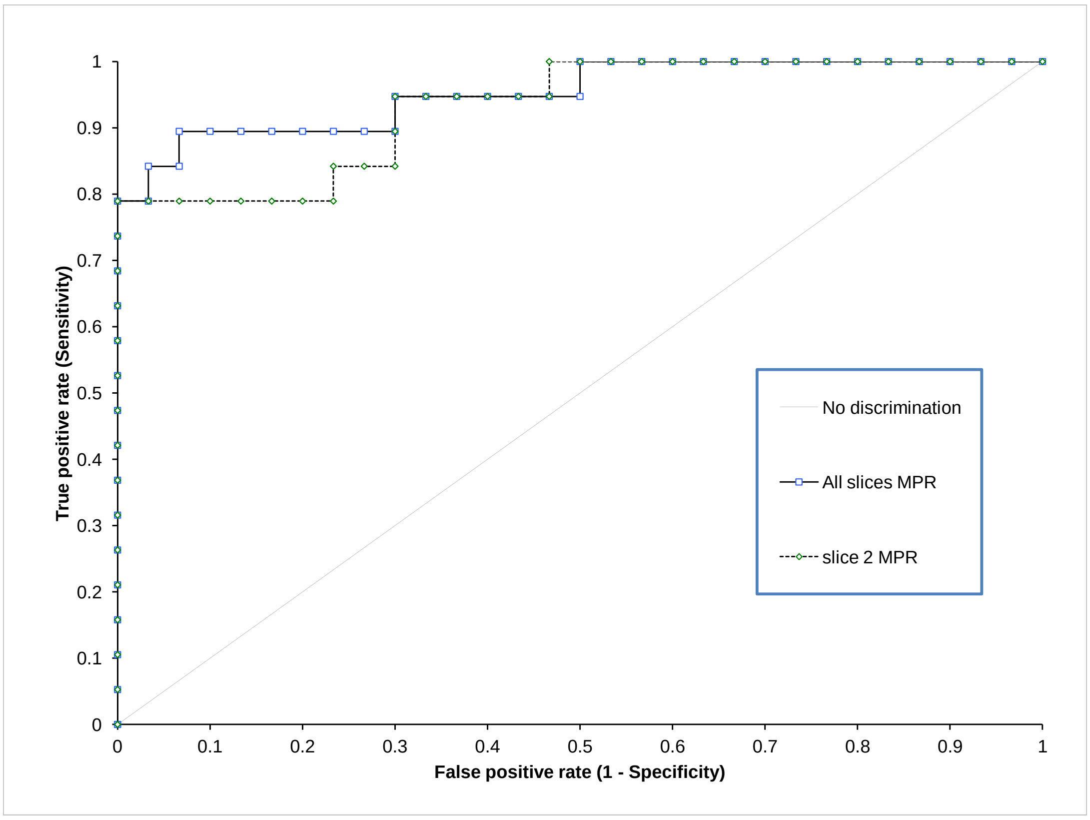

Figure 8-10 – ROC curves generated using data from all three slices versus data from the middle slice (slice 2) only.

4) What is the power of the test using a global MPR?

Figure 8-11 shows the ROC curves generated using the AHA regional MPR analysis and using only the global MPR value for each slice. The curves are significantly different (p=0.02), with the regional AUC at 0.95 (0.89, 1.00) and the global AUC at 0.84 (0.73, 0.95) with optimal MPR cut-offs of 1.30 and 2.12 respectively.

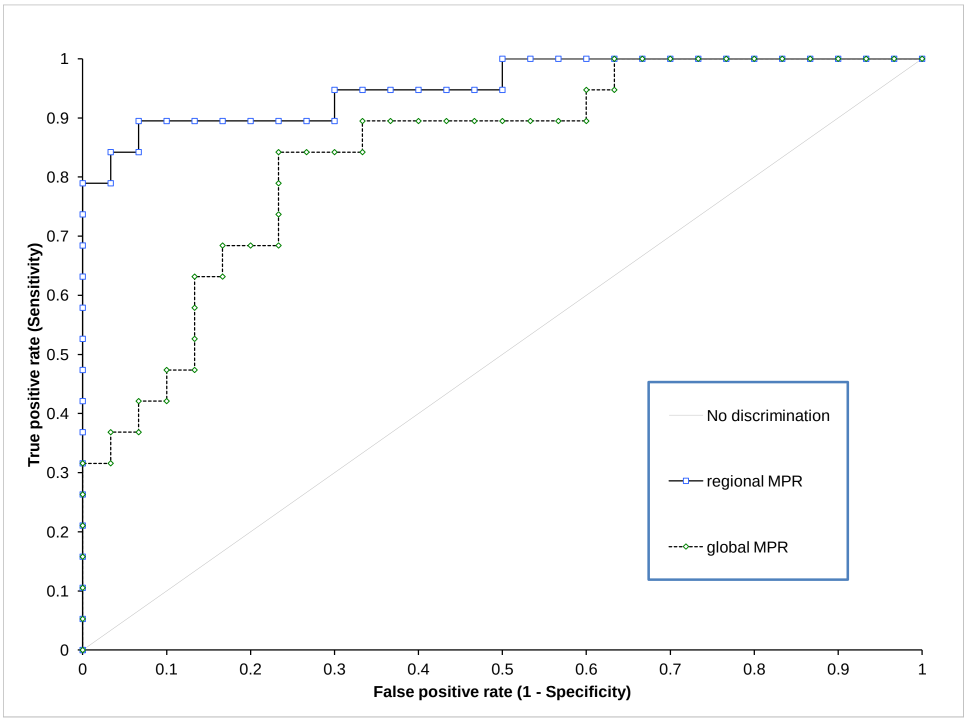

Figure 8-11 – ROC curves generated using AHA regions versus those generated using only the global myocardial MPR

8.5.4. Discussion

<u>1) Does using the AHA mapping to assign regions to separate coronary arteries before analysis improve the diagnostic power of the test?</u>

The ROC curve generated using all regions obtained the best AUC value and the narrowest confidence interval. Of the coronary specific analyses the LAD ROC curve achieved the best AUC, however this may well be due to the fact that there were more coronary stenoses attributed to the LAD than the other two arteries. The confidence intervals for all the AUCs overlapped suggesting that there was no difference between the diagnostic performances. However, it is interesting that the MPR cut-off values generated independently for the four curves were almost identical. This suggests that assuming a single MPR cut-off across the heart is a valid assumption and that subdividing the myocardium into coronary territories will not improve diagnosis. The LCX had a lower AUC than the RCA or LAD, though not significantly different. As the LCX is more likely to be the shortest reaching artery this might suggest that stenoses in the LCX cause less profound perfusion defects (due to a higher compensatory ability in the other two, larger arteries) but a larger study would be required to see if this were a significant observation.

2) Is the mean or minimum regional MPR a more powerful diagnostic indicator?

The analysis method using the minimum MPR of all the regions is significantly more powerful than the mean method. This is clear evidence for using the minimum regional MPR value for quantitative diagnosis of coronary artery disease.

3) What is the power of the test if only the middle slice is used?

There was not a statistically significant difference between the ROC curve generated using the middle slice only and the ROC curve generated using all three slices. 50 patients (with 19 classed as ischaemic) is only a moderate sized dataset and this investigation could be criticised for being underpowered. However the fact that the AUCs and their confidence intervals were so similar implies that the basal and apical slices are adding little to the diagnostic power of the test. This result could have significant implications for pulse sequence design for cardiac MR perfusion imaging. If a comparable diagnostic performance can be obtained from a single imaging slice then more imaging time can be dedicated to improving image resolution, or perhaps imaging a more reliable AIF. This should be an area of further investigation.

The choice of the middle slice as the single slice was based on the higher rate of imaging and analysis problems with the apical and basal slices. Setting these aside there may be reasons to consider these slices as the single slice instead of the middle slice. For instance, the apical slice is at the end of the coronary tree so might be most sensitive to stenoses, whereas the middle slice may not manifest defects with stenoses far down the coronary pathway. For this reason the investigation should be repeated using the basal and apical slices as the single slice.

4) What is the power of the test using a global MPR?

Regional analysis is significantly better at diagnosing coronary artery disease than global analysis. This implies that the coarse resolution measure of considering the whole myocardium as a single segment discards important information. In corroboration with 2) this implies that the SNR for the AHA regions is adequate for diagnosing ischaemia.

8.6. Conclusion

The recommendations, based on the studies presented in this chapter, are that analysis should be done on uptake curves after applying non-linear correction (Section 8.4). The regional territories recommended by the AHA should be used (Section 8.5 Qu4) and interpreted by taking the minimum MPR value from all the regions (Section 8.5 Qu2). A global (all arteries) rather than artery specific MPR cut-off should be used (Section 8.5 Qu1). Further evidence has been presented suggesting that a middle slice only analysis may have comparative diagnostic power to a three slice investigation (Section 8.5 Qu3), but further work is necessary to confirm this finding.

9. Comparisons of tracer kinetic models applied to cardiac magnetic resonance perfusion data

9.1. Introduction

The primary clinical motivation for quantifying MBF is to assist in the diagnosis of coronary artery disease. However, there are a range of methods for quantifying myocardial blood flow (MBF) from dynamic contrast enhanced cardiac perfusion MRI datasets, with no consensus on which is the best method to use. The methods vary in complexity and in the strength of their underlying assumptions. They have all been validated in terms of the resulting MBF values against other measurements of MBF, such as radiolabelled microspheres (77,81,157) in animals, or PET measurements in humans (6,29). Furthermore, a comparison of quantitative analysis methods has been performed on data from 14 healthy human subjects (4), finding non-significant differences between the methods in terms of MBF value. However, to provide a persuasive evidence base for choosing one method over another, evaluation of these methods should be carried out in terms of their diagnostic capabilities. It was the aim of this study to compare the diagnostic performance of four perfusion quantitation methods on a 50 patient cohort selected from the CE-MARC dataset (section 8.2).

9.2. Method

9.2.1. Patient imaging

A 50 patient subset, with patient risk factors and disease characteristics representative of the whole trial dataset was taken from the CE-MARC trial (2). The selection criteria are described in section 8.2 and the imaging methodology is described in section 5.2.1. The selected subset consisted of clear healthy, and ischaemic, cases with ambiguous diagnoses removed in order to create the cleanest reference standard possible.

9.2.2. Data analysis

The myocardium, and a region in the left blood pool representing the AIF, were manually contoured and manual correction for breathing motion, limited to rigid translation, was performed using the method described in section 5.3. The Fermi-constrained deconvolution (*Fermi)*, model-Independent deconvolution (*ModI*), uptake analysis (*Uptake*) and the one compartment model (*OneCP*) algorithms described in chapter 4 for quantifying MBF were implemented in Matlab®. The methods differ in terms of how much of the full dynamic series they utilise. These differences may be significant in the final performance of the methods, as a method that can incorporate more data in the analysis may be more robust to noise. Therefore each analysis method functioned on a bespoke curve preparation scheme. The full curve analysis scheme is outlined as follows:

1. The AIF was taken from the blood pool of the basal slice, where the saturation time was shortest in order to minimise signal saturation (see Figure 5-1), whilst myocardial uptake curves were taken from each individual slice.
2. The myocardium was subdivided into regions according to the AHA recommendations as described in chapter 8.
3. The stress curve pre-contrast baseline signal (S_o) was calculated as described in section 5.4.1.
4. Signals were converted to concentrations using the non-linear conversion process described in chapter 6. The stress S_o was used in both stress and rest conversions as the rest time series is contaminated by remnant Gd from the stress bolus.
5. The rest data series was baseline corrected for remnant contrast agent (C_i - C_o).
6. All data were interpolated by a factor of four using piecewise hermitian interpolation (pchip MATLAB®) in order to increase the apparent temporal resolution (see section 5.4.3).
7. The AIF curve was temporally shifted so that the bolus arrival times of the two curves matched as described in section 5.4.3.

8. Method specific curve preparation was applied before estimating the MBF as follows:
    1. Fermi-Constrained deconvolution:
        1. The pre-contrast baseline data points were cropped from the dataset as described in section 5.4.1.
        2. The dataset was cropped after the first pass, defined as the first valley following the largest peak in the AIF as described in section 5.4.2.
    2. Model Independent deconvolution:
        1. No further preparation necessary
    3. Uptake model:
        1. The pre-contrast baseline data points were cropped from the dataset.
        2. All data after the AIF peak were cropped from the dataset.
    4. One compartment model:
        1. The pre-contrast baseline data points were cropped from the dataset.

Although the pre-contrast baseline data is essential for non-linearity correction it is irrelevant to the perfusion model, which considers only signal changes due to contrast agent. Therefore, once the curve is converted to concentration, the baseline data points will not aid the model fitting. Conversely, if there are large variations in signal in the baseline due to noise or artifacts these will adversely affect the model fitting, which tries to generate a response function for all the data. For these reasons the pre-contrast baseline data was cropped from the curves before model fitting.

Further to the exclusions based on image artifacts and contouring problems described in section 8.3 exclusions were made based on extreme MBF or MPR values. All results with a value less than 0 were excluded from the analysis. The upper tolerance was set at twice the maximum expected value: stress MBF = 8 ml/g/min, rest MBF = 4 ml/g/min and MPR = 8. The reasons for these extreme outliers are explained later (Section 9.3.2). In most cases the errors causing these outliers could have been addressed by modifying the pre-curve analysis. However, it is important to evaluate the methods in terms of a fully automated analysis, as this must be in place before these methods could hope to be accepted in clinical practice, given the already heavy time-expenditure necessary for manual contouring. As the outliers are easy to detect based on the specified criteria the decision was taken to exclude them from the analysis so that the results reflect what might be achieved with a fully automated analysis.

9.2.3. Generation of diagnostic results

Based on the findings of section 8.5 regional MPRs were mapped to SPECT and quantitative X-ray consensus diagnosis by taking the minimum regional MPR from all slices as the MPR measure. ROC curves were generated for each method.

9.2.4. Statistical analysis of results

Each method was compared with every other method using Bland-Altman analysis to assess the agreement between methods in stress MBF, rest MBF and MPR. Paired t-test and Pearson's correlation were also performed between each model to look for significant differences in results and correlations in results.

ROC curves from all of the methods were compared using the DeLong, DeLong, Pearson method (155).

9.3. Results

9.3.1. Exclusions

Table 9-1 records the number of exclusions for each model. Note MPR exclusions are only counted where both rest and stress MBF values were within tolerance but produced an out of tolerance MBF.

Method	Rest MBF	Stress MBF	MPR
Fermi	1	0	0
Uptake	7	0	19
One CP	0	0	0
Modl	9	6	7

Table 9-1 – Number of exclusions for stress, rest MBF and MPR for each of the quantitation models. The exclusion criterion was 0 ≤ x ≤ 8 for stress MBF and MPR and 0 ≤ x ≤ 4 for rest MBF.

Method	Diagnosis	Stress MBF (mean ± SD) [ml/g/min]	Rest MBF (mean ± SD) [ml/g/min]	MPR (mean ± SD)
Fermi	*Healthy*	1.77 ± 0.88	0.76 ± 0.36	2.45 ± 0.72
	Ischemic	1.56 ± 0.89	0.97 ± 0.51	1.59 ± 0.58
Uptake	*Healthy*	1.57 ± 0.81	0.64 ± 0.33	2.66 ± 0.94
	Ischemic	1.41 ± 0.82	0.88 ± 0.42	1.77 ± 0.82
OneCP	*Healthy*	1.70 ± 0.86	0.78 ± 0.38	2.25 ± 0.64
	Ischemic	1.60 ±0.83	1.07 ± 0.56	1.57 ± 0.50
Modl	*Healthy*	1.53 ± 0.74	0.68 ± 0.31	2.26 ± 0.64
	Ischemic	1.32 ± 0.73	0.82 ± 0.39	1.70 ± 0.56

Table 9-2 – Mean ± standard deviation stress and rest MBFs and MPR values for the four methods in the healthy and ischaemic patient populations as diagnosed by X-ray angiography and the AHA mapping.

r	Fermi	Uptake	OneCP	Modl
Fermi	1	0.87 (0.78, 0.93)	0.97 (0.94, 0.98)	0.86 (0.76, 0.92)
Uptake		1	0.90 (0.84, 0.94)	0.75 (0.60, 0.85)
OneCP			1	0.84 (0.73, 0.91)
Modl				1

Table 9-3 – Pearson's correlation r-values for comparisons between the four models. In all comparisons p<0.0001.

Table 9-2 shows the mean and standard deviation (SD) MBF at rest and stress and the MPR for each of the four models over all of the healthy and all of the ischaemic patients.

Table 9-3 shows the Pearson’s correlation scores between all of the models, with all models having a highly significant correlation ($p<0.0001$). Table 9-4 shows the Bland-Altman bias scores for the comparisons between each of the models, with confidence intervals for the biases in brackets. Paired t-test p-values were all highly significant ($p<0.001$) except uptake versus model independent MPR ($p=0.08$). The corresponding standard deviations of the differences are shown in Table 9-5.

Stress	Fermi	Uptake	OneCP	ModI
Fermi	0	0.19 (-0.41, 0.79)	0.04 (-0.37, 0.44)	0.22 (-0.20, 0.64)
Uptake		0	-0.15 (-0.82, 0.51)	0.03 (-0.59, 0.65)
OneCP			0	0.19 (-0.29, 0.67)
ModI				0

Rest	Fermi	Uptake	OneCP	ModI
Fermi	0	0.11 (-0.43, 0.65)	-0.04 (-0.23, 0.14)	0.07 (-0.24, 0.37)
Uptake		0	-0.15 (-0.70, 0.40)	-0.04 (-0.57, 0.50)
OneCP			0	0.11 (-0.24, 0.46)
ModI				0

MPR	Fermi	Uptake	OneCP	ModI
Fermi	0	-0.18 (-1.80, 1.43)	0.17 (-0.43, 0.77)	0.14 (-0.86, 1.13)
Uptake		0	0.36 (-1.37, 2.05)	0.31 (-1.60, 2.23)
OneCP			0	-0.03 (-1.05, 0.99)
ModI				0

Table 9-4 – Bland-Altman bias values with confidence intervals when different models are compared in terms of stress MBF [ml/g/min], rest MBF [ml/g/min] and MPR.

Stress	Fermi	Uptake	OneCP	ModI
Fermi	0	0.31	0.21	0.22
Uptake		0	0.34	0.32
OneCP			0	0.24
ModI				0

Rest	Fermi	Uptake	OneCP	ModI
Fermi	0	0.28	0.09	0.16
Uptake		0	0.28	0.27
OneCP			0	0.18
ModI				0

MPR	Fermi	Uptake	OneCP	ModI
Fermi	0	0.83	0.30	0.51
Uptake		0	0.88	0.98
OneCP			0	0.52
ModI				0

Table 9-5 – Standard deviation of differences between models for all model comparisons in terms of stress MBF [ml/g/min], rest MBF [ml/g/min] and MPR.

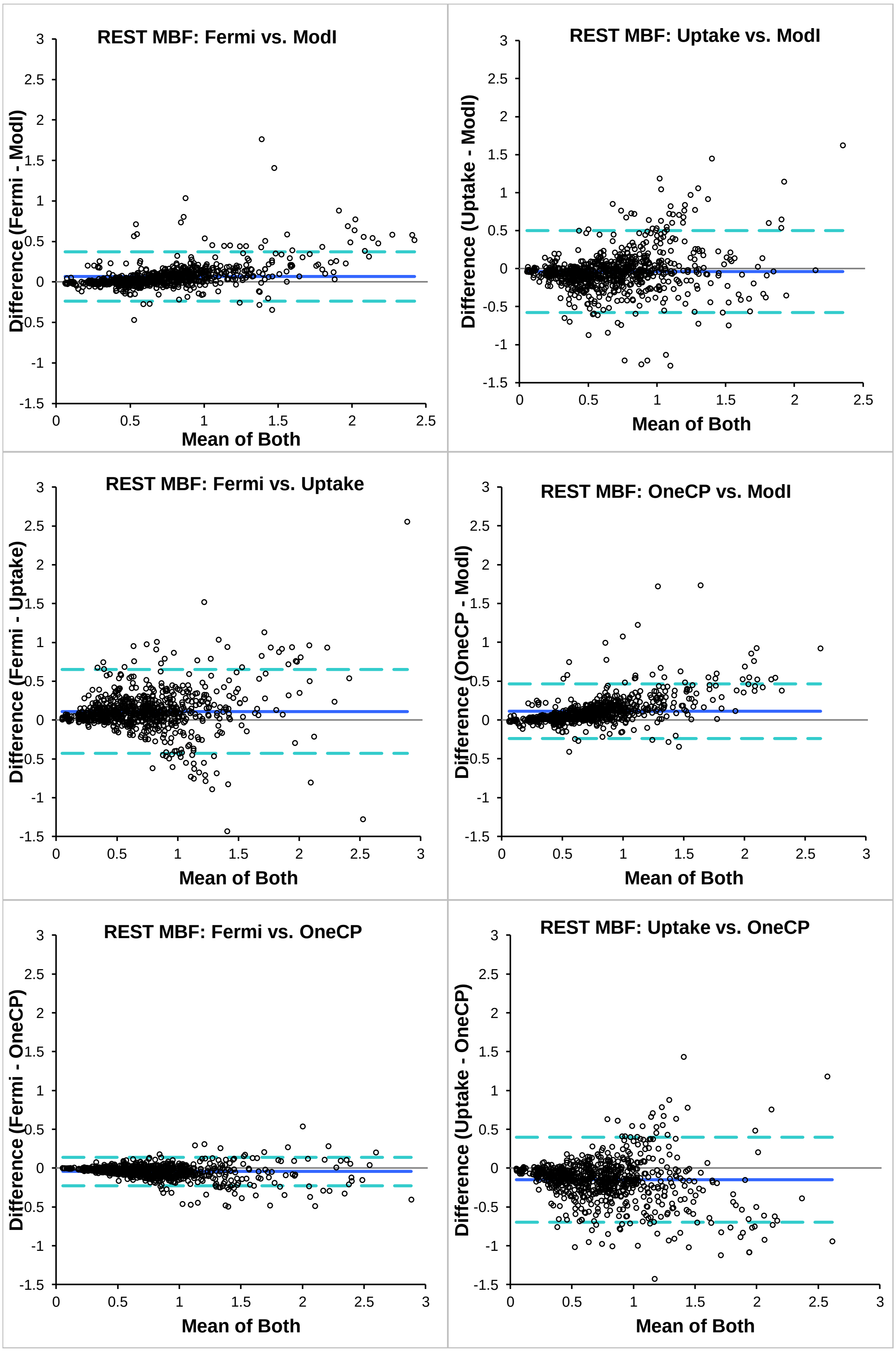

Figure 9-1 – Bland-Altman comparison plots for rest MBF for all models. Solid line shows mean bias, dashed lines show confidence intervals. (axes scales locked for comparison).

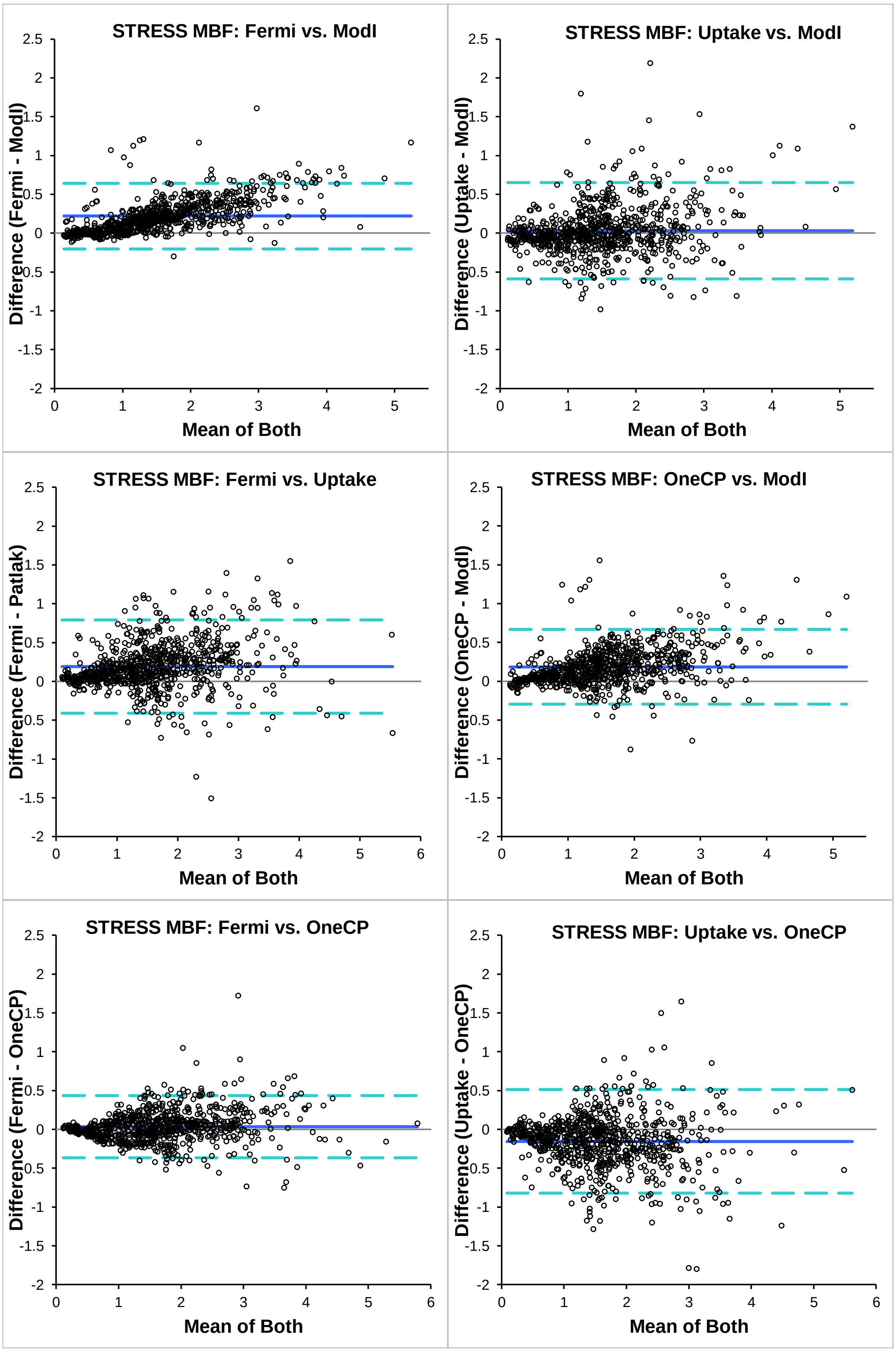

Figure 9-2 – Bland-Altman comparison plots for stress MBF for all models. Solid line shows mean bias, dashed lines show confidence intervals (axes scales locked for comparison).

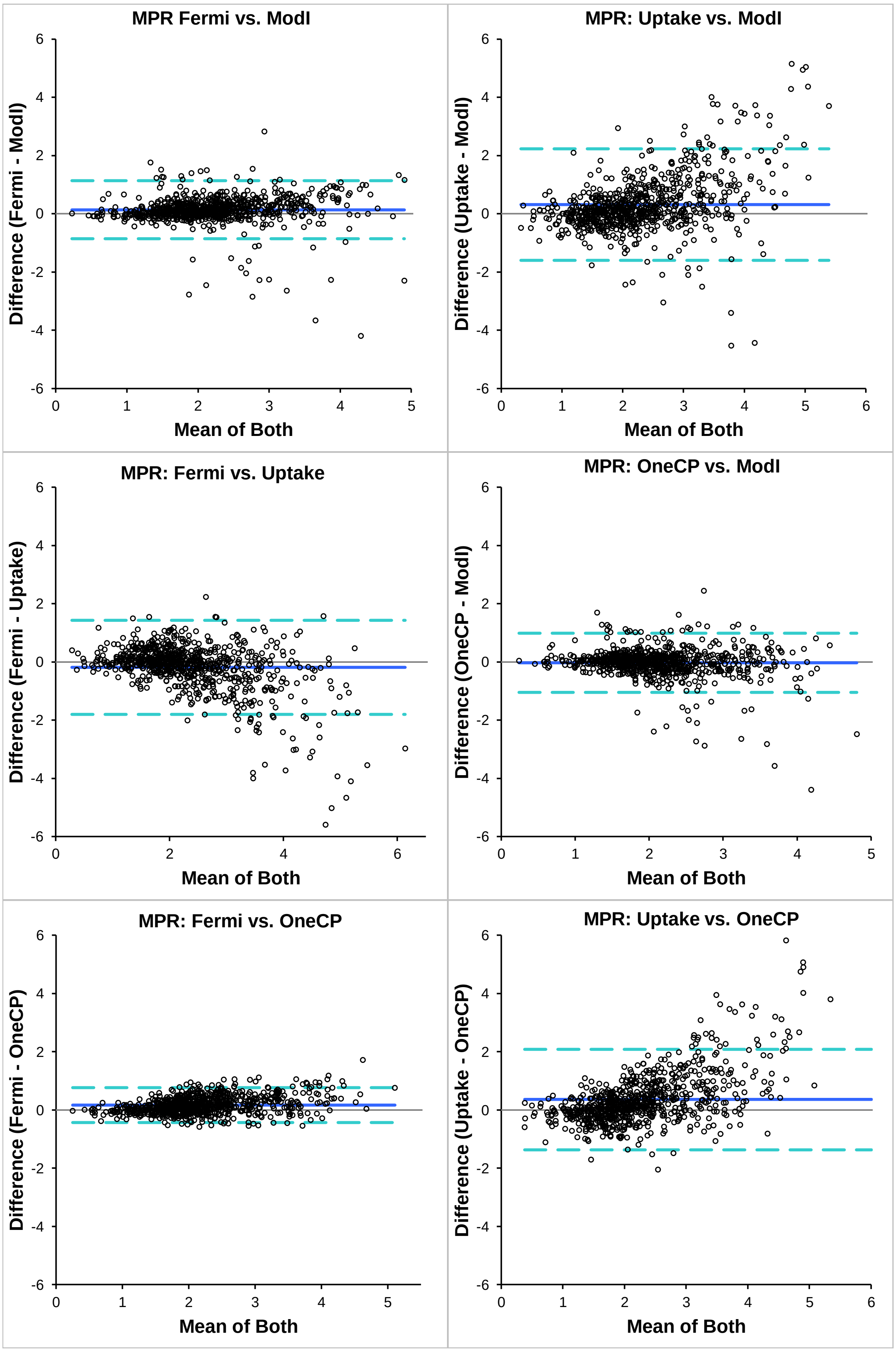

Figure 9-3 – Bland-Altman comparison plots for MPR for all models. Solid line shows mean bias, dashed lines show confidence intervals (axes scales locked for comparison).

Aggregate, flow-weighted response functions from the Fermi, one compartment and model independent models are shown in Figure 9-7 along with the point wise standard deviation. In order to generate these plots each plot was interpolated to a standard set of time points before a point wise average of the response functions was performed. Figure 9-4 shows the ROC curves for MPRs generated with the four models as curve to curve comparisons. The corresponding DeLong, DeLong, Pearson p-values are shown in

Table 9-6. The descriptive parameters for the ROC curves are shown in Table 9-7.

MPR	Fermi	Uptake	OneCP	ModI
Fermi	1	0.11	0.05	0.91
Uptake		1	0.54	0.29
OneCP			1	0.41
ModI				1

Table 9-6 - ROC curve comparison p-values (curves shown in Figure 9-4)

MPR	Fermi	Uptake	OneCP	ModI
AUC	0.93 (0.84, 1.00)	0.86 (0.73, 0.98)	0.88 (0.77, 0.99)	0.92 (0.85, 0.99)
Optimal MPR cut-off	1.34	1.18	1.43	1.32
Sensitivity [%]	89.5 (0.67, 0.99)	0.84 (0.60, 0.97)	0.90 (0.67, 0.99)	0.95 (0.74, 1.00)
Specificity [%]	90.0 (0.74, 0.98)	0.83 (0.65, 0.94)	0.77 (0.58, 0.90)	0.80 (0.61, 0.92)

Table 9-7 – ROC curve descriptive parameters for the four models, Area under the curve (AUC), optimal MPR cut-off value, sensitivity and specificity at the optimal cut-off, confidence intervals in brackets.

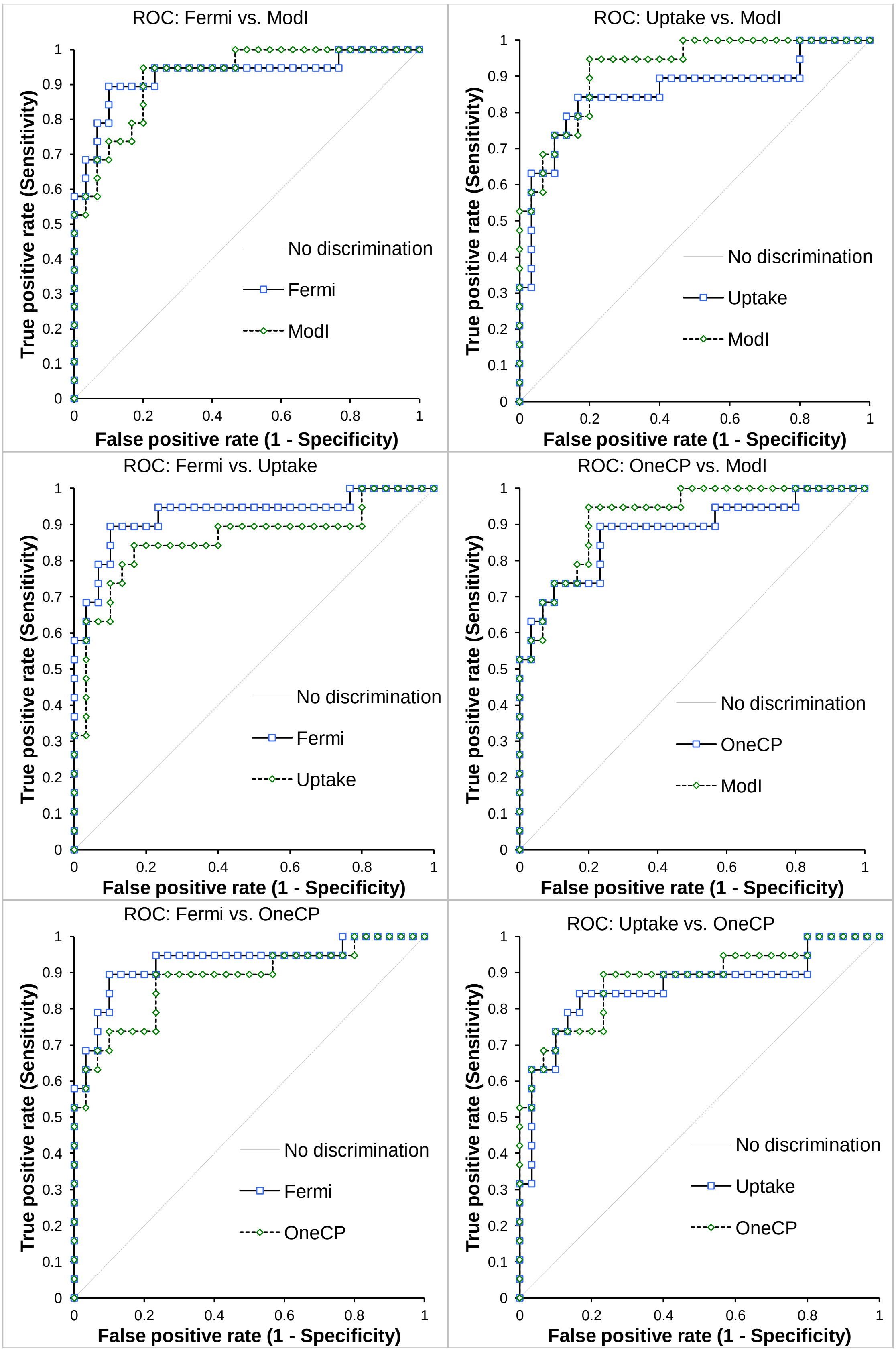

Figure 9-4 - ROC curve comparisons between each of the models (p-values shown in

Table 9-6.

9.3.2. Discussion

Exclusions

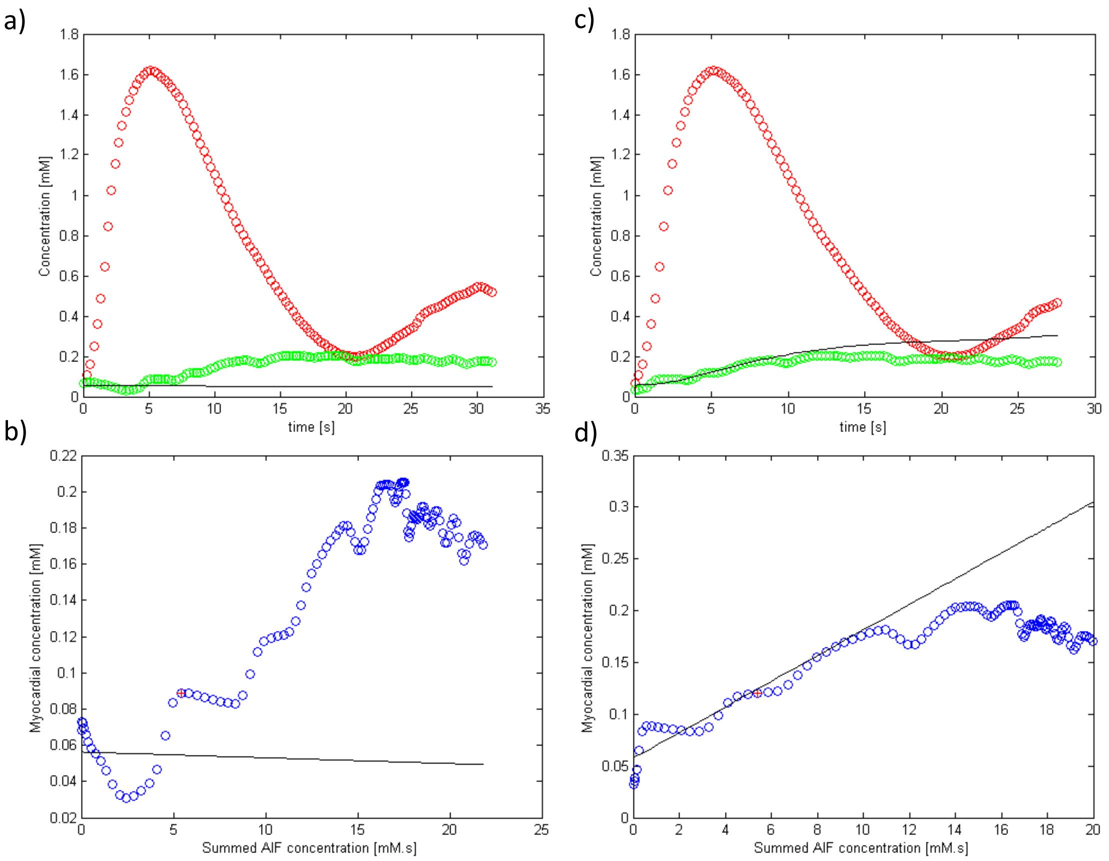

Figure 9-5 – Example of a failure in the uptake curve processing. The red dotted curves are the AIFs, the green are the myocardial uptake curves, black solid lines are the model fit lines. The blue dotted curve is the uptake plot (tissue vs. sum of AIF). The red cross marks the cut-off point dictated by the peak of the AIF. A shallow uptake curve results in a poor choice of delay time shift *dt* (a). When the uptake curve (b) is plotted, noise in the AIF coupled with an early cut-off point results in a negative fit to the data (up to the cut-off point) giving a negative MBF. For illustration purposes the problem has been corrected by manually correcting the delay time shift *dt* in panes (c) and (d).

No MPR values had to be excluded from the one-compartment model results and only a single exclusion was made from Fermi model results. The number of exclusions for the uptake model and the model independent method were small (a total of 4% and 3% respectively). The exclusions for the uptake model were due to very small or even negative rest MBFs. The reasons for this are illustrated in Figure 9-5. A shallow uptake curve makes the bolus arrival time in the myocardium difficult to detect resulting in a poor estimate of *dt* (the delay time between bolus arrival in the myocardium and AIF). This results in baseline data points being included in the analysis resulting in a very shallow uptake curve, thus a low MBF. Coupled with noise spikes in the baseline this scenario can actually generate negative MBFs.

Excluded MPR values from the model-independent dataset were due to high frequency oscillations in the response function generating very high MBFs. An example is illustrated in Figure 9-6. In this example high frequency spikes in the latter part of the tissue curve meant that a smooth impulse response function was not able to fit all of the data well. The L-curve analysis in this case had two ‘L-corners’. The maximum curvature was identified at the left most corner corresponding to a small value for λ so the smoothness constraint was minimised. This resulted in high frequency, high amplitude oscillations in the response function that generated very large, erroneous flow estimates. For illustration purposes only the curves after manually correcting the λ value are also shown.

All of these errors could be dealt with by simple manual interventions. They are also easy to detect and exclude post-hoc as described in the methods section. Section 8.5 recommends that regional analysis of the heart yields the best diagnostic power and such a diagnosis requires a large number of quantitations per patient (32 using the AHA recommendation on three slices). Manual analysis on this number of curves would be prohibitively time consuming for clinical practice in a field that already has the large time penalty of manual contouring to contend with. For these reasons the methodology in this study is restricted to a fully automated analysis with post-hoc exclusions based on outlying MBF values as described.

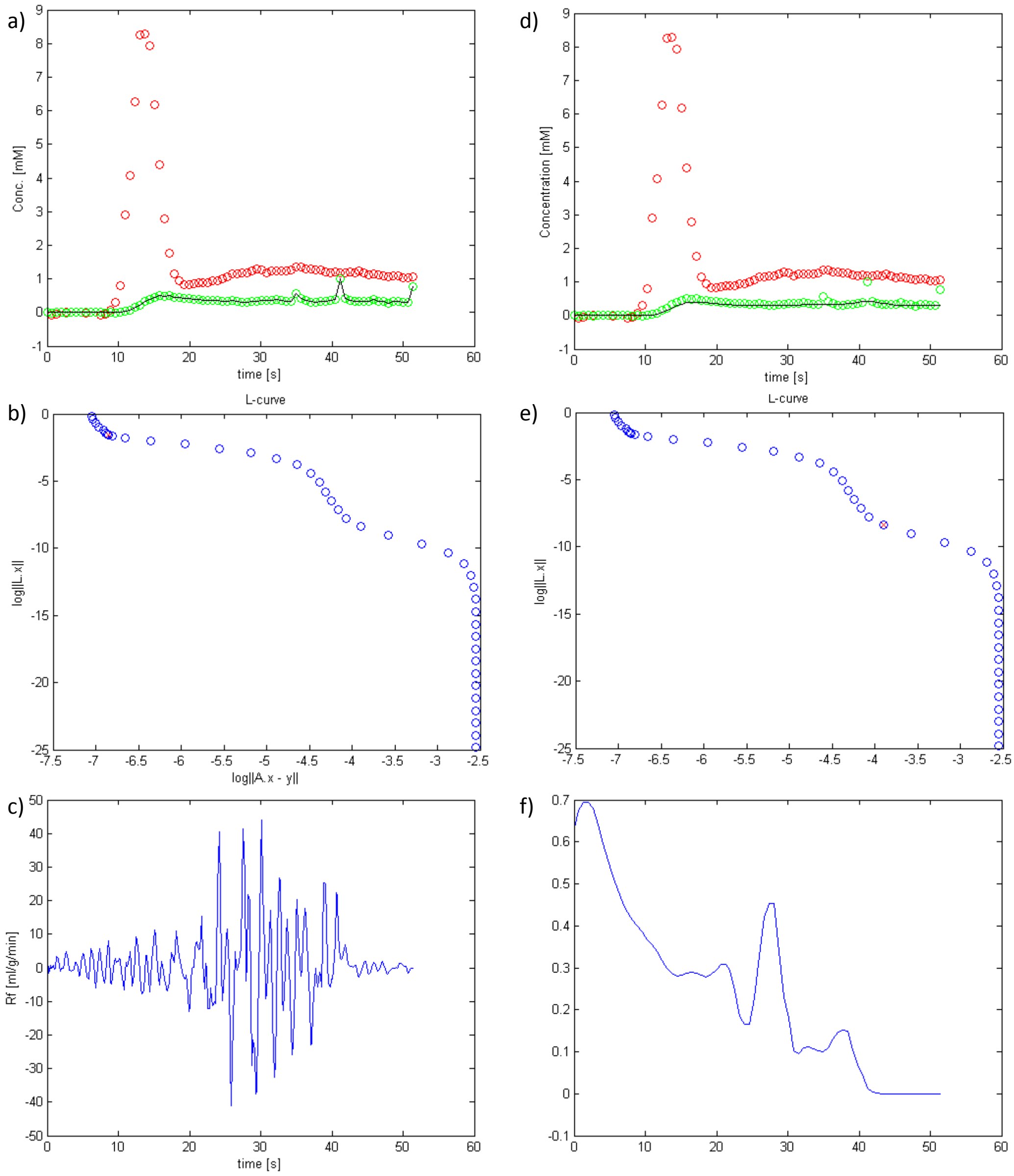

Figure 9-6 – Example of a model independent deconvolution failure. Due to the high frequency ‘spikes’ in the latter portion of the tissue curve (a) the L-curve analysis has a double corner (b). Thus a small λ value has been chosen (red cross) causing insufficient smoothing in the response function (c) and a subsequent high, and incorrect, MBF. For illustration purposes the corresponding plots when the λ value has been manually corrected to the second L-curve point are also shown (d-f).

9.3.3. MBF Estimates

The MPR values for all the methods shown in Table 9-2 are comparable with healthy and ischaemic MPRs based on quantitative MBFs reported previously

(91,104). Healthy and ischaemic resting MBFs are comparable with those previously published when non-linearity effects have been excluded (see Table 6-7 and Table 6-8). The healthy stress MBFs are smaller than the average MBFs reported in these tables. However, considering specific studies, they agree with the values found by (5) and exceed those of (27) emphasising the large variation in the ‘normal’ MBF values between studies. Stress MBFs are reduced in response to ischaemia, although the effect here is less significant than the effect observed in terms of MPR.

The aggregate response functions shown in Figure 9-7 reflect the nature of the different models. The one compartment model is a single exponential whereas the Fermi function, with the addition of an early shoulder has more flexibility, although on aggregate this appears as a flattening of the response function rather than a clear shoulder. The model-independent function shows clear shoulders in both rest and stress curves.

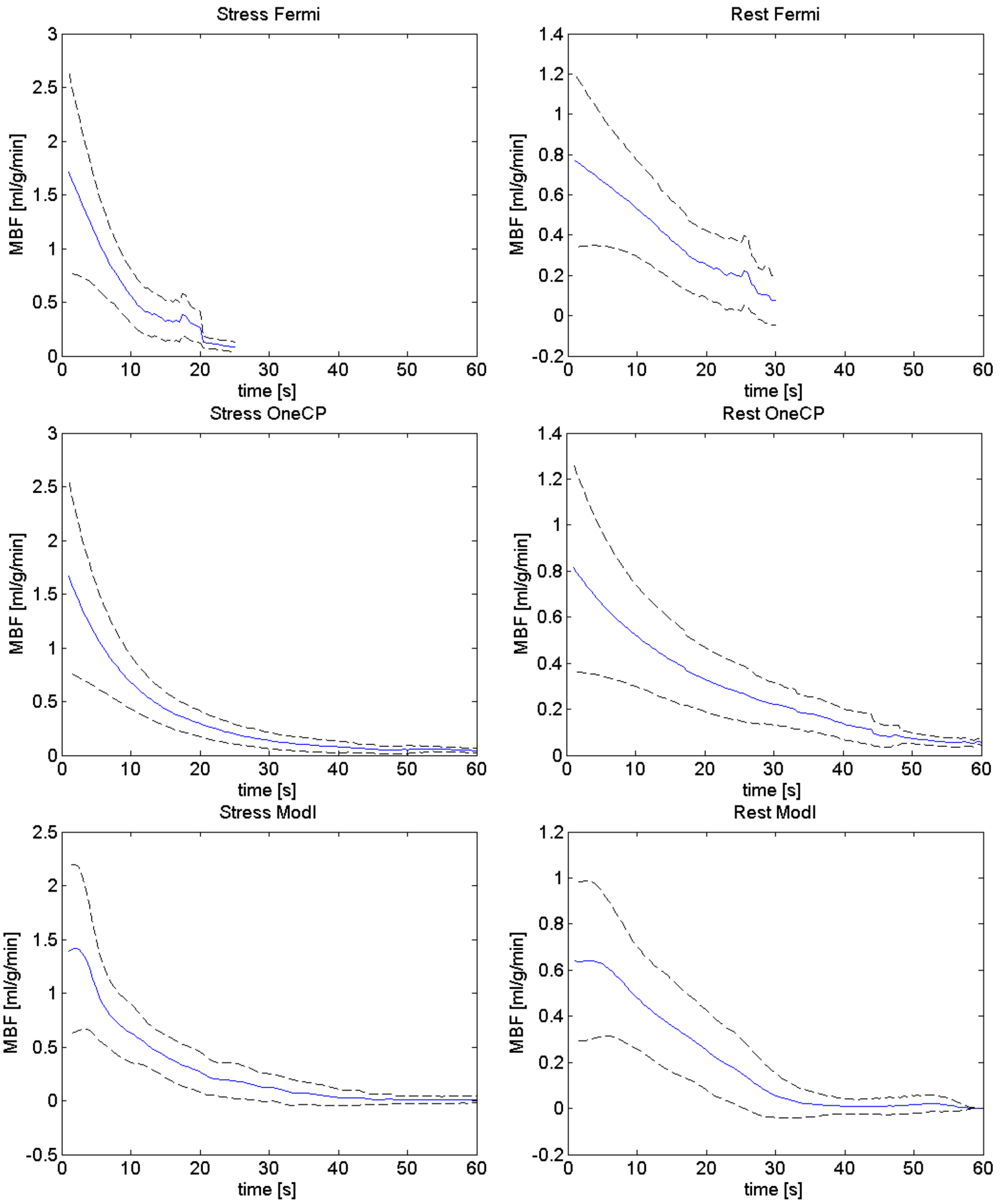

Figure 9-7 – Aggregate flow-weighted impulse response functions for Fermi-constrained deconvolution, one compartment model and model-independent deconvolution. The solid line is the mean R_f at the given time with standard deviations shown as dashed lines.

9.3.4. Comparison of perfusion models

The four models were highly correlated (Table 9-3). Small but significant differences were found between the models at rest MBF, stress MBF and at MPR. These results differs from those of (4) who found significant differences only at stress MBF and no significant differences in MPR using similar quantitation models. The differences in the results presented here may be due to the much larger dataset in this study, 50 subjects, rest and stress vs. 20 rest and 14 stress in Pack et al. (4) , and the fact that ischaemic patients are included in this. The differences observed are small with the largest bias in MBF at 0.22 ml/g/min between Fermi and model-independent at stress and biases in MPR not exceeding the 0.36 difference found between the uptake model and the one compartment model. Furthermore the 95% confidence interval in each case encompasses the zero difference point, thus there is insufficient evidence to favour any method over the others based on these differences. The width of these confidence intervals in all cases is similar to those in (4) suggesting that any differences in implementations between the studies have not increased variations between methods. Considering the variations of the comparisons (Table 9-5) the uptake model tends to be associated with larger variations in comparison with all models (an observation also noted by Pack et al.). This may be due to the fact that the uptake model uses less data than the other models and is thus more susceptible to noise and artifacts in the curves. It could also be due to the occurrence of similar, but less dramatic and so not excluded, errors to those illustrated in Figure 9-5. Pack et al. observed a larger positive MBF bias using Fermi-deconvolution (even after limiting analysis to the first pass) than with the other two methods. The data presented here does not corroborate this observation.

9.3.5. Comparison of diagnostic power of the tests

All of the models had a good diagnostic power with the poorest AUC from the uptake model still achieving an area under ROC curve of 0.86, associated with a sensitivity and specificity of 0.84 and 0.83 respectively. It is not the aim of this study to establish the power of the tests clinically as ambiguous cases have been removed from the dataset, however it is encouraging that the tests perform well. There were no statistically significant differences ($p<0.05$) between ROC curves of the different models, however Fermi vs. uptake ($p=0.11$) and Fermi vs. One compartment model ($p=0.05$), approached a statistically significant result, with the Fermi model performing better in both cases. The poorer diagnostic performance of the uptake model might be explained in terms of the larger variability and susceptibility to underestimates of

MBF described earlier. The stronger difference observed between Fermi and the one compartment model is surprising. The main difference between these models is the shoulder in the Fermi function. The model-independent response functions tend to incorporate this shoulder as can be seen in the aggregate response function in Figure 9-7. This implies that the 'true' response function should have such a shoulder. Indeed this appearance was the original motivation for utilising the Fermi function in CMR perfusion. Furthermore, the AUC scores and MPR-cut-off values for Fermi and model-independent are almost identical, whereas the other two models have lower AUCs and different MPR-cut-offs. It may be then that the Fermi function's ability to mimic this shoulder shape has made it a closer approximation to the true response function in this dataset. It should be stressed however that the differences observed here are only borderline significant and further work should be done before making an absolute recommendation for clinical practice.

9.4. Conclusion

All of the models generated MPRs and quantitative MBF estimates that were consistent with the literature. Numbers of exclusions (based on MBF and MPR figures) were small enabling a fully automated analysis (post-contouring). This important point means that the analysis methods described here do not place any extra time-processing pressure on the acceptance of such methods into clinical practice.

Corroborating the work of (4) this study has shown that there is a strong correlation between the MBFs measured using four different models. Due to the increased power of this investigation over (4) significant differences in the MBF estimates have been found, although the magnitudes of these differences are small. Importantly it has been shown that these small differences do not have a significant impact on the diagnostic power of the MPR estimates. In conclusion any of the methods described are equally capable of generating MPR figures for diagnosing CAD.

In the absence of an overriding winner in terms of diagnostic power the decision about which model to use might be made based on the simplicity of implementation. Model-independent deconvolution is the most difficult algorithm to implement. However, Fermi-deconvolution and the uptake model, although simple implementations in principle, become more difficult when automated curve processing is required as they both require a cut-off point, after which perfusion data is discarded. In the case of the uptake model this was the reason for a number of exclusions in this study. For the Fermi model only one exclusion was required. The simplest model, taking into account the pre-processing steps, was the one compartment model. The only pre-processing steps required were baseline correction and delay time estimation and the deconvolution step is a simple exponential fit. The simplicity of this analysis meant that no one-compartment model data was excluded.

On the basis of robustness then the one-compartment and Fermi-models were superior. However, although a statistically significant difference in diagnostic performance was not observed between these models on this dataset, it is interesting to note that the Fermi model achieved a specificity of 90% whereas the one-compartment model achieved only 77%, with comparable sensitivities. On this dataset there is insufficient evidence to know whether this is a chance observation or a genuine difference in the models, at the 95% confidence level. However, the borderline significance of this difference ($p=0.05$) suggests that a larger investigation might provide evidence in favour of the Fermi model in terms of both accuracy and robustness.

10. Conclusions, limitations and future direction

10.1. Limitations and future work

The aim of this research has been to provide an evidence basis upon which decisions about a standard protocol for quantitative analysis of cardiac DCE-MRI perfusion might be made. The philosophy has been to use diagnostic accuracy as the evaluation tool as diagnosis is the ultimate purpose of the quantitative MBF measurements. This has been achieved regarding the question of the perfusion model in chapter 9. The conclusion reached was that, for the data considered, there was insufficient evidence to favour one method above another in terms of diagnostic accuracy. There were observable, though not statistically significant, differences between the diagnostic performances of the models which should motivate still larger studies to be conducted in future. However, based on the evidence presented here the decision concerning which is the ‘best’ method should be made on robustness, i.e. how many exclusions were necessary? Based on this criterion the Fermi-constrained and one-compartment models are superior. However, robustness was not the planned primary outcome measure in this work and the way in which it has been assessed could be improved. The use of a simple cut-off MBF or MPR to exclude measurements is simplistic. Better assessments might be devised by taking into account the shape of the derived response function and the model fit. Ultimately any measure will have to be reduced to a cut-off value but taking account of these more fundamental factors might be a fairer test of whether a model has ‘failed’.

The conclusions could also be criticised in terms of the pre-processing steps (section 5.4). Perhaps, the automated pre-processing used was inadequate and better algorithms would have yielded different results? The methods used in this thesis have only been evaluated qualitatively. In fact these methods are typically not evaluated at all in quantitative DCE-MRI publications and are sometimes not even described. Nevertheless, they can have a profound effect on MBF estimates and so an objective analysis of these methods would be beneficial. This could be achieved using simulated data, with different delay time and baseline noise levels etc. It would also be interesting to establish what impact different automated pre-processing algorithms had on the final diagnostic performance using the methodology set out in chapter 9.

Exclusion of data from the dataset prior to analysis was also performed qualitatively (section 8.3). Clearly an objective method for excluding datasets would be preferable as it aids generalisation of the results. For problems such as LV bleed and dark rim artefact this could prove to be a research project in itself. However the largest contributor to excluding data was a thin myocardium, which is simple to measure and this should be assessed automatically in future work.

Given the impetus within the DCE-MRI cardiac perfusion community for avoiding non-linearity in the AIF it is perhaps surprising that correcting for these effects did not have a significant impact on diagnostic performance (section 8.4). Indeed, the results shown in this thesis agree with those of Groothius et al. (25), who compared non-linear with linear dual-bolus MR data and found no difference in diagnostic performance. The results are not generalisable, as more profound non-linearity in other datasets could have more severe effects. However, they do demonstrate that non-linearity does not have a significant effect on diagnostic accuracy for the CE-MARC dataset. The non-linearity conversion algorithm has been tested on phantom data to show that it is accurately modelling the signal intensities generated by the imaging system. However, further validation against PET measurements or animal studies would have provided more reassurance that the method is indeed correcting for these effects.

The evaluation of contour errors study (chapter 7) has shown that standard measures of contour errors do not correlate with MBFs, which is relevant for the evaluation of automated contouring algorithms applied to cardiac perfusion DCE-MRI. This research has also provided a framework for investigating the effects of contour errors using simulated contour errors, which have been shown to be representative of human contourer errors. The study is currently limited in applicability as it was carried out on healthy volunteers only. As it stands the method could not be extended to ischaemic patients as it would not be possible to separate MBF changes due to contour errors and those due to ischaemia. However, using the methodologies outlined in chapters 8 and 9 diagnostic performance could be used as an outcome measure to evaluate contour errors on ischaemic patients. This would provide much more clinically relevant information about the required accuracies in contour errors across the heart.

Although 50 patients would be considered large in most quantitative perfusion publications it represents only 6.5% of the CE-MARC dataset. To repeat these studies on the full CE-MARC dataset would greatly increase the evidence basis for driving forward a consensus opinion on analysis methods. The wealth of questions that could be answered using such a dataset is substantial. Consider again Figure 1-1, representing the quantitation pathway with which this thesis commenced. It is apparent that the depth of focus of the research represented in this thesis is not uniform across the steps of the analysis pathway. The choice of perfusion model has been investigated thoroughly, however only one of many concentration conversion methods has been assessed. Some aspects of mapping regions to arteries have been considered and localisation errors have been characterised but not related to diagnostic performance. A comprehensive analysis of each of these steps in terms of diagnostic performance would provide a much needed evidence base for standardising quantitative cardiac perfusion analysis. Such a standard would be a significant step towards the clinical acceptance of quantitative MBF estimates and the benefits they bring to the patient population and should therefore be a focus of research effort in the future.

10.2. Conclusion

Considering the quantitation pathway illustrated in Figure 1-1, the research presented in this thesis has made contributions to each step in the pathway. In the area of myocardial contouring a novel methodology has been described for investigating the relationship between contour errors and MBF. This has been used to show that established segmentation metrics such as Dice's similarity coefficient and Hausdorff distance are insufficient evaluators of contour errors. A set of contour error limits, based on volunteer datasets, has then been presented. This approach highlights what level of contour accuracy is actually required; focusing researcher's efforts on potentially more important areas such as robustness in automated localisation algorithms.

Regarding the mapping of AHA regions to the final diagnosis, the novel use of diagnostic performance to evaluate the methodology has produced a number of insights. The fact that the AHA regional analysis performs better than simply averaging the myocardium is perhaps not surprising but, to the author's knowledge, this is the first time that it has been evidenced with this method. The insight that the middle slice alone performs almost as well as all three slices is interesting and could be the basis of an argument for focussing scan time on a single slice for quantitation allowing better resolution. Again, to the author's knowledge this has not been shown before in terms of diagnostic performance using quantitative MBF estimates. The result that DCE-MRI data in the linear concentration to signal intensity regime do not perform better than those in a non-linear regime has been shown before in the context of dual-bolus imaging (25), on a similar sized dataset (n=49). However, the results presented in this thesis are the first time that this has been shown using a non-linear correction method.

The non-linear conversion of signal intensities to concentrations presented in this thesis is closely based on methods that have been previously published (30,31). To the author's knowledge, the use of an assumed T_1 for blood in this method is novel in cardiac DCE-MRI. The use of the full signal equation, incorporating flip angle sweep is also novel in this context. The conversion has been tested in simulations and on T_1-gel phantoms. The method has not been tested in-vivo because of doubts about the validity of the dual-bolus protocol used and the evidence for these doubts has been described in detail.

A comparison of perfusion models has been presented previously, and evaluated in terms of the estimated MBF values (4). Besides using a much larger patient cohort than that of Pack et al., the perfusion model comparison presented in this thesis is novel in that it has compared the models in terms of diagnostic performance. The results are therefore directly applicable to clinical practice. Although the performances did not differ significantly there was evidence for favouring Fermi-constrained deconvolution or the one-compartment model due to their increased robustness and ease of implementation.

Every innovation in a complicated process such as quantitative DCE-MRI analysis must, of course, be initially evaluated in terms of its primary outcome, be it a measure of contrast agent concentration, contour accuracy or MBF. Ultimately, however, the entire methodological pathway must be linked and evaluated in terms of the decision it was designed to make. In this case this is the diagnosis of myocardial ischaemia. This thesis has proposed methods for making this link for each step of the analysis pathway for quantitative cardiac DCE-MRI perfusion. For some steps a full diagnostic performance evaluation has been performed and it is to be hoped that these data will contribute towards the evidence base upon which a consensus methodology will be agreed upon. For other steps only the initial evaluations have been performed. However, the methods for relating each step to a final evaluation in terms of diagnostic performance are now clear. It is hoped that these methods will be used in future to evaluate the entire pathway and help to provide an evidence based consensus methodology for quantitative cardiac perfusion DCE-MRI.

11. References

1. Scarborough P, Bhatnagar P, Wickramasinghe K, Smolina K, Mitchell C, Rayner M. Coronary heart disease statistics 2010 edition. 2010.

2. Greenwood JP, Maredia N, Younger JF, Brown JM, Nixon J, Everett CC, et al. Cardiovascular magnetic resonance and single-photon emission computed tomography for diagnosis of coronary heart disease (CE-MARC): a prospective trial. The Lancet. 2012 Feb 4;379(9814):453–60.

3. Schwitter J, Wacker CM, Wilke N, Al-Saadi N, Sauer E, Huettle K, et al. MR-IMPACT II: Magnetic Resonance Imaging for Myocardial Perfusion Assessment in Coronary artery disease Trial: perfusion-cardiac magnetic resonance vs. single-photon emission computed tomography for the detection of coronary artery disease: a comparative. European heart journal. 2012 Mar 4;

4. Pack NA, DiBella EVR. Comparison of myocardial perfusion estimates from dynamic contrast-enhanced magnetic resonance imaging with four quantitative analysis methods. Magnetic Resonance in Medicine. 2010;64:125–37.

5. Ritter C, Brackertz A, Sandstede J, Beer M, Hahn D, Kostler H. Absolute quantification of myocardial perfusion under adenosine stress. Magnetic Resonance in Medicine. 2006;56(4):844–9.

6. Pack N a, DiBella EVR, Rust TC, Kadrmas DJ, McGann CJ, Butterfield R, et al. Estimating myocardial perfusion from dynamic contrast-enhanced CMR with a model-independent deconvolution method. Journal of cardiovascular magnetic resonance. 2008 Jan;10:52.

7. Hanson LG. Is quantum mechanics necessary for understanding magnetic resonance? Concepts in Magnetic Resonance Part A. 2008 Sep;32A(5):329–40.

8. Levitt MH. Spin Dynamics: basics of nuclear magnetic resonance. John Wiley & Sons, Ltd.; 2001.

9. Biglands J, Radjenovic A, Ridgway J. Cardiovascular magnetic resonance physics for clinicians: part II. Journal of Cardiovascular Magnetic Resonance. 2012;14(66).

10. Grobner T. Gadolinium--a specific trigger for the development of nephrogenic fibrosing dermopathy and nephrogenic systemic fibrosis? Nephrology, dialysis, transplantation. 2006 Apr;21(4):1104–8.

11. Marckmann P, Skov L, Rossen K, Dupont A, Damholt MB, Heaf JG, et al. Nephrogenic systemic fibrosis: suspected causative role of gadodiamide used for contrast-enhanced magnetic resonance imaging. Journal of the

American Society of Nephrology. 2006 Sep;17(9):2359–62.

12. Kanal E, Barkovich a J, Bell C, Borgstede JP, Bradley WG, Froelich JW, et al. ACR guidance document for safe MR practices: 2007. American journal of roentgenology. 2007 Jun;188(6):1447–74.

13. Rohrer M, Bauer H, Mintorovitch J, Requardt M, Weinmann H-J. Comparison of magnetic properties of MRI contrast media solutions at different magnetic field strengths. Investigative radiology. 2005 Nov;40(11):715–24.

14. Jerosch-herold M, Wilke N, Wang Y, Gong G, Mansoor AM, Huang H, et al. Direct comparison of an intravascular and an extracellular contrast agent for quantifcation of myocardial perfusion. International journal of cardiac imaging. 1999;15:453–64.

15. Lyne JC, Gatehouse PD, Assomull RG, Smith GC, Kellman P, Firmin DN, et al. Direct comparison of myocardial perfusion cardiovascular magnetic resonance sequences with parallel acquisition. Journal of magnetic resonance imaging. 2007 Dec;26(6):1444–51.

16. Wang Y, Moin K, Akinboboye O, Reichek N. Myocardial first pass perfusion: steady-state free precession versus spoiled gradient echo and segmented echo planar imaging. Magnetic resonance in medicine. 2005 Nov;54(5):1123–9.

17. Fenchel M, Helber U, Simonetti OP, Stauder NI, Kramer U, Nguyen C-N, et al. Multislice first-pass myocardial perfusion imaging: Comparison of saturation recovery (SR)-TrueFISP-two-dimensional (2D) and SR-TurboFLASH-2D pulse sequences. Journal of magnetic resonance imaging. 2004 May;19(5):555–63.

18. Kellman P, Arai AE. Imaging sequences for first pass perfusion --a review. Journal of Cardiovascular Magnetic Resonance. 2007;9(3):525–37.

19. Gerber BL, Raman S V, Nayak K, Epstein FH, Ferreira P, Axel L, et al. Myocardial first-pass perfusion cardiovascular magnetic resonance: history, theory, and current state of the art. Journal of Cardiovascular Magnetic Resonance. 2008;18(10):1–18.

20. Cerqueira MD, Weissman NJ, Dilsizian V, Jacobs AK, Sanjiv K, Laskey WK, et al. Standardized Myocardial Segmentation and Nomenclature for Tomographic Imaging of the Heart: A Statement for Healthcare Professionals From the Cardiac Imaging Committee of the Council on Clinical Cardiology of the American Heart Association. Circulation. 2002 Jan;105(4):539–42.

21. Jerosch-Herold M. Quantification of myocardial perfusion by cardiovascular magnetic resonance. Journal of cardiovascular magnetic resonance. BioMed Central Ltd; 2010 Jan;12(1):57.

22. Di Bella EVR, Parker DL, Sinusas a J. On the dark rim artifact in dynamic contrast-enhanced MRI myocardial perfusion studies. Magnetic resonance in medicine. 2005 Nov;54(5):1295–9.

23. Greenwood JP, Maredia N, Radjenovic A, Brown JM, Nixon J, Farrin AJ, et al. Clinical evaluation of magnetic resonance imaging in coronary heart disease: the CE-MARC study. Trials. 2009 Jan;10(62).

24. Utz W, Niendorf T, Wassmuth R, Messroghli D, Dietz R, Schulz-Menger J. Contrast-dose relation in first-pass myocardial MR perfusion imaging. Journal of magnetic resonance imaging. 2007 Jun;25(6):1131–5.

25. Groothuis JGJ, Kremers FPPJ, Beek AM, Brinckman SL, Tuinenburg AC, Jerosch-Herold M, et al. Comparison of dual to single contrast bolus magnetic resonance myocardial perfusion imaging for detection of significant coronary artery disease. Journal of magnetic resonance imaging. 2010 Jul;32(1):88–93.

26. Gatehouse PD, Elkington AG, Ablitt N a, Yang G-Z, Pennell DJ, Firmin DN. Accurate assessment of the arterial input function during high-dose myocardial perfusion cardiovascular magnetic resonance. Journal of magnetic resonance imaging. 2004 Jul;20(1):39–45.

27. Hsu L-Y, Kellman P, Arai AE. Nonlinear myocardial signal intensity correction improves quantification of contrast-enhanced first-pass MR perfusion in humans. Journal of magnetic resonance imaging. 2008 Apr;27(4):793–801.

28. Cernicanu A, Axel L. Theory-based signal calibration with single-point T1 measurements for first-pass quantitative perfusion MRI studies. Academic radiology. 2006 Jun;13(6):686–93.

29. Fritz-Hansen T, Hove JD, Kofoed KF, Kelbaek H, Larsson HBW. Quantification of MRI measured myocardial perfusion reserve in healthy humans: A comparison with positron emission tomography. Journal of Magnetic Resonance Imaging. 2008;27(4):818–24.

30. Fritz-Hansen T, Rostrup E, Larsson HB, Søndergaard L, Ring P, Henriksen O. Measurement of the arterial concentration of Gd-DTPA using MRI: a step toward quantitative perfusion imaging. Magnetic resonance in medicine. 1996 Aug;36(2):225–31.

31. Larsson HBW, FritzHansen T, Rostrup E, Sondergaard L, Ring P, Henriksen O. Myocardial perfusion modeling using MRI. Magnetic Resonance in Medicine. 1996;35(5):716–26.

32. Arai AE. Magnetic resonance first-pass myocardial perfusion imaging. Topics in magnetic resonance imaging. 2000;11(6):383–98.

33. Schreiber WG, Schmitt M, Kalden P, Mohrs OK, Kreitner K-F, Thelen M. Dynamic contrast-enhanced myocardial perfusion imaging using saturation-prepared TrueFISP. Journal of Magnetic Resonance Imaging.

2002 Dec;16(6):641–52.

34. Elkington AG, Gatehouse PD, Cannell TM, Moon JC, Prasad SK, Firmin DN, et al. Comparison of hybrid echo-planar imaging and FLASH myocardial perfusion cardiovascular MR imaging. Radiology. 2005 Apr;235(1):237–43.

35. Storey P, Chen Q, Li W, Edelman RR, Prasad P V. Band artifacts due to bulk motion. Magnetic resonance in medicine. 2002 Dec;48(6):1028–36.

36. Kim RJ, Chen EL, Lima JA, Judd RM. Myocardial Gd-DTPA kinetics determine MRI contrast enhancement and reflect the extent and severity of myocardial injury after acute reperfused infarction. Circulation. 1996;94(12):3318–26.

37. Kim R, Edwin W, Allen R, Enn_ling C, Parker M, Simonetti O, et al. The use of contrast-enhanced magnetic resonance imaging to identify reversible myocardial dysfunction. New England Journal of Medicine. 2000;343(20):1445–53.

38. Nesto RW, Kowalchuk GJ. The ischemic cascade: temporal sequence of hemodynamic, electrocardiographic and symptomatic expressions of ischemia. The American journal of cardiology. 1987 Mar 9;59(7):23C–30C.

39. Bache RJ, Schwartz JS. Effect of perfusion pressure distal to a coronary stenosis on transmural myocardial blood flow. Circulation. 1982 May 1;65(5):928–35.

40. Panting JR, Gatehouse PD, Yang G, Grothues F, Firmin DN, Collins P, et al. Abnormal subendocardial perfusion in cardiac syndrome X detected by cardiovascular magnetic resonance imaging. New England Journal of MedicineEnglish Journal. 2002;346(25):1948–53.

41. Klocke FJ. Measurements of coronary flow reserve: defining pathophysiology versus making decisions about patient care. Circulation. 1987 Dec 1;76(6):1183–9.

42. Gibbons RJ. ACC/AHA 2002 Guideline Update for Exercise Testing: Summary Article: A Report of the American College of Cardiology/American Heart Association Task Force on Practice Guidelines (Committee to Update the 1997 Exercise Testing Guidelines). Circulation. 2002 Oct 1;106(14):1883–92.

43. Zir LM, Miller SW, Dinsmore RE, Gilbert JP, Harthorne JW. Interobserver Variability in Coronary Angiography. Circulation. 1976;53:627–32.

44. Detre KM, Wright E, Murphy ML, Takaro T. Observer agreement in evaluating coronary angiograms. Circulation. 1975 Dec 1;52(6):979–86.

45. Beauman GJ, Vogel RA. Accuracy of individual and panel visual interpretations of coronary arteriograms: Implications for clinical

decisions. Journal of the American College of Cardiology. 1990;16(1):108–13.

46. Keane D, Haase J, Slager CJ, Van Swijndregt EM, Lehmann KG, Ozaki Y, et al. Comparative Validation of Quantitative Coronary Angiography Systems: Results and Implications From a Multicenter Study Using a Standardized Approach. Circulation. 1995 Apr 15;91(8):2174–83.

47. Marcus ML, Hiratzka LF, Doty DB, Wright CB, Harrison DG, White CW. Coronary Obstructive Lesions: Assessing Their Physiological Significance in Humans. The Annals of Thoracic Surgery. The Society of Thoracic Surgeons; 1986 Dec;42(6):S5–S8.

48. Kirkeeide RL, Gould KL, Parsel L. Assessment of Coronary Stenoses by Myocardial Perfusion Imaging During Pharmacologic Coronary Vasodilation . VII . Validation of Coronary Flow Reserve as a Single Integrated Functional Measure of Stenosis Severity Reflecting All Its Geometric Dimensions. Journal of the American College of Cardiology. American College of Cardiology Foundation; 1986 Jan;7(1):103–13.

49. Berrington de González A, Darby S. Risk of cancer from diagnostic X-rays: estimates for the UK and 14 other countries. Lancet. 2004 Jan 31;363(9406):345–51.

50. Razavi R, Hill DLG, Keevil SF, Miquel ME, Muthurangu V, Hegde S, et al. Cardiac catheterisation guided by MRI in children and adults with congenital heart disease. Lancet. 2003 Dec 6;362(9399):1877–82.

51. Acampa W, Cuocolo A, Sullo P, Varrone A, Nicolai E, Pace L, et al. Direct comparison of technetium 99m-sestamibi and technetium 99m-tetrofosmin cardiac single photon emission computed tomography in patients with coronary artery disease. J Nucl Cardiol. 1998;5(3):265–74.

52. Kapur A, Latus KA, Davies G, Dhawan RT, Eastick S, Jarritt PH, et al. A comparison of three radionuclide myocardial perfusion tracers in clinical practice: the ROBUST study. European Journal of Nuclear Medicine and Molecular Imaging. 2002;29(12):1608–16.

53. Gupta NC, Esterbrooks DJ, Hilleman DE, Mohiuddin SM. Comparison of Adenosine and Exercise Thallium-201 Single-Photon Emission Computed Tomography (SPECT) Myocardial Perfusion Imaging. JACC. 1991;19(2):248–57.

54. Dondi M, Monetti N, Levorato M, Corbelli C, Zagni P, Tartagni F, et al. Diagnostic accuracy of single photon emission computed tomography with thallium-201 for the identification of diseased coronary arteries. Comparison between dipyridamole infusion and exercise stress test. J Nucl Med Allied Sci. 1990;34(1):19–23.

55. Onoguchi M, Maruno H, Fujinaga T, Komiyama N, Takayama T, Murata H. Comparison of regional myocardial technetium-99m-MIBI uptake between ECG-gated and ungated SPECT imaging. J Nucl Med Technol.

1997;25(3):181–6.

56. Fricke E, Fricke H, Weise R, Kammeier A, Hagedorn R, Lotz N, et al. Attenuation correction of myocardial SPECT perfusion images with low-dose CT: evaluation of the method by comparison with perfusion PET. Journal of nuclear medicine. 2005 May;46(5):736–44.

57. Masood Y, Liu Y, Depuey G, Taillefer R, Araujo L, Allen S, et al. Clinical validation of SPECT attenuation correction using x-ray computed tomography-derived attenuation maps: multicenter clinical trial with angiographic correlation. Journal of nuclear cardiology. 2005;12(6):676–86.

58. DePasquale EE, Nody a. C, DePuey EG, Garcia E V., Pilcher G, Bredlau C, et al. Quantitative rotational thallium-201 tomography for identifying and localizing coronary artery disease. Circulation. 1988 Feb 1;77(2):316–27.

59. Mahmarian JJ, Boyce TM, Goldberg RK, Cocanougher MK, Roberts R, Verani MS. Quantitative exercise thallium-201 single photon emission computed tomography for the enhanced diagnosis of ischemic heart disease. Journal of the American College of Cardiology. American College of Cardiology Foundation; 1990 Feb;15(2):318–29.

60. Tamaki N, Yonekura Y, Mukai T, Kodama S, Kadota K, Kambara H, et al. Stress thallium-201 transaxial emission computed tomography: Quantitative versus qualitative analysis for evaluation of coronary artery disease. Journal of the American College of Cardiology. American College of Cardiology Foundation; 1984 Dec;4(6):1213–21.

61. Di Carli MF, Dorbala S, Meserve J, El Fakhri G, Sitek A, Moore SC. Clinical myocardial perfusion PET/CT. Journal of nuclear medicine. 2007 May;48(5):783–93.

62. Knuuti J, Kajander S, Mäki M, Ukkonen H. Quantification of myocardial blood flow will reform the detection of CAD. Journal of nuclear cardiology. 2009;16(4):497–506.

63. Araujo LI, Lammertsma a a, Rhodes CG, McFalls EO, Iida H, Rechavia E, et al. Noninvasive quantification of regional myocardial blood flow in coronary artery disease with oxygen-15-labeled carbon dioxide inhalation and positron emission tomography. Circulation. 1991 Mar;83(3):875–85.

64. Bergmann SR, Fox K a., Rand a. L, McElvany KD, Welch MJ, Markham J, et al. Quantification of regional myocardial blood flow in vivo with H215O. Circulation. 1984 Oct 1;70(4):724–33.

65. Kuhle WG, Porenta G, Huang SC, Buxton D, Gambhir SS, Hansen H, et al. Quantification of regional myocardial blood flow using 13N-ammonia and reoriented dynamic positron emission tomographic imaging. Circulation. 1992 Sep;86(3):1004–17.

66. Muzik O, Beanlands RS, Hutchins GD, Mangner TJ, Nguyen N, Schwaiger M. Validation of nitrogen-13-ammonia tracer kinetic model for quantification of myocardial blood flow using PET. Journal of nuclear medicine. 1993 Jan;34(1):83–91.

67. Schwaiger M, Muzik O. Assessment of myocardial perfusion by positron emission tomography. The American journal of cardiology. 1991 May 21;67(14):35D–43D.

68. Jaarsma C, Leiner T, Bekkers SC, Crijns HJ, Wildberger JE, Nagel E, et al. Diagnostic performance of noninvasive myocardial perfusion imaging using single-photon emission computed tomography, cardiac magnetic resonance, and positron emission tomography imaging for the detection of obstructive coronary artery disease: a meta-anal. Journal of the American College of Cardiology. Elsevier Inc.; 2012 May 8;59(19):1719–28.

69. Morton G, Chiribiri A, Ishida M, Hussain ST, Schuster A, Indermuehle A, et al. Quantification of absolute myocardial perfusion in patients with coronary artery disease: comparison between cardiovascular magnetic resonance and positron emission tomography. Journal of the American College of Cardiology. Elsevier Inc.; 2012 Oct 16;60(16):1546–55.

70. Bengel FM, Higuchi T, Javadi MS, Lautamäki R. Cardiac positron emission tomography. Journal of the American College of Cardiology. American College of Cardiology Foundation; 2009 Jun 30;54(1):1–15.

71. Gould KL. Does coronary flow trump coronary anatomy? JACC. Cardiovascular imaging. American College of Cardiology Foundation; 2009 Aug;2(8):1009–23.

72. Kaul S, Kelly P, Oliner JD, Glasheen WP, Keller MW, Watson DD. Assessment of regional myocardial blood flow with myocardial contrast two-dimensional echocardiography. Journal of the American College of Cardiology. 1989 Feb;13(2):468–82.

73. Kaul S, Senior R, Dittrich H, Raval U, Khattar R, Lahiri A. Detection of Coronary Artery Disease With Myocardial Contrast Echocardiography Comparison With 99mTc-Sestamibi Single-Photon Emission Computed Tomography. Circulation. 1997;96:785–92.

74. Wolfkiel CJ, Ferguson JL, Chomka E V, Law WR, Labin IN, Tenzer ML, et al. Measurement of myocardial blood flow by ultrafast computed tomography. Circulation. 1987 Dec;76(6):1262–73.

75. Ludman P, Coats A, Burger P, Yang G, Poole-Wilson P, Underwood S, et al. Validation of measurement of regional myocardial perfusion in humans by ultrafast x-ray computed tomography. American Journal of Cardiac Imaging. 1993;7(4):267–79.

76. Bell MR, Lerman LO, Rumberger J a. Validation of minimally invasive measurement of myocardial perfusion using electron beam computed

tomography and application in human volunteers. Heart (British Cardiac Society). 1999 Jun;81(6):628–35.

77. Christian TF, Rettmann DW, Aletras AH, Liao SL, Taylor JL, Balaban RS, et al. Absolute myocardial perfusion in canines measured by using dual-bolus first-pass MR imaging. Radiology. 2004;232:677–84.

78. Kraitchman DL, Wilke N, Hexeberg E, JeroschHerold M, Wang Y, Parrish TB, et al. Myocardial perfusion and function in dogs with moderate coronary stenosis. Magnetic Resonance in Medicine. 1996;35(5):771–80.

79. Lee DC, Simonetti OP, Harris KR, Holly TA, Judd RM, Wu E, et al. Magnetic resonance versus radionuclide pharmacological stress perfusion imaging for flow-limiting stenoses of varying severity. Circulation. 2004;110(1):58–65.

80. Vallee JM, Sostman HD, Macfall JR, Degrado TR, Zhang J, Sebbag L, et al. Quantification of Myocardial Perhsion by MRI After Coronary Occlusion. Magnetic Resonance in Medicine. 1998;40:287–97.

81. Jerosch-Herold M, Swingen C, Seethamraju RT. Myocardial blood flow quantification with MRI by model-independent deconvolution. American Association of Physicsists in Medicine. 2002;29(5):886–97.

82. Pärkkä JP, Niemi P, Saraste A, Koskenvuo JW, Komu M, Oikonen V, et al. Comparison of MRI and positron emission tomography for measuring myocardial perfusion reserve in healthy humans. Magnetic resonance in medicine. 2006 Apr;55(4):772–9.

83. Chih S, Macdonald PS, Feneley MP, Law M, Graham RM, McCrohon J a. Reproducibility of adenosine stress cardiovascular magnetic resonance in multi-vessel symptomatic coronary artery disease. Journal of cardiovascular magnetic resonance. 2010 Jan;12:42.

84. Elkington A, Gatehouse P, Ablitt N, Yang G-Z, Firmin D, Pennell D. Interstudy Reproducibility of Quantitative Perfusion Cardiovascular Magnetic Resonance. Journal of Cardiovascular Magnetic Resonance. 2005 Oct 1;7(5):815–22.

85. Morton G, Jogiya R, Plein S, Schuster A, Chiribiri A, Nagel E. Quantitative cardiovascular magnetic resonance perfusion imaging: inter-study reproducibility. European heart journal cardiovascular Imaging. 2012 May 25;1–7.

86. Jerosch-Herold M, Vazquez G, Wang L, Jacobs DRJ, Folsom ARM. Variability of Myocardial Blood Flow Measurements by magnetic resonance imaging in the multi-ethnic study of atherosclerosis. Investigative Radiology. 2008;43(3):155–61.

87. Chareonthaitawee P, Kaufmann P a, Rimoldi O, Camici PG. Heterogeneity of resting and hyperemic myocardial blood flow in healthy humans. Cardiovascular research. 2001 Apr;50(1):151–61.

88. Sawada S, Muzik O. Interobserver and interstudy variability of myocardial blood flow and flow-reserve measurements with nitrogen 1 3 ammonia-labeled positron emission tomography. Journal of Nuclear Cardiology. 1995;2:413–22.

89. Schwitter J, Wacker CM, Van Rossum AC, Lombardi M, Al-Saadi N, Ahlstrom H, et al. MR-IMPACT: comparison of perfusion-cardiac magnetic resonance with single-photon emission computed tomography for the detection of coronary artery disease in a multicentre, multivendor, randomized trial. European heart journal. 2008 Feb;29(4):480–9.

90. Paetsch I, Jahnke C, Wahl A, Gebker R, Neuss M, Fleck E, et al. Comparison of dobutamine stress magnetic resonance, adenosine stress magnetic resonance, and adenosine stress magnetic resonance perfusion. Circulation. 2004 Aug 17;110(7):835–42.

91. Patel AR, Antkowiak PF, Kramer CM. Assessment of Advanced Coronary Artery Disease: Advantages of Quantitative Cardiac Magnetic Resonance Perfusion Analysis. J Am Coll Cardiol. 2010;56(7):561–9.

92. Klem I, Greulich S, Heitner JF, Kim H, Vogelsberg H, Kispert E-M, et al. Value of cardiovascular magnetic resonance stress perfusion testing for the detection of coronary artery disease in women. JACC. Cardiovascular imaging. 2008 Jul;1(4):436–45.

93. Ishida N, Sakuma H, Motoyasu M, Okinaka T, Isaka N, Nakano T, et al. Noninfarcted Myocardium: Myocardial MR Imaging and Quantitative Coronary. Radiology. 2003;229:209–16.

94. Wolff SD, Schwitter J, Coulden R, Friedrich MG, Bluemke D a, Biederman RW, et al. Myocardial first-pass perfusion magnetic resonance imaging: a multicenter dose-ranging study. Circulation. 2004 Aug 10;110(6):732–7.

95. Sakuma H, Suzawa N, Takeda K. Diagnostic Accuracy of Stress First-Pass Contrast-Enhanced Myocardial Perfusion MRI Compared with Stress Myocardial Perfusion Scintigraphy. American journal of roentgenology. 2005;185:95–102.

96. Watkins S, McGeoch R, Lyne J, Steedman T, Good R, McLaughlin M-J, et al. Validation of magnetic resonance myocardial perfusion imaging with fractional flow reserve for the detection of significant coronary heart disease. Circulation. 2009 p. 2207–13.

97. Giang TH, Nanz D, Coulden R, Friedrich M, Graves M, Al-Saadi N, et al. Detection of coronary artery disease by magnetic resonance myocardial perfusion imaging with various contrast medium doses: first European multi-centre experience. European heart journal. 2004 Sep;25(18):1657–65.

98. Rieber J, Huber A, Erhard I, Mueller S, Schweyer M, Koenig A, et al. Cardiac magnetic resonance perfusion imaging for the functional assessment of coronary artery disease: a comparison with coronary

angiography and fractional flow reserve. European heart journal. 2006 Jun;27(12):1465–71.

99. Schwitter J, Nanz D, Kneifel S, Bertschinger K, Büchi M, Knüsel PR, et al. Assessment of myocardial perfusion in coronary artery disease by magnetic resonance: a comparison with positron emission tomography and coronary angiography. Circulation. 2001 May;103(18):2230–5.

100. Plein S, Radjenovic A, Ridgway JP, Barmby D, Greenwood JP, Ball SG, et al. Coronary artery disease: myocardial perfusion MR imaging with sensitivity encoding versus conventional angiography. Radiology. 2005 May;235(2):423–30.

101. Al-Saadi N, Nagel E, Gross M, Bornstedt A, Schnackenburg B, Klein C, et al. Noninvasive detection of myocardial ischemia from perfusion reserve based on cardiovascular magnetic resonance. Circulation. 2000 Mar;101(12):1379–83.

102. Nagel E, Klein C, Paetsch I, Hettwer S, Schnackenburg B, Wegscheider K, et al. Magnetic resonance perfusion measurements for the noninvasive detection of coronary artery disease. Circulation. 2003 Jul;108(4):432–7.

103. Huber A, Sourbron S, Klauss V, Schaefer J, Bauner KU, Schweyer M, et al. Magnetic resonance perfusion of the myocardium: semiquantitative and quantitative evaluation in comparison with coronary angiography and fractional flow reserve. Investigative radiology. 2012 Jun;47(6):332–8.

104. Costa MA, Shoemaker S, Futamatsu H, Klassen C, Anglolillo DJ, Nguyen M, et al. Quantitative magnetic resonance perfusion imaging detects anatomic and physiologic coronary artery disease as measured by coronary angiography and fractional flow reserve. Journal of the American College of Cardiology. 2007;50(6):514–22.

105. Utz W, Niendorf T, Wassmuth R, Messroghli D, Dietz R, Schulz-Menger J. Contrast-dose relation in first-pass myocardial MR perfusion imaging. Journal of magnetic resonance imaging. 2007 Jun;25(6):1131–5.

106. Cerqueira MD. Standardized Myocardial Segmentation and Nomenclature for Tomographic Imaging of the Heart: A Statement for Healthcare Professionals From the Cardiac Imaging Committee of the Council on Clinical Cardiology of the American Heart Association. Circulation. 2002 Jan;105(4):539–42.

107. Maredia N, Radjenovic A, Kozerke S, Larghat A, Greenwood JP, Plein S. Effect of improving spatial or temporal resolution on image quality and quantitative perfusion assessment with k-t SENSE acceleration in first-pass CMR myocardial perfusion imaging. Magnetic Resonance in Medicine. 2010 Dec;64(6):1616–24.

108. Larghat A, Biglands J, Maredia N, Greenwood JP, Ball SG, Jerosch-Herold M, et al. Endocardial and epicardial myocardial perfusion determined by semi-quantitative and quantitative myocardial perfusion

magnetic resonance. The international journal of cardiovascular imaging. 2011 Nov 29;28(6):1499–511.

109. Lelieveldt BPF, Geest RJ, Reiber JHC. Towards “One-Stop” Cardiac MR Image Analysis. Imaging Decisions MRI. 2004 Jul;8(2):2–12.

110. Plein S, Ridgway JP, Jones TR, Bloomer TN, Sivananthan MU. Coronary Artery Disease: Assessment with a Comprehensive MR Imaging Protocol Initial Results. Radiology. 2002 Aug 12;225(1):300–7.

111. Marckmann P, Skov L, Rossen K, Dupont A, Damholt MB, Heaf JG, et al. Nephrogenic systemic fibrosis: suspected causative role of gadodiamide used for contrast-enhanced magnetic resonance imaging. Journal of the American Society of Nephrology. 2006 Sep;17(9):2359–62.

112. Kanal E, Barkovich a J, Bell C, Borgstede JP, Bradley WG, Froelich JW, et al. ACR guidance document for safe MR practices: 2007. AJR. American journal of roentgenology. 2007 Jun;188(6):1447–74.

113. Grobner T. Gadolinium--a specific trigger for the development of nephrogenic fibrosing dermopathy and nephrogenic systemic fibrosis? Nephrology, dialysis, transplantation. 2006 Apr;21(4):1104–8.

114. Broome DR, Girguis MS, Baron PW, Cottrell AC, Kjellin I, Kirk G a. Gadodiamide-associated nephrogenic systemic fibrosis: why radiologists should be concerned. American journal of roentgenology. 2007 Feb;188(2):586–92.

115. Klocke FJ, Simonetti OP, Judd RM, Kim RJ, Harris KR, Hedjbeli S, et al. Limits of Detection of Regional Differences in Vasodilated Flow in Viable Myocardium by First-Pass Magnetic Resonance Perfusion Imaging. Circulation. 2001 Nov;104(20):2412–6.

116. Zierler KL. Equations for Measuring Blood Flow by External Monitoring of Radioisotopes. Circulation Research. 1965;(16):309–21.

117. Zierler KL. Theoretical Basis of Indicator-Dilution Methods For Measuring Flow and Volume. Circulation Research. 1962;10:393–407.

118. Jerosch-Herold M. Quantification of myocardial perfusion by cardiovascular magnetic resonance. Journal of cardiovascular magnetic resonance. BioMed Central Ltd; 2010 Jan;12(1):57.

119. Axel L. Tissue mean transit-time from dynamic computed-tomography by a simple deconvolution technique. Investigative Radiology. 1983;18(1):94–9.

120. Jerosch-Herold M, Wilke N, Stillman AE. Magnetic resonance quantification of the myocardial perfusion reserve with a Fermi function model for constrained deconvolution. American Association of Physicists in Medicine. 1998;25(1):73–84.

121. Hansen. PC. Rank-Deficient and Discrete ill-posed Problems, Numerical Aspects of Linear Inversion. SIAM monographs on Mathematical Modeling and Computation (Society for Industrial and Applied Mathematics). 1998.

122. Press WH, Teukolsky SA, Vetterling WT, Flannery B. Numerical Recipes in C. The Art of Scientific Computing. Second Edi. Cambridge University Press; 1992.

123. Pack NA. Comparison of MBF estimates from DCE-MRI with four quantitative analysis methods. Proc. Intl. Soc. Mag. Reson. Med. 2009;29(5):3621–3621.

124. Sourbron SP, Buckley DL. Tracer kinetic modelling in MRI: estimating perfusion and capillary permeability. Physics in medicine and biology. 2011 Dec 15;57(2):R1–R33.

125. Sourbron SP, Buckley DL. On the scope and interpretation of the Tofts models for DCE-MRI. Magnetic resonance in medicine. 2011 Sep;66(3):735–45.

126. Ichihara T, Ishida M, Kitagawa K, Ichikawa Y, Natsume T, Yamaki N, et al. Quantitative Analysis of First-Pass Contrast-Enhanced Myocardial Perfusion MRI Using a Patlak Plot Method and Blood Saturation Correction. Magnetic Resonance in Medicine. 2009;62(2):373–83.

127. Messroghli DR, Bainbridge GJ, Alfakih K, Jones TR, Plein S, Ridgway JP, et al. Assessment of regional left ventricular function: accuracy and reproducibility of positioning standard short-axis sections in cardiac MR imaging. Radiology. 2005 Apr;235(1):229–36.

128. Radjenovic A, Biglands JD, Larghat A, Ridgway JP, Ball SG, Greenwood JP, et al. Estimates of systolic and diastolic myocardial blood flow by dynamic contrast-enhanced MRI. Magnetic Resonance in Medicine. 2010 Oct;64(6):1696–703.

129. Cheong LH, Koh TS, Hou Z. An automatic approach for estimating bolus arrival time in dynamic contrast MRI using piecewise continuous regression models. Physics in medicine and biology. 2003 Mar;48(5):N83–8.

130. Fritsch F, Carlson R. Monotone piecewise cubic interpolation. 1980;17(2):238–46.

131. Ishida M, Schuster A, Morton G, Chiribiri A, Hussain S, Paul M, et al. Development of a universal dual-bolus injection scheme for the quantitative assessment of myocardial perfusion cardiovascular magnetic resonance. Journal of cardiovascular magnetic resonance. BioMed Central Ltd; 2011 Jan;13(1):28.

132. Larsson HBW, Rosenbaum S, Fritz-Hansen T. Quantification of the effect of water exchange in dynamic contrast MRI perfusion measurements in

the brain and heart. Magnetic Resonance in Medicine. 2001;46(2):272–81.

133. Higgins D. T1 measurement for quantitative myocardial perfusion assessment with magnetic resonance imaging. University of Leeds; 2005.

134. Brent, Brent R. Algorithms for Minimization Without Derivatives. (Englewood Cliffs, NJ: Prentice-Hall); 1973.

135. Flacke SJ, Fischer SE, Lorenz CH. Measurement of the Gadopentetate Dimeglumine Partition Coefficient in Human Myocardium in Vivo: Normal Distribution and Elevation in Acute and Chronic Infarction. Cardiac Imaging. 2001;218(3):703–10.

136. Klein C, Schmal TR, Nekolla SG, Schnackenburg B, Fleck E, Nagel E. Mechanism of late gadolinium enhancement in patients with acute myocardial infarction. Journal of cardiovascular magnetic resonance. 2007 Jan;9(4):653–8.

137. Sharma P, Socolow J, Patel S, Pettigrew RI, Oshinski JN. Effect of Gd-DTPA-BMA on blood and myocardial T-1 at 1.5T and 3T in humans. Journal of Magnetic Resonance Imaging. 2006;23(3):323–30.

138. Messroghli DR, Radjenovic A, Kozerke S, Higgins DM, Sivananthan MU, Ridgway JP. Modified Look-Locker inversion recovery (MOLLI) for high-resolution T-1 mapping of the heart. Magnetic Resonance in Medicine. 2004;52(1):141–6.

139. Van Osch MJP, Vonken EP a, Viergever M a, Van der Grond J, Bakker CJG. Measuring the arterial input function with gradient echo sequences. Magnetic resonance in medicine. 2003 Jun;49(6):1067–76.

140. Vallee JM, Kasuboski L, Chatelain P, Howarth N, Righetti A, Didier D. Quantification of Myocardial Perfusion With FAST Sequence and Gd Bolus in Patients With Normal Cardiac Function. Journal of magnetic resonance imaging. 1999;203:197–203.

141. Köstler H, Ritter C, Lipp M, Beer M, Hahn D, Sandstede J. Prebolus quantitative MR heart perfusion imaging. Magnetic Resonance in Medicine. 2004 Aug;52(2):296–9.

142. Hsu L-Y, Rhoads KL, Holly JE, Kellman P, Aletras AH, Arai AE. Quantitative myocardial perfusion analysis with a dual-bolus contrast-enhanced first-pass MRI technique in humans. Journal of magnetic resonance imaging□ : JMRI. 2006 Mar;23(3):315–22.

143. Jerosch-Herold M, Seethamraju RT, Swingen CM, Wilke NM, Stillman AE. Analysis of myocardial perfusion MRI. Journal of Magnetic Resonance Imaging. 2004;19(6):758–70.

144. Stegmann MB, Olafsdóttir H, Larsson HBW. Unsupervised motion-compensation of multi-slice cardiac perfusion MRI. Medical image

analysis. 2005 Aug;9(4):394–410.

145. Santarelli M. Automated cardiac MR image segmentation: theory and measurement evaluation. Medical Engineering & Physics. 2003 Mar;25(2):149–59.

146. Adluru G, Dibella EVR, Whitaker RT. Automatic Segmentation of Cardiac Short Axis Slices in Perfusion MRI. IEEE transactions on image processing. 2006;133–6.

147. Massey F. The Kolmogorov–Smirnov test for goodness of fit. Joutnal of the American Statistical Association. 1951;48:68–78.

148. Beauchemin M, Thomson KPB, Edwards G. On the Hausdorff distance used for the evaluation of segmentation results. Canadian Journal of Remote Sensing. 1998;24:3–8.

149. Yasnoff W A, Mui J K BJW, Yasnoff W a., Mui JK, Bacus JW. Error measures for scene segmentation. Pattern Recognition. 1977;9(4):217–31.

150. Dice LR. Measures of the Amount of Ecologic Association Between Species. Ecology. 1945;26(3):297–302.

151. Ball RM, Bache RJ, Cobb FR, Greenfield JC. Regional Myocardial Blood-flow During Graded Treadmill Exercise in the Dog. Journal of Clinical Investigation. 1975;55(1):43–9.

152. Parks CM, Manohar M. Transmural coronary vasodilator reserve and flow distribution during severe exercise in ponies Transmural distribution coronary vasodilator reserve and flow during severe exercise in ponies. Journal of Applied Physiology. 1983;54:1641–52.

153. Al-Saadi N, Nagel E, Gross M, Schnackenburg B, Paetsch I, Klein C, et al. Improvement of myocardial perfusion reserve early after coronary intervention: Assessment with cardiac magnetic resonance imaging. Journal of the American College of Cardiology. 2000;36(5):1557–64.

154. Kozerke S, Plein S. Journal of Cardiovascular Magnetic Accelerated CMR using zonal , parallel and prior knowledge driven imaging methods. Journal or Cardiovascular Magnetic Resonance. 2008;18:1–18.

155. DeLong ER, DeLong DM, Clarke-Pearson DL. Comparing the areas under two or more correlated receiver operating characteristic curves: a nonparametric approach. Biometrics. 1988 Sep;44(3):837–45.

156. Utz W, Greiser A, Niendorf T, Dietz R, Schulz-Menger J. Single- or dual-bolus approach for the assessment of myocardial perfusion reserve in quantitative MR perfusion imaging. Magnetic resonance in medicine. 2008 Jun;59(6):1373–7.

157. Christian TF, Aletras AH, Arai AE. Estimation of absolute myocardial

blood flow during first-pass MR perfusion imaging using a dual-bolus injection technique: Comparison to single-bolus injection method. Journal of Magnetic Resonance Imaging. 2008;27(6):1271–7.

158. Biglands J, Larghat A, Plein S, Buckley D, Jerosch-Herold M, Magee D, et al. Saturation Correction of Dynamic Contrast Enhanced MRI Uptake Curves for Quantitative Myocardial Blood Flow Measurements Using an Assumed T1 for Blood. Proc. Int. Soc. Mag. Res. 2010 (Stockholm, Sweden). 2010;abstract 3734.

159. Biglands J, Magee D, Boyle R, Larghat A, Plein S, Radjenović A. Evaluation of the effect of myocardial segmentation errors on myocardial blood flow estimates from DCE-MRI. Physics in medicine and biology. 2011 Apr;56(8):2423–43.